UNIVERSITY OF OKLAHOMA

GRADUATE COLLEGE

ASSIMILATION OF GROUND-BASED REMOTE SENSORS FOR IMPROVING THE PREDICTION OF BORE-GENERATING NOCTURNAL CONVECTION

A DISSERTATION

SUBMITTED TO THE GRADUATE FACULTY

in partial fulfillment of the requirements for the

Degree of

DOCTOR OF PHILOSOPHY

By

Hristo Georgiev Chipilski
Norman, Oklahoma
2021

Downloaded from SHAREOK. Persistent Handle URL: https://hdl.handle.net/11244/330164

ASSIMILATION OF GROUND-BASED REMOTE SENSORS FOR IMPROVING THE PREDICTION OF BORE-GENERATING NOCTURNAL CONVECTION

A DISSERTATION APPROVED FOR THE
SCHOOL OF METEOROLOGY

BY THE COMMITTEE CONSISTING OF

Dr. Xuguang Wang, Chair

Dr. David B. Parsons, Co-Chair

Dr. Alan Shapiro

Dr. Evgeni Fedorovich

Dr. Nikola Petrov

© Copyright by HRISTO GEORGIEV CHIPILSKI 2021
All Rights Reserved.

Acknowledgments

I dedicate this dissertation to my beloved mother Donka who is sadly not around us anymore. She worked as an aviation meteorologist and forged my passion for the weather at a very young age. I still remember how I would ask her countless questions about the different cloud types and get fascinated by the colorful screens in her office. Having realized my strong interest in meteorology, my mother motivated me to put additional efforts at school and was always willing to go over my homeworks, regardless of how busy her day was. She also played an instrumental role in my undergraduate years, closely following my academic progress and helping me grasp important concepts through practical examples. But what I appreciated the most during her final years were our numerous holiday trips: I consider myself very lucky to have spent so many great moments with my mother and will forever treasure them in my heart.

I am also thankful to the rest of my family for providing moral support during this PhD degree. Ever since my father Georgi first introduced me to the fascinating sport of tennis, I have learnt to be a highly disciplined and motivated person. His rational way of thinking and positive attitude have taught me how to quickly get back on my feet at difficult times. Being in a senior leadership position, my father has also shared many important lessons that I still apply on a daily basis.

I extend my appreciation toward my grandparents Petra and Hristo who devoted 13 years of their life to raise me as a kid. I could not have asked for a happier childhood: from unhurried weekend train rides to intense evening chess games, my grandfather was always ready to engage in my next adventure. My grandmother was similarly caring – she helped me develop a great work ethic, but also taught me how to be a kind and considerate person.

It goes without saying that becoming a doctor would have not been possible without the dedication, mentorship and support of my PhD committee. Xuguang, it has been pleasure to work with you over the last 5 years. You have showed me how to nurture scientific

curiosity and achieve success through hard work and determination. Dave, thank you for your active participation in my academic endeavours, be it through interesting discussions or detailed feedback on paper submissions. Your insightful career advice over the past year has been of tremendous help. I will miss our casual chats in the NWC hallways! Alan, I am honored to have been able to take so many of your classes in fluid dynamics. Devoting time and effort on topics not directly related to my main PhD project has encouraged me to tackle research problems in a much more comprehensive way. Evgeni, thank you for letting me enrol in your boundary layer class as an exchange student from Reading. Believe or not, the knowledge acquired from this course has helped me finish both of my degrees. Nikola, getting to know you was certainly one of the highlights of my graduate school experience – it has not only furthered my interest in mathematics, but has also allowed me to make another good friend from Bulgaria. I am very grateful to have spent so many enjoyable moments with you and your wonderful family.

I am further indebted to numerous other people from the School of Meteorology for making my PhD journey a lot smoother. Fred and Elinor, your commitment to Reading's exchange program and friendly interaction with my university colleagues was an important factor in my decision to come back to OU. Cameron, you are one of the very few academics who would be willing to chat with students at any time during the day – I am so glad to have been one of them and to hear your delightful stories. Christie, Debbie and Shelby, thank you for navigating me through important Graduate School requirements and carefully listening to my concerns as an international student. Shawn, Ben and David, your readiness to offer IT support even outside of office hours has always been deeply appreciated. Tanya, I sincerely thank you for patiently explaining to me the ins and outs of reporting travel expenses and managing GRA stipends.

Lucy Lane once said that friendships can happen any 'where' and any 'when'. I cannot agree more with her and would like to express my deep gratitude toward all friends I have made during my stay in Oklahoma. Starting a new life in a foreign country can be a

rather daunting experience, but quickly turns into a thrilling adventure when it is shared with the right people around you. I am equally thankful to my other friends from Bulgaria and the UK who have kept me sane throughout this time – either by inviting me to breathtaking RV trips or by simply chatting to me over the phone.

The final acknowledgements go to my extraordinary girlfriend Dania. Your charisma, warm-heartedness, native wit and contagious laughter instantly won my heart during our first meeting. It is impossible to describe how thankful I am for all the great moments we have shared together ever since. Without your unconditional love and support, my road to obtaining a PhD degree would have been much more difficult. I am very proud of all your achievements and cannot wait to see what the future holds for both of us.

Table of Contents

Acknowledgments **iv**

List of Tables **x**

List of Figures **xiii**

Abstract **xxxiv**

1 Introduction **1**
1.1 Background . . . 1
1.1.1 The Global Observing System . . . 1
1.1.2 The observation gap in the Planetary Boundary Layer . . . 3
1.1.3 The need for ground-based remote sensing . . . 5
1.2 Contributions and dissertation overview . . . 7

2 Theory, data and methods **10**
2.1 Atmospheric bores . . . 10
2.1.1 Hydraulic theory . . . 12
2.1.1.1 Setup . . . 12
2.1.1.2 Steady state solutions without jump conditions . . . 15
2.1.1.3 Steady state solutions with jump conditions . . . 16
2.1.2 Limitations of hydraulic theory . . . 19
2.2 Ensemble Kalman filtering . . . 21
2.2.1 Data assimilation overview . . . 21
2.2.2 The general filtering problem and its solution . . . 22
2.2.3 Kalman filter (KF) . . . 25
2.2.4 EnKF as a Monte Carlo implementation of the KF . . . 28
2.2.5 Ensemble square root filter (EnSRF) . . . 30
2.3 Overview of the PECAN field campaign . . . 32
2.4 Assimilated datasets . . . 33
2.4.1 Conventional observations . . . 33
2.4.2 Thermodynamic remote sensors . . . 34
2.4.3 Kinematic remote sensors . . . 35

2.4.4 In situ PECAN observations . . . 35
2.5 GSI-EnKF-WRF system . . . 36

3 Object-based algorithm for the identification and tracking of convective outflow boundaries in numerical models 38
3.1 Introduction . . . 38
3.2 Identification of convective outflow boundaries . . . 42
3.2.1 Concept . . . 42
3.2.2 Implementation . . . 47
3.2.3 Grid-spacing considerations . . . 50
3.3 Tracking of convective outflow boundaries . . . 53
3.3.1 Concept . . . 53
3.3.2 Implementation . . . 54
3.4 Applications of the object-based algorithm . . . 61
3.4.1 Theoretical prediction of bores based on environmental profiles from NWP models . . . 61
3.4.2 Analysis of object attributes based on explicitly resolved convective outflow boundaries . . . 66
3.4.3 Object-based probabilities of explicitly resolved convective outflow boundaries . . . 72
3.5 Summary . . . 74

4 Impact of assimilating PECAN profilers on the prediction of bore-driven nocturnal convection: a multiscale forecast evaluation for the 6 July 2015 case study 78
4.1 Introduction . . . 78
4.2 Case study overview and PECAN data availability . . . 82
4.3 Methods . . . 85
4.3.1 Experimental design . . . 85
4.3.2 Verification and diagnostics of the bore forecasts . . . 88
4.4 Bore environment . . . 90
4.4.1 Observed bore environment . . . 92
4.4.2 Forecast impacts . . . 96
4.4.3 Examination of the forecast impacts . . . 98
4.5 Explicitly resolved bore . . . 99
4.5.1 UWKA observations and forecast impacts . . . 101
4.5.2 Examination of the forecast impacts . . . 107
4.6 Bore-initiated convection . . . 112
4.6.1 Radar observations and forecast impacts . . . 112
4.6.2 Examination of the forecast impacts . . . 118
4.7 Summary . . . 119

5 The value of assimilating different ground-based profiling networks on the forecasts of bore-generating nocturnal convection 123
5.1 Introduction . . . 123
5.2 Problem statement . . . 126
5.3 Experimental design . . . 128
5.3.1 System configurations . . . 130
5.3.2 PECAN observations . . . 132
5.3.3 Experiments . . . 133
5.4 Results . . . 133
5.4.1 Convective impacts . . . 133
5.4.1.1 Aggregated statistics . . . 133
5.4.1.2 Dependence of the forecast impacts on the convective predictability . . . 135
5.4.2 Bore impacts . . . 138
5.4.2.1 Verification methodology . . . 138
5.4.2.2 Spatial impacts . . . 139
5.4.2.3 Structural impacts . . . 143
5.5 Case studies . . . 143
5.5.1 Low predictability case: 11 July 2015 . . . 145
5.5.2 High predictability case: 2 July 2015 . . . 148
5.5.3 Medium predictability case: 5 June 2015 . . . 153
5.6 Summary . . . 158

6 Conclusions 161
6.1 Overall summary . . . 161
6.2 Discussion . . . 163
6.3 Future work . . . 164

Reference List 166

List of Tables

3.1 Parameter values for the identification and tracking components of the object-based algorithm. The identification thresholds refer to the smoothed and/or filtered model identification fields. 43

3.2 Dependence of the algorithm's identification component on the horizontal resolution of convection-allowing NWP models. The second and third columns show the median and interquartile range (IQR) ratios of the coarser 3-km identification variables to the original 1-km ones. To obtain these ratios, the median and IQR values from one of the ensemble members are averaged throughout the 6-h model integration period used in the 6 July 2015 case study. The fourth column shows the scaling factor $\alpha^{1\rightarrow3}$ that needs to be applied to the identification thresholds corresponding to the 3-km model output so that the algorithm results from the 1-km and 3-km model outputs match. As explained in the text, $\alpha^{1\rightarrow3}$ is derived using the quantile mapping (QM) technique. The star (*) next to $\alpha^{1\rightarrow3}_{w^{1\text{km}}}$ indicates that the threshold scaling factor for $w^{1\text{km}}$ refers to both of its thresholds, i.e. $w^{-}_{1} = 0.6$ ms^{-1} and $w^{-}_{2} = 0.2$ ms^{-1} 52

4.1 PECAN instruments assimilated during the 6 July 2015 case study. The variables T, M_v, U and V stand for temperature, mixing ratio and the two components of the horizontal wind. The asterisk (*) in the last row indicates that the NSSL's Mobile Mesonet (NSSL MM) suite consists of 6 vehicles in total – 2 NSSL vehicles, 2 NSSL MGAUS vehicles, 1 CSU MGAUS vehicle, and the NSSL NOXP scout vehicle. 84

4.2 WRF-ARW model physics. 87

4.3 List of all numerical experiments conducted as part of the 6 July 2015 case study. AIRCRAFT contains both NOAA P-3 flight level data and NASA DC-8 LASE mixing ratio profiles, while WIND_PROF only considers the assimilation of the 915 MHz radio wind profiler at the FP4 site. Note that the AERI retrievals in AERI_REDUCED are assimilated at the frequency of the FP4 radiosonde data. The horizontal and vertical EnKF localization values in the second and third columns are optimally tuned to maximize the skill of the convective forecasts (*cf.* Section 4.6). Note that the two localization values reported next to BASELINE refer to the conventional and radar observations, respectively. 87

4.4 Pre-processing and error statistics associated with the PECAN observations from IOP20. 88

4.5 Density current and flow regime characteristics according to the radiosonde observations from the MG2 (NSSL2) and MG3 (CSU) mobile sites. The variables d_0 and C_g refer to the depth and propagation speed of the cold pool, while D and F denote the non-dimensional density current depth and Froude number. The flow regime classification in the last column follows Rottman and Simpson (1989). 95

4.6 Example PECAN impacts on the forecasted bore structure for a reference grid with 10 points and based on the MAE results in Fig. 4.11. The numbers in the first row refer to the UWKA-derived bore estimates, while the remaining rows display forecast results from the main numerical experiments presented in this study. The bracketed numbers next to each experiment denote changes relative to BASELINE. 107

4.7 Summary of the key PECAN impacts for the 6 July 2015 case study. The upward- and downward-pointing arrows correspond to positive and negative forecast impacts with respect to BASELINE, while the neutral forecast impacts are denoted with a dash. The number of arrows in each of the three forecast categories provides a subjective ordering of the data assimilation experiments according to the magnitude of their impacts. 121

5.1 List of WRF physics options. 130

5.2 EnKF cycling period and assimilated PISA sites for the 10 PECAN cases used in this study. The numbers in the last 7 columns of the table indicate how many radiosondes were launched at each of the assimilated PISA site. . 132

5.3 Subjective evaluation of the forecast impacts pertaining to the spatial characteristics of the explicitly resolved bores; the + and − symbols denote positive and negative impacts, respectively. Some of the entries in the last column contain the word *synergy*, which indicates that the positive impacts in ALLPROF and/or ALL exceed those caused by the assimilation of single profiling instruments. 140

List of Figures

1.1 The physical components of the Earth system and their interactions. Schematic adopted from IPCC (2007). 2

1.2 The Global Observing System (GOS). Schematic adopted from WMO (2021). 3

1.3 Characteristic scales of meteorological processes according to Orlanski (1975). Schematic adopted from the COMET® Program (2018). 5

2.1 The typical evolution of a convectively generated density current in the nocturnal environment of the U.S. Great Plains. Schematic adopted from Haghi et al. (2017). 11

2.2 Setup of single-layer hydraulic theory (modified following Haghi 2017). *Panel a*: Flow behavior in the absence of nonlinear upstream disturbances. The variables d_0, d and η correspond to the solid obstacle's height, the fluid's depth and the fluid's displacement relative to its unperturbed height h_0. *Panel b*: Flow behavior in the presence of an upstream hydraulic jump (bore) that moves away from the solid obstacle at a constant speed c_1. As it passes through the bore, the fluid transitions from a supercritical to a subcritical state, which causes an abrupt decrease in its speed (from u_0 to u_1) and an abrupt increase in its depth (from h_0 to h_1). The flow returns back to a supercritical state downstream of the obstruction. For the quasi-steady state bore assumed in the derivation of single-layer hydraulic theory, critical flow conditions are reached at the highest point of the obstacle (with maximum height d_m) where the depth and speed of the fluid are h_c and u_c, respectively. 14

3.1 Workflow for the identification component of the algorithm. The variables p^{mslp}, $w^{1\mathrm{km}}$, $T^{2\mathrm{m}}$, $|\nabla p|$ and A^O refer to the mean sea level pressure, 1-km Above Ground Level (AGL) vertical velocity, 2-m temperature, horizontal gradient of mean sea level pressure and object area. The current and previous algorithm processing times are denoted as t and $t - \Delta t$, while t_{sep} represents the separation time beyond which the numerical noise magnitude is significantly reduced (see text for more details). To simplify the notation, superscripts are removed upon taking temporal differences between variables (e.g., Δp is equivalent to Δp^{mslp}). The parallelograms symbolically represent data I/O, the rectangles – the execution of specific algorithm routines, while the rhombi – the decision-making process needed for classifying the identified convective outflow objects as density currents or bores. The parameter values associated with the identification component of the algorithm are summarized in the first half of Table 3.1. 44

3.2 Illustrating the identification component of the algorithm. Panels (a) and (d) show the 15-min changes in the mean sea level pressure (Δp) and 2-m temperature (ΔT), respectively, after these fields have been smoothed and/or filtered with the Discrete Cosine Transform (DCT). Panel (b) displays the 1-km AGL vertical velocity ($w^{1\mathrm{km}}$, color shaded) and the 35-dBZ contour of simulated radar reflectivity (dark cyan contours). Panel (c) shows all convective outflow boundaries identified by the object-based algorithm; the target objects tracked in this particular algorithm run are plotted in black, while the rest of the convective outflow objects detected at the current model time step (06:45 UTC on 6 July 2015) – in gray. 46

3.3 Example of classifying convective outflow objects for two different forecast times – 04:00 UTC (first row) and 06:30 UTC (second row). Panels (a) and (c) show the location of the identified objects. The color shading inside them corresponds to the object morphology as determined by the identification component of the algorithm: blue represents density currents (DC), red – bores (B), while gray marks those parts of the convective outflow objects whose morphology cannot be determined unambiguously (CO). The final shape of the objects is additionally modified with the medial axis transform. The cross sections in panels (b) and (d) are taken along the line segment AA' and show the vertical velocity (w; color shading) as well the virtual potential temperature (θ_v; black curves). The thick black contours embedded within the cross sections outline the subjectively determined density current and bore, while the stippled gray shading represents the terrain height. 48

3.4 A schematic showing the concept behind the tracking component of the algorithm as well as the typical evolution of a convective outflow boundary in the night-time environment starting from an analysis time t_0. The blue (red) objects represent density currents (atmospheric bores), while the arrows denote the objects' motion vectors. 53

3.5 Workflow for the tracking component of the algorithm that illustrates the association procedure between a target object identified in a previous image frame (T) and a candidate object from the current image frame (O). The meaning of different diagram blocks remains the same as in Fig. 3.1. The superscripts TM/CD refer to the template matching/closest distance approaches used in calculating the candidate object's motion vector $\vec{V}_O$; $-\nabla\Pi$ is the pressure gradient force (PGF), while $\angle\beta(\vec{V}_O, -\nabla\Pi)$ denotes the angle between $\vec{V}_O$ and $-\nabla\Pi$. The parameter values associated with the tracking component of the algorithm are summarized in the second half of Table 3.1. 55

3.6 Application of the object tracker to a splitting case scenario (panel a). The black and gray color shading shows the position of the target and candidate objects, respectively. Their centroids are marked with a blue dot and used to estimate the candidate object's motion vector $\vec{V}_O$ (green arrow). The red arrows show the direction of the PGF ($-\nabla\Pi$) computed from the cluster of red points along the target object. The yellow boxes to the right of each candidate object summarize the output of the object tracker. Panel (b) illustrates the cross-correlation coefficient (CC) field between the target object and candidate object 1. The red star and the boxed text in the lower-left corner of the figure show the location and value of the maximum cross-correlation coefficient $CC^{\max}$. Panel (c) shows the mean sea level pressure (p^{mslp}; blue color shading) and the direction of the pressure gradient force (PGF, $-\nabla\Pi$; red arrows) along the target object. 56

3.7 A schematic illustration highlighting the benefits of using dynamical constraints in the object tracker. The black-filled shape represents a target object from a previous image frame, while the three gray-filled shapes (numbered 1, 2 and 3) – candidate objects identified in the current image frame. The black arrow indicates the direction of the PGF ($-\nabla\Pi$), while the meaning of the blue dots is the same as in Fig. 3.6. The red circle and green semicircle correspond to the static and dynamic tracker search areas whose radii is given by $R = R_s$ and $R = V_O^+ \Delta t$, respectively 60

3.8 Four-dimensional (4D) distance minimization of convective outflow objects with respect to a user-defined reference point. The schematic in panel (a) demonstrates the minimization procedure for an idealized example in which a convective outflow boundary propagates in the positive x-direction at a constant speed C. The minimum distance ($d_{\min}$) between the reference point (R; dark blue dot) and the pivot point within the convective outflow object (P; cyan dot) occurs during the second image frame at $t = \Delta t = t_{\min}$. The red line segment AA', parallel to the PGF ($-\nabla\Pi$), displays the position of the vertical cross section required for the theoretical and explicit object analyses. Panel (b) shows the application of the 4D minimization method to the ensemble forecast experiment from 6 July 2015, with point R prescribed to have a latitude of 42.4° and a longitude of -96.4°. The gray curves show the minimum distance between R and the convective outflow object at a particular forecast lead time, i.e. $\min(\mathbf{D}_t)$. The red circles mark the values of $(d_{\min}, t_{\min})$ for each ensemble member, while the black triangles indicate where the trajectory of a particular ensemble member is terminated. 63

3.9 Theoretical bore predictions performed over a reference point R with a latitude of 43.4° and a longitude of -97.7°. Panel (a) shows the ensemble flow regime distribution upstream of a density current. Forecast results are plotted in the parameter space of the Froude number (F; y-axis) and the non-dimensional height (H; x-axis). The solid black curves separate different flow regimes, while the dashed black curves mark phase regions with constant bore strength $S = h_1/h_0$. The partially blocked regime is located between the thick solid black curves. The red color shading displays the ensemble probability of a particular flow regime; probability contours (blue curves) are plotted at intervals of 0.3, starting from 0.05. The green dot indicates the position of the most likely flow regime, i.e. the mode of the ensemble distribution. Panel (b) displays the ensemble forecast results associated with the vertical Scorer parameter (l^2) profile; the black curve refers to the median Scorer profile, while the gray-shaded region shows the interquartile range of l^2 at a given height. The dashed blue curve corresponds to $l^2 = 0$. 65

3.10 Evaluating the propagation speed C_R of a convective outflow object in proximity of the user-defined reference point R=(41.7°,-97.4°). Panel (a) shows the methodology for calculating C_R based on the length of the pivot lines (PLs; purple to red colors indicating increasing PL lengths) as well as the variability of C_R in the neighborhood of R (box-and-whisker diagram in the figure inset). The meaning of the other symbols is summarized in the legend at the bottom right-hand side of the figure. Panel (b) displays the ensemble distribution of C_R. The values associated with the first, second and third quartiles (q_1,q_2 and q_3) of this distribution are shown at the top left corner of the figure. The second quartile (the median) is additionally plotted as a dashed red line. 67

3.11 Evaluating the effective bore amplitude $S_R = \left[\frac{h_1}{h_0}\right]_R$ in proximity of the user-defined reference point $R = (41.7°, -97.4°)$. The methodology for finding S_R (panel a) is illustrated with the aid of a cross-section showing the vertical velocity (w; color shading) and the virtual potential temperature (θ_v; black solid curves) along the central pivot line from Fig. 3.10a. The gray dots show the original SBL height estimate provided by the theoretical bore analysis. The minimum and maximum heights of the original SBL height estimate ($\widehat{h_0}$ and $\widehat{h_1}$) are marked with the two gray diamonds, while its uncertainty range – with the two dashed gray curves. The green dots refer to the optimal SBL height, i.e. the θ_v surface experiencing maximum bore lifting. The minimum and maximum values of this optimal SBL height define h_0 and h_1 (green diamonds), which are used in the S_R estimate. Note that the gray and the green diamonds in this example overlap due to their similar location along the cross section. Finally, panel (b) shows the ensemble distribution of S_R. The meaning of the symbols in this histogram are the same as Fig. 3.10b 70

3.12 Object-based density current (panels a and b) and bore (panels c and d) probabilities computed with respect to the largest convective outflow boundary in the 1-km ensemble forecasts of the 6 July 2015 case study. The first set of probabilities (left column) is generated for 03:15 UTC and coincides with the time when the largest convective outflow object is initialized by the algorithm. The second set of probabilities (right column) is plotted for 06:30 UTC or after the algorithm has tracked the largest convective outflow boundary for 3 hours and 15 minutes. Probability fields are smoothed with a Gaussian kernel (σ=2 km). The 35%, 65% and 95% probability values are plotted with solid lime contours. 73

4.1 Radar evolution of the 6 July 2015 nocturnal MCS case study based on a 1-km NEXREAD reflectivity mosaic (http://www2.mmm.ucar.edu/imagearchive). The locations corresponding to the first and second episodes of bore-initiated convection are indicated with a magenta ellipse in panels (d) and (g), while the horizontal scale of the maps – in the upper right corner of panel (a). . . 83

4.2 Spatial distribution of the IOP20 PECAN observations during (a) the final analysis time at 0300 UTC (*cf.* Fig. 4.3) and (b) the first episode of bore-initiated convection at 0500 UTC. Observation locations are plotted over a 10-minute period centered around these two times. Overlaid on the two panels are composite reflectivity from the Multi-Radar Multi-Sensor (MRMS) system (color shading) and the ensemble mean 2-m mixing ratio from the BASELINE experiment (solid black contours with values in gkg^{-1}). 85

4.3 Experimental design. *Panel (a)*: Model domains used for the numerical experiments in this study. The horizontal grid spacing of domains d01, d02 and d03 is 9km, 3km and 1km, respectively. Each model domain consists of 50 model levels distributed according to the default WRF settings. *Panel (b)*: Timeline of the data assimilation cycling and ensemble free forecasts. Based on initial and lateral boundary conditions from GEFS/SREF, a 40-member ensemble forecast is run between 12 UTC and 15 UTC to provide the ensemble background for the first data assimilation cycle on the outer 9-km (d01) domain. Conventional (NDAS) observations are then assimilated every 3 hours until 00 UTC on 6 July 2015, at which point the data assimilation calculations switch to the highest-resolution (d03) domain for another 3 hours. During this period, assimilation frequency is reduced to 10 minutes and the conventional observations are complemented by radar and PECAN IOP20 data. Finally, the 1-km ensemble analyses at 0300 UTC are used to launch 6-hour ensemble forecasts in order to evaluate the PECAN data impacts. 89

4.4 Neighborhood verification of the ensemble bore forecasts. Panel (a) illustrates schematically the construction of a reference grid in proximity to a verifying bore observation. The new version of the algorithm performs a four-dimensional (4D) distance minimization at each reference point (*cf.* panel b) in order select which convective outflow boundaries to analyze for each ensemble member. Once these objects are determined, the algorithm generates cross sections oriented parallel to the direction of the surface Pressure Gradient Force (PGF; solid magenta vector) to calculate various object attributes, such as the pre- and post-bore heights (h_0 and h_1). Panel (c) displays the location of the 3 reference grids used for the analysis in this study. Additional information overlaid on this panel figure includes the position of the verifying bore observations (e.g., mobile array, UWKA **I2** and **I6**), the location of the KUEX and KOAX radar sites, and the 30 dBZ MRMS reflectivity during the first episode of bore-initiated convection (0546 UTC; thin solid blue contours). The letters **N** and **S** refer to the northern and southern clusters of bore-initiated convection, while **I2** and **I6** — to the 2nd and 6th bore intercepts from the UWKA aircraft. 91

4.5 Observations of the ambient bore environment from the mobile array in southeastern South Dakota showing the temporal evolution of (a) the SBL depth (h_0) and (b) the mean inversion wind projected in the direction of density current propagation (U_0). The cross markers in the time series show Mobile PISA (MP) estimates derived from either AERI (panel a) or Doppler wind lidar (panel b) retrievals. The gray box between 0345 UTC and 0430 UTC highlights the 45-minute time period used for deriving the observed flow regime in Section 4.4. 93

4.6 Verification of the bore environment forecasts. The color shading displays the ensemble forecasts from different experiments based on the nearest 49 reference points from the northern most reference grid in Fig. 4.4 (number of ensemble members contributing to each experiment, denoted by S, is shown in the upper-left corner of each panel). The flow regime forecasts are verified against individual flow regime estimates from the NSSL2 (pink rectangle) and CSU (cyan rectangle) radiosonde units as well as the set of possible flow regime values derived from all available mobile units in South Dakota (red crosses; see text for more details). 97

4.7 Understanding how the assimilated PECAN data affects the forecasted bore environment. *Panel (a)*: Percentage change differences between PECAN_ALL and BASELINE for all 5 flow regime variables and 8 different neighborhood radii using 9, 16, 25, 36, 49, 64, 81 and 99 reference points (from left to right). *Panel (b)*: A composite density current cross section based on the northernmost reference grid in Fig. 4.4 with 99 reference points. The buoyancy field from PECAN_ALL is color shaded, while its difference relative to BASELINE is contoured in red (contours plotted every 1×10^{-2} ms^{-2}, starting from $\pm 1 \times 10^{-2}$ ms^{-2}). The $B = -5 \times 10^{-2}$ ms^{-2} value from BASELINE is marked with a heavy solid blue curve as a reference. Additionally, the solid (dashed) black contours display the virtual potential temperature from PECAN_ALL (BASELINE), which is used for the calculation of the density current and SBL depths (solid black and gray horizontal lines for BASELINE and PECAN_ALL, respectively). *Panel (c)*: Ambient wind speed from BASELINE (solid black curve) and PECAN_ALL (dashed black curve) projected in the direction opposite to density current propagation and averaged over the last 10 km of the density current cross section in panel (b). The wind profile from the corresponding radiosonde and Doppler wind lidar data is overlaid using gray color shading. Note that the verifying observations are averaged between 0345 UTC and 0430 UTC, consistent with the gray box in Fig. 4.5. The width of the gray color shading shows the variability over this 45-min period. 100

4.8 Evolution of the observed bore in Nebraska based on moisture profiles from UWKA's Compact Raman Lidar (CRL) system. The heavy black curves denote the 11.25 gkg^{-1} mixing ratio contour used to approximate the height of the SBL in the supercritical and subcritical portions of the bore (see text for more details). 101

4.9 Verification of the explicit bore forecasts near UWKA I2 (~0500 UTC). Panel (a) displays mixing ratio (color shading) and virtual potential temperature (solid black contours) from the BASELINE experiment. The heavy solid blue contour marks the SBL depth, while the two horizontal lines correspond to the UWKA-derived pre-bore and post-bore SBL heights, respectively. Note that all forecasted SBL heights are calculated using the 11.25 gkg^{-1} mixing ratio value, consistent with Fig. 4.8. The rest of the panel figures (b-h) display mixing ratio differences associated with various data assimilation experiments. The virtual potential temperature and SBL height from BASELINE are overlaid as thin and heavy dashed black contours, respectively. 103

4.10 Verification of the explicit bore forecasts near UWKA I6 (~0550 UTC). The meaning of all symbols remains the same as in Fig. 4.9. 105

4.11 Summary of the verification statistics associated with the explicit bore forecasts over UWKA I2 and UWKA I6. Solid curves with filled markers display the Mean Average Errors (MAEs) with respect to the (a) pre-bore height (h_0) and (b) post-bore height (h_1) for a different number of reference points (x-axis). The gray box at the bottom of the two panel figures shows the percentage of Statistically Different Reference Points (SDRP) relative to the BASELINE experiment. 106

4.12 Flow regime diagnostics on the bore-generating cold pool in Nebraska for the (a) AERI and (b) WIND_PROF experiments. The color shading on the two cross sections shows the ensemble mean inversion wind projected in the direction of density current propagation (U_0; color shading), with negative (positive) values indicating flow oriented towards (away) from the density current. Negative (positive) differences in U_0 with respect to the BASELINE experiment are displayed as solid blue (red) contours. The virtual potential temperature from AERI/WIND_PROF and BASELINE is plotted with solid and dashed black contours, respectively. 109

4.13 Moisture impacts on the explicit bore forecasts for the AERI (left column) and WIND_PROF (right column) experiments. Color shading refers to ensemble mean differences in mixing ratio relative to BASELINE (the letters **A** and **F** stand for analysis and forecast differences). Contours are plotted every 2 gkg^{-1} with solid lime and bisque colors (first contour appears at $\pm$1 gkg^{-1}). Black and magenta arrows show the ensemble mean wind in AERI/WIND_PROF and their difference with BASELINE. The 30 dBZ composite reflectivity and the regions where vertical velocity at 1km AGL exceeds 0.5 ms^{-1} are visualized as solid black contours and purple dots. (*Continue to Fig. 4.14*) 110

4.14 (*Continued from Fig. 4.13*) The 3 red stars at the bottom portion of the panel figures show the location of the FP4 site and the two UWKA intercepts (labelled in panel a), while the heavy solid black line – the position of the density current cross section from Fig. 4.12. Note that both the mixing ratio and vertical velocity fields are smoothed using a Gaussian filter with $\sigma = 2.0$ km. 111

4.15 Equivalent radar reflectivity (lowest elevation angle) from the KOAX radar site (Omaha, Nebraska) depicting the evolution of the first episode of bore-initiated convection for the 6 July 2015 case study. The letters **N** and **S** show the location of the northern and southern convective clusters. Radar images are generated using the Python Atmospheric Radiation Measurement (ARM) Radar Toolkit (Py-ART Helmus and Collis 2016). 113

4.16 Impact of assimilating PECAN observations on the forecasts of bore-initiated convection. The first row shows results for the BASELINE experiment through the Neighborhood Ensemble Probability (NEP; color shading) of model-simulated reflectivity exceeding 30 dBZ with a neighborhood radius of 8 km. (*Continue to Fig. 4.17*) 114

4.17 (*Continued from Fig. 4.16*) The rest of the panel figures display differences in NEP with respect to the other data assimilation experiments. The observed 30 dBZ composite reflectivity from the Multi-Radar Multi-Sensor (MRMS) system is contoured in black. 115

4.18 Sensitivity of the AERI convective forecasts to different data assimilation configurations. NEP fields from 0530 UTC are shown for the original (a) AERI and (d) RADIOSONDE experiments as well as the additionally conducted (b) AERI_SOUNDERR and (c) AERI_REDUCED experiments, which test the forecast sensitivity to different observation errors and assimilation frequencies, respectively. The rest of the symbols remain the same as in the first row of Fig. 4.16. 117

4.19 Composite cross sections for the BASELINE, AERI and WIND_PROF experiments generated in the neighborhood of the southern convective cluster (*S*; refer to the aqua reference points in Fig. 4.4). The first column shows the distribution of moisture from these three experiments (mixing ratio for BASELINE and differences in mixing ratio for AERI and WIND_PROF). The SBL height (based on the 11.25 gkg^{-1} mixing ratio value) is plotted either with a heavy solid blue curve for individual experiments or with a heavy dashed black curve for the BASELINE experiment in panels (d) and (g). The pre- and post-bore heights from UWKA I6 are overlaid as heavy horizontal magenta lines. The color shading in the second and third columns shows the composite CAPE and CIN fields for the three experiments. Virtual potential temperature is plotted in all panels with solid black contours. . . . 120

5.1 A schematic illustrating the typical evolution of a bore-generating convective system in the context of the ground-based profiling instruments assimilated in this study. Our main objective is to evaluate the impact of the assimilated profilers on the forecasted parent MCS, bore-induced convection initiation (CI; both direct and indirect) and explicitly resolved atmospheric bore (all shown in panel c). 128

5.2 Some aspects of the experimental design used in this study. *Panel a*: Location of the outer 12-km (d01; thick white rectangle) and inner 4-km (d02; thinner white rectangles) model domains as well as the assimilated fixed PISA (FP) sites (red stars). *Panel b*: Location of the assimilated mobile PISAs (MPs) (filled stars) and thermodynamic remote sensors used for bore verification (filled dots). *Panel c*: A timeline corresponding to our analysis-forecast system. Following Section 5.2, the final analysis time in each PECAN case (t_a) is chosen such that the bore-generating (parent) MCS has a well-developed cold pool. The alternating red and blue lines between 21 UTC and 00 UTC indicate that the d02 EnKF cycling can begin at either of these two times (see main text for more details). 131

5.3 Fractions skill scores (FSSs) averaged over the 10 PECAN cases and calculated for 3 different neighborhood radii (5, 25 and 150 km). The markers at the bottom of each panel indicate whether the FSS differences between a given PECAN experiment and CTL are statistically significant at the $\alpha = 0.01$ level, as determined by a bootstrap method with 10,000 resamples. The + and – symbols differentiate between positive and negative impacts, respectively. 135

5.4 As in Fig. 5.3, but the FSSs here are conditioned on the 3 predictability categories (LP, MP and HP; see main text for more details) and are only shown for $R = 25$ km. Note that statistical significance has not been tested here due to the small number of cases in each predictability category. 136

5.5 Violin plots showing the predictability-dependent FSS differences between the 5 PECAN experiments and CTL. The LP and MP cases combine all FSS differences during the first 2 hours, whereas the HP category only considers FSS differences with lead times between 2 and 5 hours. 138

5.6 Example of how the assimilation of different ground-based profiling networks affects the predicted bore extent during the 5 July 2015 case. *Panel a*: Observed low-level reflectivity mosaic at 0554 UTC (taken from the PECAN field catalogue). *Panels b-g*: Analysis mean vertical velocity at 1 km AGL (w; color shading) and 30 dBZ composite MRMS reflectivity (black contours) at 0600 UTC. The dashed ellipses in panels (a) and (c) mark the location of the eastern bore segment discussed in the main text. 141

5.7 Same as Fig. 5.6, but with respect to the propagation direction of the explicitly resolved bore during the 5 June 2015 case. Both observed and forecasted data are displayed at 0530 UTC on that day. 142

5.8 Systematic verification of the forecasted bore lifting (Δh). The bias and root-mean-square error (RMSE) associated with different experiments are summarized in the upper left corner of each panel. 144

5.9 Convective forecasts for the 11 July 2015 case, valid at 0700 UTC (corresponding to a 1h forecast lead time). The color shading in panel (a) represents the NEP values associated with CTL, whereas the color shading in the remaining panels – the NEP differences between a given PECAN experiment and CTL. Overlaid on these plots are also the 30 dBZ composite MRMS reflectivity (solid black contours), the experimental differences in the ensemble mean of water vapor mixing ratio at 500 m above the ground (Δq; light and dark green dots correspond to areas where Δq exceeds 0.5 and 1 gkg^{-1}, respectively) as well as the position of assimilated ground-based PISA sites (yellow stars). 146

5.10 FP3 innovation time series of specific humidity (d_q) averaged over the 950-850 hPa layer and shown for the second half of the 6-hour EnKF cycling period on 11 July 2015. Note that the innovation values plotted here represent the ensemble mean minus observation differences; the blue and red colors refer to the background (bg) and analysis (anl) innovations, respectively. . . 147

5.11 Comparing the 500 m AGL analysis increments in (a) TQPROF and (b) UVPROF during the last EnKF cycle on 11 July 2015. The color shading, black arrows and solid black contours represent the background ensemble means of water vapor mixing ratio (q), wind and 30 dBZ reflectivity, respectively. Positive (negative) q increments are shown as red (blue) contours and are displayed for the following values: ±0.15, ±0.25, ±0.5, ±1, ±1.5, ±2 and ±2.5 gkg^{-1}. Wind increments are shown as white arrows and are additionally magnified ∼10.6 times relative to the background wind. Note that the moisture and wind increments inside the parent MCS are deliberately clipped in order to better highlight the environmental changes brought by the assimilated ground-based remote sensors (see yellow stars). . 149

5.12 Same as Fig. 5.9, but for 0600 UTC on 2 July 2015 (corresponding to a 3h forecast lead time). The green (yellow) dots show negative (positive) differences in the u-component of the ensemble mean wind at 500 m AGL; the lighter (darker) colors mark regions where these differences exceed 0.5 (1) ms^{-1}. 150

5.13 Vertical cross sections through the cold pool associated with the parent MCS on 2 July 2015. The color shading displays the horizontal wind speed parallel to the cross section $\left(V_{||}\right)$, with positive (negative) values indicating flow oriented in the positive (negative) x-direction. The solid black contours show the virtual potential temperature and are plotted every 2 K, starting from 310 K near the surface. Vertical velocities are also shown as solid blue contours whose spacing and initial value are both set to 0.25 ms^{-1}. The maximum value of the vertical velocity (Wmax) is additionally labelled in the lower-left corner of each panel. All cross sections are valid at 0530 UTC, which corresponds to a 2.5h forecast lead time for this PECAN case. 151

5.14 Observation space diagnostics for the 2 July 2015 case. *Panel a*: Background u-wind bias profiles for UVPROF and SONDE (blue and red colors, respectively) at the FP3 site. The two solid curves show statistics from a single cycle ($c1$ or $c18$; see legend), while the dashed curve – an average bias profile calculated between the 2nd and 18th cycles. *Panel b*: Background root-mean-square innovation (RMSI) profiles of specific humidity (Q) associated with TQPROF for the 2 July 2015 (solid curve) and 11 July 2015 (dashed curves) cases. All RMSI profiles are averaged over the last 3 hours prior to model initialization. 153

5.15 As in Fig. 5.9, but for 0600 UTC on 5 June 2015 (corresponding to a 1.5h forecast lead time). 154

5.16 Dynamical interpretation of the forecast improvements during the 5 June 2015 case. *Panel a*: Analysis increments for SONDE at 0300 UTC. The meaning of all symbols is the same as in Fig. 5.11, except that the q increments are drawn at ±0.5, ±1, ±2 and ±4 gkg^{-1}, whereas the ratio of background to increment wind (represented by the black and white arrows, respectively) is ~1:3. The dashed yellow ellipse shows the position of the northeasterly wind increment discussed in the main text. *Panel b*: SONDE-CTL analysis mean q differences (Δq; color shading) at 2 km AGL and valid at 0300 UTC. Regions where Δq is equal to -0.5 gkg^{-1} are highlighted with bisque contours. The solid black contours and black arrows represent SONDE's analysis mean of 30 dBZ reflectivity and wind at 2 km AGL, respectively, while the purple dots indicate grid points where the analysis mean vertical velocity at 1 km AGL exceeds 0.15 ms^{-1}. *Panel c*: SONDE's analysis mean updraft strength at 1 km AGL (w_+; blue shading) and its change relative to CTL (red contours starting at 0.1 ms^{-1} and plotted every 0.2 ms^{-1}) at 0310 UTC. The solid black contours and black arrows have the same meaning as in panel (b), but are shown for 1 km AGL. Finally, the position of the FP3 site is marked with a yellow star in all panels. 156

5.17 Comparing the low-level analysis increments in TQPROF and UVPROF during two EnKF cycles on 5 June 2015: one before and another after the initiation of convection over the FP3 site (top and bottom rows, respectively). The data shown in these panels are the same as in Fig. 5.16a, except that the ratio of background to increment wind (black and white arrows, respectively) here is ~2:5 and the ±0.25 gkg^{-1} q increment is additionally plotted. 157

Abstract

Advances in Numerical Weather Prediction (NWP) require a synchronous improvement in the structure of the underlying Global Observing System (GOS). However, recent progress toward high-resolution modeling has not been accompanied by a commensurate increase in the number of available observations. For more than two decades, the meteorological community has identified a striking gap in the observational coverage within the Planetary Boundary Layer (PBL). This gap is particularly detrimental for convective-scale models whose forecasts depend strongly on the initial PBL structure. In an effort to confront the existing observational limitations, scientists and engineers have begun to rapidly develop novel ground-based remote sensing technology. Its ability to describe the diurnal evolution of the PBL is expected to bring large benefits for the next generation of convective-scale NWP models. In this dissertation, we support this hypothesis by showing how ground-based remote sensing instruments can improve the forecasts of bore-generating nocturnal convection observed during the Plains Elevated Convection at Night (PECAN) field campaign.

To evaluate the forecast impact of these novel instruments, we first develop an object-based algorithm for the identification and tracking of convective outflow boundaries in NWP models. The most distinct feature of the algorithm, which sets it apart from previously suggested frameworks, is its ability to seamlessly analyze density currents and bores, both of which play an important role in the dynamics of bore-generating nocturnal convection. The unified classification of these morphologically different phenomena is achieved through a multivariate approach combined with appropriate image processing techniques. The tracking component of the algorithm utilizes two dynamical constraints, which improve the object association results in comparison to methods based on statistical assumptions alone. We use a retrospective PECAN case study to illustrate how the newly developed algorithm can objectively analyse both the structure of atmospheric bores as well as the environmental conditions in which they form.

The original version of the algorithm is then extended to allow for an object-based, neighborhood verification of the ensemble bore forecasts against data from thermodynamic remote sensors. This new framework is utilized to investigate the impact of different PECAN observations on the forecasts of a bore-driven convective event that took place on 6 July 2015. Specifically, we examine the forecast impacts with respect to (i) the bore environment, (ii) the explicitly resolved bore, and (iii) the bore-initiated convection. Our findings suggest that ground-based remote sensors provide considerable advantages over conventional in situ observations, especially when the retrieved data are assimilated at a high temporal frequency. The clearest forecast improvements are seen in terms of the predicted bore environment where the assimilation of kinematic remote sensors reduces a preexisting bias in the structure of the low-level jet.

Finally, the aforementioned single case findings are generalized by performing systematic experiments with 10 additional PECAN cases that feature a diverse spectrum of convective dynamics. The purpose of these systematic experiments is to compare the forecast benefits coming from different ground-based profiling networks. Aggregated verification statistics demonstrate that the best forecast skill is achieved by simultaneously assimilating in situ and remote sensing profilers, both in terms of the parent convective system as well as the explicitly resolved bore. Our analysis suggests that it is often advantageous to collocate thermodynamic and kinematic profilers. On the other hand, the impacts from single profiler networks tend to be highly flow-dependent, with thermodynamic (kinematic) profilers playing a dominant role in cases with relatively low (high) convective predictability. In addition, deficiencies in the underlying data assimilation (DA) system as well as complexities in the governing moisture dynamics can further limit the efficacy of such networks.

Chapter 1

Introduction

1.1 Background

1.1.1 The Global Observing System

The Earth is comprised of many physical components, such as the atmosphere, hydrosphere, cryosphere, and biosphere (Fig. 1.1). Understanding the complex processes happening on Earth requires not only accurate knowledge of the dynamics associated with individual components, but also the interactions between them. Historically, the meteorological community has dedicated significant efforts to study the behaviour of the atmosphere because of its direct influence on our everyday weather. In recent years, however, there has been a gradual shift toward the development of coupled Earth system approaches that are capable of representing how the atmospheric state is influenced by other Earth system components (e.g., Penny and Hamill 2017). Aside from improving our overall physical understanding, these coupled systems hold great promise for a variety of important applications. For example, the ability to describe how snow and ice loss affects the global circulation is crucial for generating reliable climate projections. On shorter time scales, correctly simulating the heat, momentum and energy exchanges between the atmosphere and underlying ocean should improve the prediction of hurricanes and, as a result, reduce their damage to the economy and infrastructure of many countries around the globe.

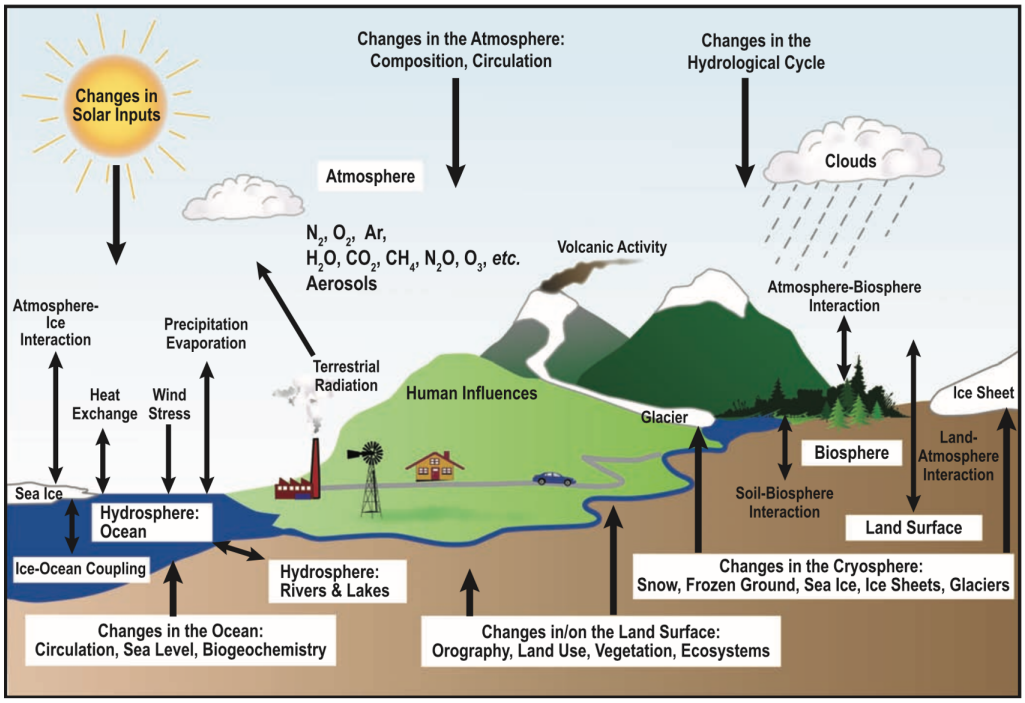

Figure 1.1: The physical components of the Earth system and their interactions. Schematic adopted from IPCC (2007).

Importantly, gleaning meaningful insights into the inner workings of the Earth system requires a comprehensive observation network. The first attempts for a more coordinated monitoring of the environmental conditions began with the deployment of a small number of surface meteorological stations during two World Wars. These stations provided valuable information for predicting the synoptic weather patterns ahead of critical military operations, such as D-Day (Persson 2020) . Since then, the number of ground-based synoptic and climatological sites has expanded rapidly to reach a truly global scale. These stations have also been complemented by measurements collected on a variety of additional observing platforms, including ships, ocean buoys, aircrafts, satellites and weather radars, that provide a more complete picture of the Earth system as a whole. Collectively, all these observations form the backbone of the so-called Global Observing System (GOS; see Fig. 1.2) maintained on behalf of the World Meteorological Organization (WMO).

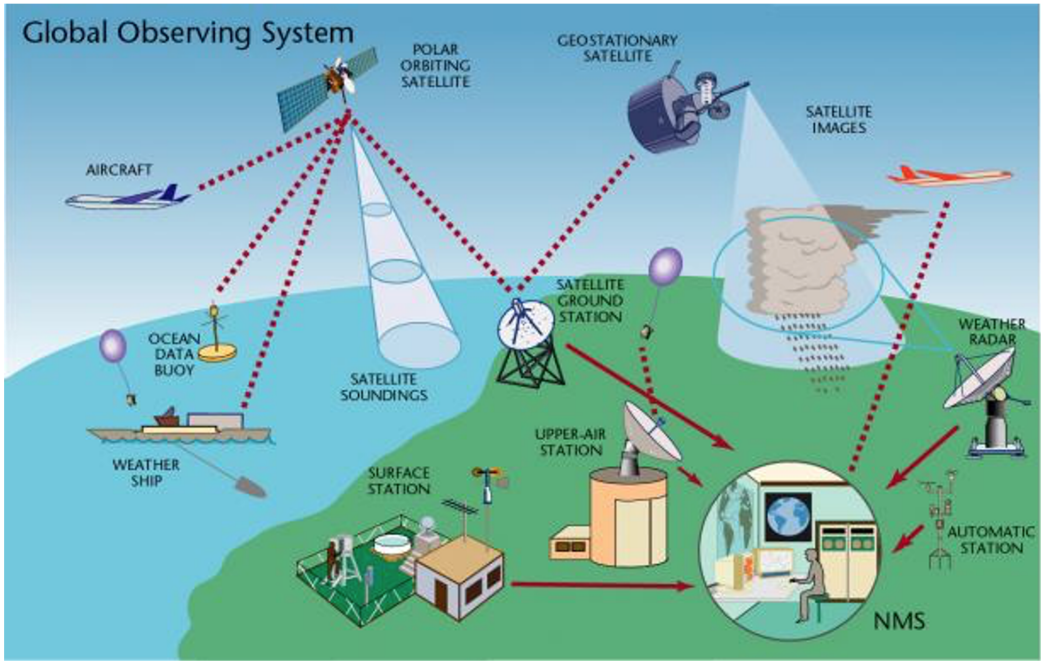

Figure 1.2: The Global Observing System (GOS). Schematic adopted from WMO (2021).

1.1.2 The observation gap in the Planetary Boundary Layer

Advances in science and technology have enabled the GOS to continue expanding its operational capabilities. The plethora of measurement techniques depicted in Fig. 1.2 speaks for the vast progress made over the last century. As a case in point, data from Doppler weather radars are now routinely assimilated in many regional numerical weather prediction (NWP) models even though the first experiments were conducted less than 20 years ago (Snyder and Zhang 2003). Despite these fast developments, some parts of the Earth system remain poorly observed. One prominent example is the Planetary Boundary Layer (PBL) – the lowest part of the atmosphere where most of the life on Earth resides. Besides having a direct influence on our daily activities, the PBL has the important function to couple the atmosphere with other Earth system components through the near-surface heat, momentum and energy exchanges. As a result, the PBL has been identified as a crucial component in both short- and long-range Earth system predictions (e.g., Stewart 1979).

There are two distinct, but closely related factors contributing to the inadequately observed PBL. The first one is linked to important gaps in the current GOS. Consider, for instance, the surface observation network: it consists of many stations around the world, but those only measure the environmental conditions directly above the surface, leaving a signficant portion of the PBL unobserved. Many ground-based synoptic stations also launch radiosondes (weather balloons), which are often regarded as the golden standard for upper-air atmospheric profiling. In an operational setting, however, radiosondes are only launched twice a day and this is far from sufficient to depict the significant diurnal changes in PBL structure. Commercial aircrafts occasionally provide lower atmospheric data during take-offs and landings, but such measurements are usually concentrated around big airports and do not capture the large spatial variability of the PBL. Referring back to Fig. 1.2, it appears that weather satellites are the only major component of the GOS not discussed so far. Although they offer a truly global coverage, satellite measurements lack the necessary resolution within the PBL. This problem is especially relevant for certain instrument types, such as microwave (MW) sounders, whose quality is much worse than that of radiosondes. The resolution within the PBL can be somewhat improved with infrared (IR) instruments, but this is limited to clear-sky conditions. Recently, the radio occultation (RO) technique has also gained popularity, especially in the midst of the COVID-19 pandemic when world-leading NWP centers demonstrated its efficacy in the absence of regular aircraft observations (Ingleby et al. 2020). However, the resolution of RO data – around 500 m in the vertical and 150-200 km in the horizontal, is still not suitable for accurately describing PBL.

The second contribution to the existing PBL gap is based on phenomenological considerations. This point can be illustrated with the aid of Fig. 1.3 by Orlanski (1975) who classified atmospheric processes according to their characteristic spatiotemporal scales. It is evident from this diagram that many of the depicted processes have their origins in the PBL – turbulence, tornadoes, dust devils, convection, urban effects and topographic disturbances. In addition, many of these processes are located in the lower-left portion of the

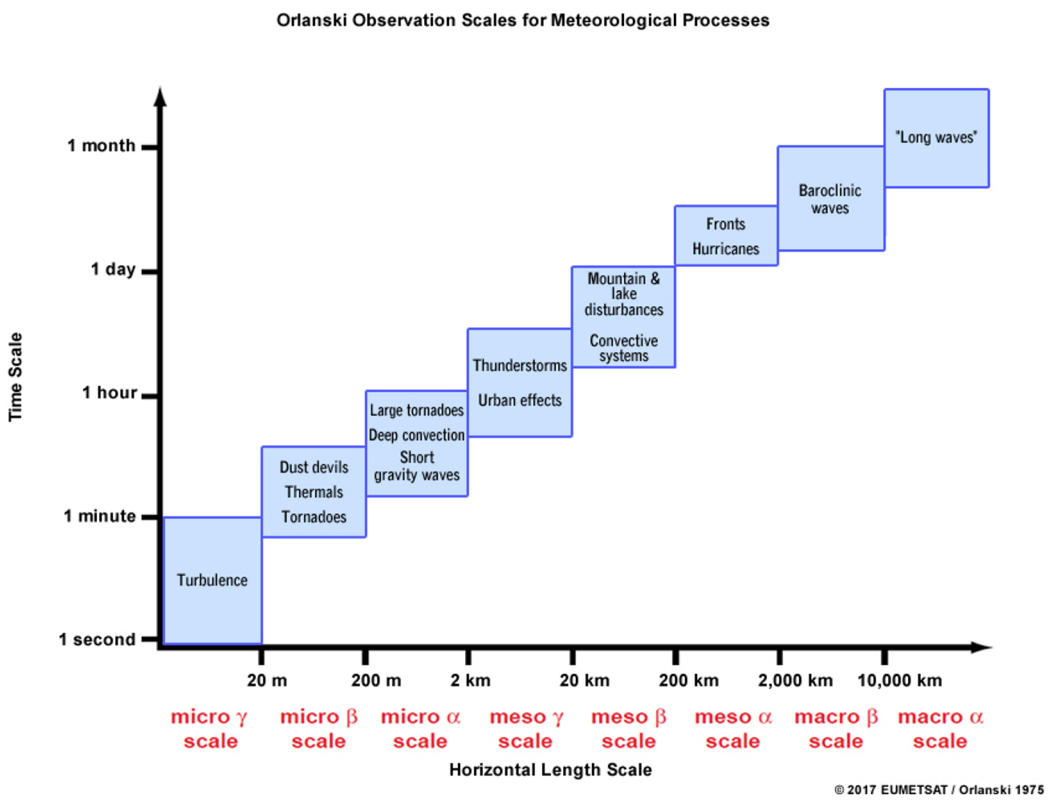

Figure 1.3: Characteristic scales of meteorological processes according to Orlanski (1975). Schematic adopted from the COMET® Program (2018).

diagram, which is associated with relatively small characteristic scales. The rapid evolution of these PBL phenomena can be captured only with an observation network whose density is considerably larger compared to other parts of the atmosphere. As an example, consider the current radiosonde network: it might be sufficient to accurately describe the characteristics of upper-level troughs and ridges, but it is too coarse for many important lower atmospheric processes, such as the transition from a diurnal, convective-driven boundary layer (CBL) to a night-time, stable boundary layer (SBL).

1.1.3 The need for ground-based remote sensing

The need for denser PBL observations in the US has been brought to the fore ever since the beginning of the 21st century by various participants in the North American Observing System (NAOS) and the US Weather Research Program (USWRP). These early efforts to raise

awareness of the existing PBL gap were, to a large extent, driven by the growing evidence that predicting severe weather can be greatly enhanced by better monitoring of the PBL processes. The strong dependence of convective initiation on the convergence of low-level PBL winds is a classic example to illustrate this link (e.g., Trier 2003). Nevertheless, more coordinated guidance on how to expand the PBL observation capabilities only arrived in 2009 with a dedicated report from the National Research Council (NRC; National Research Council 2009). After concluding that the present observation capabilities are *highly variable in quantity, quality, accessibility, instrument set, site selection, and metadata*, this NRC report offered a vision for a new mesoscale observation network. In agreement with our earlier discussion, the NRC panel found that the vertical component of the US mesoscale network is particularly inadequate and that the largest number of unmet requirements lies below 5 km. To address these deficiencies, the NRC committee members recommended the procurement of an adaptive network of networks that *integrates existing and new mesoscale networks into a national "network of networks"*. The committee further suggested that these new mesoscale networks should consist of ground-based remote sensing instruments on account of their high prospects for measuring the PBL structure at a sufficiently high resolution. Their assessment also found that a nationwide deployment of 400 profiling sites would be a great first step toward closing the existing PBL observation gap.

This original NRC report was crucial for increasing the community awareness of the existing observational deficiencies. Since then, a lot of attention has been focused on determining the optimal requirements for the newly planned mesoscale observation network. For example, a workshop was organized shortly after the NRC report which identified several candidate instruments and determined both their desired measurement accuracy (1 K and 1 gkg^{-1}) and resolution (30-100 m in the vertical). A more recent report from the National Academy of Sciences, Engineering and Medicine (NASEM; 2018) further refined these observation requirements and reinforced the value of ground-based remote sensing. In particular, high-resolution water vapor (WV) profiles in the PBL were labelled as an

Essential Climate Variable by WMO's Global Climate Observing System (GCOS) program. Enhancing the current PBL wind observations was similarly found to be a priority for both the research and private sectors.

More recently, the recognition for the value of ground-based remote sensing profilers has spread even beyond the US. For example, Illingworth et al. (2019) discuss how existing ground-based profiling instruments in Europe have great prospects to improve the quality of weather forecasts over this region. Fruitful collaborations between several European agencies and instrument manufacturers have resulted in improved retrieval algorithms, unified calibration procedures and real-time flow of PBL-relevant measurements.

1.2 Contributions and dissertation overview

The 2018 Decadal Survey by NASEM stated that a better understanding of the PBL processes is crucial for improving NWP. This need is even more pertinent for high-resolution, limited area models (LAMs) where the PBL plays an important role for the initiation and evolution of explicitly resolved convection (World Meteorological Organization 2018). Compared to global NWP models, LAMs exhibit greater sensitivity to the initial moisture fields which are much more variable compared to other state variables (temperature, wind and pressure). The latter serves as an important motivation for the currently ongoing efforts to establish a denser ground-based PBL network.

According to Section 1.1.3, the present consensus is that ground-based remote sensing profilers represent the most promising candidate for confronting the PBL observation gap. As explained earlier, enhancing the current GOS with these novel instruments is expected to be particularly beneficial for convective-scale models due to their increased sensitivity to PBL processes. In this dissertation, we will support this claim by utilizing data collected during the 2015 Plains Elevated Convection at Night (PECAN; Geerts et al. 2017) field campaign. Specifically, we add to the growing evidence that ground-based remote sensors could be a valuable component of the GOS by demonstrating their positive impact on a particularly

challenging meteorological phenomenon – that of *bore-generating nocturnal convection* (Parsons et al. 2019a). As will be explained in Chapter 4, these convective systems are very difficult to simulate in contemporary LAMs due to their complex dependence on many different PBL processes, including the night-time PBL stability and Nocturnal Low-Level Jets (NLLJs). Nevertheless, our numerical experiments will demonstrate that a frequent assimilation of thermodynamic and kinematic profilers can bring forecast improvements as a result of the better initial conditions within the PBL. Our detailed analysis will examine the value of various ground-based remote sensing instruments and discuss why their impacts are sensitive to the underlying atmospheric predictability.

In addition to showing the potential of ground-based remote sensing for convective-scale NWP, the second contribution of this dissertation is the formulation of a new verification method for atmospheric bores. The application of suitable forecast verification techniques has always been a crucial element at every NWP center because any change to an existing numerical model needs to be rigorously tested prior to its operational implementation. Assessing the quality of LAM forecasts poses even greater challenges due to the discontinuous and intermittent nature of the simulated processes. The use of traditional verification metrics often leads to the so-called *double penalty problem*, wherein a small displacement of the forecasted phenomenon can result in extremely poor categorical scores. To alleviate this problem and foster future advances in convective-scale modeling, there is currently a move afoot to develop new, object-based (or feature-based) verification methods whose output agrees more favorably with subjective human assessment. So far, most of these algorithms have focused on achieving a better comparison between forecasted and observed convective storms (Davis et al. 2006). However, there are many other features in convective-scale NWP models whose adequate verification can offer useful guidance for future model development. Atmospheric bores are one prominent example as their dynamics are crucial for the maintenance of bore-generating convection. Therefore, one should expect that an

objective identification and tracking of these PBL features will help us better understand the forecast errors associated with this challenging mode of convection.

We conclude our discussion here by briefly outlining how the remainder of this dissertation is structured. Chapter 2 offers a more technical introduction to this work and describes the PECAN datasets assimilated in our numerical experiments. Chapter 3 presents the identification and tracking components of the newly developed object-based bore algorithm and provides examples of its application in convective-scale model output. Next, we demonstrate the value brought by ground-based remote sensing instruments on the forecasts of bore-generating nocturnal convection – first for a single case study (Chapter 4) and then for a collection of 10 additional cases which feature diverse convective dynamics (Chapter 5). The purpose of the single case study is two-fold: (i) to help us determine the optimal configuration of the employed analysis-forecast system and (ii) to guide us develop a set of meaningful research questions for the following systematic study. Finally, Chapter 6 gives an overall summary of the main results and discusses future research directions.

It is also noted that significant parts of this dissertation are direct excerpts of Chipilski et al. (2018, ©American Meteorological Society) and Chipilski et al. (2020, ©American Meteorological Society).

Chapter 2

Theory, data and methods

The research conducted in this dissertation spans a broad range of topics from the fields of DA, NWP, fluid dynamics and remote sensing. Therefore, we first introduce some preliminaries that will help in the interpretation of subsequent Chapters. Rather than reviewing the highly technical details, we instead focus on introducing some of the key theoretical concepts .

2.1 Atmospheric bores

Atmospheric bores are an inseparable part of the night-time environment in the U.S. Great Plains. Recently, our community has started to pay closer attention to these features as they are believed to play an important role in the initiation and maintenance of nocturnal convection (Parsons et al. 2019a). Interestingly, much of the diagnostic tools employed for their analysis come from century-long developments in fluid dynamics. For instance, the flow regime diagrams used to evaluate the environmental conditions in which atmospheric bores form have their origins in *hydraulic theory*. In what follows next, we outline the main considerations behind this theory and then briefly discuss its limitations.

The dynamics of bores is intimately related to that of density (or gravity) currents, which form due to differences in the near-surface density field and propagate as a result of the corresponding pressure gradient force. There are many different ways in which such low-level density variations might be generated, including thunderstorms, sea breezes

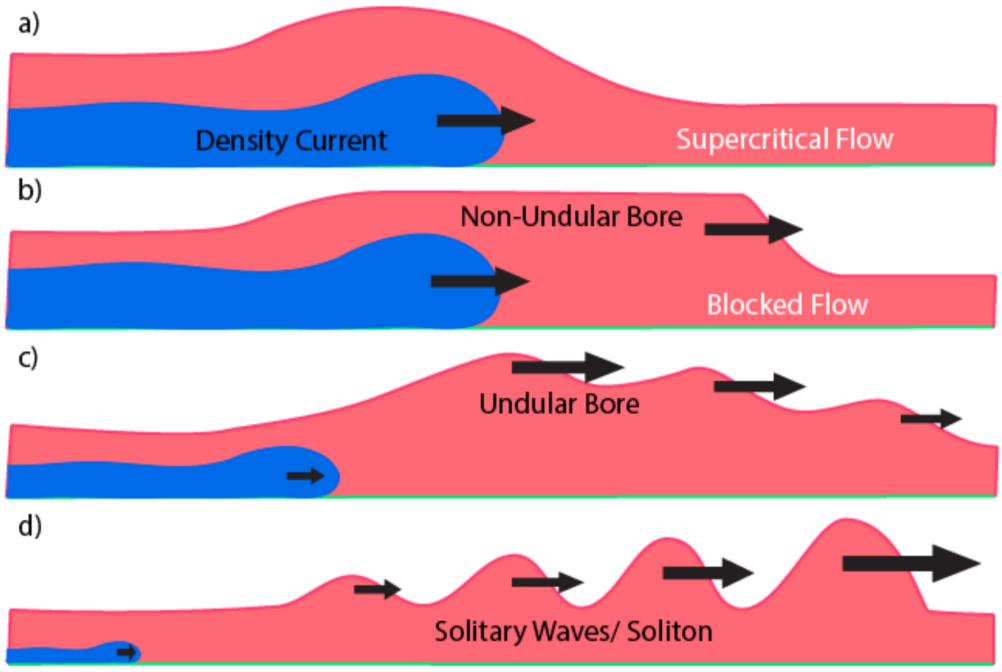

Figure 2.1: The typical evolution of a convectively generated density current in the nocturnal environment of the U.S. Great Plains. Schematic adopted from Haghi et al. (2017).

and river discharges. The first quantitative understanding of density current propagation comes from the seminal work of Benjamin (1968) who studied the classical problem of lock-exchange with a neutrally stratified environment (ambient). In an atmospheric context, Benjamin's theory is relevant for understanding the behavior of daytime density currents which propagate in a well-mixed, convective PBL (CBL). However, the presence of ambient stratification – a prominent characteristic of the night-time, stable PBL (SBL) present in our numerical simulations, complicates the theoretical treatment of density currents. Under certain conditions, formally referred to as *transcritical resonance*, we observe a transfer of energy from the density current to the ambient environment, which in turn gives rise to nonlinear internal waves (see Fig. 2.1). Bores and solitary waves are two particular examples of these nonlinear disturbances and tend to occur frequently in the night-time atmosphere of the Great Plains (Haghi et al. 2017).

2.1.1 Hydraulic theory

The framework that is most often used to describe atmospheric bores is based on a variant of *two-layer hydraulic theory* presented in Rottman and Simpson (1989; RS hereafter). Its main application is to determine the extent to which the mesoscale environment is favourable for the generation of bores upstream of a nocturnal cold pool, which is typically done by assessing the flow regime in a parameter space defined by the Froude number and non-dimensional density current height (defined later). In Chapter 4.4, the RS89 flow regime diagrams are also used to assess the impact of ground-based remote sensors on the forecasts of the bore environment (*cf.* Fig. 4.6).

Throughout the remainder of this Section, we will sketch the derivation of RS89's flow regime diagram by considering *the behavior of single-layer flow around a solid obstacle*[1]. As explained in RS89, the transition to a two-layer hydraulic theory is made by simply replacing the acceleration due to gravity g with a reduced gravitational constant $g' \coloneqq g\frac{\rho_1-\rho_2}{\rho_1}$ (where the subscripts 1 and 2 correspond to the bottom and top fluid layers, respectively). In our exposition, however, the primes shall be omitted for notational convenience.

2.1.1.1 Setup

As a starting point in our exposition, consider the Navier-Stokes equations of motion and mass continuity, *viz.*

$$\frac{D\mathbf{u}}{Dt} = -\frac{1}{\rho}\nabla p - g\hat{\mathbf{k}} + \nu\nabla^2\mathbf{u}, \tag{2.1a}$$

$$\frac{1}{\rho}\frac{D\rho}{Dt} + \nabla\cdot\mathbf{u} = 0, \tag{2.1b}$$

[1] From a meteorological point of view, the solid obstacle represents the cold pool generated by a night-time thunderstorm.

where $\frac{D}{Dt} \coloneqq \frac{\partial}{\partial t} + u\frac{\partial}{\partial x} + v\frac{\partial}{\partial y} + w\frac{\partial}{\partial z}$ is the material derivative, $\mathbf{u}$ – the three-dimensional velocity of the fluid, ρ and p – the fluid's density and pressure, respectively, whereas ν – the kinematic viscosity coefficient. Assuming that the flow is incompressible, inviscid and hydrostatic, the above set of equations can be transformed into a new set which is more appropriate for the single-layer setup drawn in Fig. 2.2a:

$$\frac{\partial u}{\partial t} + u\frac{\partial u}{\partial x} = -\frac{1}{\rho}\frac{\partial p}{\partial x}, \tag{2.2a}$$

$$0 = -g - \frac{1}{\rho}\frac{\partial p}{\partial z}, \tag{2.2b}$$

$$\nabla \cdot \mathbf{u} = 0. \tag{2.2c}$$

Let p_0 be the fluid pressure at $z_0 = h_0 + \eta$. Integrating the hydrostatic relation in (2.2b) from z_0 to an arbitrary height z within the fluid yields

$$p(x, z, t) = p_0 + \rho g(h_0 + \eta - z), \tag{2.3}$$

which can be used to rewrite the pressure gradient force on the right-hand side of (2.2a) as

$$-\frac{1}{\rho}\frac{\partial p}{\partial x} = -g\frac{\partial \eta}{\partial x}. \tag{2.4}$$

Analagous to the classic shallow water theory, we integrate the mass continuity equation (2.2c) over the depth of the fluid, imposing the following lower and upper kinematic boundary conditions on the vertical component of velocity:

$$w(x, 0, t) \coloneqq \frac{Dd_0}{Dt} = u\frac{\partial d_0}{\partial x}, \tag{2.5a}$$

$$w(x, h_0 + \eta, t) \coloneqq \frac{D(h_0 + \eta)}{Dt} = \frac{\partial \eta}{\partial t} + u\frac{\partial \eta}{\partial x}. \tag{2.5b}$$

With that, our new system of governing equations becomes

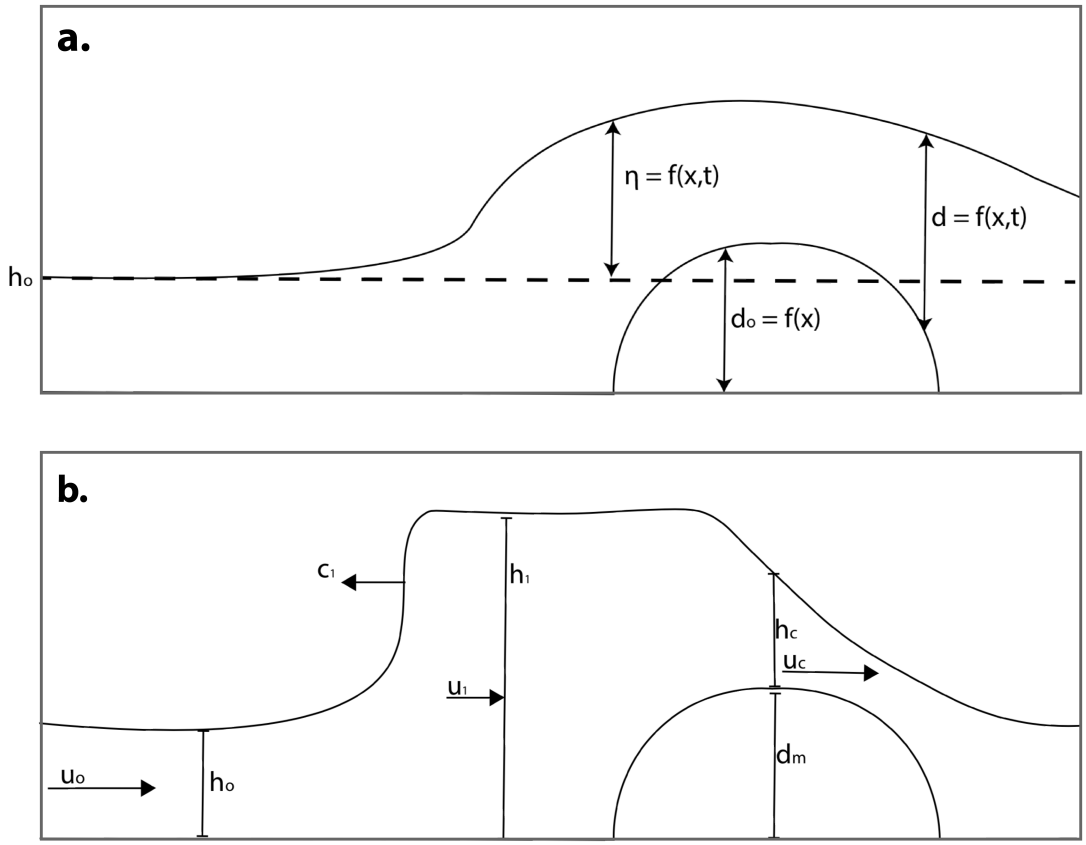

Figure 2.2: Setup of single-layer hydraulic theory (modified following Haghi 2017). *Panel a*: Flow behavior in the absence of nonlinear upstream disturbances. The variables d_0, d and η correspond to the solid obstacle's height, the fluid's depth and the fluid's displacement relative to its unperturbed height h_0. *Panel b*: Flow behavior in the presence of an upstream hydraulic jump (bore) that moves away from the solid obstacle at a constant speed c_1. As it passes through the bore, the fluid transitions from a supercritical to a subcritical state, which causes an abrupt decrease in its speed (from u_0 to u_1) and an abrupt increase in its depth (from h_0 to h_1). The flow returns back to a supercritical state downstream of the obstruction. For the quasi-steady state bore assumed in the derivation of single-layer hydraulic theory, critical flow conditions are reached at the highest point of the obstacle (with maximum height d_m) where the depth and speed of the fluid are h_c and u_c, respectively.

$$\frac{\partial u}{\partial t} + u\frac{\partial u}{\partial x} = -g\frac{\partial \eta}{\partial x}, \tag{2.6a}$$

$$\frac{\partial \eta}{\partial t} + \frac{\partial}{\partial x}(ud) = 0. \tag{2.6b}$$

2.1.1.2 Steady state solutions without jump conditions

To evaluate the behaviour of the flow around the solid obstacle, we consider the steady-state versions of Eqs. (2.6a) and (2.6b), which can be combined into

$$(F-1)\frac{\partial d}{\partial x} = \frac{\partial d_0}{\partial x}. \tag{2.7}$$

The variable $F \coloneqq \frac{u^2}{gd}$ in (2.7) is referred to as the *Froude number*. This non-dimensional parameter plays a key role in hydraulic theory (e.g., Baines 1984) and is often interpreted in the following two ways:

- the ratio of the fluid's speed and the phase speed of shallow water waves;
- the ratio of the fluid's kinetic and potential energies.

If $F > 1$ ($F < 1$), we say that the flow is supercritical (subcritical). The relationship in (2.7) implies that supercritical (subcritical) flows increase (decrease) their depth as they pass over the solid obstacle. For critical flows ($F \to 1$), however, this relationship does not provide sufficient information for describing the flow properties because $\frac{\partial d_0}{\partial x} = 0$, which would only be true far away from the obstacle or along its crest. To avoid this singularity, we first integrate the system (2.6) in the x-direction, making use of the upstream flow conditions ($u = u_0$, $d_0 = 0$ and $d = h_0$) to pin down the coefficients of integration. The resulting two expressions are then combined by grouping into powers of u. This procedure results in

$$\frac{V^3F^2}{2} + V\left(D - \frac{F^2}{2} - 1\right) + 1 = 0, \tag{2.8}$$

where $D \coloneqq \frac{d_0}{h_0}$ is the non-dimensional obstacle (density current) height and $V \coloneqq \frac{u}{u_0}$ is the normalized fluid velocity. Next, to obtain the AB+AD curve from RS89, we follow Houghton and Kasahara (1968) who find that $V = F^{-2/3}$ when the flow reaches a critical state at the crest. Substituting this relation in (2.8), we get

$$D = \frac{1}{2}F^2 - \frac{3}{2}F^{2/3} + 1, \tag{2.9}$$

which is the mathematical expressions for AB+AD. From a physical point of view, this boundary curve describes the largest obstacle height for which flows with a fixed upstream value of F remain symmetric about the obstruction; a further increase in D breaks down the flow symmetry and gives rise to a *blocked* or *partially blocked* regime. Another consequence from the shape of the AB+AD curve is that critical upstream flows ($F \longrightarrow 1$) tend to quickly become unstable regardless of the obstacle's height. By contrast, if upstream flows remain far away from such critical conditions, their behavior is increasingly less sensitive to the characteristics of the underlying topography.

2.1.1.3 Steady state solutions with jump conditions

Although the AB+AD boundary curve gives useful information about the expected flow regime, it does not reveal what type of disturbances will form in transcritical resonance conditions when the flow loses its symmetry. However, early laboratory experiments (Long 1954, 1974; Baines 1984) have demonstrated that flows which transition to a critical state near an obstruction often develop upstream and downstream hydraulic jumps or *bores*, motivating fluid dynamicists to start incorporating *jump conditions* in their treatment of critical hydraulic phenomena. In essence, the purpose of these hydraulic jumps is to split the flow into multiple segments which are then dynamically reconnected through the application of conservation laws.

To derive the remaining RS89 boundary curves, we consider a special type of bores which form upstream of the obstacle (Fig. 2.2b) and cause an abrupt increase (decrease) in the fluid's height (speed). Furthermore, a quasi-steady state is assumed such that the fluid reaches a critical state at the obstacle's peak (i.e., $u = u_c = \sqrt{g d_c}$). In this idealized setup, there are 4 unknown variables we need to solve for: u_1 (the speed of the fluid downstream of the jump), d_1 (the depth of the fluid downstream of the jump), c_1 (the speed of the bore) and d_c (the critical fluid depth over the crest). Therefore, 4 independent constraints are needed to describe the flow behavior subject to this jump condition. The first two can be obtained by imposing mass conservation at the two locations where critical flow conditions are observed, i.e. across the bore and over the obstacle's crest, i.e.

$$(u_0 + c_1)h_0 = (u_1 + c_1)h_1, \tag{2.10a}$$

$$u_1 h_1 = u_c h_c. \tag{2.10b}$$

Note that the addition of c_1 in (2.10a) is necessary to ensure the legitimate use of mass conservation within a reference frame moving with the bore. The third constraint comes from the momentum principle

$$\frac{\partial \rho u^2}{\partial x} + \frac{\partial \rho u w}{\partial z} + \frac{\partial p}{\partial x} = 0, \tag{2.11}$$

which can be easily obtained by merging the steady state equations for mass conservation $\left(\frac{\partial u}{\partial x} + \frac{\partial w}{\partial z} = 0\right)$ and momentum in the x-direction $\left(u\frac{\partial u}{\partial x} + \frac{1}{\rho}\frac{\partial p}{\partial x} = 0\right)$[2]. Integrating over a control volume enclosing the hydraulic jump, applying the divergence theorem and using the hydrostatic relation, we get

[2] In particular, multiply the momentum and mass conservation equations by ρ and $u\rho$, respectively, and then collect terms.

$$\rho(u_0+c_1)^2 h_0 + \frac{1}{2}\rho g h_0^2 = \rho(u_1+c_1)^2 h_1 + \frac{1}{2}\rho g h_1^2, \tag{2.12}$$

which can be further simplified to

$$(u_0+c_1)^2 = \frac{1}{2} g h_1 \left(1+\frac{h_1}{h_0}\right) \tag{2.13}$$

in view of (2.10a). The final restriction is based on Bernoulli's principle, which is applied from an arbitrary point within the subcritical flow downstream of the bore to the obstacle's crest. In particular, we integrate the steady state form of the momentum equation (2.6a) along the x-direction, upon which we find that

$$\frac{1}{2}u_1^2 + g h_1 = \frac{1}{2}u_c^2 + g(d_m + d_c). \tag{2.14}$$

Having obtained the complete set of constraints, we now examine two limiting cases. In the first one, we set the bore speed c_1 to 0, which, after some extensive algebraic manipulations, recovers the AE boundary curve from RS89:

$$D = \frac{1+(1+8F^2)^{3/2}}{16F^2} - \frac{3}{2}F^{2/3} - \frac{1}{4}. \tag{2.15}$$

Note that the region between AE and AD has been previously shown to give rise to both supercritical and partially blocked regimes depending on the underlying experimental design (Pratt 1983). In the second limiting case, we set u_1 to 0 to obtain another relation between F and D, namely

$$F = (D-1)\sqrt{\frac{1+D}{2D}}, \tag{2.16}$$

which corresponds to curve BC and marks the separation between partially and completely blocked regimes.

Another distinct feature in Fig. 4.6 are the dashed black curves which demarcate the bore strength $S \coloneqq \frac{h_1}{h_0}$ in partially blocked regimes. These can be derived after dividing the Bernoulli relation in (2.14) by gh_0 and substituting in the definition for u_c. The result is

$$S = D - \frac{1}{2}\frac{u_1^2}{gh_0} + \frac{3}{2}\left(S\frac{u_1}{\sqrt{gh_0}}\right)^{2/3}, \tag{2.17}$$

with

$$\frac{u_1}{\sqrt{gh_0}} = \frac{F}{S} - \frac{S-1}{S}\frac{c_1}{\sqrt{gh_0}}. \tag{2.18}$$

Note that u_1 is obtained separately by applying mass conservation (2.10a) across the bore.

One important observation from Eqs. (2.17) and (2.18) is that the bore strength S is directly proportional to the bore speed c_1. A similar conclusion can be drawn after we slightly modify the momentum principle in (2.13) such that

$$\frac{c_1}{\sqrt{gh_0}} = \sqrt{\frac{1}{2}S(1+S)} - F. \tag{2.19}$$

2.1.2 Limitations of hydraulic theory

While the aforedescribed variant of hydraulic theory has been successfully used to predict the properties of many observed atmospheric bores (Koch et al. 1991; Koch and Clark 1999; Koch et al. 2008a,b), the representation of density currents as solid obstacles is an oversimplification, which allows its height and shape to be prescribed independently of the background flow. In reality, however, the height of a density current is closely related to its speed (Benjamin 1968), whereas its shape is often deformed by the environmental flow

(Khodkar et al. 2018). To address these deficiencies, White and Helfrich (2012) proposed an alternative two-layer hydraulic theory where the density current is seen as a free boundary subject to a separate momentum constraint of the form

$$\int \left(p + \rho u^2\right) dz = \text{const.} \tag{2.20}$$

The authors proposed an improved jump condition and further extended the RS89 framework to an ambient with arbitrary thickness. Analogous to the setup with a solid obstacle, their new theory predicts the existence of subcritical and supercritical regimes as well as a transcritical resonant band within which upstream disturbances are generated. More recently, a *vorticity-based approach* has also been adopted in lieu of the classic hydraulic treatment to describe the behaviour of two-layer flows (Khodkar et al. 2018) as well as more general flows with arbitrary stratification and shear profiles (Nasr-Azadani and Meiburg 2016).

The second notable limitation of hydraulic theory is that its steady-state nature does not offer any insights into the temporal evolution of bores. Traditionally, the maintenance of these night-time disturbances has been assessed through linear wave theory (Scorer 1949), which gives first-order accounts on the properties of the ambient waveguide (Haghi et al. 2017). However, this can lead to significant errors due to the highly nonlinear nature of the internal waves forming ahead of the density current. In fact, very recent work from Haghi and Durran (2021) suggests that linear wave dynamics do not to govern the dynamics of bores and can give misleading information on the ambient waveguide characteristics. A nonlinear treatment of the transcritical resonant problem exists (White and Helfrich 2012, 2014), but its validity is yet to be confirmed with atmospheric bore observations.

2.2 Ensemble Kalman filtering

2.2.1 Data assimilation overview

Despite their abundance, the measurements provided by the Global Observing System (GOS) do not give sufficient information to adequately determine the initial conditions in NWP models. One reason for this obstacle is related to their insufficient number relative to the total degrees of freedom in the simulated dynamical system. As alluded to in Chapter 1, some components of the Earth system are especially prone to this problem, such as the Planetary Boundary Layer (PBL) located in the lowest parts of the atmosphere. Another closely related problem is the inhomogeneous character of the GOS – dense continental observation networks often border with sparsely observed regions over the oceans.

In an effort to overcome these challenges, the field data assimilation (DA) estimates the model's initial conditions (ICs) by combining the highly irregular observation networks with short-range model predictions. This procedure is especially important for poorly observed regions where the ICs are heavily weighted toward the model forecasts. The statistical blending of two information sources has the additional benefit of relaxing the otherwise stringent requirements for optimally sampling the rapidly evolving components of the Earth system (National Research Council 2009).

In the geosciences, there are two commonly used approaches for defining the model's ICs. The first one utilizes a variational framework in which the resulting analysis minimizes some objective functional that measures the distance of the model state to both the short-term forecast and the current observations. Variational methods, such as 4D-Var (e.g., Courtier et al. 1994), are very popular for global NWP. Their success comes from the ability to explicitly incorporate dynamical balances, which are well-known at the relatively large scales governing the global model dynamics. However, a significant disadvantage of these methods is that the error properties of short-range model predictions (the model *background*) remain constant in time – a significant restriction for the type of convective scale applications

discussed in this dissertation. For instance, one should anticipate that background errors near regions of convective activity are significantly larger than other parts of the model domain. One way to address this problem is to use an ensemble-based approach wherein the background errors are estimated from the sample statistics of a short-range ensemble forecast. This idea lies at the core of the so-called *Ensemble Kalman Filter* (EnKF), which was originally developed by Evensen (1994) and is now widely used in high-resolution LAM models. In this work, we adopt one particular variant of the EnKF method to assimilate the ground-based remote sensing retrievals collected during the PECAN field campaign. The following sections provide a short overview of the method, tracing its origins to earlier developments in estimation theory.

2.2.2 The general filtering problem and its solution

The theoretical basis for many DA methods is often masked by extensive details about their algorithmic implementation, commonly expressed in the language of matrix algebra (Bertino et al. 2002). Unfortunately, such algorithmic representation often hinders our ability to abstract ideas and develop new DA techniques. To circumvent this problem, we first present some key concepts from the field of *estimation theory*, which is a unifying framework for all existing DA methods (Cohn 1997).

As explained in the previous section, the goal of DA is to optimally combine observations with short-range model predictions. In estimation theory, these two information sources are formally encoded through the so-called *state-space model representation*, first introduced in the pioneering work of Kalman (1960). The state-space model is often written as a system of two discrete-time, discrete-state (DTDS) stochastic processes, *viz.*

$$\mathbf{x}_n = f(\mathbf{x}_{n-1}, \boldsymbol{\xi}_{n-1}), \tag{2.21a}$$

$$\mathbf{y}_n = h(\mathbf{x}_n, \boldsymbol{\varepsilon}_n). \tag{2.21b}$$

The first equation above represents the evolution of our model state $\mathbf{x}$ (a vector with N_x components) from time t_{n-1} to time t_n, whereas the second one indicates how state measurements $\mathbf{y}$ (a vector with N_y components) are being made at time t_n. Here we should also point out that the high-dimensional maps $f : \mathbb{R}^{N_x} \to \mathbb{R}^{N_x}$ and $h : \mathbb{R}^{N_x} \to \mathbb{R}^{N_y}$ have two arguments corresponding to the deterministic and stochastic components of the state-space model, respectively. In the DA literature, the stochastic terms $\boldsymbol{\xi}_n$ and $\boldsymbol{\varepsilon}_n$ are often referred to as the *model* and *observation errors* and their specification is crucial for the derivation of different estimation algorithms.

Having established this notation, we are now in a position to give a more precise definition of the filtering problem that EnKF tries to solve. Let $\mathcal{Y}_n \coloneqq \{\mathbf{y}_1, \mathbf{y}_2, ..., \mathbf{y}_n\}$ denote the observation stochastic process. Given this history of observations, the ultimate goal of filtering is to find the conditional probability density function $p(\mathbf{x}_n|\mathcal{Y}_n)$ at each time t_n. This is to be contrasted with 4D-Var's smoothing problem where the objective is to evaluate $p(\mathbf{x}_n|\mathcal{Y}_{n+l})$ for some fixed $l \in \mathbb{Z}$. Even without presenting the derivation of these two commonly used methods, the general definitions above suggest that EnKF and 4D-Var are solving two fundamentally different problems. In particular, filtering provides state estimates which are only based on current and past observations, whereas the model trajectory in the smoothing problem is further constrained by observations collected at future times.

Following Cohn (1997), the general solution of the filtering problem can be obtained after repeatedly applying the definition of conditional probability, which gives

$$p(\mathbf{x}_n|\mathcal{Y}_n) = \frac{p(\mathbf{y}_n|\mathbf{x}_n, \mathcal{Y}_{n-1})\, p(\mathbf{x}_n|\mathcal{Y}_{n-1})}{p(\mathbf{y}_n|\mathcal{Y}_{n-1})}. \tag{2.22}$$

Written in this form, the filtering solution can be interpreted as a special version of Bayes' theorem in high dimensions, with $p(\mathbf{x}_n|\mathcal{Y}_{n-1})$ and $p(\mathbf{y}_n|\mathbf{x}_n, \mathcal{Y}_{n-1})$ corresponding to the prior density and likelihood function, respectively. To further establish the connection to Bayes' theorem, observe that the denominator in (2.22) can be equivalently obtained after integrating

the numerator over the current model state $\mathbf{x}_n$. Indeed, upon applying the definitions of marginal and conditional probability to the denominator, we get

$$p(\mathbf{y}_n|\mathcal{Y}_{n-1}) = \int p(\mathbf{y}_n|\mathbf{x}_n, \mathcal{Y}_{n-1}) p(\mathbf{x}_n|\mathcal{Y}_{n-1}) d\mathbf{x}_n. \tag{2.23}$$

One of the commonly used assumptions in filtering theory is that the stochastic process $\{\varepsilon_t\}$ is white in time ($\mathbb{E}[\varepsilon_m \varepsilon_n^{\mathrm{T}}] = \mathbf{0}$ for $m \neq n$). The latter allows us to further simplify the likelihood function as

$$p(\mathbf{y}_n|\mathbf{x}_n, \mathcal{Y}_{n-1}) = p(\mathbf{y}_n|\mathbf{x}_n). \tag{2.24}$$

Here we note that (2.24) can be readily obtained by applying a change of variables in (2.21b). To evaluate the prior density, we first rewrite it in a more convenient form. Once again, using the definitions of marginal and conditional probability, we have that

$$\begin{aligned} p(\mathbf{x}_n|\mathcal{Y}_{n-1}) &= \int p(\mathbf{x}_n|\mathbf{x}_{n-1}, \mathcal{Y}_{n-1}) p(\mathbf{x}_{n-1}|\mathcal{Y}_{n-1}) d\mathbf{x}_{n-1} \\ &= \int p(\mathbf{x}_n|\mathbf{x}_{n-1}) p(\mathbf{x}_{n-1}|\mathcal{Y}_{n-1}) d\mathbf{x}_{n-1}. \end{aligned} \tag{2.25}$$

The simplification in the second equality follows from another commonly used assumption in filtering theory which states that the two error processes and the model state are mutually independent at all times t_n. Furthermore, note that (2.25) represents a special form of the *Chapman-Kolmogorov equation* (*cf.* Jazwinski 1970). Similar to our manipulation of the likelihood function, the transition density $p(\mathbf{x}_n|\mathbf{x}_{n-1})$ in this equation can be evaluated by applying a change of variables to (2.21a).

The aforementioned prior representation is particularly appealing because the second density in the integrand $p(\mathbf{x}_{n-1}|\mathcal{Y}_{n-1})$ represents the filtering solution from the previous time

step. Then, starting with some initial model state distribution $p(\mathbf{x}_0)$, the filtering solution at the present time can be found *recursively*, by alternating between a *forecast step*, in which one evaluates the prior density through the Chapman-Kolmogorov relation, and an *update (analysis) step*, where the Bayes' theorem is used to update the prior state estimates based on the newly arrived batch of observations. In theory, the application of such a recursive algorithm can provide a complete description of the model state uncertainty. In practice, however, its application is not feasible for the type of high-dimensional problems considered in our work since the probability density of the initial state $p(\mathbf{x}_0)$ and the exact form of the state-space model are rarely known. Moreover, evaluating the multivariate integrals in the forecast and analysis steps of our recursive algorithm is simply not possible with any currently available technique.

2.2.3 Kalman filter (KF)

The Kalman filter (KF) and its ensemble-based implementation make several important assumptions that lead to a closed-form solution of the general filtering problem. First, we consider a linear and additive version of the general state-space model

$$\mathbf{x}_n = \mathbf{M}_{n-1}\mathbf{x}_{n-1} + \boldsymbol{\xi}_{n-1}, \tag{2.26a}$$

$$\mathbf{y}_n = \mathbf{H}_n\mathbf{x}_n + \varepsilon_n, \tag{2.26b}$$

where the $\mathbf{M} \in \mathbb{R}^{N_x \times N_x}$ and $\mathbf{H} \in \mathbb{R}^{N_y \times N_x}$ are the Jacobians of the dynamical propagator and observation operator, respectively. We further assume that

$$\boldsymbol{\xi}_n \sim \mathcal{N}(\mathbf{0}, \mathbf{Q}_n), \tag{2.27a}$$

$$\varepsilon_n \sim \mathcal{N}(\mathbf{0}, \mathbf{R}_n), \tag{2.27b}$$

$$\mathbf{x}_0 \sim \mathcal{N}\left(\mathbf{x}_0^a, \mathbf{P}_0^a\right). \tag{2.27c}$$

Eqs. (2.27a) and (2.27b) state that the model and observation errors follow a Gaussian distribution with a zero mean (unbiased) and some known covariance. Likewise, we also

assume that the initial state is drawn from a known Gaussian distribution with a mean $\mathbf{x}_0$ and covariance $\mathbf{P}_0^a$.

Applying some of these assumptions in (2.26a) gives (*cf.* Cohn 1997)

$$\mathbf{x}_n^f = \mathbf{M}_{n-1}\mathbf{x}_{n-1}^a, \tag{2.28a}$$

$$\mathbf{P}_n^f = \mathbf{M}_{n-1}\mathbf{P}_{n-1}^a\mathbf{M}_{n-1}^{\mathrm{T}} + \mathbf{Q}_{n-1}, \tag{2.28b}$$

where

$$\mathbf{x}_n^f \coloneqq \mathbb{E}\left[\mathbf{x}_n|\mathcal{Y}_{n-1}\right], \tag{2.29a}$$

$$\mathbf{P}_n^f \coloneqq \mathbb{E}\left[(\mathbf{x}_n - \mathbf{x}_n^f)(\mathbf{x}_n - \mathbf{x}_n^f)^{\mathrm{T}}|\mathcal{Y}_{n-1}\right], \tag{2.29b}$$

and

$$\mathbf{x}_{n-1}^a \coloneqq \mathbb{E}\left[\mathbf{x}_{n-1}|\mathcal{Y}_{n-1}\right], \tag{2.30a}$$

$$\mathbf{P}_{n-1}^a \coloneqq \mathbb{E}\left[(\mathbf{x}_{n-1} - \mathbf{x}_{n-1}^a)(\mathbf{x}_{n-1} - \mathbf{x}_{n-1}^a)^{\mathrm{T}}|\mathcal{Y}_{n-1}\right] \tag{2.30b}$$

are the conditional mean/covariances of the prior distribution at time t_n and the posterior distribution at time t_{n-1}, respectively. The system (2.28) describes how the mean and covariance of the posterior distribution propagate from t_{n-1} to t_n. Moreover, since Gaussian distributions are completely described by these two quantities, the system (2.28) gives an exact solution of the Chapman-Kolmogorov equations (the forecast step in our recursive filtering solution). Similarly, we can use the linearized version of the stochastic observation model (2.26b) to find that the first two moments of $p(\mathbf{y}_n|\mathbf{x}_n)$ and $p(\mathbf{y}_n|\mathcal{Y}_{n-1})$ are $\{\mathbf{H}_n\mathbf{x}_n, \mathbf{R}_n\}$ and $\{\mathbf{H}_n\mathbf{x}_n^f, \mathbf{R}_n + \mathbf{H}_n\mathbf{P}_n^f\mathbf{H}_n^{\mathrm{T}}\}$, respectively. Having completely described all three densities on the right-hand of the general filtering solution (2.22), we can now multiply them together

and work out that the filtering (posterior) density $p(\mathbf{x}_n|\mathcal{Y}_n)$ is also Gaussian with a mean $\mathbf{x}_n^a$ and covariance $\mathbf{P}_n^a$ given by

$$\mathbf{x}_n^a = \mathbf{x}_n^f + \mathbf{K}_n \left(\mathbf{y}_n - \mathbf{H}_n \mathbf{x}_n^f \right), \tag{2.31a}$$

$$\mathbf{P}_n^a = (\mathbf{I} - \mathbf{K}_n \mathbf{H}_n) \, \mathbf{P}_n^f, \tag{2.31b}$$

where

$$\mathbf{K}_n \coloneqq \mathbf{P}_n^f \mathbf{H}_n^{\mathrm{T}} \left(\mathbf{R}_n + \mathbf{H}_n \mathbf{P}_n^f \mathbf{H}_n^{\mathrm{T}} \right)^{-1} \tag{2.32}$$

is known as the *Kalman gain* in the DA literature.

While this presentation of the KF may not be the shortest one, it establishes a clear link to the general filtering problem and, importantly, exposes the role of different assumptions in obtaining the KF solutions. For example, it turns out that the Gaussian approximations in (2.27) are not explicitly needed until one proceeds to the KF update step (see Cohn 1997). In other words, the forecast equations in (2.28), which describe how the first two moments of the filtering distribution evolve, are valid for any state-space model of the form (2.26), regardless of the nature of the underlying stochastic processes.

A much simpler KF derivation, widely used in atmospheric DA textbooks, *assumes* that the model state at the current time step $\hat{\mathbf{x}}_n^a$ can be written as a linear combination of the forecasted state estimate from the previous time $\hat{\mathbf{x}}_n^f$ and the current observations $\mathbf{y}_n$, i.e.

$$\hat{\mathbf{x}}_n^a = \hat{\mathbf{x}}_n^f + \mathbf{W} \left(\mathbf{y}_n - \mathbf{H}_n \hat{\mathbf{x}}_n^f \right), \tag{2.33}$$

where $\mathbf{W}$ is some weight that is chosen to minimize the total variance of $\hat{\mathbf{x}}_n^a$. Upon explicitly writing the covariance matrix of $\hat{\mathbf{x}}_n^a$ and differentiating its trace with respect to $\mathbf{x}_n$, we find that $\mathbf{W}$ is none other but the Kalman gain matrix $\mathbf{K}$ defined in (2.32). Even more generally, it can be shown (*cf.* Cohn 1997) that given the stochastic observation model (2.26b) together

with (2.27b) and no assumptions on the underlying distributions, the Kalman gain in (2.32) minimizes the scalar $\mathbb{E}\left[\left(\hat{\mathbf{x}}_n^a - \mathbf{x}_n\right)\mathbf{S}\left(\hat{\mathbf{x}}_n^a - \mathbf{x}_n\right)^{\mathrm{T}}\right]$ for any choice of the positive definite matrix $\mathbf{S}$. This result is formally referred to as the *best linear unbiased estimate* (BLUE) property of the KF.

We conclude our discussion on the KF by stating its perhaps most fundamental property: under the filtering assumptions considered so far, the KF provides the *minimum error-variance solution*, which is a direct consequence of the following powerful result in estimation theory:

Theorem 1. *Consider the quadratic functional* $\mathcal{J} : \mathbb{R}^{N_x} \to \mathbb{R}$ *defined by*

$$\mathcal{J} \coloneqq (\mathbf{x}_n - \hat{\mathbf{x}}_n)^{\mathrm{T}}\mathbf{S}(\mathbf{x}_n - \hat{\mathbf{x}}_n),$$

where $\mathbf{x}_n$ *and* $\hat{\mathbf{x}}_n$ *are the model state and its estimate at time* t_n*, and* $\mathbf{S}$ *is some positive definite matrix.*

Then $\mathbb{E}(\mathcal{J})$ *is minimized uniquely for any* $\mathbf{S}$ *if* $\hat{\mathbf{x}}_n$ *is taken to be the conditional mean* $\mathbb{E}[\mathbf{x}_n|\mathcal{Y}_n]$*. Furthermore, this particular choice of* $\hat{\mathbf{x}}_n$ *is unbiased.*

Proof. See Appendix A of Cohn (1997). □

To verify the minimum error-variance property of the KF under the assumption of a Gauss-linear state-space model (2.26), recall that $(2.31a)$ represents the conditional mean of the filtering (posterior) density $p(\mathbf{x}_n|\mathcal{Y}_n)$. In this special case, it can be further shown that the conditional mean (i) minimizes a much broader class of cost functions $\mathcal{J}$ and (ii) coincides with the conditional mode (maximum *a posteriori*) estimate. The latter property is often used in textbooks to demonstrate the equivalence between the Kalman filter and the three-dimensional variational DA method.

2.2.4 EnKF as a Monte Carlo implementation of the KF

The KF and other linear filtering algorithms were originally developed for aeronautical applications and played a crucial role in the success of several important missions, such

as Apollo (Hutchinson 1984). However, the large size of the KF covariance matrices and the restriction to Gauss-linear state-space models make these filters impractical for most Earth system applications. To overcome this, Evensen (1994) proposed a Monte Carlo implementation of the KF method – the *ensemble Kalman filter* (EnKF), where one uses a small number of ensemble forecasts to approximate the evolution of the state and its uncertainty. In particular, each member is evolved according to the nonlinear dynamics in (2.21a) to generate a sample from the prior density $p(\mathbf{x}_n|\mathcal{Y}_{n-1})$. The sample statistics from the propagated ensemble members are then used to approximate the true prior mean $\mathbf{x}_n^f$ with $\hat{\mathbf{x}}_n^f$ and the true prior covariance $\mathbf{P}_n^f$ with $\hat{\mathbf{P}}_n^f$.

With this in mind, the main idea of every EnKF algorithm is to update the prior ensemble mean $\hat{\mathbf{x}}_n^f$ and covariance $\hat{\mathbf{P}}_n^f$ such that they converge to the true KF analysis mean $\mathbf{x}_n^a$ and covariance $\mathbf{P}_n^a$ in the limit of an infinite ensemble size (see Mandel et al. 2011). Within the original EnKF formulation, this is achieved by updating each prior ensemble member $\mathbf{x}_k^f$ [3] ($k = 1, ..., K$; K being the ensemble size) according to (see Burgers et al. 1998)

$$\mathbf{x}_k^a = \mathbf{x}_k^f + \mathbf{K}\left(\mathbf{y}_k - \mathbf{H}\mathbf{x}_k^f\right), \tag{2.34}$$

where $\mathbf{y}_k \coloneqq \mathbf{y} + \boldsymbol{\varepsilon}_k$ and $\boldsymbol{\varepsilon}_k$ is sampled from $\mathcal{N}(\mathbf{0}, \mathbf{R})$. This analysis scheme is inherently stochastic as each prior member $\mathbf{x}_k^f$ is corrected with a perturbed version of the original observation vector[4]. By contrast, deterministic EnKFs avoid the need to sample from $\boldsymbol{\varepsilon}$ by solving for the matrix square root of $\hat{\mathbf{P}}^a$, i.e. $\mathbf{X}'^a$ such that $\mathbf{X}'^a(\mathbf{X}'^a)^{\mathrm{T}} = \hat{\mathbf{P}}^a$. Now, since $\mathbf{X}'^a$ can be also written as a matrix holding the analysis member perturbations, *viz.*

$$\mathbf{X}'^a = \left[\mathbf{x}_1'^a, ..., \mathbf{x}_K'^a\right], \tag{2.35}$$

[3] Note that the explicit time dependence will be omitted hereafter.

[4] Very recently, van Leeuwen (2020) showed that a more consistent interpretation of the stochastic EnKF requires that the noise term $\boldsymbol{\varepsilon}_k$ is added to the observed prior $\mathbf{H}\mathbf{x}_k^f$ instead of the observations $\mathbf{y}_k$.

with $\mathbf{x}_k^{'a} := \mathbf{x}_k^a - \mathbf{x}^a$ and $\mathbf{x}^a$ being the KF analysis mean from (2.31a), the posterior ensemble members in deterministic filters can be recovered by simply setting

$$\mathbf{X}^a = \left[\mathbf{x}_1^a, ..., \mathbf{x}_K^a\right] = \mathbf{x}^a \mathbf{1}_{N_x}^{\mathrm{T}} + \mathbf{X}^{'a}, \tag{2.36}$$

where $\mathbf{1}_{N_x}$ is a vector of N_x ones. Due to the inherent non-uniqueness of $\mathbf{X}^{'a}$, past studies have introduced several deterministic EnKF approaches to solve $\mathbf{X}^{'a}$ in a different way (Tippett et al. 2003). Nevertheless, they all share the same motivation – to improve the numerical properties of the ensemble-based analysis covariance matrix $\hat{\mathbf{P}}^a$. In particular, note that $\hat{\mathbf{P}}^a = \mathbf{X}^{'a}(\mathbf{X}^{'a})^{\mathrm{T}}$ is guaranteed to be a positive semidefinite matrix, which is a key requirement for every covariance matrix (e.g., Jazwinski 1970).

2.2.5 Ensemble square root filter (EnSRF)

The ground-based profiling instruments studied in this work are assimilated with a particular deterministic EnKF variant called the *ensemble square root filter* (EnSRF), which was first proposed by Whitaker and Hamill (2002). To make a clear distinction between their method and the stochastic (perturbed-observation) EnKF, the authors begin their presentation by first *assuming* that the ensemble perturbation update in any EnKF method can be written as

$$\mathbf{x}_k^{'a} = \mathbf{x}_k^{'f} + \tilde{\mathbf{K}}\left(\mathbf{y}_k' - \mathbf{H}\mathbf{x}_k^{'f}\right). \tag{2.37}$$

Albeit rather heuristic at first sight, this representation has a form that mimics the covariance update in square root KFs (e.g., see Eq. 2.39 below). The stochastic EnKF of Burgers et al. (1998) can be recovered by setting $\tilde{\mathbf{K}} = \mathbf{K}$, upon which $\mathbb{E}\left[\mathbf{x}^{'a}\mathbf{x}^{'a\mathrm{T}}\right] = \mathbf{P}^a$ as $K \to \infty$ (Mandel et al. 2011). In deterministic EnKFs, $\mathbf{y}_k' = \mathbf{0}$ and the goal is to find $\tilde{\mathbf{K}}$ such that $\mathbb{E}\left[\mathbf{x}^{'a}\mathbf{x}^{'a\mathrm{T}}\right] = \mathbf{P}^a$ as $K \to \infty$ still holds.

One solution for $\tilde{\mathbf{K}}$ was given by Potter (1964) in the special case of *serially assimilated* observations[5]. Under this restriction, the matrix sum $\mathbf{R}+\mathbf{H}\mathbf{P}^f\mathbf{H}^T$ appearing in the Kalman gain (2.32) reduces to a scalar and can be trivially inverted. In his derivation, Potter rewrites the KF covariance update (2.31b) based on the matrix square roots $\mathbf{S}^f$ and $\mathbf{S}^a$ of $\mathbf{P}^f$ and $\mathbf{P}^a$, respectively, upon which he shows that

$$\tilde{\mathbf{K}} = \left(1+\sqrt{\frac{\mathbf{R}}{\mathbf{R}+\mathbf{H}\mathbf{P}^f\mathbf{H}^T}}\right)^{-1}\mathbf{K}. \tag{2.38}$$

This *reduced Kalman gain* is then used to solve the square root version of the KF covariance update

$$\mathbf{S}^a = (\mathbf{I}-\tilde{\mathbf{K}}\mathbf{H})\mathbf{S}^f. \tag{2.39}$$

It can be easily verified that if $\mathbf{y}'_k = \mathbf{0}$ in (2.37), then $\mathbb{E}\left[\mathbf{x}'^a\mathbf{x}'^{a\mathrm{T}}\right]$ correctly recovers the true analysis covariance $\mathbf{P}^a$ obtained by taking the transpose of (2.39).

The EnSRF represents a Monte Carlo extension of Potter's square root KF in which the traditional Kalman gain $\mathbf{K}$ is used to update the ensemble mean $\mathbf{x}^f$ according to (2.31a), whereas its reduced version $\tilde{\mathbf{K}}$ – the ensemble perturbations following (2.37). The serial nature of the algorithm is implemented as follows: each time a new observation becomes available, the input ensemble members are updated and subsequently used as a new prior (background) for the next available one. In this case, since the evaluation of $\tilde{\mathbf{K}}$ pertains to a simple rescaling of $\mathbf{K}$, the computational costs of EnSRF are comparable to those required by stochastic EnKFs.

[5] This rather strong assumption is only valid if the observation errors are uncorrelated, i.e. if $\mathbf{R}$ is diagonal.

2.3 Overview of the PECAN field campaign

The data from the ground-based remote sensors used in this dissertation come from the Plains Elevated Convection at Night (PECAN) field campaign (Geerts et al. 2017), which took place during the months of June and July 2015. The main objective for their deployment was to better understand and predict mesoscale convective systems (MCSs) forming in the nocturnal environment of the Great Plains. These systems are important from a societal point of view as they contribute to the well-known maximum of warm-season precipitation in this region (e.g., Wallace 1975).

The decrease in surface-based instability at night means that the mechanisms responsible for convective maintenance differ substantially from those observed during the day. Prior to the PECAN field campaign, there were several possible hypotheses to explain the dynamics of nocturnal MCSs. They all envisioned a multistep process, in which convection first initiates over the Rocky Mountains and then propagates eastward over the Great Plains where it is maintained by some favourable processes in the night-time environment. However, the exact mechanisms leading to convective maintenance were not well understood. Some past work has suggested that nocturnal convection is sustained thanks to the *deep-tropospheric gravity waves* (e.g., Fovell et al. 2006) and *mesoscale potential vorticity (PV) anomalies* (Li and Smith 2010) generated in the early evolution of these systems. Other investigators (e.g., Parsons et al. 2019a) have argued in favour of *atmospheric bores*, which, by contrast, occur in the later stages of convective development. The transport of low-level moisture from *nocturnal low-level jets* (NLLJs; Shapiro et al. 2016) is another external factor that can additionally enhance the ongoing convective activity (Arritt et al. 1997). Very likely, all of the aforementioned mechanisms play some role in the nocturnal convective dynamics. However, the rich datasets collected during PECAN can help us quantify some of their relative contributions. For example, Reif (2020) recently conducted idealized numerical simulations based on 108 proximity radiosondes from PECAN and concluded that atmospheric bores and

NLLJs are more important than PV anomalies for the initiation of no-boundary convective events.

Despite their dynamical importance, nocturnal convective systems are still poorly represented in contemporary NWP models (Trenberth et al. 2003; Surcel et al. 2010). In the case of global NWP, convective parameterizations appear to be ill-suited for the night-time environment of the Great Plains (Davis et al. 2003; Clark et al. 2007). However, even convection-permitting LAMs have been found to experience problems associated with the timing, location and duration of nocturnal convective events. Therefore, the second important goal of the PECAN project was to understand whether the unique datasets collected during PECAN can systematically improve the nocturnal convective forecasts. As explained in Section 1.2, this dissertation attempts to partially address this objective by studying the impact of ground-based remote sensors on the forecasts of bore-generating nocturnal MCSs. The companion studies of Degelia et al. (2019) and Degelia et al. (2020) complement our work by evaluating the impact of these instruments on the closely related problem of nocturnal CI. In what follows next, we provide a brief summary of all datasets assimilated in our experiments.

2.4 Assimilated datasets

2.4.1 Conventional observations

The numerical experiments presented in Chapters 4 and 5 use a data addition approach whereby ground-based remote sensing retrievals are assimilated on top of operationally relevant (conventional) observations. In our case, the conventional datastream consists of in situ measurements coming from surface stations, radiosondes, commercial aircrafts, ships, and buoys (NDAS; Rogers et al. 2009) as well as WSR-88D radar reflectivity and radial velocity data processed with the WDSS-II software package (Lakshmanan et al. 2007).

Here we make the important remark that in several past studies, the impact of ground-based remote sensors has been studied in the absence of radar data (e.g., Zhang and Pu

2011; Zhang et al. 2016b; Lewis et al. 2020; Wang et al. 2020). Throughout this dissertation, however, we consider these observations to be part of our conventional dataset in view of their operational use in many convection-permitting LAMs. While the assimilation of radar observations will likely decrease the overall impact of ground-based remote sensors, we believe this is an important prerequisite for objectively examining the value of these novel systems in future NWP models.

2.4.2 Thermodynamic remote sensors

The primary thermodynamic remote sensor considered in this dissertation is the *Atmospheric Emitted Radiance Interferometer* (AERI). This instrument retrieves high-frequency profiles of temperature and moisture in the lower troposphere by measuring the downwelling infrared radiation for wavelengths ranging between 3.3 and 19 μm. Each AERI retrieval also comes with its own uncertainty estimate that is obtained from the imaginary component of the instrument's calibration equation (Revercomb et al. 1988). In Chapter 4, we test the sensitivity of the forecasts to a simple scaling of these original error estimates, whereas in Chapter 5 we further modify the AERI uncertainties to account for the representation component of the observation errors (Janjić et al. 2018).

Since the observation impacts in Chapter 4 were only examined for a single case study, we had the computational resources to assimilate additional PECAN observations and compare their forecast impacts against those obtained with ground-based remote sensors. One of these special datasets comes from the *Lidar Atmospheric Sensing Experiment* (LASE) on-board the NASA DC-8 aircraft (Browell et al. 1998). This instrument is a differential absorption lidar (DIAL) which operates in two different wavelength – an absorbing and a non-absorbing one. The vertical water vapor profiles in LASE are obtained by taking the ratio of the returned (backscattered) signals from these two wavelengths.

2.4.3 Kinematic remote sensors

There were two different types of ground-based kinematic remote sensors assimilated in this work. The first one is the *radar wind profiler* (RWP) – a pulsed Doppler radar which typically operates in the ultrahigh frequency (UHF) range (300-3000 MHz) in the context of PBL applications. The RWPs measure the amount of backscattered electromagnetic signal from turbulence-induced gradients in the refractive index. A key assumption in the retrieval process is that the turbulent eddies causing the scattering are carried along with the mean flow.

The second source of vertical wind profiles comes from the *Doppler wind lidar* (DWLs). Its measurement principle is very similar to that of the RWP, but the emitted signal represents laser light instead of radio waves. Another key difference is that the backscattered signal comes from aerosol particles, which are assumed to be ideal tracers for atmospheric winds. Although the temporal resolution of DWLs is significantly better compared to RWPs, the fact that most aerosol particles are concentrated within the PBL limits its operational range. Optically thick clouds are another prominent obstacle as they tend to attenuate the transmitted signal. The reader is referred to Reitebuch et al. (2001) for a more detailed discussion on the differences between these two instruments.

2.4.4 In situ PECAN observations

The remote sensors described above were also supplemented with frequent radiosonde measurements. As will be discussed separately in Chapter 5, the collocation of in situ and remotely sensed observations is crucial for objectively measuring the impact of different ground-based profiling networks. During PECAN, the number of radiosondes was typically between 2 and 4, although on 20 June 2015 one of the PECAN sites collected measurements every 30 minutes for a total of 6 hours. To account for this high temporal frequency, the special PECAN radiosondes were treated as a distinct observation type and were thus removed from the conventional datasets.

Our experiments in Chapter 4 also considered surface data from both fixed and mobile PECAN sites. Similar to the special PECAN radiosondes, the temporal frequency of these surface measurements was very high (1-5 min) and required the construction of a special experiment that can differentiate them from the operational datastream.

2.5 GSI-EnKF-WRF system

The numerical simulations presented in this dissertation are conducted with the convective-scale analysis-forecast system of Johnson et al. (2015). This system integrates three distinct software packages and provides an end-to-end capability for performing real-time DA experiments. Below we briefly outline key facts about each of these components.

Prior to their assimilation, observations are processed and quality controlled with version 3.4 of the Gridpoint Statistical Interpolation (GSI) package. This software was originally developed by the National Center for Environmental Prediction (NCEP) for their legacy Spectral Statistical Interpolation (SSI) analysis system (Parrish and Derber 1992). Since then, GSI has been modified to operate in physical space and to take advantage of newly emerging parallel architectures. The main contribution of Johnson et al. (2015) was to introduce a new GSI capacity that allows for an efficient processing of radar reflectivity and radial velocity observations, both of which are an essential component of our conventional datasets. In addition to preparing observations for their subsequent assimilation, another important feature of GSI is its comprehensive observation operator $h : \mathbb{R}^{N_x} \rightarrow \mathbb{R}^{N_y}$ which projects the prior ensemble members $\left\{\mathbf{x}_k^f : k = 1, .., K\right\}$ to observation space.

The output from GSI comes in the form of diagnostic files containing all necessary observation-space statistics for calculating the serial EnSRF analysis. Here we use version 1.0 of a GSI-based EnSRF code developed by the National Oceanic and Atmospheric Administration (NOAA) Earth System Research Lab (ESRL) in collaboration with the research community. To make efficient use of the high-performance computing architectures on which our experiments are performed, the parallel EnKF implementation of Anderson

and Collins (2007) is adopted. The main idea behind this approach is to avoid the inefficient re-evaluation of the observed prior ensemble $\left\{h\left(\mathbf{x}_k^f\right) : k = 1, .., K\right\}$ every time a new observation is assimilated. This problem can be ameliorated by solving two additional equations which are analogous to (2.31a) and (2.37), but instead update the observed prior ensemble corresponding to the remaining observations in the sequence. Aside from this highly efficient EnSRF implementation, we also use standard techniques to tackle problems commonly encountered in ensemble-based DA. Specifically, the adverse impact of sampling errors is limited through the Gaspari-Cohn localization technique (Gaspari and Cohn 1999), whereas the lack of ensemble diversity during model integration – through the constant multiplicative inflation and relaxation to prior spread (RTPS) methods of Whitaker and Hamill (2012). Following Wang and Wang (2017), random Gaussian noise is also added during each EnSRF cycle so that newly formed storms can be quickly introduced in the EnSRF analysis.

Finally, the forecast component of our system is driven by the Weather Research and Forecasting (WRF) model which solves the fully compressible, non-hydrostatic Euler equations (Skamarock et al. 2008). First developed in the late 1990s as a multi-agency effort, this community tool now accommodates diverse Earth system applications with scales from a few meters to thousands of kilometers. Similar to the GSI and EnKF packages, WRF has been found to perform very well on parallel computing architectures (e.g., Michalakes et al. 2004), which is a critical requirement for efficiently running ensemble forecasts at convection-permitting resolutions. In this dissertation, we use the Advanced Research WRF (ARW) dynamical core largely maintained by the Mesoscale and Microscale Meteorology (MMM) laboratory at the National Center for Atmospheric Research (NCAR). More details regarding the exact configuration of the WRF-ARW model in our experiments are deferred to Chapters 4 and 5.

Chapter 3

Object-based algorithm for the identification and tracking of convective outflow boundaries in numerical models

3.1 Introduction

Convectively generated outflow boundaries, such as density currents and bores, have an important contribution to the dynamics of mesoscale convective systems (MCSs). The theoretical importance of density currents is well established due to their critical role in the MCS evolution (e.g., Rotunno et al. 1988; Weisman and Rotunno 2004). On the other hand, atmospheric bores are still less familiar to the meteorological community, but these disturbances have received considerable attention recently, including being a focus of the Plains Elevated Convection at Night Field Campaign (PECAN; Geerts et al. 2017). The increasing interest in bores is largely driven by their ability to initiate and maintain nocturnal MCSs (Carbone et al. 1990; Crook et al. 1990; Locatelli et al. 2002; Parker 2008; Blake et al. 2017; Parsons et al. 2019a). Recent work has also shown that bores occur commonly in association with warm season nocturnal convection over the Great Plains (Haghi et al. 2017).

The dynamical significance of convective outflow boundaries has prompted the scientific community to create automated algorithms for identifying and tracking these features. The earliest algorithm developed for this purpose was entirely based on observational data and closely connected to the procurement plans for the Next-Generation Radar (NEXRAD) system (e.g., Crum and Alberty 1993). In particular, Uyeda and Zrnić (1986) as well as

Smith et al. (1989) were the first to describe radar-based algorithms for gust front (density current) detection that relied on the velocity convergence along radials. Later enhancements to these algorithms included the addition of radar reflectivity in the Advanced Gust Front Algorithm (AGFA; Eilts et al. 1991) and the use of knowledge-based signal processing in the Machine Intelligent Gust Front Algorithm (MIGFA; Delanoy and Troxel 1993; Troxel et al. 1996; Smalley et al. 2005). Likewise, advances in computational resources have made it possible to identify and track convective outflow boundaries in high-resolution model outputs. Previous model-based algorithms have focused on detecting density currents by incorporating various physical parameters, such as temperature (Torri et al. 2015; Gentine et al. 2016), buoyancy (Tompkins 2001; Seigel 2014), wind (Langhans and Romps 2015), radial gradients in the density potential temperature (Drager and van den Heever 2017) or a combination of several relevant parameters (Li et al. 2014).

Although the aforementioned methodologies have greatly enhanced our understanding of density current and gust front dynamics, these approaches are somewhat restricted in their application compared to the algorithm presented in this chapter. On the one hand, the previously mentioned approaches are not suitable for detecting multiple types of convective outflow boundaries. This limitation can be problematic with regards to typical night-time environments in which density currents can trigger atmospheric bores upon their interaction with the stable boundary layer (White and Helfrich 2012). The frequent generation of bores during the night-time hours (Haghi et al. 2017) and their important role in the maintenance of nocturnal MCSs (Parker 2008; Blake et al. 2017) necessitate the development of methods to detect and track bores as well as their parent density currents. The other limitation of earlier convective outflow algorithms is that they have been mostly applied in idealized modeling frameworks, which may make them inappropriate for real-time forecasting applications.

In order to understand the interplay between nocturnal outflow boundaries and convective systems in real-time high-resolution Numerical Weather Prediction (NWP) models, this study presents a novel object-based algorithm that is capable of seamlessly identifying

density currents and bores. The latter is achieved by employing a multivariate approach similar to the dryline identification algorithm of Clark et al. (2015). Rather than attempting to detect all convective outflow boundaries present in high-resolution model simulations, the objective of this algorithm is to isolate only those that provide sufficient lifting for the initiation and maintenance of nocturnal MCSs. The latter goal falls in line with the recent findings of Parker (2008), French and Parker (2010) and Parsons et al. (2019a) who suggest that the primary lifting mechanism for nocturnal MCSs can change from a density current to an internal bore with the onset of nocturnal cooling.

Aside from the specific choice of identification parameters, the proposed algorithm differs from the previously discussed methods in terms of how it tracks the identified objects in time. Traditionally, object tracking techniques rely on statistical methods to match objects from two different model time steps (Lakshmanan 2012). By contrast, the object tracker proposed in this study accounts for the dynamics of convective outflow boundaries in an explicit manner. As will be shown later in the chapter, imposing dynamical constraints in the algorithm yields more robust tracking results compared to an algorithm based on statistical considerations alone. It is also worth remarking that developing algorithms with due regard to the dynamical aspects of the tracked objects was a key recommendation of Davis et al. (2009b) – one of the first studies focusing on object-based identification and verification using NWP data.

In addition to the technical details behind the algorithm framework, this chapter also highlights a spectrum of additional algorithm applications relevant for bore research and operational forecasting of nocturnal storms. Generally speaking, these algorithm applications can be utilized in two different ways. The first one pertains to the verification of numerically simulated convective outflow boundaries. With the advance of convection-allowing NWP models, object-based verification techniques like the Method for Object-based Diagnostic Evaluation (MODE; Davis et al. 2006) have become a popular choice for validating the accuracy of localized and spatially inhomogeneous fields such as precipitation (e.g., Davis

et al. 2009a; Johnson et al. 2011a,b; Johnson and Wang 2012; Johnson et al. 2013; Johnson and Wang 2013; Clark et al. 2014). Unfortunately, the majority of these object-based methods cannot be readily extended to verify bore forecasts. MODE, for instance, relies on the presence of continuous observational data sets in order to verify model forecasts, which is not feasible in the case of convective outflow boundaries.

Secondly, the algorithm applications proposed in this chapter can be also used to obtain a better understanding of the underlying bore dynamics as well as the role of bores in initiating and maintaining nocturnal MCSs. In order to examine the characteristics of numerically simulated bores, previous studies (e.g., Martin and Johnson 2008; Koch et al. 2008a) had to first identify their location by subjectively examining the appropriate model output fields. While this is a reasonable approach in terms of single case studies, analyzing the dynamical properties of bores in large data sets spanning a large number of numerical simulations is considerably more time consuming and, additionally, prone to human errors.

The algorithm framework and the attendant algorithm applications in this study are illustrated through a forecast experiment based on the 6 July 2015 PECAN case study. Using the Weather Research and Forecasting (WRF) model (Powers et al. 2017), 40 ensemble members with a horizontal grid spacing of 1 km are run between 03 UTC and 09 UTC. These high-resolution forecast members are initialized with a Gridpoint Statistical Interpolation (GSI)-based convection-allowing ensemble data assimilation system (Johnson et al. 2015; Johnson and Wang 2017; Wang and Wang 2017) after assimilating both radar and conventional data over a time window of 3 and 12 hours, respectively.

The rest of the chapter is organized as follows. Sections 3.2 and 3.3 introduce the identification and tracking components of the algorithm. Section 3.4 describes several algorithm tools and their application to the 6 July 2015 case study. Finally, Section 3.5 summarizes the main aspects of the algorithm, outlines some of its limitations and suggests possible ways to overcome those in future work.

3.2 Identification of convective outflow boundaries

3.2.1 Concept

As elucidated in Section 3.1, the novelty of this algorithm comes from the unified description of density currents and bores, which is made possible by taking into account the *dynamical similarities* between these two convective outflow boundaries. Specifically, it is well known that (i) density currents and bores are characterized by high values of vertical velocity along their leading edge and that (ii) their passage leads to a sudden jump in pressure near the surface. The pressure rise in density currents is mostly hydrostatic in nature and arises due to the horizontal advection of cold air behind them, but it also contains a non-hydrostatic component associated with the deceleration of the density current relative inflow. This is to be contrasted with the pressure increase in a bore, which is caused by the net upward displacement and subsequent adiabatic cooling of near-surface stable air. The identification component of the algorithm parameterizes these effects through the 1-km above the ground level (AGL) vertical velocity ($w^{1\mathrm{km}}$) and the temporal change in mean sea level pressure (Δp), where Δ represents the model time step and is set to be 15 min in this study. Although the choice of a particular height level for the vertical velocity is somewhat arbitrary, the 1-km AGL was selected because it (i) marks the location where the prefrontal updraft of a convective outflow boundary is likely to be found (e.g., Rotunno et al. 1988) and (ii) has been used in some real-time NWP forecast products to assist the bore missions during the PECAN field campaign (Johnson and Wang 2017). After carefully choosing representative threshold values for these two model variables (see Section 3.2.2 for details), their corresponding binary fields are combined through a binary AND operation (1 and 0 for meeting or not meeting the criteria, respectively; see bottom left-hand side of Fig. 3.1). Later on, the algorithm utilizes the temporal change in the 2-m temperature (ΔT) to determine the morphology of the identified objects. By definition, density currents cause a drop in the near-surface temperature, i.e. $\Delta T < 0°\mathrm{C}\ (15\mathrm{min})^{-1}$. Nevertheless, the algorithm

Table 3.1: Parameter values for the identification and tracking components of the object-based algorithm. The identification thresholds refer to the smoothed and/or filtered model identification fields.

Parameter	Meaning	Value
Identification component		
Δp^-	Δp identification threshold for $t > t^{\text{sep}}$	0.25 hPa (15 min)$^{-1}$
w_2^-	$w^{1\text{km}}$ identification threshold for $t > t^{\text{sep}}$	0.2 m s^{-1}
$\lvert\vec{\nabla}p\rvert^-$	$\lvert\vec{\nabla}p\rvert$ identification threshold for $t < t^{\text{sep}}$	0.2 hPa km^{-1}
w_1^-	$w^{1\text{km}}$ identification threshold for $t < t^{\text{sep}}$	0.6 m s^{-1}
ΔT^{DC}	ΔT threshold for identifying density currents	-1.0 °C (15 min)$^{-1}$
ΔT^{B}	ΔT threshold for identifying bores.	0.0 °C (15 min)$^{-1}$
t_{sep}	separation time	150 min
λ_{sep}	separation wavelength for the Discrete Cosine Transform	150 km
$\sigma_{\Delta p}$	standard deviation for smoothing the Δp field	1.5 km
σ_w	standard deviation for smoothing the $w^{1\text{km}}$ field	3 km
$\sigma_{\lvert\vec{\nabla}p\rvert}$	standard deviation for smoothing the $\lvert\vec{\nabla}p\rvert$ field	2 km
$\sigma_{\Delta T}$	standard deviation for smoothing the ΔT field	5 km
i^{bo}	number of iterations for the binary opening operation	10
i^{bc}	number of iterations for the binary closing operation	1
A^-	minimum object size at the end of object identification	360 km^2
Tracking component		
CC^-	minimum allowed cross-correlation coefficient threshold	0.3
CC^+	maximum allowed cross-correlation coefficient threshold	1.0
β^+	maximum allowed angle deviation from the PGF direction	90°
V_O^+	maximum allowed object propagation speed	30 m s^{-1}
δ	maximum allowed $\vec{V}_O^{\text{TM}}$-$\vec{V}_O^{\text{CD}}$ difference	3 m s^{-1}

classifies the identified objects as density currents only if $\Delta T < \Delta T^{\text{DC}} = -1°\text{C}\ (15\text{min})^{-1}$, where the superscript DC denotes that the ΔT threshold refers specifically to density currents (see Table 3.1). The lower ΔT^{DC} value is chosen deliberately to ensure that the algorithm (i) captures only sufficiently strong density currents that are likely to have dynamic significance and (ii) accounts for the overall cooling of the nocturnal boundary layer. Since the passage of bores either does not change the 2-m temperature or leads to a slight near-surface warming (Koch and Clark 1999), a convective outflow object is classified as a bore only if $\Delta T \geq \Delta T^{\text{B}} = 0°\text{C}\ (15\text{min})^{-1}$, where the superscript B is a shorthand for bores. *It is namely these distinct surface temperature responses that permit the object-based algorithm to determine the morphology of the identified convective outflow boundaries*.

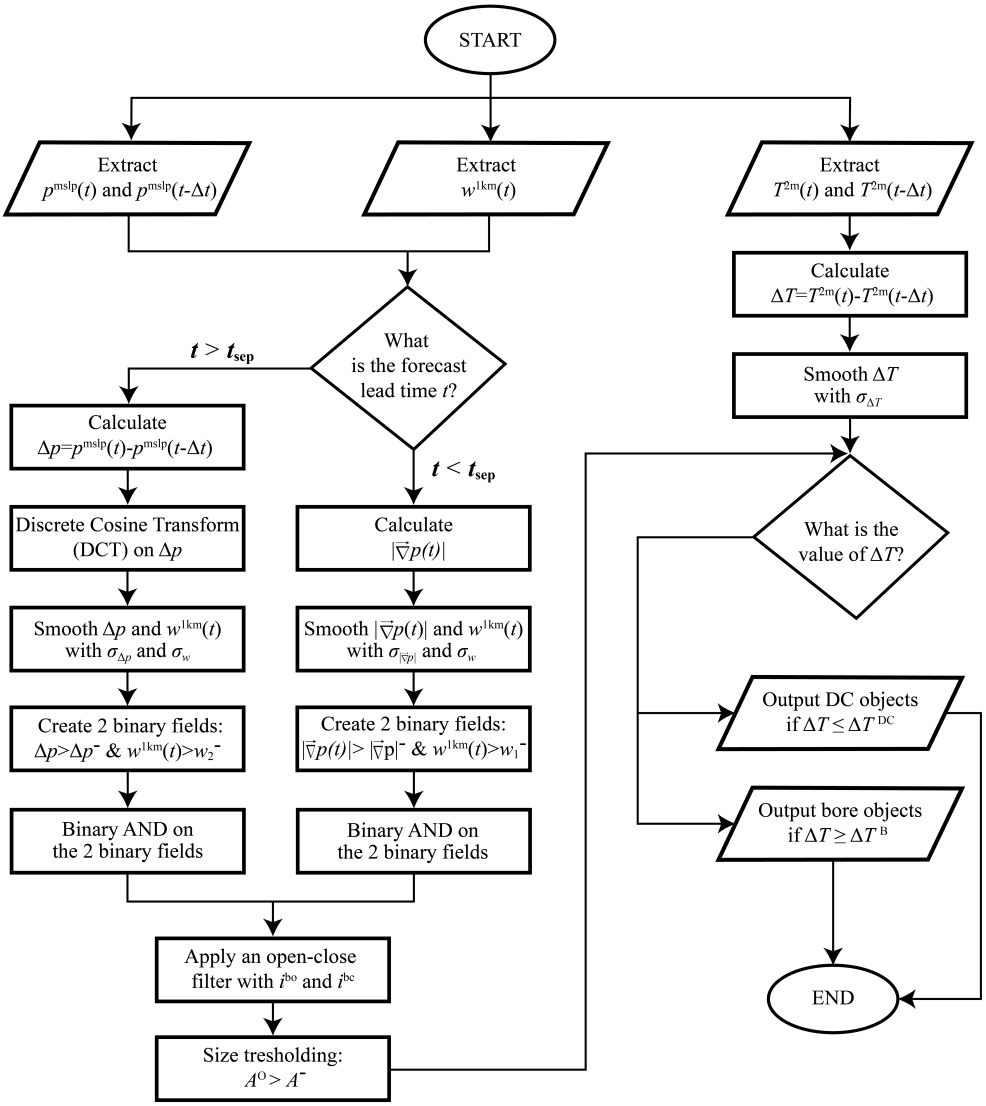

Figure 3.1: Workflow for the identification component of the algorithm. The variables p^{mslp}, $w^{1\mathrm{km}}$, $T^{2\mathrm{m}}$, $|\nabla p|$ and A^{O} refer to the mean sea level pressure, 1-km Above Ground Level (AGL) vertical velocity, 2-m temperature, horizontal gradient of mean sea level pressure and object area. The current and previous algorithm processing times are denoted as t and $t-\Delta t$, while t_{sep} represents the separation time beyond which the numerical noise magnitude is significantly reduced (see text for more details). To simplify the notation, superscripts are removed upon taking temporal differences between variables (e.g., Δp is equivalent to Δp^{mslp}). The parallelograms symbolically represent data I/O, the rectangles – the execution of specific algorithm routines, while the rhombi – the decision-making process needed for classifying the identified convective outflow objects as density currents or bores. The parameter values associated with the identification component of the algorithm are summarized in the first half of Table 3.1.

The workflow associated with the identification component of the algorithm is further illustrated through the 1-km horizontal grid spacing simulation of the 6 July 2015 case study (Fig. 3.2), the details of which are summarized in Section 3.1. In particular, the information contained within the Δp and $w^{1\text{km}}$ fields from Figs. 3.2a,b is used to create the convective outflow objects shown in Fig. 3.2c. The ΔT field from Fig. 3.2d emphasizes the heterogeneous morphology of the identified objects. For example, the southern portion of the tracked object (refer to the black contours in Fig. 3.2c) resembles an atmospheric bore (ΔT is neutral or positive), while the northern portion behaves like a density current (ΔT is mostly negative). As expected, the model-simulated reflectivity field in Fig. 3.2b suggests that the density current is located next to a convectively active region – in contrast to the bore, which has already propagated away from the parent MCS.

Additional evidence for the discriminating capabilities of the algorithm is provided in Fig. 3.3. The first column of this figure shows the algorithm output for two consecutive times during which the tracked object splits into two additional objects and the southern one changes its morphology from a density current to a bore. The objectively-determined outflow classification results (Figs. 3.3a,c) verify successfully against the vertical cross sections for the corresponding forecast lead times (Figs. 3.3b,d). More specifically, the vertical cross section from Fig. 3.3b shows classical density current signatures, such as an enhanced prefrontal updraft and a sudden drop in the virtual potential temperature (θ_v) following the passage of the boundary. Contrastingly, there is an amplitude-ordered wave train in the wake of the first convective outflow boundary on Fig. 3.3d (for x between 0 and 10 km on the cross-section), which is typical for the passage of an undular bore. It is worth remarking that the bore on Fig. 3.3d is immediately followed by its parent density current. The latter is located around x=0 km on the cross-section and appears to be considerably shallower in comparison to the previously shown forecast lead time (Fig. 3.3b). Note that the significantly weaker vertical velocities at the leading edge of the shallow density current prevent the object-based algorithm from identifying it. This example portrays the algorithm's

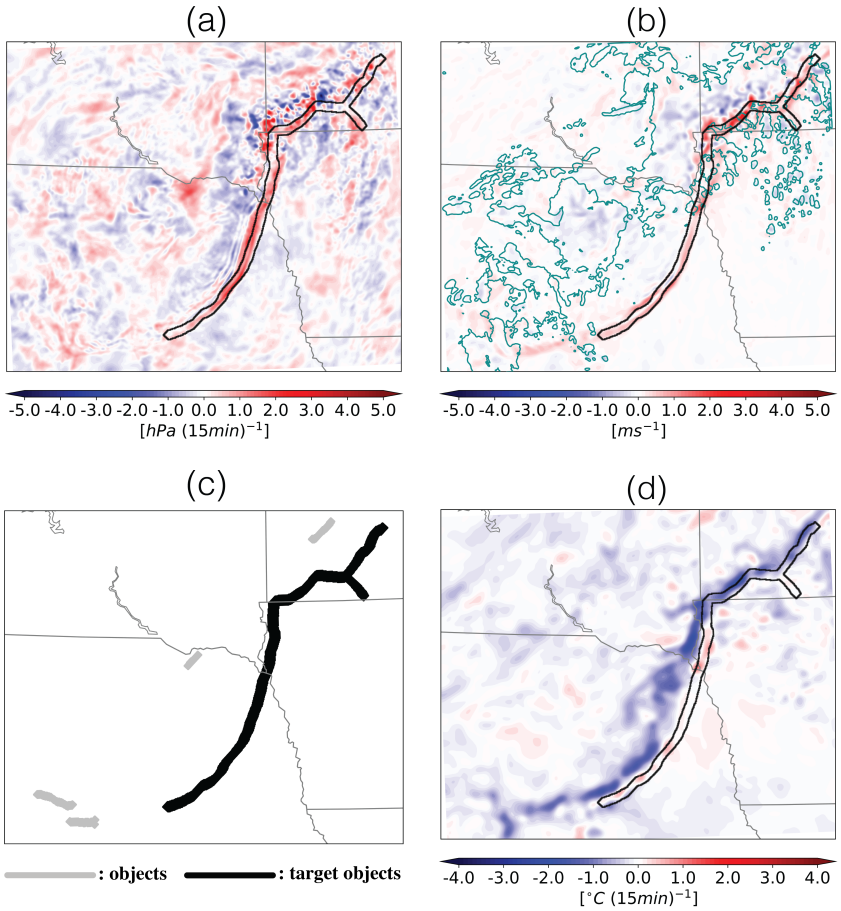

Figure 3.2: Illustrating the identification component of the algorithm. Panels (a) and (d) show the 15-min changes in the mean sea level pressure (Δp) and 2-m temperature (ΔT), respectively, after these fields have been smoothed and/or filtered with the Discrete Cosine Transform (DCT). Panel (b) displays the 1-km AGL vertical velocity ($w^{1\text{km}}$, color shaded) and the 35-dBZ contour of simulated radar reflectivity (dark cyan contours). Panel (c) shows all convective outflow boundaries identified by the object-based algorithm; the target objects tracked in this particular algorithm run are plotted in black, while the rest of the convective outflow objects detected at the current model time step (06:45 UTC on 6 July 2015) – in gray.

objective to only detect convective outflow boundaries that provide sufficient lifting for the initiation and maintenance of nocturnal convection. The scenario depicted in Fig. 3.3 corresponds quite well to the idealized simulations of Parker (2008), wherein the primary lifting mechanism required for the sustenance of a nocturnal squall line changes from a density current to a bore following the stabilization of the underlying boundary layer.

3.2.2 Implementation

All variables used in the identification component of the algorithm are modified in order to yield meaningful identification results. As far as the $w^{1\text{km}}$ and ΔT fields are concerned, Gaussian filters with standard deviations of σ_w = 3 km and $\sigma_{\Delta T}$ = 5 km are applied to remove any small-scale noise (Table 3.1). The alteration of Δp is slightly more involved due to the presence of numerical noise for short forecast lead times. Specifically, the use of data assimilation (DA) in the numerical simulations from this study introduces spurious inertia-gravity waves due to the imbalance between mass and wind fields (Lynch and Huang 1992; Wang et al. 2013). Although it is possible to remove this spurious numerical noise by exploiting initialization techniques such as the nonlinear normal mode initialization (Baer and Tribbia 1977) and digital filter initialization (Lynch and Huang 1992), this work proposes an alternative technique to remove the numerical noise within the formulation of the algorithm itself. In particular, the Discrete Cosine Transform (DCT; Ahmed et al. 1974) is applied to the pressure tendency field Δp in an attempt to filter out the spurious inertia-gravity waves whose wavelength is considerably larger than the wavelength of the Δp signal defining the convective outflow boundaries. The choice of DCT was guided by the study of Denis et al. (2002), which emphasized the suitability of the method for limited area models with aperiodic model fields. Although the choice of a scale separation wavelength λ_{sep} is somewhat arbitrary, tuning experiments over 3 diverse case studies showed that λ_{sep} = 150 km is optimal. In order to filter out the large-scale Δp features, the spectral coefficients corresponding to $\lambda_{\text{sep}} > 150$ km are set to 0 before inverting the Δp field back to physical

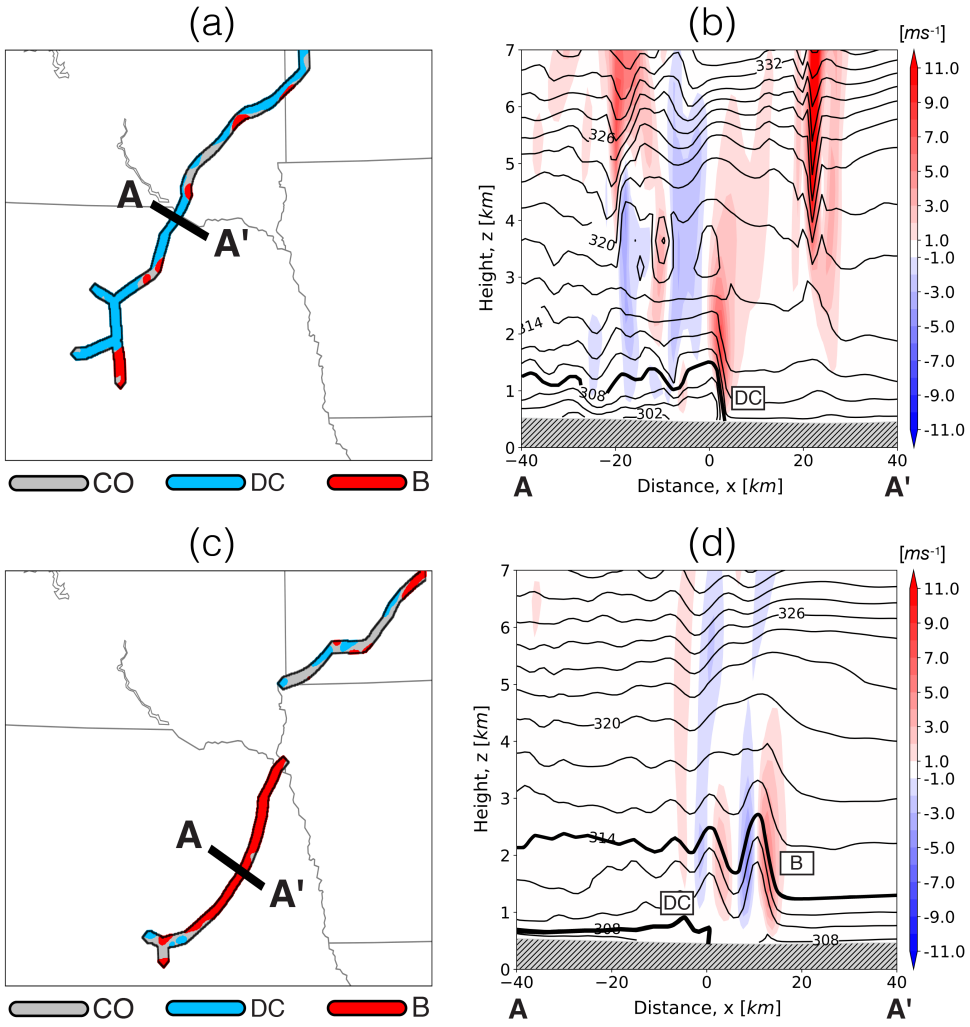

Figure 3.3: Example of classifying convective outflow objects for two different forecast times – 04:00 UTC (first row) and 06:30 UTC (second row). Panels (a) and (c) show the location of the identified objects. The color shading inside them corresponds to the object morphology as determined by the identification component of the algorithm: blue represents density currents (DC), red – bores (B), while gray marks those parts of the convective outflow objects whose morphology cannot be determined unambiguously (CO). The final shape of the objects is additionally modified with the medial axis transform. The cross sections in panels (b) and (d) are taken along the line segment AA' and show the vertical velocity (w; color shading) as well the virtual potential temperature (θ_v; black curves). The thick black contours embedded within the cross sections outline the subjectively determined density current and bore, while the stippled gray shading represents the terrain height.

space. Finally, since the filtered Δp field still contains small-scale features that can degrade the identification capabilities of the algorithm, a Gaussian filter with $\sigma_{\Delta p} = 1.5$ km is applied to the filtered Δp field. The relatively small value of $\sigma_{\Delta p}$ allows the object-based algorithm to detect dissipating bore objects, in which the Δp signature is weak.

It is worth mentioning that the DCT filter may be not as effective during the first hour or two of model integration when the spurious gravity wave activity is prolific and spans a larger spectrum of wavelengths. To address this issue, the algorithm has the option to substitute the Δp field with the magnitude of the horizontal mean sea level pressure gradient $|\nabla p|$ close to the model initialization time (upper-left portion of Fig. 3.1). Similar to Δp, the $|\nabla p|$ field is smoothed via a Gaussian filter with $\sigma_{|\nabla p|} = 2$ km. The time at which the pressure identification variable changes from $|\nabla p|$ back to Δp is referred to as a separation time t^{sep} and is defined to be the forecast lead time beyond which the absolute value of the domain-averaged $|\nabla p|$ does not show significant temporal trends ($t^{\text{sep}} = 2$h 30min for the numerical simulation used in this study). Algorithm tests comparing its performance with the two pressure identification variables confirmed that $|\nabla p|$ is a reasonable substitute of Δp for very short forecast lead times, but degrades the object identification results in the absence of significant numerical noise. Further note that the threshold value of $w^{1\text{km}}$ for $t < t^{\text{sep}}$ is 3 times larger compared to its counterpart value for $t > t^{\text{sep}}$, i.e. $w_1^- = 3w_2^-$ (refer to Table 3.1). The latter is intended to help the algorithm identify decaying convective outflow objects with weak vertical motions. Alternative approaches for optimally defining the threshold values of the identification parameters are examined in Section 3.5.

Lastly, we discuss the application of morphological image processing techniques within the identification component of the object-based algorithm. The latter aims to address the discontinuous nature of the convective outflow objects produced as a result of merging the $w^{1\text{km}}$ and Δp (or $|\nabla p|$) fields through the binary AND operation. More specifically, the algorithm incorporates the so-called *open-close filter* (Dougherty 1992) defined as the sequential application of 1 binary opening and 10 binary closing iterations (see Table 3.1).

This filter was chosen because of its restoration property, which removes both union and subtractive noises (Dougherty and Lotufo 2003). In particular, binary opening removes small-scale objects identified incorrectly by the algorithm, while binary closing fills the gaps between adjacent outflow objects, making their structure more coherent. Note that binary opening is applied first in order to prevent the spurious growth of small-scale objects. The choice of binary iterations (i^{bo} and i^{bc}; Table 3.1) was based on several tuning experiments, in which the structure of the identified outflow objects was assessed qualitatively. To ensure that only sufficiently large objects are considered by the algorithm, an additional size thresholding is applied ($A^O > A^-$; bottom-left corner of Fig. 3.1 and Table 3.1 for the value of A^-) prior to the classification of the identified convective outflow boundaries as density currents or bores.

3.2.3 Grid-spacing considerations

Apart from the need to choose appropriate model parameters, the identification of convective outflow boundaries in the algorithm is ultimately dependent on the ability of NWP models to correctly represent their dynamical characteristics (e.g., surface warming, pressure rise). Past studies (Koch et al. 2008a; Martin and Johnson 2008; Johnson and Wang 2017) alongside with additional analyses based on the 6 July 2015 simulations (see Fig. OS1 in the supplement material of Chipilski et al. (2018)) have concluded that the adequate representation of atmospheric bores in NWP models requires a horizontal grid spacing of less than 4 km. This, in turn, implies that the object-based algorithm should be only used in conjunction with data from higher-resolution convection-permitting NWP models. With a view of making our algorithm applicable to a broader range of model configurations, the remainder of this section discusses how changes in the horizontal resolution of convection-allowing models impact its identification capabilities. In particular, we comment on the key modifications required to successfully adapt the algorithm to a coarser 3-km model output,

which is more typical of the currently operational convection-allowing NWP systems such as the High-Resolution Rapid Refresh model (HRRR; Smith et al. 2008).

It is well known that coarser resolution model simulations tend to have a smoothing effect on the underlying model fields, which can, in turn, have downstream impacts on the number and/or extent of objects identified by the algorithm. Nonetheless, the application of a Gaussian filter implicitly circumvents this problem as it smooths the identification variables from different model resolutions to the same spatial scale. This statement is supported both by Table 3.2 and Figs. OS2a,b in the supplementary material of Chipilski et al. (2018), which show that the median and interquartile range (IQR) values associated with the smoothed identification variables are nearly identical on the 1-km and 3-km model domains, i.e. their ratio is ∼1. The only exception is the magnitude of the mean sea level pressure gradient $|\nabla p|$, for which the median and IQR values on the 3-km domain are lower than their respective values on the 1-km domain (refer to Figs. OS2c,d in the supplementary material of Chipilski et al. (2018)). The aforementioned discrepancy arises because the Gaussian filter is applied to model variables with different statistical characteristics: $|\nabla p| \in [0, \infty)$, while $w^{1\text{km}}, \Delta p, \Delta T \in (-\infty, \infty)$. In order to use the pressure gradient magnitude as an identification variable on the coarser 3-km model output, the threshold value $|\nabla p|^{-}$ from Table 3.1 needs to be scaled accordingly. In this study, the latter was achieved via the quantile mapping (QM) technique (e.g., Reiter et al. 2018). The QM results summarized in Table 3.2 indicate that the scaling factor for the $|\nabla p|^{-}$ threshold is $\alpha_{|\nabla p|}^{1\rightarrow 3} \sim 0.6$, i.e. the $|\nabla p|^{-}$ value needs to be reduced by 40% on the 3-km grid in order for the algorithm to provide equivalent object identification results. As expected, the scaling factors for the other identification variables are ∼1, suggesting that their corresponding thresholds do not need to be changed if the algorithm is to be run on numerical simulations with a horizontal grid spacing of 3 km.

Another important consequence of using coarser convection-allowing model simulations with the object-based algorithm is the requirement to adjust the number of iterations in the open-close filter, i.e. i^{bo} and i^{bo} in Table 3.1. Assuming there is a one-to-one correspondence

Table 3.2: Dependence of the algorithm's identification component on the horizontal resolution of convection-allowing NWP models. The second and third columns show the median and interquartile range (IQR) ratios of the coarser 3-km identification variables to the original 1-km ones. To obtain these ratios, the median and IQR values from one of the ensemble members are averaged throughout the 6-h model integration period used in the 6 July 2015 case study. The fourth column shows the scaling factor $\alpha^{1\rightarrow3}$ that needs to be applied to the identification thresholds corresponding to the 3-km model output so that the algorithm results from the 1-km and 3-km model outputs match. As explained in the text, $\alpha^{1\rightarrow3}$ is derived using the quantile mapping (QM) technique. The star (*) next to $\alpha^{1\rightarrow3}_{w^{1\mathrm{km}}}$ indicates that the threshold scaling factor for $w^{1\mathrm{km}}$ refers to both of its thresholds, i.e. $w^{-}_{1} = 0.6$ ms^{-1} and $w^{-}_{2} = 0.2$ ms^{-1}

Identification variable	**Median ratio**	**IQR ratio**	**Threshold scaling factor ($\alpha^{1\rightarrow3}$)**
$w^{1\mathrm{km}}$	1.00	0.97	0.97*
Δp	1.00	0.97	0.99
$\lvert\nabla p\rvert$	0.74	0.63	0.59

between the binary fields on two different model domains with a horizontal grid spacing of Δ_1 and Δ_2, it can be shown that

$$\left(i^{\mathrm{bo}}_{\Delta_2}, i^{\mathrm{bc}}_{\Delta_2}\right)\Delta_2 = \left(i^{\mathrm{bo}}_{\Delta_1}, i^{\mathrm{bc}}_{\Delta_1}\right)\Delta_1, \tag{3.1}$$

i.e. the number of open-close iterations on the new domain is inversely proportional to the change in model resolution. To account for the fact that the number of iterations must be an integer number, i.e. $i^{\mathrm{bo}}_{\Delta}, i^{\mathrm{bc}}_{\Delta} \in \mathbb{Z}$, the relationship from (3.1) is further approximated as

$$\left(i^{\mathrm{bo}}_{\Delta_2}, i^{\mathrm{bc}}_{\Delta_2}\right) = \left(i^{\mathrm{bo}}_{\Delta_1}, i^{\mathrm{bc}}_{\Delta_1}\right) \backslash \frac{\Delta_2}{\Delta_1}, \tag{3.2}$$

where \ represents an integer division. Applying (3.2) and using the information from Table 3.1 gives $i^{\mathrm{bo}}_{3\mathrm{km}} = 0$ and $i^{\mathrm{bc}}_{3\mathrm{km}} = 3$, suggesting that the algorithm should not use any binary opening iterations if it is run on model data with a horizontal grid spacing of 3 km.

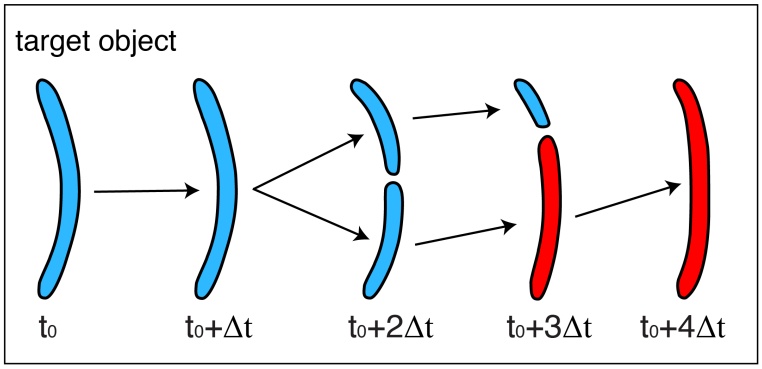

Figure 3.4: A schematic showing the concept behind the tracking component of the algorithm as well as the typical evolution of a convective outflow boundary in the night-time environment starting from an analysis time t_0. The blue (red) objects represent density currents (atmospheric bores), while the arrows denote the objects' motion vectors.

3.3 Tracking of convective outflow boundaries

3.3.1 Concept

The concept behind the object tracker is presented in Fig. 3.4. This schematic shows how a convective outflow boundary might evolve in a typical night-time environment and also highlights the key processes that the object tracker is expected to handle. Suppose that the left-most object in Fig. 3.4 is one of the many objects identified by the algorithm at some initial time t_0. Throughout its evolution, the aforementioned object could undergo various changes including (i) translation ($t_0 \rightarrow t_0 + \Delta t$), (ii) splitting ($t_0 + \Delta t \rightarrow t_0 + 2\Delta t$), (iii) merging ($t_0 + 3\Delta t \rightarrow t_0 + 4\Delta t$) and (iv) morphology transformation ($t_0 + 2\Delta t \rightarrow t_0 + 3\Delta t$; blue to red color shading). The purpose of the object tracker is to recognize all of these changes by associating objects between two consecutive image frames (separated by the model time step Δt).

3.3.2 Implementation

Association of objects from two neighboring image frames is a challenging problem, particularly in cases of object splitting, merging or rapid evolution (all of which are common for convective outflow boundaries). Past work on multi-object tracking has examined several techniques with a varying degree of complexity (Lakshmanan 2012). Those methods range from a simple minimization of object distances (greedy approach; Dijkstra 1959) to Kalman Filter applications (Kalman 1960). Nevertheless, the aforementioned tracking techniques are prone to errors, especially when the identified objects undergo rapid structural changes. To address these problems, Lakshmanan et al. (2003) developed a hybrid tracking approach that exhibits superior performance over the aforementioned methods. In this work, we use a variation of the hybrid tracking approach to formulate our object tracker.

The components of the object tracker are summarized by the block diagram in Fig. 3.5 and further illustrated in Fig. 3.6 through a representative case scenario, in which a target object (black shading) splits into two smaller objects (#1 and #2; gray shading) at the current model time step. In addition to these two objects, the binary field in Fig. 3.6 contains an additional third object (#3), which is not physically related to the target object. Ideally, the tracking component of the algorithm should only associate objects 1 and 2 with the target object. Within the framework of the object tracker, this is achieved through a sequential application of three different constraints, the technical details of which are explained in the remainder of this section.

The first constraint is purely statistical in nature and utilizes the template matching technique (Brunelli 2009). Template matching calculates the 2D cross-correlation between an image $I(x, y)$ and a kernel $K(x, y)$, i.e.

$$I(x,y) \circ K(x,y) = \sum_{i=-w/2}^{i=w/2} \sum_{i=-h/2}^{i=h/2} I(x+i, y+j) K(i,j), \tag{3.3}$$

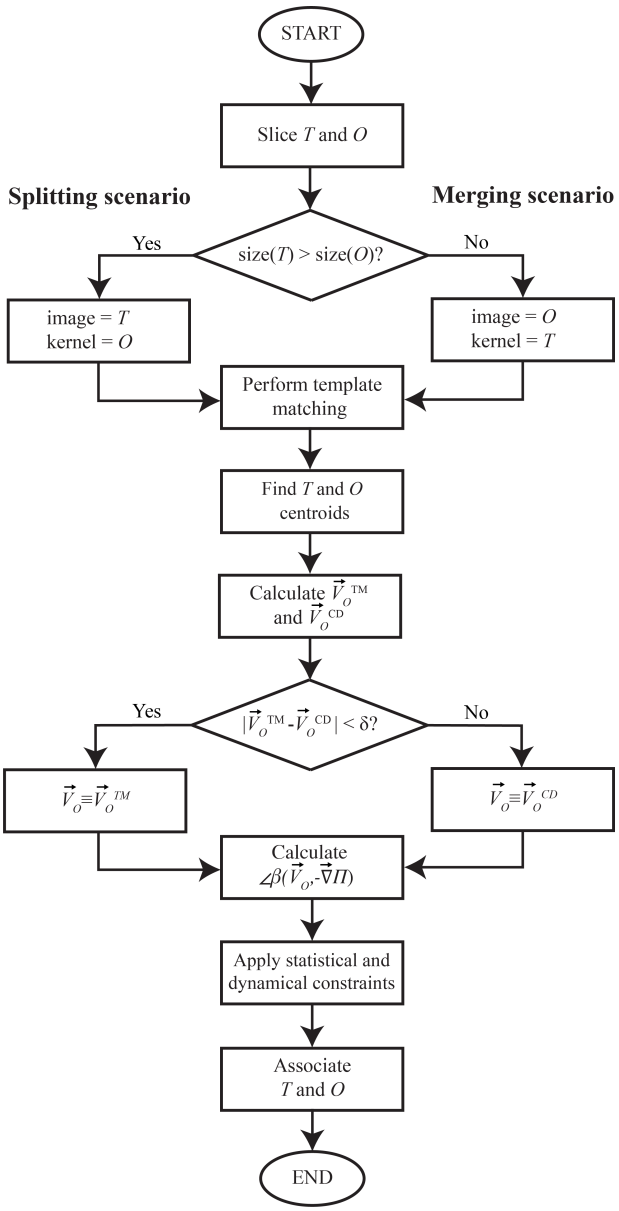

Figure 3.5: Workflow for the tracking component of the algorithm that illustrates the association procedure between a target object identified in a previous image frame (T) and a candidate object from the current image frame (O). The meaning of different diagram blocks remains the same as in Fig. 3.1. The superscripts TM/CD refer to the template matching/closest distance approaches used in calculating the candidate object's motion vector $\vec{V}_O$; $-\nabla\Pi$ is the pressure gradient force (PGF), while $\angle\beta(\vec{V}_O, -\nabla\Pi)$ denotes the angle between $\vec{V}_O$ and $-\nabla\Pi$. The parameter values associated with the tracking component of the algorithm are summarized in the second half of Table 3.1.

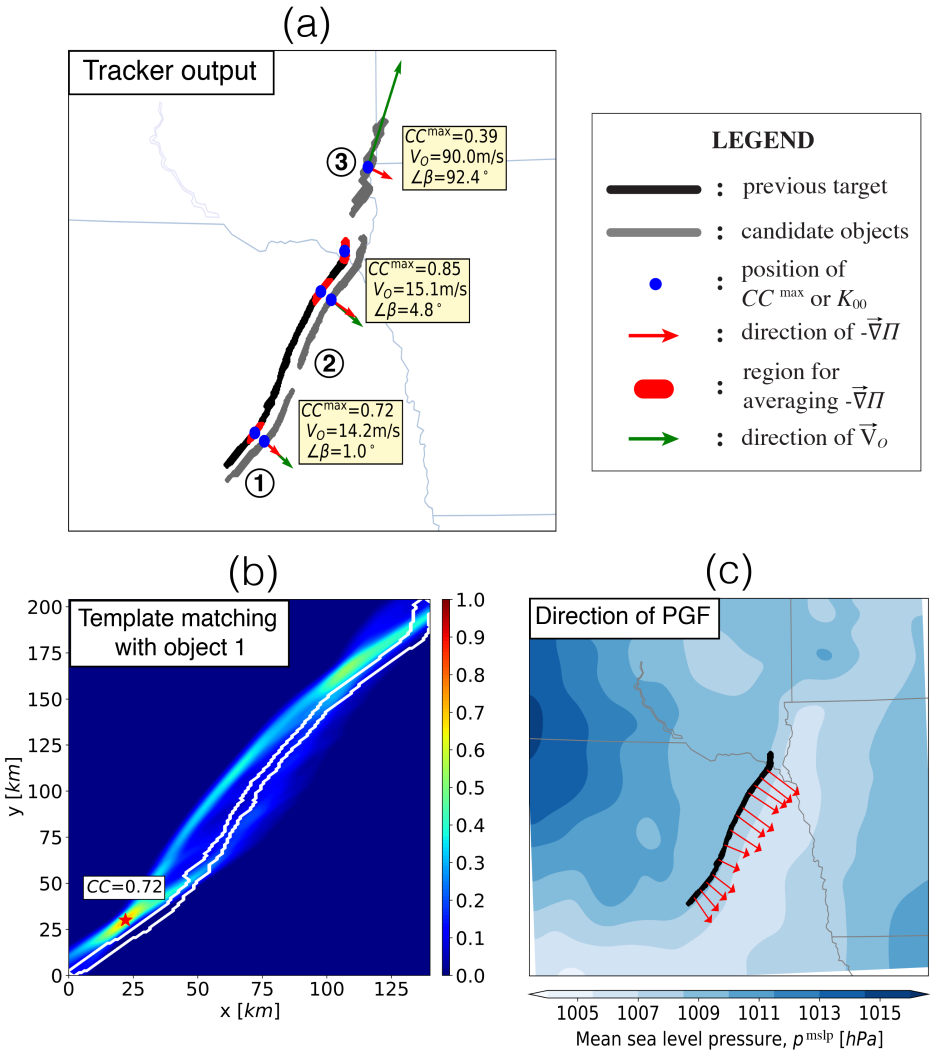

Figure 3.6: Application of the object tracker to a splitting case scenario (panel a). The black and gray color shading shows the position of the target and candidate objects, respectively. Their centroids are marked with a blue dot and used to estimate the candidate object's motion vector $\vec{V}_O$ (green arrow). The red arrows show the direction of the PGF ($-\nabla\Pi$) computed from the cluster of red points along the target object. The yellow boxes to the right of each candidate object summarize the output of the object tracker. Panel (b) illustrates the cross-correlation coefficient (CC) field between the target object and candidate object 1. The red star and the boxed text in the lower-left corner of the figure show the location and value of the maximum cross-correlation coefficient $CC^{\max}$. Panel (c) shows the mean sea level pressure (p^{mslp}; blue color shading) and the direction of the pressure gradient force (PGF, $-\nabla\Pi$; red arrows) along the target object.

where (x, y) is a coordinate pair from the model domain, while w and h denote the width and height of the kernel. The purpose of template matching is to measure the degree of statistical similarity between a candidate object[1] from the current image frame and a target object identified in the previous image frame.

Template matching is performed on each target-candidate object pair for a given algorithm analysis time. We let the smaller of those objects be the kernel $K(x, y)$, while the larger one – the image $I(x, y)$ (refer to splitting and merging scenarios in Fig. 3.5). To account for different kernel shapes and sizes, the result from (3.3) is normalized by the sum of the kernel values to yield the 2D cross-correlation coefficient CC, i.e.

$$CC = \frac{\sum_{i=-w/2}^{i=w/2} \sum_{i=-h/2}^{i=h/2} I(x+i, y+j) K(i, j)}{\sum_{i=-w/2}^{i=w/2} \sum_{i=-h/2}^{i=h/2} K(i, j)}. \tag{3.4}$$

The object tracker assumes that two objects are statistically related to each other for sufficiently large values of the maximum correlation coefficient ($CC^{\max}$). The value of 0.72 for $CC^{\max}$ on Fig. 3.6b implies there is a high likelihood that candidate object 1 is associated with the target object. Furthermore, the location of $CC^{\max}$ suggests that object 1 originates from the southern portion of the target object. Both of these inferences are consistent with the object splitting scenario depicted on Fig. 3.6a.

Apart from measuring the statistical similarity between candidate and target objects, the template matching procedure provides an estimate for the motion vector $\vec{V}_O$ (denoted as $\vec{V}_O^{\text{TM}}$; see Fig. 3.5). In particular, $\vec{V}_O^{\text{TM}}$ is calculated by dividing the Euclidean distance between the location of the central kernel point[2] K_{00} ($X_{K_{00}}$) and the location of $CC^{\max}$ ($X_{CC^{\max}}$), i.e. the distance between the two object centroids, through the model time step Δt. Mathematically,

$$\vec{V}_O^{\text{TM}} = \frac{\| X_{CC^{\max}}, X_{K_{00}} \|}{\Delta t} = \frac{\sqrt{(x_{CC^{\max}} - x_{K_{00}})^2 + (y_{CC^{\max}} - y_{K_{00}})^2}}{\Delta t}. \tag{3.5}$$

[1] A candidate object is an object to be associated with the target object.
[2] Note that the centre of the kernel K_{00} is taken to be the closest point to $K(0, 0)$ where $K = 1$.

Past algorithm tests have shown that the $\vec{V}_O^{\mathrm{TM}}$ estimates can be impacted negatively if objects undergo rapid structural changes. To address this issue, the tracker incorporates a second estimate of $\vec{V}_O$ ($\vec{V}_O^{\mathrm{CD}}$; see Fig. 3.5), which is based on the "greedy approach" of Dijkstra (1959) and measures the shortest distance between the center of the kernel $X_{CC^{\max}}$ and the collection of image points $\mathbf{I} = \{(x_I, y_I) : I(x, y) = 1\}$ corresponding to the coordinates of the larger object, i.e.

$$\vec{V}_O^{\mathrm{CD}} = \frac{\min\{\|X_{K_{00}}, \mathbf{I}\|\}}{\Delta t}. \tag{3.6}$$

As indicated in Fig. 3.5, $\vec{V}_O = \vec{V}_O^{\mathrm{TM}}$ only if $|\vec{V}_O^{\mathrm{TM}} - \vec{V}_O^{\mathrm{CD}}| < \delta = 3\ \mathrm{ms}^{-1}$.

Unlike other approaches, the tracker presented in this chapter prioritizes the dynamics of convective outflow boundaries by adding two dynamical constraints as part of the object association procedure. The first one makes use of the pressure gradient force (PGF, $-\nabla\Pi$[3]) in an attempt to restrict the direction towards which objects are allowed to propagate. Given that density currents and bores are associated with jumps in the surface pressure, one should expect them to move approximately in the direction of the PGF (red arrows in Fig. 3.6c). Having said that, a candidate object can be associated with a target object only if the angle between the object's motion vector and the PGF, i.e. $\angle\beta(\vec{V}_O, -\nabla\Pi)$, is sufficiently small. The second dynamical constraint imposes an upper limit on the object's propagation speed and is denoted as V_O^+. Ideally, V_O^+ should be derived from theoretical considerations regarding either the density current speed (e.g., Eq. 2 in Koch et al. 1991) or the bore speed (e.g., Eqs. 2.4 and 3.1 in Rottman and Simpson 1989). However, to assess the overall feasibility of the second dynamical constraint in the initial algorithm tests, V_O^+ was assumed to remain constant throughout the algorithm runs. A similar approach was undertaken by Davis et al. (2006) in their definition of "*rain systems*".

[3] $\Pi \equiv -\frac{1}{\rho_0} p^{\mathrm{mslp}}$ is the mean sea level pressure normalized by the reference density value.

Association between a target and a candidate object occurs only if the following three conditions are met simultaneously: $[CC^{\max} \in (CC^{-}, CC^{+})] \ \wedge \ [\angle\beta(\vec{V}_O, -\nabla\Pi) < \beta^{+}] \ \wedge \ [|\vec{V}_O| < V_O^{+}]$ (refer to the second half of Table 3.1 for the values of CC^{-}, CC^{-}, β^{+} and V_O^{+}). According to the object splitting scenario in Fig. 3.6a, all candidate objects are able to pass the template matching threshold of $CC^{-} = 0.3$. However, only candidate objects #1 and #2 successfully meet the additional dynamical requirements regarding the object's propagation speed and direction. Therefore, *this example shows how the tracker is able to handle the complex dynamical behavior of convective outflow boundaries by exploiting their statistical and dynamical properties simultaneously*.

The addition of dynamical constraints in the object tracker is beneficial for several reasons. Firstly, the simultaneous fulfillment of three different conditions relaxes the prescribed threshold values used for object association (Table 3.1). Tracking objects only with the aid of template matching, e.g. the hybrid tracking approach of Lakshmanan et al. (2003), would have required significantly higher value of CC^{-} in order to avoid spurious object associations. While a higher CC^{-} would decrease the amount of false alarms, it can also lower the probability of detection, especially when convective outflow objects undergo significant structural changes.

Another benefit of incorporating dynamical constraints in the algorithm's tracker is to make the search area, i.e. the area within which target and candidate objects are associated, flow-dependent (dynamic). This idea is illustrated in the schematic from Fig. 3.7 where all 3 candidate objects are perfectly correlated with the target object ($CC^{\max} = 1.0$), but only the first one is physically associated. In this example, both the statically- and dynamically-defined search areas correctly discard object #3 from the association process. Nevertheless, due to its isotropic search radius ($R = R_s$), the static method will spuriously associate object #2 with the target object despite that the aforementioned candidate object is located upstream of the target's propagation direction. This result is contrasted by our flow-dependent tracking method, which would shrink the search area in accordance to the PGF direction and correctly

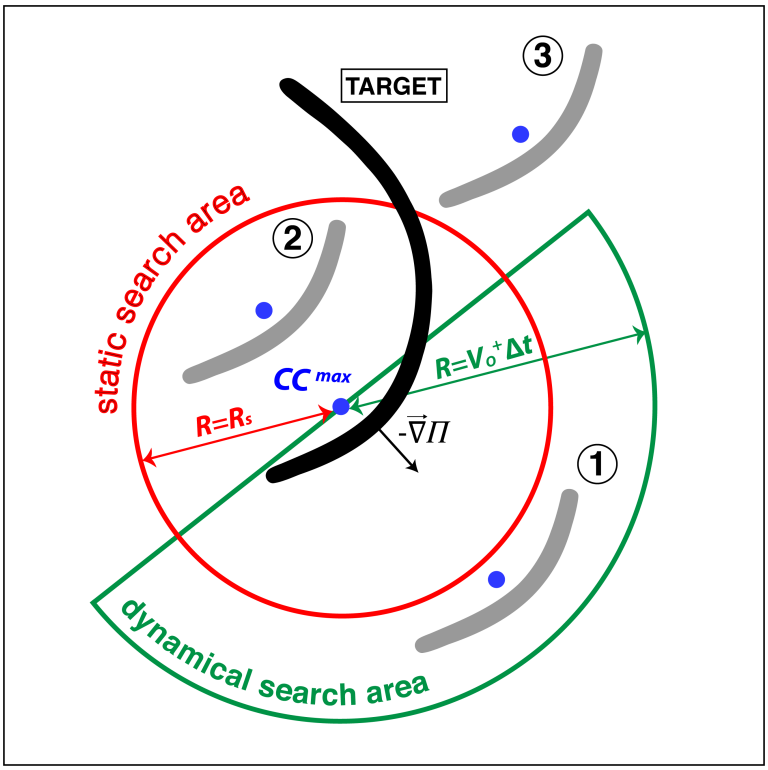

Figure 3.7: A schematic illustration highlighting the benefits of using dynamical constraints in the object tracker. The black-filled shape represents a target object from a previous image frame, while the three gray-filled shapes (numbered 1, 2 and 3) – candidate objects identified in the current image frame. The black arrow indicates the direction of the PGF ($-\nabla\Pi$), while the meaning of the blue dots is the same as in Fig. 3.6. The red circle and green semicircle correspond to the static and dynamic tracker search areas whose radii is given by $R = R_s$ and $R = V_O^+ \Delta t$, respectively

disassociate candidate object #2 from the target object. It is also worth noting that a tracking method using a static search radius will underperform in cases featuring extreme environmental conditions for which the convective outflow boundaries propagate faster than usual. For instance, candidate object #1 in Fig. 3.7 fails to pass the object association test for the static approach since it moves beyond $R = R_s$ in a single model time step. Provided that V_O^+ is defined according to theory, the model-derived environmental information should increase the value of V_O^+ and, as a result, extend the search radius $R = V_O^+ \Delta t$ of the tracker. As revealed by the schematic example in Fig. 3.7, object #1 falls within this extended search area and will be correctly associated with the target object.

The use of dynamical constraints is essential when candidate objects are perfectly correlated with the target object, i.e. $CC^{\max} = 1$ (e.g., all candidate objects on Fig. 3.7). While a perfect match between a candidate and a target object is certainly possible, these situations typically occur if one of the objects is so small that it can fit entirely into the other one. In such cases, the additional dynamical information provided by $\angle\beta$ and V_O^+ is essential in determining whether the two objects are physically related to one another.

3.4 Applications of the object-based algorithm

The intention of this section is to discuss the development of specific algorithm tools relevant for both research and operational forecasting applications. Special emphasis is placed on using the algorithm in conjunction with convection-allowing ensemble prediction systems.

3.4.1 Theoretical prediction of bores based on environmental profiles from NWP models

One application of the object-based algorithm is to use hydraulic and linear wave theories in order to determine whether a density current can trigger a bore and whether this bore will be maintained in the night-time environment. Predicting the development and longevity of bores is desirable due to their potential role in modifying convective instability and initiating deep convection (Carbone et al. 1990; Karyampudi et al. 1995; Koch and Clark 1999; Locatelli et al. 2002; Wilson and Roberts 2006). During the PECAN field campaign, such theoretical predictions were made by manually picking two environmental profiles on both sides of a numerically-simulated density current (Haghi et al. 2015; Geerts et al. 2017). Despite the encouraging results from such a forecasting approach, its application is highly subjective and time consuming. In the context of ensemble prediction systems where information from multiple ensemble members is integrated to provide probabilistic bore forecasts, an automated objective method is much more desirable. As a result, the

algorithm introduced in Sections 3.2 and 3.3 is extended to objectively determine whether the night-time environment can support convectively generated bores using environmental profiles from NWP models.

The method for extracting environmental profiles of meteorological variables on both sides of a density current will be referred to as a *four-dimensional (4D) distance minimization* and is schematically portrayed in Fig. 3.8a. The key variable in this method is the user defined reference point $R = (x_r, y_r)$ (blue dot on Fig. 3.8a), which indicates where the theoretical bore analysis is to be performed. For the sake of explaining the minimization procedure, Fig. 3.8a considers a collection of 3 target objects identified by the algorithm for the first 3 algorithm time steps, i.e. $\mathbf{T} = \{\mathbf{T}_0, \mathbf{T}_{\Delta t}, \mathbf{T}_{2\Delta t}\}$. Here the set $\mathbf{T}_t = \{T_s^{\mathbf{T}_t} = (x_s^{\mathbf{T}_t}, y_s^{\mathbf{T}_t}) : 1 < s < N^{\mathbf{T}_t}, s \in \mathbb{Z}\}$ represents the target coordinates at time t, while N^{T_t} – the total number of points associated with $\mathbf{T}_t$. Let the Euclidean distance between R and a point located within target $\mathbf{T}_t$ be defined as $d_s^{\mathbf{T}_t} := \|T_s^{\mathbf{T}_t}, R\|$. Analogous to the previous definitions, we now define the corresponding set $\mathbf{D} = \{\mathbf{D}_0, \mathbf{D}_{\Delta t}, \mathbf{D}_{2\Delta t}\}$, where $\mathbf{D}_t = \{d_s^{\mathbf{T}_t} : 1 < s < N^{\mathbf{T}_t}, s \in \mathbb{Z}\}$ represents the collection of Euclidean distances between the reference point R and the coordinate points comprising $\mathbf{T}_t$. The objective of the 4D minimization procedure is to find the smallest distance from point R to any of the three target objects $\mathbf{T} = \{\mathbf{T}_0, \mathbf{T}_{\Delta t}, \mathbf{T}_{2\Delta t}\}$ considered in this example, i.e. $d_{\min} := d_{s_{\min}}^{\mathbf{T}_{t_{\min}}} = \min\{\mathbf{D}\}$. The previous expression indicates that the distance $d_{\min}$ is uniquely associated with the positional index $s_{\min}$ from the nearest target object $\mathbf{T}_{t_{\min}}$. The latter positional index defines the so-called pivot point $P = T_{s_{\min}}^{\mathbf{T}_{t_{\min}}}$ (light blue dot on Fig. 3.8a). In the schematic diagram from Fig. 3.8a, $t_{\min} = \Delta t$ and the pivot point P is located in the middle parts of $\mathbf{T}_{\Delta t}$. The main purpose of point P is to mark the center of the pivot line (PL) segment AA' (red line on Fig. 3.8a), which intersects the density current needed for the theoretical bore analysis. Note that the orientation of AA' is parallel to the direction of the PGF ($-\nabla\Pi$), i.e. approximately in the direction of density current propagation.

The 4D minimization procedure is typically applied throughout the entire time period for which the algorithm is run, such as in the example from Fig. 3.8b. The time series

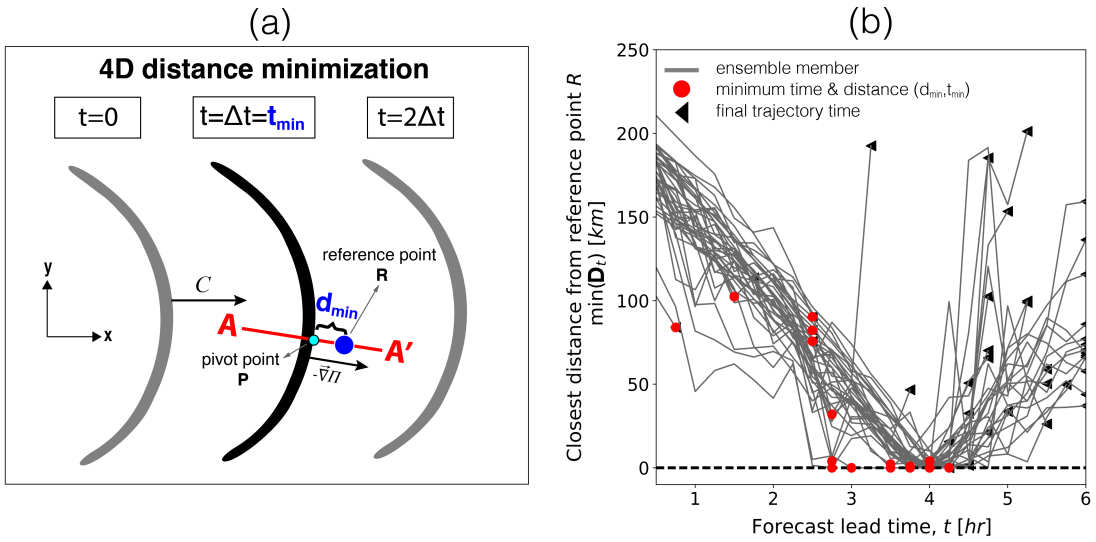

Figure 3.8: Four-dimensional (4D) distance minimization of convective outflow objects with respect to a user-defined reference point. The schematic in panel (a) demonstrates the minimization procedure for an idealized example in which a convective outflow boundary propagates in the positive x-direction at a constant speed C. The minimum distance ($d_{\min}$) between the reference point (R; dark blue dot) and the pivot point within the convective outflow object (P; cyan dot) occurs during the second image frame at $t = \Delta t = t_{\min}$. The red line segment AA', parallel to the PGF ($-\nabla\Pi$), displays the position of the vertical cross section required for the theoretical and explicit object analyses. Panel (b) shows the application of the 4D minimization method to the ensemble forecast experiment from 6 July 2015, with point R prescribed to have a latitude of 42.4° and a longitude of -96.4°. The gray curves show the minimum distance between R and the convective outflow object at a particular forecast lead time, i.e. $\min(\mathbf{D}_t)$. The red circles mark the values of $(d_{\min}, t_{\min})$ for each ensemble member, while the black triangles indicate where the trajectory of a particular ensemble member is terminated.

showing the minimal distances for different time steps suggests that the objects from most of the ensemble members pass over the user-selected reference point $R \sim 4$ hours after the numerical model is initialized. It is worth pointing out that the time of passage $t_{\min}$ is not necessarily identical between different ensemble members. The latter results from the inherent ensemble diversity with regards to the simulated density currents and highlights the ability of the 4D minimization framework to analyse those density currents in a dynamically consistent way, i.e. at the time of their passage over the reference point R.

An example of a probabilistic bore prediction using theoretical considerations is shown in Fig. 3.9 and refers to a specific choice of R with a latitude of 43.4° and a longitude of -97.7°. The two environmental profiles needed for the theoretical bore forecasts are extracted from the end points of the PL segment AA'. The total length of AA' is relatively large (80 km) to ensure that the aforementioned profiles are taken sufficiently away from the non-hydrostatic density current head. The first part of this analysis uses the two-layer hydraulic theory of Rottman and Simpson (1989) in order to determine the likelihood of bore development. According to this theory, the development of a bore is dependent upon the value of the Froude number (F) and non-dimensional height (H) (see more details in Rottman and Simpson 1989). The analysis of the vertical profiles from points A and A' allows us to calculate the flow regime for each of the ensemble members and plot their distribution in the parameter space of F and H. For instance, the ensemble forecast results shown on Fig. 3.9a suggest a partially blocked flow regime, in which an atmospheric bore is expected to form ahead of the analyzed density current. Moreover, the mode of the ensemble distribution reveals that the most likely bore strength is $S = 2.2$, which corresponds to a weakly turbulent atmospheric bore.

The second part of the probabilistic bore prediction utilizes linear wave theory and estimates whether the environmental conditions are favorable for maintaining the convectively generated atmospheric bore. In particular, the algorithm calculates the ensemble distribution of the Scorer parameter l^2 (Scorer 1949) ahead of the density current, i.e. at point A'. The

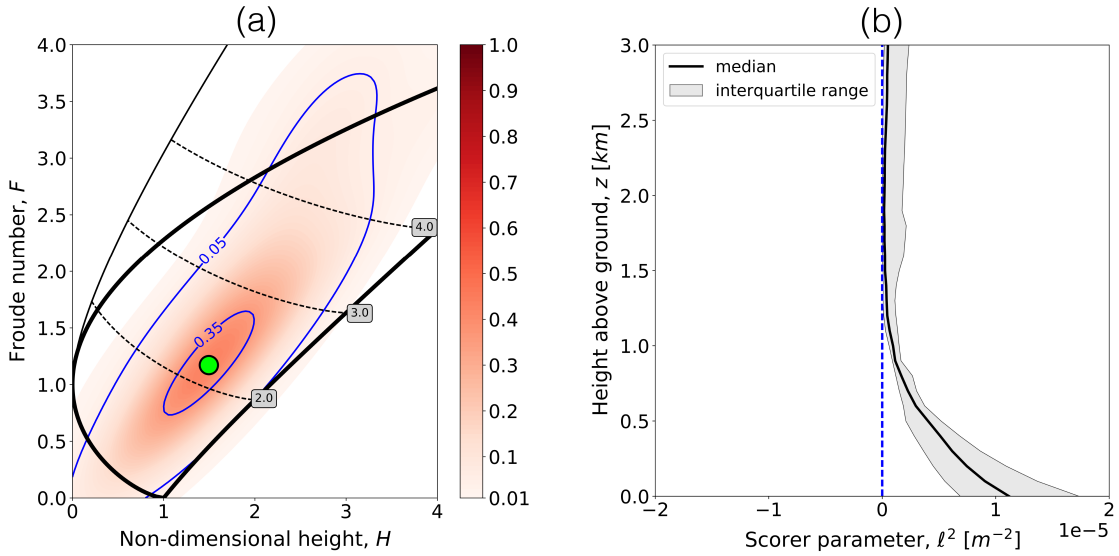

Figure 3.9: Theoretical bore predictions performed over a reference point R with a latitude of 43.4° and a longitude of -97.7°. Panel (a) shows the ensemble flow regime distribution upstream of a density current. Forecast results are plotted in the parameter space of the Froude number (F; y-axis) and the non-dimensional height (H; x-axis). The solid black curves separate different flow regimes, while the dashed black curves mark phase regions with constant bore strength $S = h_1/h_0$. The partially blocked regime is located between the thick solid black curves. The red color shading displays the ensemble probability of a particular flow regime; probability contours (blue curves) are plotted at intervals of 0.3, starting from 0.05. The green dot indicates the position of the most likely flow regime, i.e. the mode of the ensemble distribution. Panel (b) displays the ensemble forecast results associated with the vertical Scorer parameter (l^2) profile; the black curve refers to the median Scorer profile, while the gray-shaded region shows the interquartile range of l^2 at a given height. The dashed blue curve corresponds to $l^2 = 0$.

example l^2 distribution from Fig. 3.9b shows a sharp decrease in l^2 from the surface to 1 km above the ground, where l^2 approaches 0 m^{-2}. The latter condition indicates that waves originating in the subcritical bore region are likely to be trapped[4], i.e. maintain the bore for a longer time. This example also highlights the enhanced variability in the ensemble forecasts of l^2 near the surface, which possibly results from the inherent difficulty of numerical models to describe the nocturnal boundary layer structure. The increased range of l^2 values near the surface is likely to yield different wave trapping characteristics (Haghi et al. 2017).

3.4.2 Analysis of object attributes based on explicitly resolved convective outflow boundaries

The ability of convection-allowing NWP models to explicitly simulate convective outflow boundaries provides a unique opportunity for the object-based algorithm to extract dynamically relevant density current and bore attributes. One of them is the propagation speed C, which has been routinely analyzed in previous work (e.g., Goff 1976; Koch et al. 1991). Although the object-algorithm already utilizes motion vector estimates for the purposes of object tracking (see discussion on $\vec{V}_O$ in Section 3.3.2), we propose an alternative method to estimate C in the neighborhood of the user-defined reference point R, i.e. C_R. *Such a consideration takes into account the scarcity of bore observations and allows the algorithm to perform model verification only in regions where such data is readily available.*

In order to calculate C_R, we consider the target object containing the pivot point P at time $t = t_{\min}$ ($\mathbf{T}_{t_{\min}}$; black color shading on Fig. 3.10a) and the target objects from the two neighboring time steps ($\mathbf{T}_{t_{\min}-\Delta t}$ and $\mathbf{T}_{t_{\min}+\Delta t}$; gray color shading in Fig. 3.10a). Prior to estimating C_R, the three target objects are skeletonized using the medial axis transform (MAT; Lakshmanan 2012), i.e. $\mathbf{T}_t \xrightarrow{\text{MAT}} \mathbf{T}_t^{\text{sk}}$ for some time t. This transform intends to

[4] If k is a horizontal wavenumber, then the square of the vertical wavenumber $m^2 = l^2 - k^2$ becomes negative for $l^2 \to 0$ m^{-2} and finite values of k. According to linear wave theory, if m^2 transitions from positive to negative values, wave trapping will occur in the layer characterized by positive m^2 values (like in the example from Fig. 3.9b).

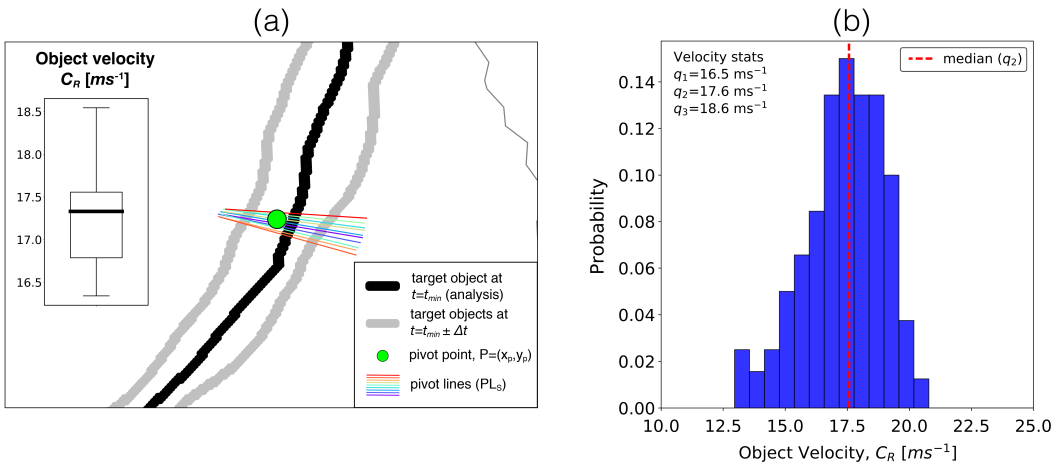

Figure 3.10: Evaluating the propagation speed C_R of a convective outflow object in proximity of the user-defined reference point R=(41.7°,-97.4°). Panel (a) shows the methodology for calculating C_R based on the length of the pivot lines (PLs; purple to red colors indicating increasing PL lengths) as well as the variability of C_R in the neighborhood of R (box-and-whisker diagram in the figure inset). The meaning of the other symbols is summarized in the legend at the bottom right-hand side of the figure. Panel (b) displays the ensemble distribution of C_R. The values associated with the first, second and third quartiles (q_1,q_2 and q_3) of this distribution are shown at the top left corner of the figure. The second quartile (the median) is additionally plotted as a dashed red line.

increase the accuracy of the C_R estimate due to its property to simplify the shape of the objects. Since the pivot point P may no longer belong to $\mathbf{T}_t^{\text{sk}}$ as a result of the MAT, we define a new pivot point P^{sk} which minimizes the distance between P and $\mathbf{T}_t^{\text{sk}}$, i.e. $P^{\text{sk}} = \min\{\|P, \mathbf{T}_t^{\text{sk}}\|\}$. Then, using the direction of the PGF ($-\nabla\Pi$) at point P^{sk} and the closest 9 neighboring points, we define a total of 10 PL segments (colored lines on Fig. 3.10a), each having a length of 80 km. If the set of coordinates for a particular PL is denoted as $\mathbf{L}$, then $\{X_{t_{\text{min}-\Delta t}}, P^{\text{sk}}, X_{t_{\text{min}+\Delta t}}\} = \{\mathbf{L} \bigcap \mathbf{T}_{t_{\text{min}-\Delta t}}, \mathbf{L} \bigcap \mathbf{T}_{t_{\text{min}}}, \mathbf{L} \bigcap \mathbf{T}_{t_{\text{min}+\Delta t}}\}$ is the set of 3 points where the PL intersects the objects considered in this analysis. Therefore, the propagation speed of the object associated with the ith pivot line (C_R^i) is defined as the Euclidean distance between the $X_{t_{\text{min}-\Delta t}}$ and $X_{t_{\text{min}+\Delta t}}$ points divided over twice the model time step (Δt), i.e.

$$C_R^i := \frac{\|X_{t_{\text{min}-\Delta t}}, X_{t_{\text{min}+\Delta t}}\|}{2\Delta t}. \tag{3.7}$$

Fig. 3.10b shows the distribution of the propagation speeds from all quality-controlled ensemble members and neighboring points (32×10=320 points in total) in proximity to point R, which has a latitude of 41.7° and a longitude of -97.4° in this example. For this particular choice of R, the median and interquartile range values turn out to be 17.6 ms^{-1} and 2.1 ms^{-1}, respectively. Similar to the theoretical bore analysis, the ensemble distribution of C_R does not refer to a single model time, but rather corresponds to the time when a convective outflow object associated with a particular ensemble member passes over the reference point R.

There are at least two advantages of calculating C_R via the aforementioned neighborhood method. On one hand, this approach takes into account the inherent uncertainty of the C_R estimate (indicated by the coloring of the PLs in Fig. 3.10a), which can arise both due the differential propagation of the tracked objects as well as the algorithm's inability to calculate the exact location of the 3 intersection points $\{X_{t_{\mathrm{min}-\Delta t}}, P^{\mathrm{sk}}, X_{t_{\mathrm{min}+\Delta t}}\}$ used in the calculation of C_R. The box-and-whisker diagram inset in Fig. 3.10a reveals that the velocity in the neighborhood of point R can vary by more than 2 ms^{-1}, making the single-valued estimates of C_R not representative of the object's propagation speed. On the other hand, the neighborhood approach also leads to a significant increase in the sample size of the C_R ensemble (Fig. 3.10b) and, as a result, improves the overall representation of ensemble uncertainty with respect to the object's propagation speed. In particular, sensitivity experiments indicated that the ensemble distribution of C_R becomes more Gaussian after including the additional speed estimates from the neighboring points (not shown).

The second explicit analysis tool concerns the evaluation of bore amplitude and lifting in the vicinity of the reference point R, i.e.

$$S_R = \left[\frac{h_1}{h_0}\right]_R \tag{3.8}$$

and

$$\Delta h_R = [h_1 - h_0]_R, \tag{3.9}$$

where h_0 and h_1 denote the height of the stable boundary layer (SBL) prior and after the passage of the bore. Calculating S_R and Δh_R rests on the assumption that the virtual potential temperature θ_v is conserved when air parcels undergo bore lifting. Note that the accuracy of this approach will decrease in the presence of convectively induced latent heating, whereby θ_v surfaces can no longer treated as material surfaces.

The procedure for estimating S_R and Δh_R starts with constructing a cross section over the central PL segment from Fig. 3.10a. The length of the resulting cross-section (Fig. 3.11a) is the same as in the theoretical bore analysis from Section 3.4.1 (80 km) and restricts the algorithm to only sample the undisturbed environment away from the bore front. Here we utilize one of the theoretical bore analysis routines in order to get a first estimate of the inversion height upstream of the approaching bore ($\widehat{h_0}$; gray diamond shape). More specifically, $\widehat{h_0}$ is defined as the depth over which the environmental lapse rate exceeds the moist adiabatic lapse rate (see Haghi et al. 2017, for more details). The height of the stable layer downstream of the bore ($\widehat{h_1}$; gray diamond shape) is then defined as the maximum height of the $\theta_v(z = \widehat{h_0})$ surface (gray dotted curve).

It is worth remarking that the definition of $\widehat{h_1}$) in this object-based algorithm differs from previous studies, wherein $\widehat{h_1}$) is typically calculated as the average stable layer height in the wake of the bore. The rationale behind our definition of $\widehat{h_1}$) is based on qualitatively analyzing the diverse bore structures in our ensemble simulations. Specifically, examination of certain ensemble members revealed that bores may either (i) not show a semi-permanent increase in the SBL height or (ii) be characterized by a rather shallow θ_v slope owing to more pronounced dispersion effects. The atypical bore characteristics in such cases meant that it is not appropriate to artificially divide a bore into subcritical and supercritical regions and then estimate the average post-bore height in the subcritical region. By letting the post-bore SBL height $\widehat{h_1}$) be the maximum height of the $\theta_v(z = \widehat{h_0})$ surface, the algorithm is able to better

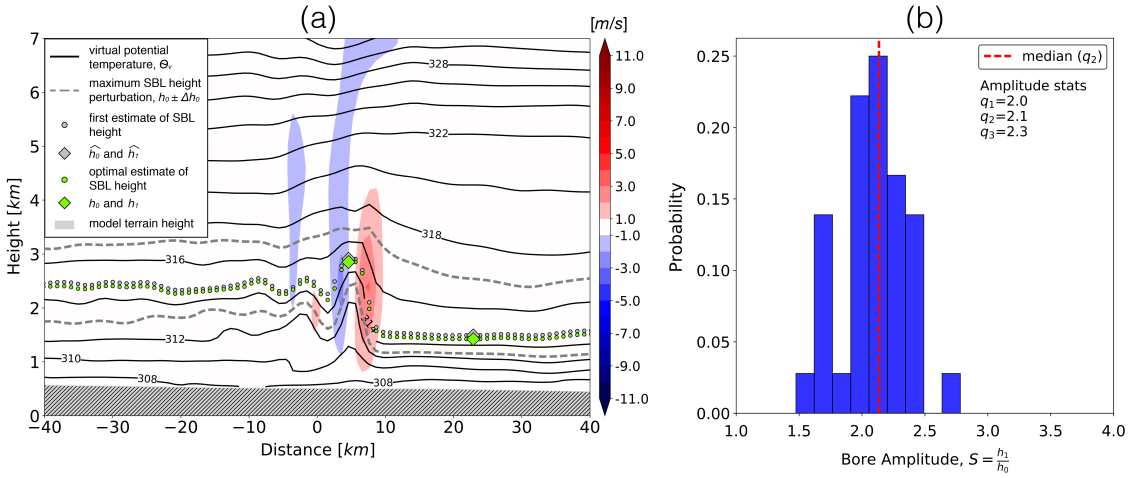

Figure 3.11: Evaluating the effective bore amplitude $S_R = \left[\frac{h_1}{h_0}\right]_R$ in proximity of the user-defined reference point $R = (41.7°, -97.4°)$. The methodology for finding S_R (panel a) is illustrated with the aid of a cross-section showing the vertical velocity (w; color shading) and the virtual potential temperature (θ_v; black solid curves) along the central pivot line from Fig. 3.10a. The gray dots show the original SBL height estimate provided by the theoretical bore analysis. The minimum and maximum heights of the original SBL height estimate ($\widehat{h_0}$ and $\widehat{h_1}$) are marked with the two gray diamonds, while its uncertainty range – with the two dashed gray curves. The green dots refer to the optimal SBL height, i.e. the θ_v surface experiencing maximum bore lifting. The minimum and maximum values of this optimal SBL height define h_0 and h_1 (green diamonds), which are used in the S_R estimate. Note that the gray and the green diamonds in this example overlap due to their similar location along the cross section. Finally, panel (b) shows the ensemble distribution of S_R. The meaning of the symbols in this histogram are the same as Fig. 3.10b

capture the intrinsic bore diversity and provide more consistent ensemble results. With these considerations in mind, our first estimates of the effective bore amplitude and lifting nearby point R can be written as $\widehat{S_R} = \left[\frac{\widehat{h_1}}{\widehat{h_0}}\right]_R$ and $\widehat{\Delta h_R} = [\widehat{h_1} - \widehat{h_0}]_R$, respectively.

Analogous to the estimation of the propagation speed C, we also give first-order accounts to the accuracy of the retrieved SBL height $\widehat{h_0}$, which is a traditionally challenging variable to estimate (Vickers and Mahrt 2004). In particular, model results have indicated that neighboring θ_v surfaces can differ significantly with respect to their post-bore displacement heights. To alleviate this sensitivity, the deterministic value of $\theta_v(z = \widehat{h_0})$ is perturbed by $\pm 2K$ to create a broad range of stable boundary layer heights (dashed gray curves on Fig. 3.11a) that accounts for errors in the retrieval technique as well as the underlying ambiguity in terms of defining the SBL height. Within this envelope of possible SBL heights, the algorithm searches for the θ_v surface with the highest vertical displacement (green dotted curve on Fig. 3.11a), which is then used to get optimal estimates of h_0 and h_1 (green diamond shapes). In particular, h_0 and h_1 are defined to be the minimum and maximum of the aforementioned θ_v surface. These optimal SBL heights are then used to redefine the bore amplitude and lifting in (3.8) and (3.9).

Repeating the outlined procedure for the entire ensemble of 36 quality-controlled members provides the ensemble distribution of bore amplitudes in Fig. 3.11b. For this specific choice of $R = (41.7°, -97.4°)$, S varies between 1.5 and 2.7 and has a median value of 2.1. The interquartile ensemble range implies that ~1/4 of the ensemble members predict the development of a bore with laminar characteristics, while the remainder ~3/4 of them anticipate a weakly turbulent bore. Further analysis also revealed that there is a positive correlation between C_R and S_R for the ensemble forecasts used in this study (not shown). The latter is consistent with the two-layer hydraulic theory presented in Rottman and Simpson (1989) [refer to their Eqs. (2.4) and (3.1)] and suggests that the explicit bore routines provide physically sound results.

3.4.3 Object-based probabilities of explicitly resolved convective outflow boundaries

Apart from its ability to objectively analyze the characteristics of explicitly resolved convective outflow boundaries, the algorithm presented herein can also provide probabilistic information regarding their representation in convection-allowing ensemble prediction systems. Given that each member in the ensemble forecast is associated with two distinct binary fields corresponding to the location of the simulated density currents and bores, object-based probabilities can be generated by simply calculating the relative frequency of the aforementioned binary fields over different model grid points. An example application of the outlined procedure is shown in Fig. 3.12 and illustrates how the object-based probabilities that are linked to the largest convective outflow object identified close to the model initialization time (03:15 UTC; refer to Figs. 3.12a,c) evolve after more than 3 hours of model integration (Figs. 3.12b,d). Note that the object-based probabilities evaluated with respect to the other target objects are not shown in Fig. 3.12 for clarity.

The sequence of images in Fig. 3.12 suggests that the largest convective outflow boundary initialized in our numerical simulations is expected to move southeast and that the main lifting mechanism associated with this particular boundary is very likely to change from a density current to a bore in the later forecast hours. Although a similar evolution is also evident in the deterministic forecast from Fig. 3.3, the algorithm-derived probabilities in this example contain additional information that could be potentially useful to operational forecasters. For instance, Figs. 3.12b,d, reveal that the bore (density current) probabilities in the southern portion of the tracked outflow boundary are higher (lower) compared to its northern parts. Given a hypothetical scenario in which the ensemble members predict the development of convection in the vicinity of the highest bore probabilities, operational forecasters would have an additional physical insight about the forcing mechanism behind the model-simulated convection. If the radar and surface observations collected later on do (or do not) confirm the presence of a bore, these operational forecasters will have strong evidence that the NWP products used as part of their analysis are accurate (inaccurate) and

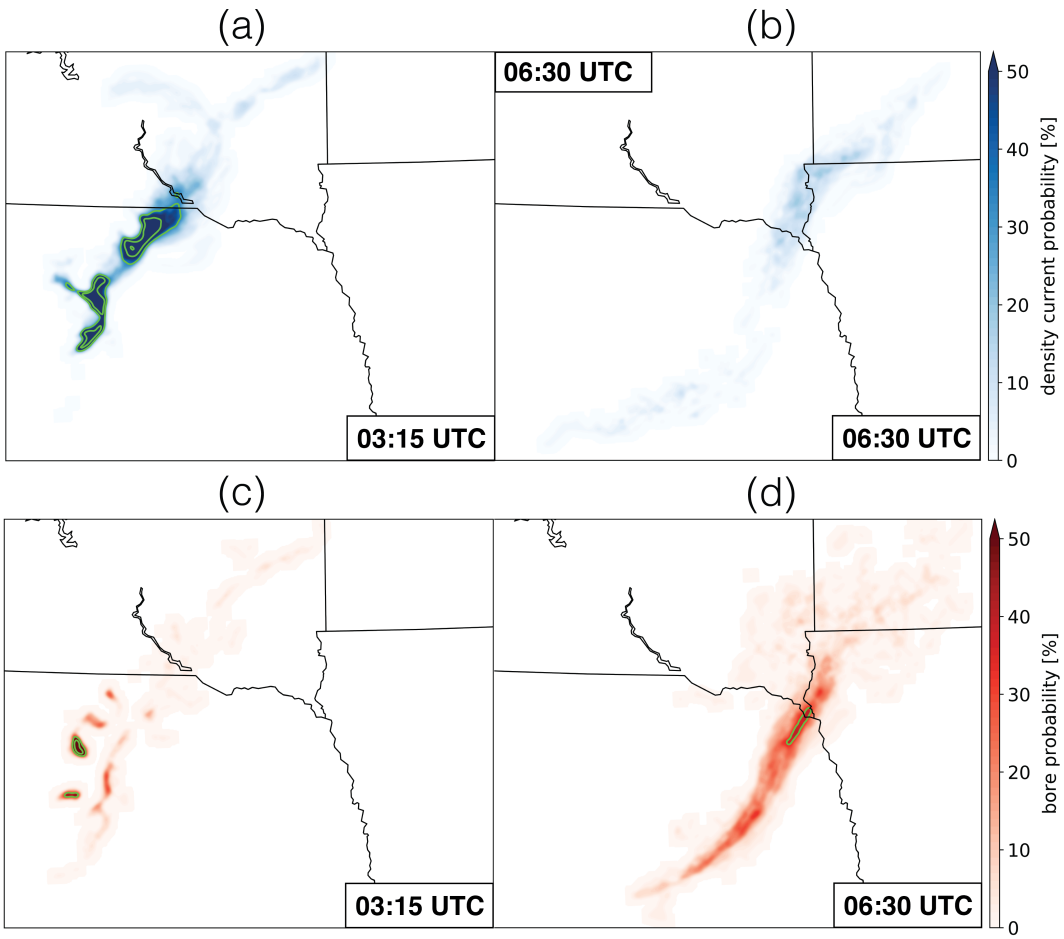

Figure 3.12: Object-based density current (panels a and b) and bore (panels c and d) probabilities computed with respect to the largest convective outflow boundary in the 1-km ensemble forecasts of the 6 July 2015 case study. The first set of probabilities (left column) is generated for 03:15 UTC and coincides with the time when the largest convective outflow object is initialized by the algorithm. The second set of probabilities (right column) is plotted for 06:30 UTC or after the algorithm has tracked the largest convective outflow boundary for 3 hours and 15 minutes. Probability fields are smoothed with a Gaussian kernel (σ=2 km). The 35%, 65% and 95% probability values are plotted with solid lime contours.

would be able to adjust their forecasts accordingly. This idealized example suggests that the ability of the object-based algorithm to discriminate between density currents and bores could serve as useful guidance for the operational forecasting of nocturnal convection.

It is important to add that the object-based probabilities calculated with respect to the initial target objects are not the only means of utilizing the ensemble information contained in convection-allowing NWP models. In particular, density current and bore probabilities can be produced by independently considering all objects identified at a given model time step. However, since the latter approach does not make use of the algorithm's tracker, operational forecasters would be unable to follow the evolution of convective outflow boundaries that are of particular interest to them. By contrast, the object-based probabilities in the example from Fig. 3.12 do not only add a temporal component to the algorithm's output, but are also quite relevant in the context of short-range and rapidly-updating NWP systems, e.g. the HRRR (Smith et al. 2008), wherein convective outflow boundaries are commonly present in the model's initial conditions.

3.5 Summary

This study describes the development of an object-based algorithm for the automatic identification and tracking of convectively generated outflow boundaries. While object-based techniques to analyze density currents have been developed previously (Li et al. 2014; Drager and van den Heever 2017), a unique aspect of this algorithm is its ability to simultaneously account for both density currents and atmospheric bores. The detection of these morphologically different convective outflow boundaries is possible only after combining several model fields. Although the use of multiple identification variables is not a new concept (e.g., Clark et al. 2015), the specific parameter choice made in this algorithm is fundamentally different from past studies and is designed to target only those convective outflow boundaries that provide sufficient lifting for the initiation and maintenance of nocturnal MCSs. It is important to note that some of the identification

variables are challenging to use without additional pre-processing steps. In particular, the spatial inhomogeneity of vertical velocity ($w^{1\text{km}}$) and the contamination of mean sea level pressure tendencies (Δp) with spurious numerical noise require the application of carefully tuned image processing/filtering techniques in order to obtain physically meaningful results.

Another novel feature of the proposed algorithm is its object tracker. Following the suggestion of Davis et al. (2009b), the object tracker is formulated to explicitly account for the dynamics of convective outflow boundaries. The inclusion of the pressure gradient force direction ($\angle\beta$) and the maximum translational velocity (V_O^+) as dynamical constraints for object association is especially important if objects experience rapid structural and/or morphological changes. In these cases, traditional statistical methods such as template matching are likely to provide erroneous tracking results. Likewise, the incorporation of dynamical information provides a better link between the algorithm and the underlying model data. For instance, it should be possible to relate differences in the speed or direction of object propagation back to the pressure gradient force used in the formulation of the algorithm.

To address the growing interest in atmospheric bores amongst researchers and operational forecasts (e.g., during the PECAN field campaign; Geerts et al. 2017), the second objective of the chapter was to describe several algorithm applications relevant to the analysis and prediction of bores in NWP models. These applications were shown in the context of a convection-allowing ensemble forecast experiment from 6 July 2015. To the authors' best knowledge, *this is the first time a dedicated methodology for describing the ensemble distribution of specific bore parameters is presented*. Such ensemble estimates are expected to provide valuable information for assessing the predictability of the studied phenomenon.

The four-dimensional minimization procedure, which lies at the heart of the suggested algorithm tools, allows algorithm users to automatically sample convective outflow boundaries and perform various diagnostics pertinent to their own research objectives. The specification of user-defined verification (reference) points through the aforementioned minimization

procedure obviates the need for a spatially continuous verification data set, which is required in other object-based verification methods such as MODE (Davis et al. 2006). The post-processing tools developed as part of this object-based algorithm represent a natural extension of previous PECAN efforts to forecast the development and maintenance of bores based on manual input from model-derived environmental profiles (Haghi et al. 2015; Geerts et al. 2017). Apart from completely automating the routines needed for the theoretical bore analysis, the ability of the algorithm to determine the likelihood of bore occurrence could prove especially beneficial to operational forecasters by guiding them where the initiation of nocturnal convection is more likely.

Despite the encouraging performance of the newly developed object-based algorithm, it is also important to point out some of its limitations. The algorithm weaknesses are largely associated with its identification component. Most evidently, the static threshold values used to define convective outflow boundaries in the model domain are global in nature and only valid over relatively short periods of time. Within this study, the aforementioned problem is addressed by introducing two different sets of threshold values dependent upon the forecast lead time and the magnitude of the spurious numerical noise. One way to improve the identification capabilities of the algorithm is to use adaptive thresholding methods, e.g. through utilizing image histograms (Tobias and Seara 2002). Alternatively, introducing more sophisticated techniques such as marker-controlled watershed segmentation (Soille 2003) could completely remove the need for prescribing threshold values. Past experience related to the development of methods for detecting and tracking convective outflow boundaries in radar data can be also helpful in bolstering the identification results of our object-based algorithm. For instance, Delanoy and Troxel (1993) show how tracking gust fronts and anticipating their location in future radar scans improves the overall identification results. Another potentially useful concept incorporated in the aforementioned study is the application of Functional Template Correlation (FCT) filters (Delanoy et al. 1992). In particular, this type of

matched filters can be designed to describe the topological characteristics of model-simulated convective outflow boundaries and, hence, reduce the number of spuriously identified objects.

Finally, it is hoped that this chapter will serve as a foundation for future studies aiming at advancing the algorithm's capabilities as well as developing other relevant algorithm applications. A particularly interesting line of research would be to determine whether the classification of convective outflow boundaries can be extended to more complex features such as solitons and deep tropospheric gravity waves. Future work should also take advantage of the algorithm's capability to objectively analyse some of the dynamical aspects of convective outflow boundaries. In line with the observational study of Toms et al. (2017), the algorithm could offer a convenient framework to examine the temporal evolution of the wave trapping characteristics following a model-simulated bore. Such an analysis could lend important insights into the two-way interactions between atmospheric bores and the ambient environment in which they develop and maintain.

Chapter 4

Impact of assimilating PECAN profilers on the prediction of bore-driven nocturnal convection: a multiscale forecast evaluation for the 6 July 2015 case study

4.1 Introduction

Convectively-generated bores forming in the Great Plains of the United States are an integral part of the night-time convection that occurs over this region (Crook et al. 1990; Koch and Clark 1999; Parker 2008; Blake et al. 2017; Haghi et al. 2017; Parsons et al. 2019a; Grasmick et al. 2018; Haghi et al. 2018). Nevertheless, the representation of bores in numerical weather prediction (NWP) models is very challenging due to the presence of multiple processes driving their initiation and subsequent evolution. For example, as with any convective system, numerical forecasts need to accurately capture both the location and timing of convection initiation (CI) as well as how the simulated convection evolves towards the late afternoon/early evening hours. Assuming that the aforementioned convective activity is simulated well, successfully predicting the formation of a bore further depends on how well the model resolves the interactions between the convectively-generated cold pools and the flow within the stable boundary layer (SBL). Capturing the evolution of the bore, on the other hand, is contingent upon the model's ability to adequately simulate the nocturnal low-level jet (LLJ), whose curvature aids in trapping wave energy behind the leading edge of

the bore (e.g., Karyampudi et al. 1995). Finally, the generation of bore-driven convection is sensitive to both the structure of the bore as well as the thermodynamic properties of the ambient environment (Crook 1986).

Given these challenges, high quality initial conditions in and above the SBL are necessary to obtain accurate forecasts of the bores and their influence on nocturnal convection. The low spatiotemporal resolution of current observational networks is insufficient to capture the salient mesoscale features in the lowest 5 km of the atmosphere (Geerts et al. 2017). The solution put forth by several reports from the National Research Council (National Research Council 2009, 2010, 2012) was to design a network of high-frequency thermodynamic and kinematic profilers capable of conducting continuous unattended measurements of the lower troposphere. Advances in remote sensing have already led to the development of such instruments, with several early studies reporting that profilers provide considerable advantages over conventional radiosondes[1] (e.g., Hogg et al. 1983b,a; Bleck and Brummer 1984; Westwater et al. 1984). A notable characteristic of these original profiling systems, which utilized VHF and UHF Doppler radars, was their ability to provide wind measurements with high vertical resolution – an important impetus for the later development of the NOAA Wind Profiler Network (e.g., Weber et al. 1990). Having recognized the potential benefits of the newly introduced kinematic profilers, the meteorological community started to examine the feasibility of these new measurements for different NWP applications. The seminal paper of Kuo et al. (1987), for instance, demonstrated that the assimilation of wind profilers can increase the short-range (0-48h) skill associated with mesoscale NWP models. Benefits from assimilating wind profilers were also found in several other papers (e.g., Cram et al. 1991; Smith and Benjamin 1993; Guo et al. 2000) and eventually led to the operational assimilation of these kinematic profilers (Bouttier 2001; Benjamin et al. 2004). More recently, several research groups have also considered the assimilation of Doppler Wind Lidar (DWL) data.

[1] Throughout Chapter 4 the term radiosonde would be used in lieu of rawinsonde to denote balloon launches with GPS readings.

The ability of DWLs to provide high-resolution wind information in the lower parts of the BL and in the near-storm environment has led to improvements in the convective forecasts from high-resolution NWP models (Zhang and Pu 2011; Kawabata et al. 2014).

Although early profiling systems, such as the prototype Profiler system discussed in Hogg et al. (1983b), did have radiometric profiling capabilities, the vertical resolution of the retrieved temperature and moisture profiles was much coarser than the corresponding wind profiles and comparable to the resolution obtained from satellites (Bleck and Brummer 1984). Later developments in remote sensing technology gave rise to new profiling strategies that allowed for a detailed description of the thermodynamics in the lower troposphere. Examples for some of these instruments include the Raman lidar (Melfi and Whiteman 1985; Melfi et al. 1989) and the Differential Absorption Lidar (DIAL; Browell et al. 1998; Weckwerth et al. 2016), both of which are based on active remote sensing techniques. The NASA Lidar Atmosphere Sensing Experiment (LASE Moore et al. 1997) is one of the most widely used DIAL instruments and has been deployed throughout multiple field campaigns. The assimilation of LASE data has also been shown to improve the forecasts of hurricanes (Kamineni et al. 2003, 2006) and deep moist convection over the Great Plains (Whiteman et al. 2006). Parallel with the steady progress in lidar technology, the development of passive infrared sensors has also made it possible to obtain simultaneous profiles of temperature and moisture in the lower troposphere. One such instrument is the Atmospheric Emitted Radiance Interferometer (AERI Revercomb et al. 1988; Feltz et al. 2003; Knuteson et al. 2004a,b; Turner and Löhnert 2014) whose experimental assimilation has improved the analysis and forecasts of large-scale extratropical systems (Hartung et al. 2011; Otkin et al. 2011) and deep moist convection (Coniglio et al. 2019; Degelia et al. 2019).

Despite the encouraging results from the previous studies, further work is still needed to justify a national observational network of profilers that can be assimilated routinely in NWP models. A critical component of establishing this justification is assessing the potential benefit of these novel instruments in predicting high impact weather, such as

nocturnal convection. To address this requirement, the Plains Elevated Convection At Night (PECAN) field campaign, which took place in the summer of 2015, utilized a rich set of thermodynamic and kinematic profilers that targeted nocturnal convective events (Geerts et al. 2017). In an effort to understand whether these state-of-the-art profiling instruments can adequately sample the broad spectrum of processes occurring in the nocturnal environment, this chapter examines how their assimilation affects the numerical prediction of the bore-driven convection event from 6 July 2015. The performance of the PECAN profilers is assessed against the operational observation network as well as the high-frequency surface and radiosonde observations collected during this PECAN Intensive Observing Period (IOP). The primary objective of this chapter is to understand whether the assimilation of thermodynamic and kinematic data from these PECAN profilers can improve the simulation of the wide range of processes accompanying bore-initiated convection. To address this goal, verification results are presented separately with respect to (i) the environment in which the bore forms, (ii) the explicitly resolved bore and (iii) the bore-initiated nocturnal convection. The benefits from remote-sensing profilers are expected to be maximized if their assimilation leads to the simultaneous improvement of all three forecast components.

Studying the impact of remote-sensing instruments on the numerical prediction of bores and bore-driven nocturnal convection is a novel aspect of this work, which has been previously hampered due the lack of appropriate verification metrics. The object-based convective outflow algorithm of Chipilski et al. (2018) was an important development that provided the necessary tools for conducting the present investigation. As detailed in Section 4.3.2, the aforementioned algorithm has been further extended to accommodate a neighborhood verification of the ensemble bore forecasts as well as diagnostic tools to examine the properties of the simulated bores in the context of the ambient environment. The results reported herein complement the work of Degelia et al. (2019) who demonstrated the ability of PECAN profilers to improve the forecasts of nocturnal CI. Despite their common focus on assimilating novel remote-sensing profilers, the two studies look at different aspects

of the nocturnal environment and differ in their underlying experimental designs. More specifically, the assimilation of PECAN data in this chapter is done in a data addition framework, wherein each new instrument type is added on top of the current conventional observation network. This approach allows us to assess the relative strengths and weaknesses of different instrument types.

The rest of this article is organized as follows: Section 4.2 provides a brief discussion of the case study used in our real-time experiments and highlights the relevancy of the assimilated data with respect to the underlying research objectives. Section 4.3 describes the experimental design as well as the methodology used for the objective verification of the ensemble forecasts. Data impacts with respect to the three forecast components are discussed separately in Sections 4.4, 4.5 and 4.6 and then reconciled in Section 4.7. The chapter concludes with a brief discussion regarding the implications of our findings and provides some suggestions on how the representation of nocturnal convection can be improved in future NWP systems.

4.2 Case study overview and PECAN data availability

The forecast impact of assimilating novel PECAN observations is assessed with respect to the 6 July 2015 case study (IOP20). The radar overview in Fig. 4.1 shows that there were three regions of afternoon convection (northwestern parts of NE as well as across the NE-SD and SD-MN borders) that grew upscale during the night and eventually merged into a large mesoscale convective system (MCS). During the development of the nocturnal SBL, the strength of the leading convective line across the northern parts of NE decreased and new convective activity developed upstream of the MCS. The presence of such convective initiation is commonly referred to as discrete propagation and has been shown to play an important role in the maintenance of nocturnal convective systems (Crook and Moncrieff 1988; Fovell et al. 2006; Bodine and Rasmussen 2017). For this PECAN case, the discrete propagation of the MCS was associated with two separate episodes of bore-initiated convection – one

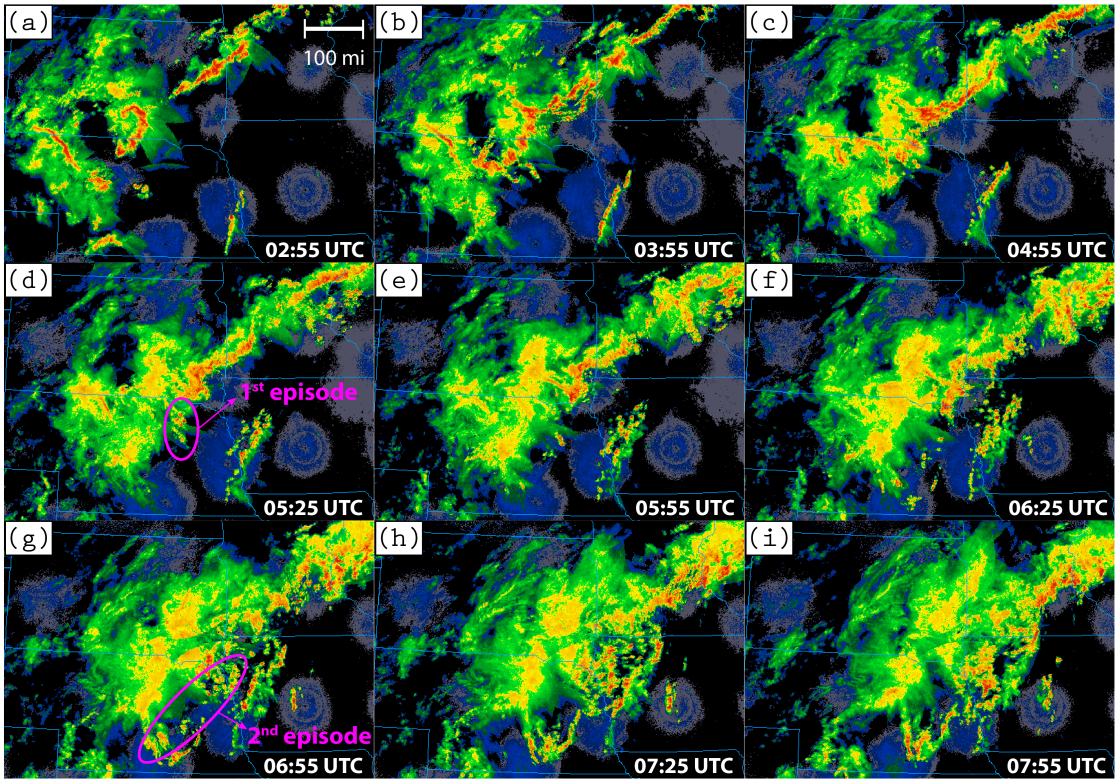

Figure 4.1: Radar evolution of the 6 July 2015 nocturnal MCS case study based on a 1-km NEXREAD reflectivity mosaic (http://www2.mmm.ucar.edu/imagearchive). The locations corresponding to the first and second episodes of bore-initiated convection are indicated with a magenta ellipse in panels (d) and (g), while the horizontal scale of the maps – in the upper right corner of panel (a).

between 0500 UTC and 0615 UTC a second one between 0630 UTC and 0800 UTC (refer to purple ellipses in Fig. 4.1). The increased longevity of the MCS as a result of the two initiation episodes makes this case especially relevant for the objectives of our study.

Selecting IOP20 to conduct our data assimilation experiments was largely driven by the large number of observations collected in this PECAN mission. The nocturnal environment on 6 July was sampled by both fixed and mobile PECAN Integrated Sounding Systems (PISAs) as well as all three research aircrafts deployed during the field campaign (refer to Table 4.1). It is apparent from Fig. 4.2 that there were two main regions of data collection. The first one was located in the south-eastern parts of South Dakota and featured a mobile array of AERI, DWL, wind profiler, radiosonde and surface instrumentation. These mobile

Table 4.1: PECAN instruments assimilated during the 6 July 2015 case study. The variables T, M_v, U and V stand for temperature, mixing ratio and the two components of the horizontal wind. The asterisk (*) in the last row indicates that the NSSL's Mobile Mesonet (NSSL MM) suite consists of 6 vehicles in total – 2 NSSL vehicles, 2 NSSL MGAUS vehicles, 1 CSU MGAUS vehicle, and the NSSL NOXP scout vehicle.

Instrument	Variable	Spatial Type	Sampling Frequency	Observing Platform	Location	Reference
AERI	T, M_v	profile	5min	FP4	Minden, NE	Turner (2016a)
				MP1	mobile	Turner (2018)
				MP3	mobile	Wagner et al. (2016a)
LASE	M_v	profile	< 1min	NASA DC-8	mobile	Ferrare et al. (2016)
Flight Level	T, M_v, U, V	point	1s	NOAA P-3	mobile	Jorgensen et al. (2016)
Doppler Wind Lidar	U, V	profile	2min	MP1	mobile	Turner (2016b)
				MP3	mobile	Wagner et al. (2016b)
915 MHz Radio Wind Profiler	U, V	profile	30min	FP4	Minden, NE	UCAR/NCAR (2015)
Radiosonde	T, M_v, U, V	profile	3h	FP4	Minden, NE	UCAR/NCAR (2016b)
			variable	MP1	mobile	Klein et al. (2016)
			variable	MP2	mobile	Knupp (2015)
			variable	MP4	mobile	UCAR/NCAR (2016d)
			variable	MG1,2,3	mobile	Ziegler et al. (2016)
Surface	T, M_v, U, V	point	5min	FP4	Minden, NE	UCAR/NCAR (2016a)
			< 1min	MP3	mobile	Wagner et al. (2016c)
			< 1min	MP4	mobile	UCAR/NCAR (2016c)
			1s	NSSL MM*	mobile	Waugh and Ziegler (2017)

units were able to observe both sides of the approaching cold pool, providing a unique opportunity to examine the accuracy of the bore environment predictions. However, it should be noted that the cold pool in South Dakota was not observed as well as the ambient environment ahead of it due to the inability of certain profiling instruments (e.g., AERI and DWL) to operate in heavy rain conditions. The other location of intensive data collection was the fixed PISA site in Minden, Nebraska (FP4 hereafter), which hosted AERI, wind profiler, radiosonde and surface instrumentation. Similar to the mobile array, the FP4 site was able to observe the region upstream of the approaching bore and bore-initiated convection. Additionally, the Compact Raman Lidar (CRL) mounted on-board the University of Wyoming King Air Research Aircraft (UWKA; Wang et al. 2016) sampled the structure of the observed bore in Nebraska (downward-pointing maroon triangles in Fig. 4.2b) and generated a valuable dataset for verifying the explicit bore forecasts (discussed in Section 4.5).

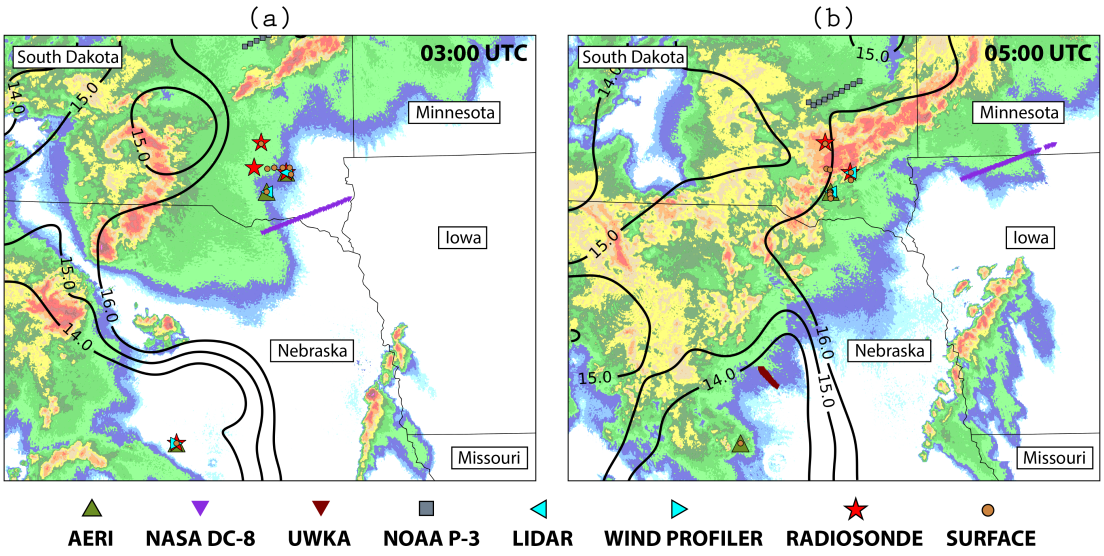

Figure 4.2: Spatial distribution of the IOP20 PECAN observations during (a) the final analysis time at 0300 UTC (*cf.* Fig. 4.3) and (b) the first episode of bore-initiated convection at 0500 UTC. Observation locations are plotted over a 10-minute period centered around these two times. Overlaid on the two panels are composite reflectivity from the Multi-Radar Multi-Sensor (MRMS) system (color shading) and the ensemble mean 2-m mixing ratio from the BASELINE experiment (solid black contours with values in gkg^{-1}).

4.3 Methods

4.3.1 Experimental design

The data assimilation experiments in this study were conducted with an ensemble data assimilation and prediction system based on version 3.7.1 of the Weather Research and Forecasting – Advanced Research core model (WRF-ARW; Skamarock et al. 2008) and a Gridpoint Statistical Interpolation (GSI)-based Ensemble Kalman Filter that was enhanced with convective scale radar data assimilation capabilities (Johnson et al. 2015; Wang and Wang 2017). The model parameterization schemes utilized in our numerical experiments follow the configuration of Johnson and Wang (2017) and are summarized in Table 4.2. The timeline in Fig. 4.3b illustrates the experimental design for the data addition experiments. First, an outer 9-km domain (d01; Fig. 4.3a) was run with initial and lateral boundary conditions based on 20 members from the Global Ensemble Forecast System (GEFS; Wei

et al. 2008) and 20 members from the Short-Range Ensemble Forecast (SREF; Du et al. 2014). In the period between 1500 UTC on 5 July 2015 and 0000 UTC on 6 July 2015, conventional data (surface, radiosonde, ship, buoy and aircraft flight level) from the North American Mesoscale Forecast System Data Assimilation System (NDAS) were assimilated at a 3-hour frequency on the d01 domain. Then, the 9-km ensemble analyses were downscaled to create two additional model nests at 3 km (d02) and 1 km (d03). Between 0000 UTC and 0300 UTC, data assimilation was conducted on the highest resolution 1-km (d03) domain and the conventional NDAS observations were assimilated together with radar data at a temporal frequency of 10 minutes, following Johnson and Wang (2017). Finally, the ensemble analyses obtained at 0300 UTC were used to launch a 40-member ensemble forecast for an additional period of 6 hours. The model configuration described so far serves as a control experiment and is referred to as BASELINE hereafter. Additional data impact experiments were also conducted, in which PECAN observations from IOP20 were assimilated on the d03 domain. The name of those experiments alongside with optimally tuned[2] localization values for EnKF are summarized in Table 4.3. Arguably, the vertical localization value in LIDAR_VAD is relatively large, especially in view of the rapidly decreasing accuracy of the DWL instrument over height. However, since additional LIDAR_VAD experiments with different horizontal and vertical localization scales resulted in very little forecast impacts (not shown), the optimal localization choices for this experiment were not explored any further in this study.

It is important to mention that all PECAN observations were pre-processed before assimilation (*cf.* Table 4.4) by closely following the methodology outlined in Degelia et al. (2019). However, a notable difference with the aforementioned study is that the AERI observation errors were not additionally inflated to account for representativeness errors. The decision to retain the original AERIoe error profiles was motivated by the better forecast skill obtained in this particular case study; nevertheless, future work is still needed to understand

[2] Localization (and observation error) values were tuned to maximize the skill of the convective forecasts.

Table 4.2: WRF-ARW model physics.

Parameterization	Scheme	Reference
Microphysics (DA)	WRF single-moment 6-class (WSM6)	Hong and Lim (2006)
Microphysics (forecast)	Thompson	Thompson et al. (2008)
Planetary Boundary and Surface Layers	Mellor-Yamada-Nakanishi-Niino (MYNN)	Nakanishi and Niino (2006)
Land surface	Unified Noah Land Surface Model	Tewari et al. (2004)
Longwave radiation	Rapid Radiative Transfer Model (RRTM)	Mlawer et al. (1997)
Shortwave radiation	Rapid Radiative Transfer Model for general circulation models (RRTMG)	Iacono et al. (2008)
Cumulus (only d01 domain)	ensemble diversity with Kain-Fritsch and Grell 3D Ensemble	Kain (2004) Grell (1993)

Table 4.3: List of all numerical experiments conducted as part of the 6 July 2015 case study. AIRCRAFT contains both NOAA P-3 flight level data and NASA DC-8 LASE mixing ratio profiles, while WIND_PROF only considers the assimilation of the 915 MHz radio wind profiler at the FP4 site. Note that the AERI retrievals in AERI_REDUCED are assimilated at the frequency of the FP4 radiosonde data. The horizontal and vertical EnKF localization values in the second and third columns are optimally tuned to maximize the skill of the convective forecasts (*cf.* Section 4.6). Note that the two localization values reported next to BASELINE refer to the conventional and radar observations, respectively.

Experiment Name	Horizontal Localization $[km]$	Vertical Localization $[\ln(P/P_{\text{ref}})]$
BASELINE	200 (conv), 18 (radar)	1.10 (conv), 0.55 (radar)
AERI	100	0.55
AERI_REDUCED	100	0.55
AIRCRAFT	200	0.28
LIDAR_VAD	200	1.10
WIND_PROF	200	1.10
RADIOSONDE	200	0.28
SURFACE	200	0.28
PECAN_ALL	combined	combined

the optimal ways of assimilating these novel thermodynamic profilers. Some insights into this question are provided in Section 4.6.1 where the sensitivity of the AERI convective forecasts is tested for different error and assimilation frequency choices. Lastly, we also note that the wind profilers from the mobile array in South Dakota were discarded from WIND_PROF and PECAN_ALL experiments due to the presence of large systematic errors[3].

[3] Examination of the raw wind profiler data revealed large deviations in wind direction when compared to the nearby mobile radiosonde units.

Table 4.4: Pre-processing and error statistics associated with the PECAN observations from IOP20.

Instrument	Averaging or Thinning	Quality Control	Observation Errors
AERI	10hPa averaging	• capping data below 3km or below cloud layer • remove data if retrieval algorithm did not converge	errors based on the AERIoe retrieval algorithm (Turner and Löhnert 2014)
LASE	-	-	GSI radiosonde errors
NOAA P-3 Flight Level	5min thinning	-	GSI ACARS aircraft errors
Doppler Wind Lidar	100m averaging	• gross check for physical values • capping data below 3km	GSI NEXRAD VAD errors
915 MHz Radio Wind Profiler	combine low and high power VAD profiles	• gross check for physical values • reject data with NIMA confidence < 0.5 • mobile array data removed	GSI NEXRAD VAD errors
Radiosonde	10hPa averaging	only preserve pressure levels with good quality markers following Loehrer et al. (1996)	GSI radiosonde errors
Surface Data	5min thinning	gross checks for physical values	GSI errors for surface land data with reported station pressure

4.3.2 Verification and diagnostics of the bore forecasts

The impact of assimilating PECAN observations on the quality of the bore forecasts was assessed objectively using the convective outflow algorithm of Chipilski et al. (2018). This algorithm tracks convective outflow boundaries simulated during an ensemble forecast and diagnoses their properties (e.g., bore height) over a user-prescribed reference point R, which is chosen to coincide with the location of the verifying bore observations. Although the aforementioned point-based approach provides a quantitative assessment of forecast accuracy, the verification results will likely not be representative as convective outflow boundary are capable of exhibiting pronounced spatial and temporal variability (Haghi et al. 2017). Moreover, the verification statistics could suffer from sampling errors due to the finite size of the ensemble forecasts.

With a view of making the verification results more statistically robust, this study extends the original formulation of the algorithm to accommodate an ensemble-based neighborhood verification of the bore forecasts. As illustrated in Fig. 4.4a, this extension is achieved by generating a reference grid close to a verifying bore observation. The reference grid

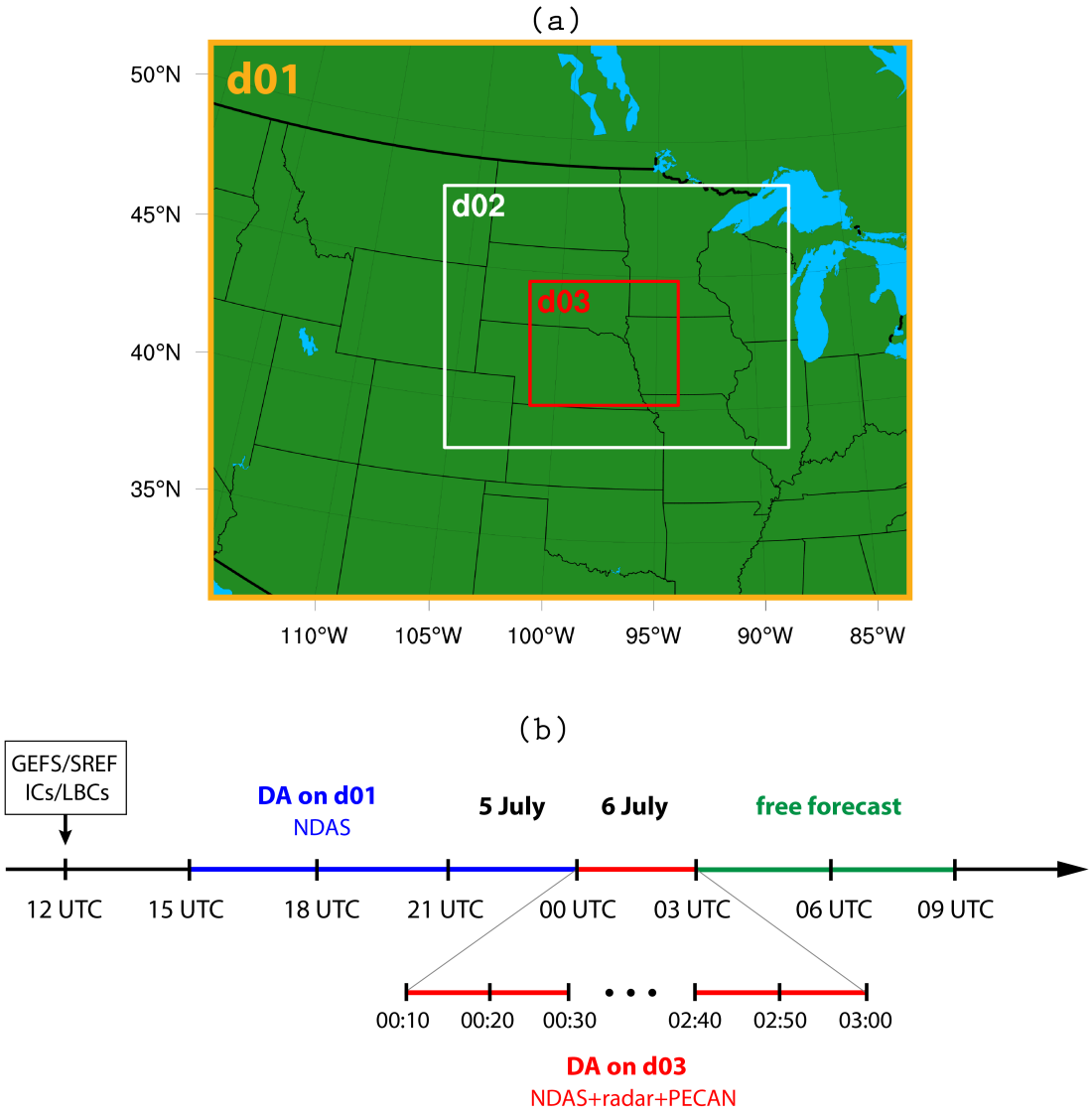

Figure 4.3: Experimental design. *Panel (a)*: Model domains used for the numerical experiments in this study. The horizontal grid spacing of domains d01, d02 and d03 is 9km, 3km and 1km, respectively. Each model domain consists of 50 model levels distributed according to the default WRF settings. *Panel (b)*: Timeline of the data assimilation cycling and ensemble free forecasts. Based on initial and lateral boundary conditions from GEFS/SREF, a 40-member ensemble forecast is run between 12 UTC and 15 UTC to provide the ensemble background for the first data assimilation cycle on the outer 9-km (d01) domain. Conventional (NDAS) observations are then assimilated every 3 hours until 00 UTC on 6 July 2015, at which point the data assimilation calculations switch to the highest-resolution (d03) domain for another 3 hours. During this period, assimilation frequency is reduced to 10 minutes and the conventional observations are complemented by radar and PECAN IOP20 data. Finally, the 1-km ensemble analyses at 0300 UTC are used to launch 6-hour ensemble forecasts in order to evaluate the PECAN data impacts.

consists of multiple reference points (four in the example from Fig. 4.4a) from which the algorithm extracts relevant attributes at the time of object passage. The three reference grids generated as part of this work are shown in Fig. 4.4c; note that their extent corresponds to a neighborhood radius consisting of 99 reference points, which is the largest number of neighboring points used in this work. The first two reference grids are used to verify the bore environment over the mobile array in South Dakota as well as the explicit bore forecasts near the two UWKA intercepts. The third reference grid is located near the region of bore-initiated convection and is used to understand whether the PECAN impacts are due to changes in the mesoscale ambient environment or the characteristics of the explicitly resolved bore. Analogous to Chipilski et al. (2018), the calculation of object attributes over a particular reference point (Fig. 4.4b) is achieved by constructing a cross section oriented along the direction of the pressure gradient force. Note, however, that unlike the original formulation of the algorithm, these cross sections are recentered about the location of the leading prefrontal updraft, which allows us to generate composite density current/bore cross sections derived from multiple ensemble members and reference points.

Verifying the bore environment forecasts is accomplished by utilizing the flow regime diagrams of Rottman and Simpson (1989). These diagrams make theoretical predictions as to whether a density current intruding into an SBL is capable of generating an atmospheric bore. The primary reason for adopting this methodology is in its relative simplicity. In particular, the flow regime diagram describes the characteristics of the bore environment as a single point in the phase space of two non-dimensional parameters – the normalized density current depth (D) and the Froude number (F).

4.4 Bore environment

The correct use of flow regime diagrams requires their application prior to the generation of an upstream bore disturbance. To ensure this criterion is met, we used time series of surface pressure and temperature from both PECAN observations and model forecasts to

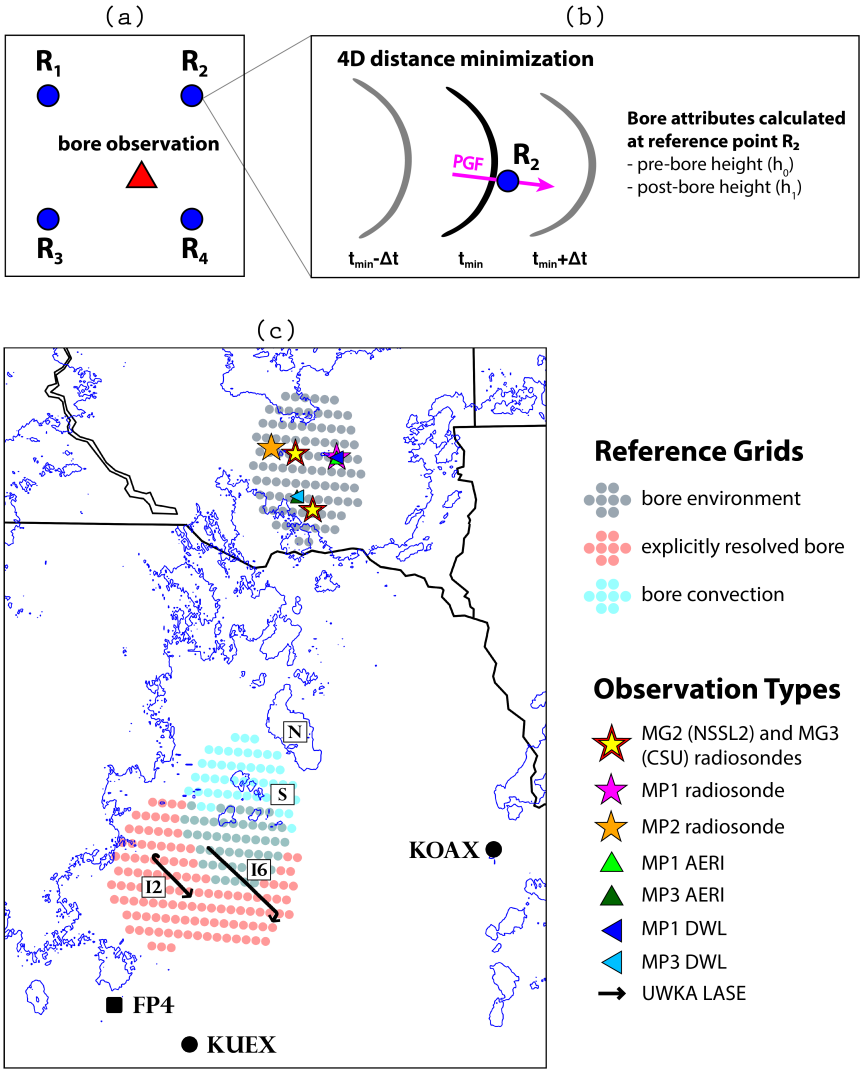

Figure 4.4: Neighborhood verification of the ensemble bore forecasts. Panel (a) illustrates schematically the construction of a reference grid in proximity to a verifying bore observation. The new version of the algorithm performs a four-dimensional (4D) distance minimization at each reference point (*cf.* panel b) in order select which convective outflow boundaries to analyze for each ensemble member. Once these objects are determined, the algorithm generates cross sections oriented parallel to the direction of the surface Pressure Gradient Force (PGF; solid magenta vector) to calculate various object attributes, such as the pre- and post-bore heights (h_0 and h_1). Panel (c) displays the location of the 3 reference grids used for the analysis in this study. Additional information overlaid on this panel figure includes the position of the verifying bore observations (e.g., mobile array, UWKA **I2** and **I6**), the location of the KUEX and KOAX radar sites, and the 30 dBZ MRMS reflectivity during the first episode of bore-initiated convection (0546 UTC; thin solid blue contours). The letters **N** and **S** refer to the northern and southern clusters of bore-initiated convection, while **I2** and **I6** — to the 2nd and 6th bore intercepts from the UWKA aircraft.

determine the morphology of the convective outflow boundary that passed over the mobile array in South Dakota. Analysis of these time series revealed a simultaneous rise in pressure and decrease in temperature between 0345 UTC and 0430 UTC (not shown), confirming that the sampled convective outflow boundary had density current characteristics.

4.4.1 Observed bore environment

For a complete description of the observed flow regime, thermodynamic and kinematic profilers need to simultaneously observe both sides of a density current, which was not always possible during IOP20. In order to make the best use of the PECAN observations collected on 6 July 2015, data from all relevant mobile sites were combined to estimate the variables needed for the flow regime calculations. Such a framework fits our object-based neighborhood approach and is justified due to the spatial proximity of the mobile instruments.

In the context of the flow regime diagram, the ambient environment ahead of the cold pool is characterized by 3 variables – the SBL depth (h_0), the phase speed of shallow water waves propagating on the SBL inversion (C_{gw}) and the mean inversion wind speed[4] projected in the direction of density current propagation (U_0). These flow regime variables were estimates using the available mobile radiosonde, AERI and DWL observations. It is evident from Fig. 4.5 that both h_0 and U_0 increase during the night, coincident with the strengthening SBL inversion and low-level jet (LLJ). It is worth pointing out that the temporal evolution of C_{gw} follows closely that of h_0 and is not displayed here for brevity. Note that observations from different mobile sites are averaged over a 45-minute time window prior to the density current arrival (gray boxes in Fig. 4.5), resulting in a single estimate from each mobile site. A closer examination of the data during this period reveals large regional differences in the observed ambient environment, with h_0 varying between 350 m and 850 m and U_0 exhibiting a bimodal distribution.

[4] Mean inversion wind is defined as the wind averaged over the depth of the SBL.

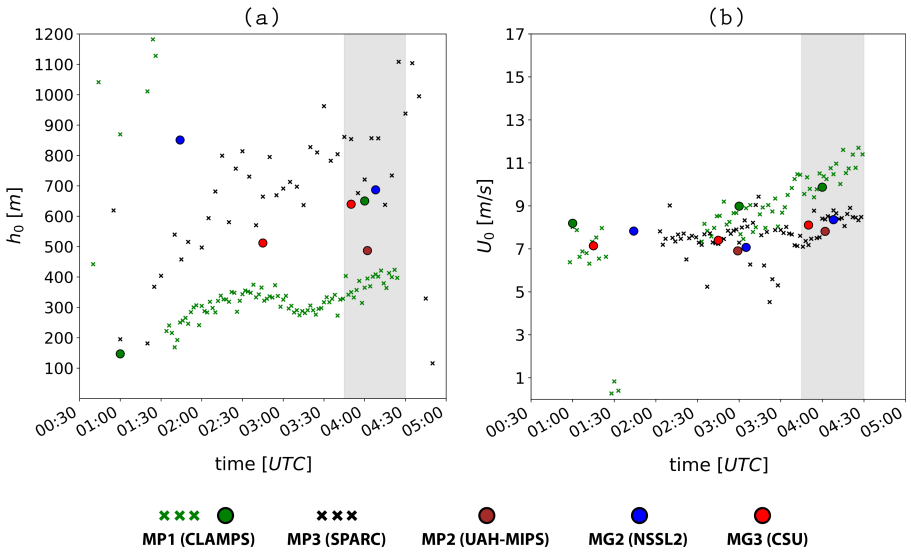

Figure 4.5: Observations of the ambient bore environment from the mobile array in southeastern South Dakota showing the temporal evolution of (a) the SBL depth (h_0) and (b) the mean inversion wind projected in the direction of density current propagation (U_0). The cross markers in the time series show Mobile PISA (MP) estimates derived from either AERI (panel a) or Doppler wind lidar (panel b) retrievals. The gray box between 0345 UTC and 0430 UTC highlights the 45-minute time period used for deriving the observed flow regime in Section 4.4.

One of the salient features of IOP20 was the spatial collocation of several instruments from the mobile array in South Dakota, which allowed us to check the quality of the retrieved ambient flow regime variables. As an example, MP1 (CLAMPS) simultaneously operated an AERI, a DWL and a mobile radiosonde; the radiosonde data made it possible to assess the accuracy of the first two remote sensing instruments. The favorable agreement between the two MP1 U_0 estimates (green colors in Fig. 4.5b) does not only demonstrate the DWL's ability to accurately measure the winds within the SBL, but also provides further evidence for the existence of regional variabilities in the observed LLJ. By contrast, the SBL depth derived from the MP1 AERI retrievals is nearly half of the corresponding radiosonde value. Further comparison of these two instruments showed that the lower AERI h_0 value arises due to a stronger vertical gradient in the virtual potential temperature, which acts to lower the SBL depth derived from the Haghi et al. (2015) method. Although the h_0 estimate from the MP1 AERI instrument is not too far from the one derived at the nearby MP2 site, we decided to discard it from any subsequent flow regime calculations due to the superior accuracy of the collocated MP1 radiosonde measurements.

The density current properties needed for the flow regime calculations are its depth (d_0) and propagation speed (C_g). For consistency with the object-based algorithm of Chipilski et al. (2018), d_0 is taken to be the height at which the virtual potential temperature in the density current profile equals its corresponding surface value in the ambient environment. Using the value of d_0, the density current's propagation speed C_g is defined as

$$C_g = \sqrt{g d_0 \frac{\Delta\rho}{\rho_a}} - \alpha U_0, \tag{4.1}$$

where g is the gravitation acceleration, $\Delta\rho = \rho_d - \rho_a$ is the difference in surface air density between the density current and the ambient environment, and $\alpha = 0.75$ is a correction coefficient that accounts for the slowing of the cold pool as a result of the ambient head wind U_0 (Liu and Moncrieff 2002). Estimates of the density current properties were only based

Table 4.5: Density current and flow regime characteristics according to the radiosonde observations from the MG2 (NSSL2) and MG3 (CSU) mobile sites. The variables d_0 and C_g refer to the depth and propagation speed of the cold pool, while D and F denote the non-dimensional density current depth and Froude number. The flow regime classification in the last column follows Rottman and Simpson (1989).

Observing Platform	d_0 **[m]**	C_g **[ms^{-1}]**	D	F	**Flow Regime**
MG2 (NSSL2)	1240.6	13.3	1.8	2.1	partially blocked; bore type B
MG3 (CSU)	647.3	3.1	1.0	1.2	partially blocked; bore type B

on the MG2[5] (NSSL2) and MG3 (CSU) mobile radiosonde units as heavy precipitation following the passage of the cold pool forced the two AERI instruments to discontinue their data collection process. It is important to remark that while the location of the NSSL2 and CSU units coincided throughout IOP20 (Fig. 4.4), the balloon launches from these two mobile units occurred at different times. Due to the slowly-varying nature of the SBL, the different launching times had very little impact on the ambient flow regime variables (Fig. 4.5). However, the values in Table 4.5 indicate that they inevitably caused large deviations in terms of the observed density current properties.

In order to provide a fair estimate of the bore environment that integrates all available mobile observations in South Dakota, we generated a set of possible flow regimes by randomly combining the values from each of the five flow regime variables. In doing so, special care was taken to account for any theoretical relationships between them. For example, low (high) values of h_0 and d_0 were only paired with low (high) values of C_{gw} and C_g. The red crosses in Fig. 4.6 display the location of all possible flow regimes alongside with the individual flow regime estimates from the CSU and NSSL2 radiosonde sites (refer to the cyan and pink rectangles in Fig. 4.6 as well as the numbers in Table 4.5). The observations collected from the mobile array in South Dakota provide strong evidence that the flow regime during IOP was partially blocked, with the majority of the theoretical bore amplitudes (dashed curves) ranging from 2 to 4. According to Rottman and Simpson (1989), these values are associated with a moderately turbulent type B bore. It is interesting to

[5] MG stands for a Mobile GPS Advanced Upper-Air Sounding System.

remark that the position of the CSU and NSSL2 estimates in phase space (relative to the set of possible flow regime values) reveals that most of the variability in the observed bore environment comes from the heterogeneous properties of the density current as the two radiosonde sites produce very similar observations of the ambient environment (*cf.* blue and red dots in Fig. 4.5).

4.4.2 Forecast impacts

The impact from assimilating PECAN observations on the forecasted bore environment was evaluated for 8 neighbourhood radii in order to investigate whether results are consistent across different scales of motion. Since the obtained verification statistics were found to be largely invariant to the chosen neighbourhood radius (e.g., Fig. 4.7a), the discussion herein is restricted to a representative grid containing 49 reference points. Examination of the ensemble forecasts from BASELINE (Fig. 4.6a) reveals that the control experiment is able to correctly predict a partially blocked flow regime. The presence of two distinct forecast modes, located at theoretical bore amplitudes of ~2 and ~2.7, is also consistent with the tendency of the flow regime observations to cluster around certain portions of the phase space. It should be also noted that while the ensemble spread in BASELINE covers most of the possible flow regime values, the forecast range appears to be slightly displaced towards the origin of the diagram. Improvements in the flow regime predictions are only visible after assimilating observation types that contain wind information, i.e. in the LIDAR_VAD (Fig. 4.6e), WIND_PROF (Fig. 4.6f), RADIOSONDE (Fig. 4.6g) and SURFACE (Fig. 4.6h) forecasts. Out of the aforementioned experiments, the best forecast performance is seen in RADIOSONDE and LIDAR_VAD, for which the number of ensemble members below the lower range of possible flow regime values is considerably reduced. In the case of LIDAR_VAD, the ensemble spread is also better aligned with the direction of the observed flow regime uncertainty, which helps increase the ensemble probability over the cluster of possible flow regime values in proximity to the NSSL2 site. As one

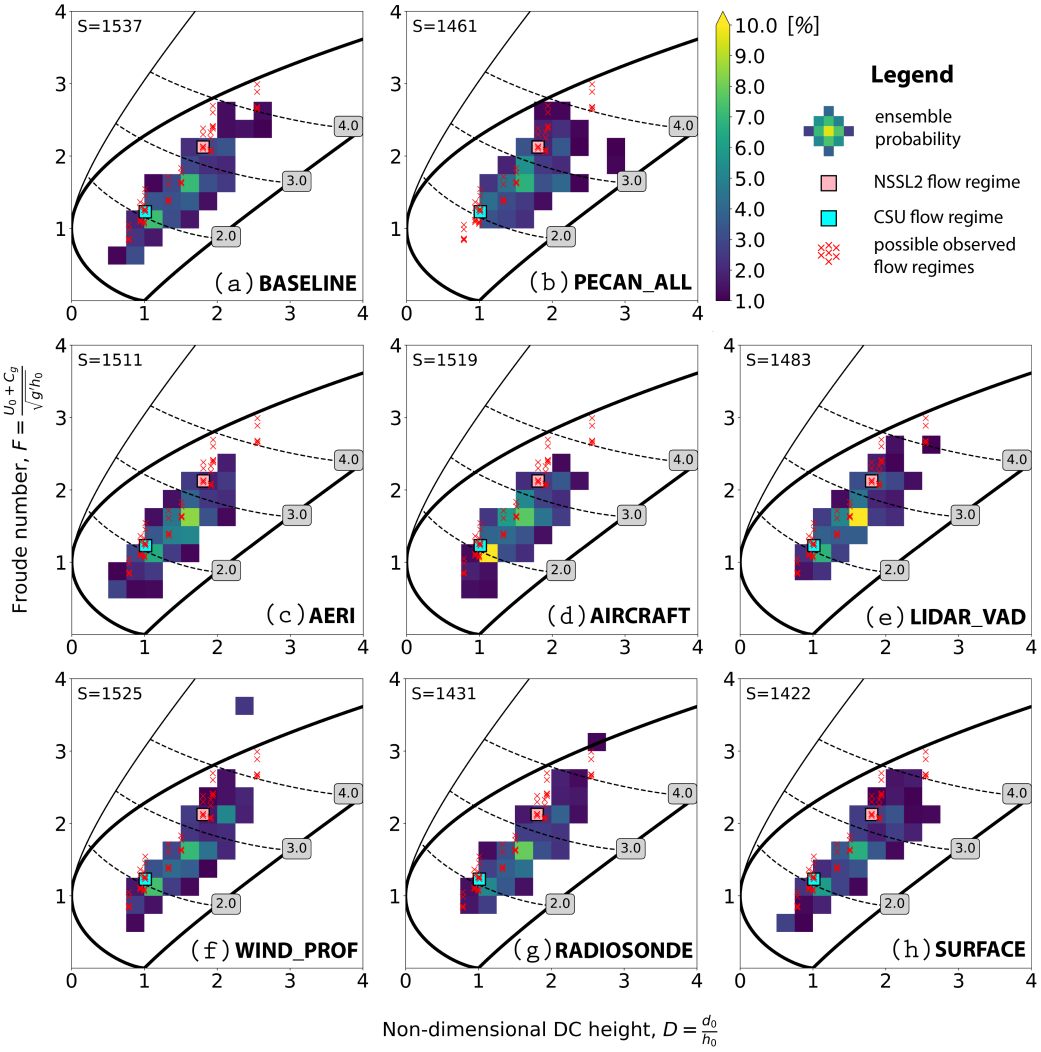

Figure 4.6: Verification of the bore environment forecasts. The color shading displays the ensemble forecasts from different experiments based on the nearest 49 reference points from the northern most reference grid in Fig. 4.4 (number of ensemble members contributing to each experiment, denoted by S, is shown in the upper-left corner of each panel). The flow regime forecasts are verified against individual flow regime estimates from the NSSL2 (pink rectangle) and CSU (cyan rectangle) radiosonde units as well as the set of possible flow regime values derived from all available mobile units in South Dakota (red crosses; see text for more details).

might expect, the assimilation of all available observations in PECAN_ALL (Fig. 4.6b) inherits a lot of the positive changes from the well-performing data addition experiments, including the lower likelihood for an undular bore (amplitude less than 2) as well as the larger number of ensemble members over the NSSL2 cluster. Nevertheless, a shortcoming of the PECAN_ALL forecasts is that they are slightly more confident compared to the empirically derived observation uncertainty and produce only a single mode in the forecasted flow regime.

4.4.3 Examination of the forecast impacts

Understanding why the assimilation of kinematic profilers contributes to improvements in the bore environment forecasts requires a careful examination of the relative changes in different flow regime variables. The bar plot in Fig. 4.7 shows a summary of those changes for the PECAN_ALL experiment which produced the largest changes with respect to BASELINE. The most significant discrepancy between the two experiments concerns the magnitude of the inversion wind (U_0), which is $\geq 30\%$ larger in PECAN_ALL for all of the examined neighborhood radii. The composite wind profiles in Fig. 4.7c confirm this finding and show that the PECAN_ALL forecasts are in much better agreement with the verifying DWL and radiosonde observations. Other notable differences between the two experiments include an 8-10% reduction in h_0 and a corresponding 10-15% reduction in C_{gw}. The lower h_0 and C_{gw} values in PECAN_ALL are caused by the smaller static stability in the SBL (compare the spacing of the first three isentropes in Fig. 4.7b), which acts to lower the height at which the θ_v gradient exceeds its threshold value in the h_0 retrieval method (Haghi et al. 2015). On the other hand, the properties of the cold pools in BASELINE and PECAN_ALL are nearly identical, most likely due to (i) the lack of observations within the cold pool and (ii) the negligible moisture differences ahead of the cold pool (which is opposite to our findings in Section 4.6). The small decrease in the strength of the cold pool

(d_0 and C_g) in PECAN_ALL can be explained by the slightly larger buoyancy values in the upper parts of the cold pool (red contours in Fig. 4.7b).

Taken as a whole, the relative experimental differences in individual flow regime variables would cause a simultaneous increase in both D and F, shifting the PECAN_ALL's forecast towards the upper-right parts of the flow regime diagram and alleviating the amplitude bias in the BASELINE experiment (Fig. 4.6a). The fact that the largest discrepancy between the two experiments pertains to the representation of the LLJ also explains why the assimilation of kinematic information is crucial in improving the bore environment predictions.

4.5 Explicitly resolved bore

The purpose of the reference grid generated in proximity to the two UWKA intercepts (red dots in Fig. 4.4c) is to investigate how the assimilated PECAN observations impact the explicit bore forecasts near the FP4 site. In this section, mixing ratio cross sections from the object-based algorithm are compared to UWKA-derived moisture profiles to determine the ability of the forecasts to correctly simulate the observed bore structure during the two verification times. Forecast errors are also quantified objectively for different neighborhood radii using the convective outflow algorithm of Chipilski et al. (2018). The SBL depth in the UWKA retrievals and in the composite model cross sections is defined based on the 11.25 gkg^{-1} mixing ratio contour, which was objectively found to provide the best description of bore structure in observations and model simulations. The values of h_0 and h_1 are determined by taking the average height of the 11.25 gkg^{-1} contour in the subcritical and supercritical portions of the bore. Note that the use of remotely-sensed mixing ratio profiles to define the SBL depth was also adopted in Johnson et al. (2018) and Johnson and Wang (2019).

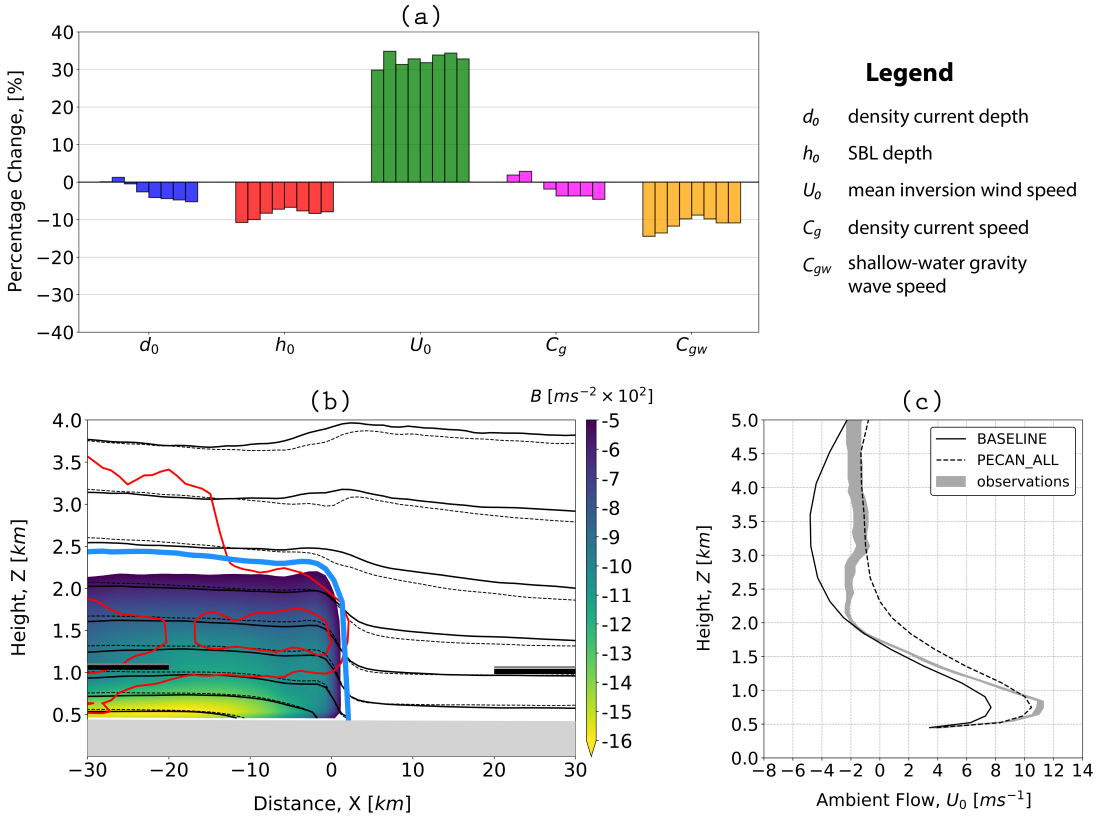

Figure 4.7: Understanding how the assimilated PECAN data affects the forecasted bore environment. *Panel (a)*: Percentage change differences between PECAN_ALL and BASELINE for all 5 flow regime variables and 8 different neighborhood radii using 9, 16, 25, 36, 49, 64, 81 and 99 reference points (from left to right). *Panel (b)*: A composite density current cross section based on the northernmost reference grid in Fig. 4.4 with 99 reference points. The buoyancy field from PECAN_ALL is color shaded, while its difference relative to BASELINE is contoured in red (contours plotted every 1×10^{-2} ms^{-2}, starting from $\pm 1 \times 10^{-2}$ ms^{-2}). The $B = -5 \times 10^{-2}$ ms^{-2} value from BASELINE is marked with a heavy solid blue curve as a reference. Additionally, the solid (dashed) black contours display the virtual potential temperature from PECAN_ALL (BASELINE), which is used for the calculation of the density current and SBL depths (solid black and gray horizontal lines for BASELINE and PECAN_ALL, respectively). *Panel (c)*: Ambient wind speed from BASELINE (solid black curve) and PECAN_ALL (dashed black curve) projected in the direction opposite to density current propagation and averaged over the last 10 km of the density current cross section in panel (b). The wind profile from the corresponding radiosonde and Doppler wind lidar data is overlaid using gray color shading. Note that the verifying observations are averaged between 0345 UTC and 0430 UTC, consistent with the gray box in Fig. 4.5. The width of the gray color shading shows the variability over this 45-min period.

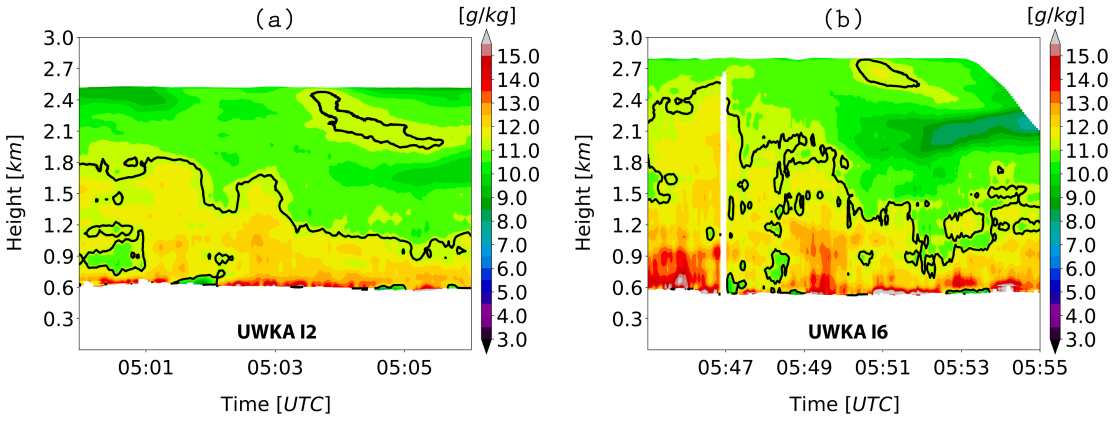

Figure 4.8: Evolution of the observed bore in Nebraska based on moisture profiles from UWKA's Compact Raman Lidar (CRL) system. The heavy black curves denote the 11.25 gkg^{-1} mixing ratio contour used to approximate the height of the SBL in the supercritical and subcritical portions of the bore (see text for more details).

4.5.1 UWKA observations and forecast impacts

The height-time resolved mixing ratio (M_v) profiles in Fig. 4.8 indicate that the observed bore experiences a rapid evolution over the 50-minute time window between the two UWKA intercepts: the post-bore height (h_1) increases from 1.3 to nearly 2 km AGL and is coincident with an increase in the pre-bore SBL height (h_0) from 450 to 600 m. As a result, the amount of bore lifting ($\Delta h := h_1 - h_0$) increases significantly between UWKA I2 and UWKA I6 and likely explains the onset of bore-initiated convection around the second verification time.

The composite cross sections in Fig. 4.9 are created in proximity to UWKA I2 and examine the structure of the simulated bore during its early evolution. First, it is clear that the control experiment (Fig. 4.9a) tends to underestimate (overestimate) the amount of moisture in the pre-bore (post-bore) environment. More pronounced improvements in the forecasted bore environment are visible only after assimilating all available PECAN observations (Fig. 4.9b), which causes an increase in the SBL mixing ratio by ~0.6 gkg^{-1}. The enhanced SBL moisture in PECAN_ALL also corrects a slight negative bias in the pre-bore height (h_0; compare the thick blue contour and the right-most magenta line in Fig. 4.9a). As far as the structure of the simulated bore is concerned, the PECAN impacts are most

evident with respect to the numerically predicted bore height (h_1), which is overestimated in BASELINE by some 300-400 m (compare the blue contour and left-most magenta line in Fig. 4.9a). Most of the data assimilation experiments exacerbate this error, with AERI and PECAN_ALL featuring the largest deviations from the UWKA-derived h_1 estimate. It is perhaps interesting to note that the post-bore SBL increases in AIRCRAFT and SURFACE are most prominent downstream of the hydraulic jump, which is opposite to AERI and PECAN_ALL where the largest changes occur immediately downstream of the bore's leading edge. On the other hand, WIND_PROF (Fig. 4.9f) shows a strong deviation from the other data assimilation experiments – it decreases h_1 by ~200-400 m and, consequently, nearly halves the bore height bias in BASELINE. Similar to AERI and PECAN_ALL, the largest changes in the WIND_PROF-predicted SBL height occur very close to the hydraulic jump. Insofar as the other experiments are concerned, LIDAR_VAD and RADIOSONDE produce the smallest differences in the explicitly resolved bore relative to BASELINE. Whereas the absence of DWL profiles upstream of the bore justifies the lack of visible forecast impacts in LIDAR_VAD, a possible explanation for the small RADIOSONDE-BASELINE differences is the coarse temporal resolution of the FP4 radiosonde measurements compared to the other observation types.

During the second verification time (UWKA I6), the ambient moisture environment in BASELINE (Fig. 4.10a) is represented much better, which in turn also improves the structure of the explicitly resolved bore. Furthermore, the experimental differences at UWKA I6 are considerably smaller than UWKA I2; only the AERI (Fig. 4.10c), WIND_PROF (Fig. 4.10f) and PECAN_ALL (Fig. 4.10b) experiments display visible deviations from BASELINE. Despite the apparent reduction in errors, however, none of the ensemble forecasts reproduces the rapid bore evolution depicted in UWKA's moisture profiles. Given that the experimental differences between the two verification times remain similar, the slower increase of the numerically simulated bore height acts to change the sign of the PECAN impacts between UWKA I2 and I6. For instance, the strongly negative impact in AERI at UWKA I2 (Fig.

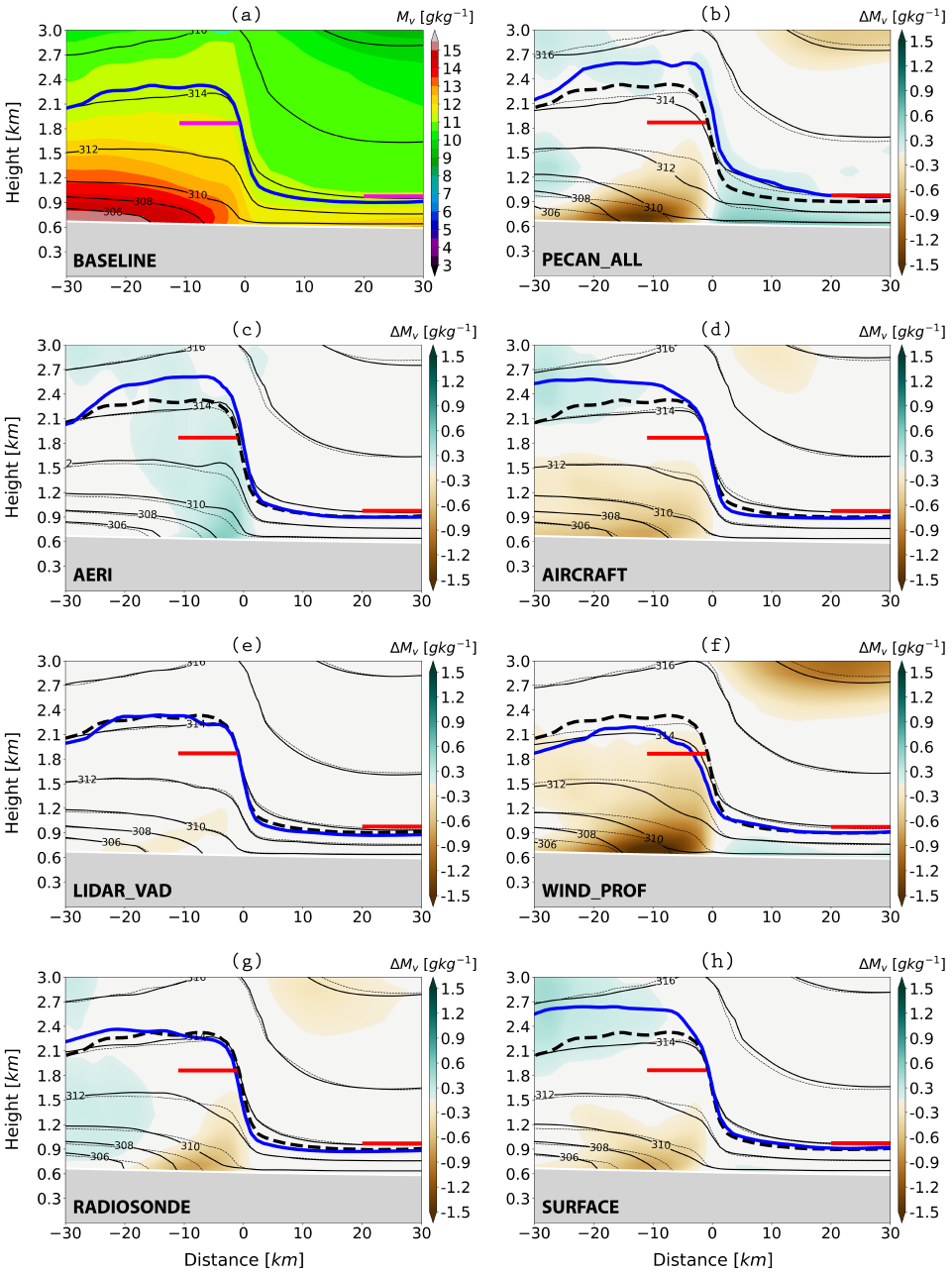

Figure 4.9: Verification of the explicit bore forecasts near UWKA I2 (~0500 UTC). Panel (a) displays mixing ratio (color shading) and virtual potential temperature (solid black contours) from the BASELINE experiment. The heavy solid blue contour marks the SBL depth, while the two horizontal lines correspond to the UWKA-derived pre-bore and post-bore SBL heights, respectively. Note that all forecasted SBL heights are calculated using the 11.25 gkg^{-1} mixing ratio value, consistent with Fig. 4.8. The rest of the panel figures (b-h) display mixing ratio differences associated with various data assimilation experiments. The virtual potential temperature and SBL height from BASELINE are overlaid as thin and heavy dashed black contours, respectively.

4.9c) on h_1 transforms into a marginal improvement at UWKA I6 (Fig. 4.10c). Likewise, the addition of boundary layer moisture in PECAN_ALL is beneficial early in the forecast (Fig. 4.9b), but it leads to an overestimate of h_0 in vicinity of UWKA I6 (Fig. 4.10b).

A summary of the average PECAN impacts on the structure of the explicitly resolved bore is presented in Fig. 4.11 through the Mean Average Errors (MAEs[6]). Note that the verification statistics in Fig. 4.11 are dominated by the forecast performance at UWKA I2 where the error magnitudes and experimental differences are significantly larger relative to UWKA I6. Despite differences in methodology, however, the MAE results in Fig. 4.11 are largely consistent with the subjective conclusions presented so far. For instance, Fig. 4.11a confirms the presence of a small positive bias in PECAN_ALL's prediction of h_0, while Fig. 4.11b highlights that the assimilation of wind profiler (AERI) data has a positive (negative) impact on the predictions of the numerically simulated bore height.

The structure of a convectively-generated bore is important as it affects errors associated with derived variables, such as bore amplitude ($S \coloneqq h_1/h_0$) and bore lifting ($\Delta h \coloneqq h_1 - h_0$). Both of these variables play a crucial role in determining the propagation of a bore (e.g., White and Helfrich 2012) as well as its ability to initiate convection (Parsons et al. 2019a). Given the additive nature of Δh errors and the fact that changes in h_1 are much greater than changes in h_0 (e.g., Fig. 4.9), the accuracy of the bore lifting predictions is mostly determined by how the assimilated PECAN observations affect the height of the explicitly resolved bore. Indeed, 4.6 confirms that the overprediction of h_1 in all experiments translates to a positive bias in the Δh forecasts. Analogous to the MAE h_1 results (Fig. 4.11b), the WIND_PROF (AERI) experiments produce the largest positive (negative) impact on the forecasts of bore lifting.

The values summarized in Table 4.6 also indicate that the bore amplitude predicted in BASELINE (3.26) is very close to the verifying UWKA retrievals (3.10) despite the

[6] The estimation of the Mean Average Errors (MAEs) is a two-step process. First, the ensemble mean error is computed at a particular reference point based on all available ensemble members. Then, the ensemble mean errors are averaged over all reference points falling within a particular neighbourhood radius.

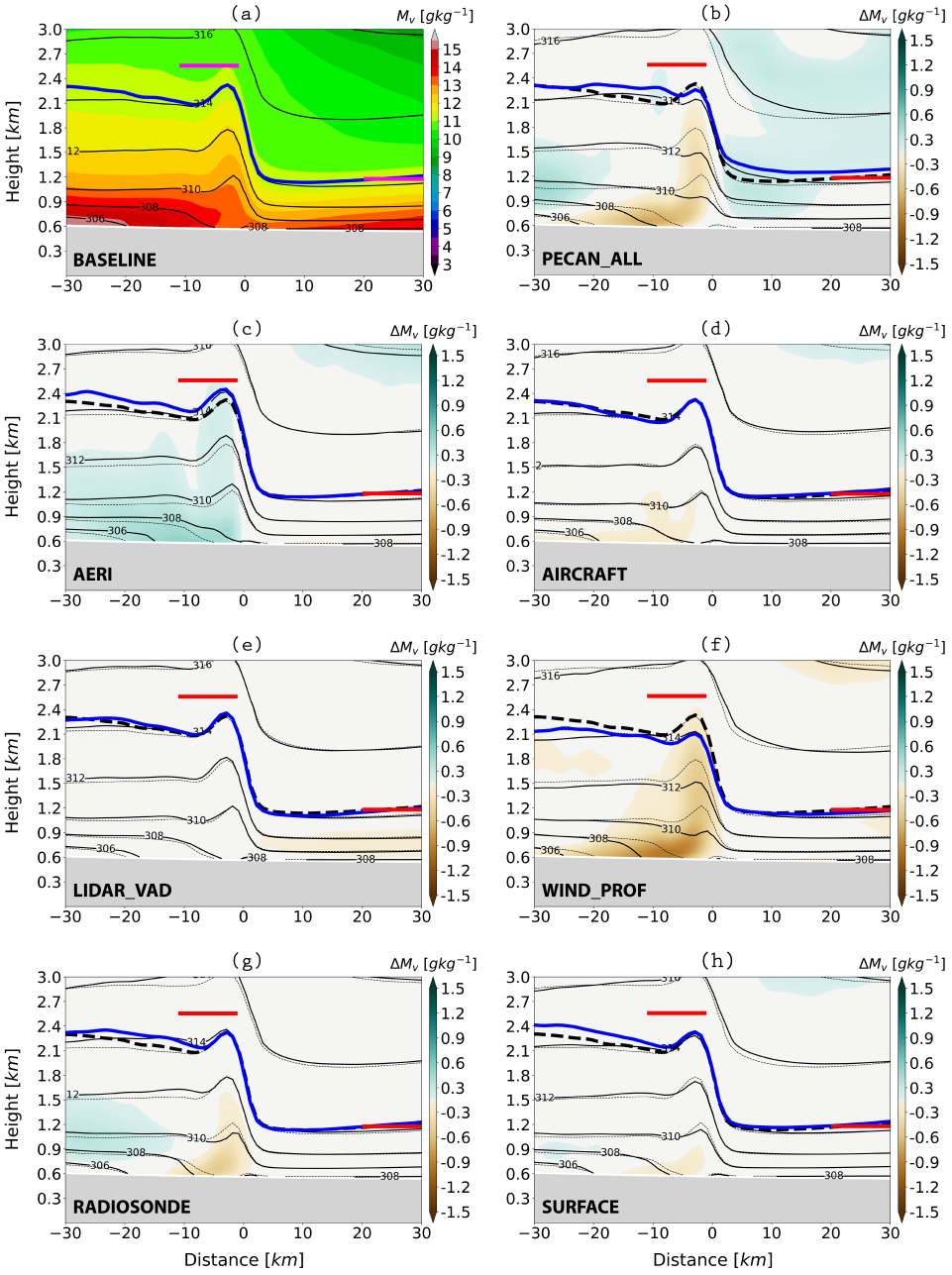

Figure 4.10: Verification of the explicit bore forecasts near UWKA I6 (~0550 UTC). The meaning of all symbols remains the same as in Fig. 4.9.

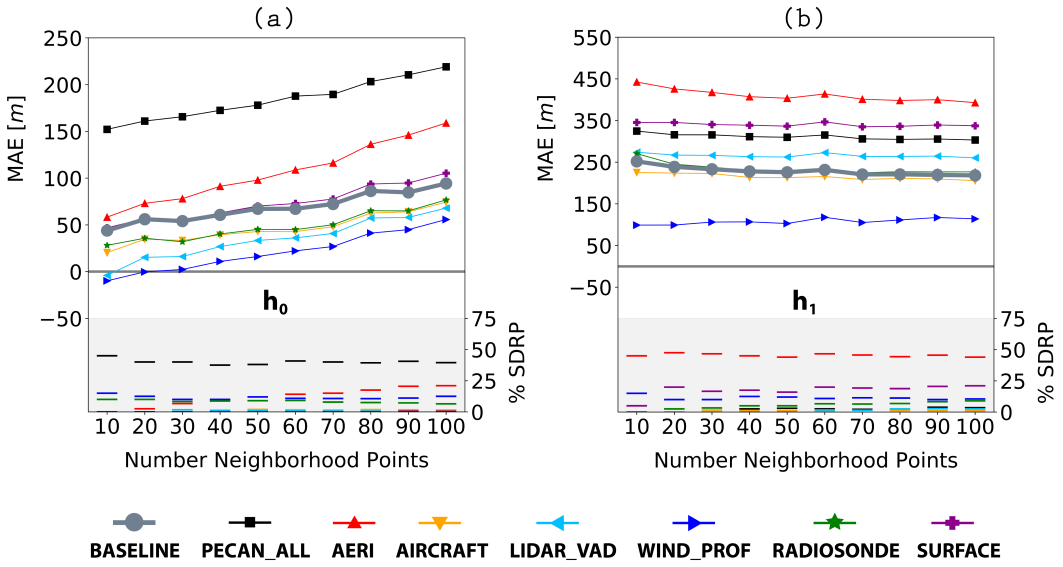

Figure 4.11: Summary of the verification statistics associated with the explicit bore forecasts over UWKA I2 and UWKA I6. Solid curves with filled markers display the Mean Average Errors (MAEs) with respect to the (a) pre-bore height (h_0) and (b) post-bore height (h_1) for a different number of reference points (x-axis). The gray box at the bottom of the two panel figures shows the percentage of Statistically Different Reference Points (SDRP) relative to the BASELINE experiment.

presence of large biases in the predicted bore height. According to Rottman and Simpson (1989), both of these S values would result in an identical flow regime characterized by the generation of an upstream bore disturbance with moderate amounts of turbulence. The small S error in BASELINE experiment can be explained by noting that (i) S is a ratio of h_1 and h_0 and (ii) errors in S are relative in nature. Since $h_0 \ll h_1$, the value of S is expected to be highly sensitive to small changes in the depth of the SBL ahead of the bore. Because the BASELINE experiment produces fairly accurate predictions of h_0 at both UWKA intercepts, the large overestimate of h_1 only contributes to a small positive bias in S. Similar arguments can be applied to justify the bore amplitude results in the other data assimilation experiments. For example, while the reduction of h_1 in WIND_PROF is almost as high as the increase of h_1 in AERI (*cf.* Table 4.6), the attendant decrease of h_0 by 50 m prevents WIND_PROF from correcting the amplitude bias in BASELINE. Likewise, the increase of h_0 and h_1 in

Table 4.6: Example PECAN impacts on the forecasted bore structure for a reference grid with 10 points and based on the MAE results in Fig. 4.11. The numbers in the first row refer to the UWKA-derived bore estimates, while the remaining rows display forecast results from the main numerical experiments presented in this study. The bracketed numbers next to each experiment denote changes relative to BASELINE.

Observations or Experiment Name	**Pre-Bore Height, h_0 [m]**	**Post-Bore Height, h_1 [m]**	**Bore Lifting, Δh [m]**	**Bore Amplitude, S [-]**
UWKA	525	1625	1100	3.10
BASELINE	575	1875	1300	3.26
PECAN_ALL	675 (+100)	1950 (+75)	1275 (-25)	2.88 (-0.38)
AERI	575 (0)	2075 (+200)	1500 (+200)	3.61 (+0.35)
AIRCRAFT	550 (-25)	1875 (0)	1325 (+25)	3.41 (+0.15)
LIDAR_VAD	525 (-50)	1875 (0)	1350 (+50)	3.57 (+0.31)
WIND_PROF	525 (-50)	1725 (-150)	1200 (-100)	3.29 (+0.03)
RADIOSONDE	550 (-25)	1875 (0)	1325 (+25)	3.41 (+0.15)
SURFACE	575 (0)	1975 (+100)	1400 (+100)	3.43 (+0.17)

PECAN_ALL is on the same order of magnitude (~100m), but the higher sensitivity of S to h_0 produces a notable reduction in the predicted bore amplitude.

4.5.2 Examination of the forecast impacts

The nonlinear dynamics of atmospheric bores makes the interpretation of the PECAN data impact results inherently challenging. This is because their formation and evolution are very sensitive to the properties of the parent convection and its cold pools. Despite these difficulties, multiple studies have demonstrated the success of hydraulic theory in explaining the complex behaviour of observed atmospheric bores (Koch et al. 1991, 2008a,b). As a result, the analysis here makes use of hydraulic theory to identify where differences in the AERI and WIND_PROF bore forecasts originate from. We focus on these two experiments not only due to their considerable deviations from the BASELINE experiment, but also to emphasize the dependence of the PECAN data impacts on the assimilated instrument types (i.e., thermodynamic vs. kinematic).

The characteristics of the bore environments in BASELINE, AERI and WIND_PROF are investigated by generating cross sections near the verifying UWKA intercepts. It is apparent from the ensemble mean fields in Fig. 4.12 that the largest differences in the three experiments are due to the depth of the bore-generating density current (d_0). The near-surface isentropes

between $x = -60$ km and $x = -20$ km indicate that the cold pool in AERI (WIND_PROF) is stronger (weaker) than BASELINE. According to well-established theoretical results (e.g., Benjamin 1968), changes in the depth of the cold pool (d_0) are also correlated to changes in its propagation speed (C_g), which was confirmed by a subjective analysis of several ensemble mean fields. Apart from changes in the cold pool characteristics, the magnitude of the inversion wind (U_0) in WIND_PROF is 1-2 ms^{-1} smaller than BASELINE (Fig. 4.12b), causing a further decrease in the forecasted Froude number F. Analogous to Section 4.4, the reduction of the mean inversion wind (U_0) in WIND_PROF is connected to the ability of the assimilated FP4 wind profiler to correct a bias in the representation of the LLJ (not shown).

The aforementioned differences in the bore-generating density current are related to perturbations in the near-surface moisture field at the FP4 site, which are subsequently transported towards this cold pool during the free forecast period (Figs. 4.13 and 4.14). As a result of their interaction with the cold pool's updraft, the positive (negative) moisture perturbations in AERI (WIND_PROF) strengthen (weaken) the parent convection and, through changes in precipitation loading, produce a stronger (weaker) cold pool. It is important to remark that while the positive moisture increments in AERI are introduced primarily due to a moisture bias at the beginning of the 1-km DA cycling period, the drying in WIND_PROF arises due to the inherent mass-wind correlations in the ensemble Kalman filter analyses. For instance, the wind perturbations at 0100 UTC are oriented towards the northeast (magenta arrows in Fig. 4.13d) and act to strengthen the magnitude of the LLJ. Further note that these perturbations are directed perpendicular to the pre-existing moisture boundary in central Nebraska (black contours in Fig. 4.2). Owing to the stronger air advection from the southwest, the SBL in WIND_PROF becomes drier, generating negative mixing ratio perturbations that are subsequently transported towards the bore-generating cold pool in Nebraska (Fig. 4.14f).

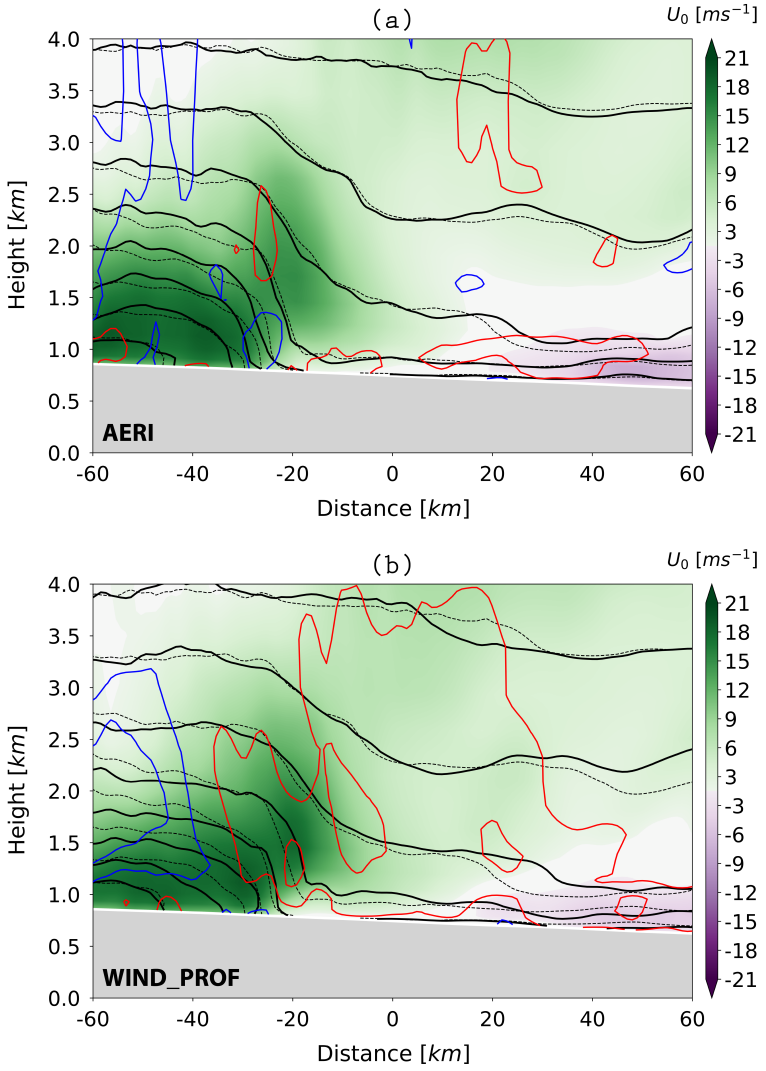

Figure 4.12: Flow regime diagnostics on the bore-generating cold pool in Nebraska for the (a) AERI and (b) WIND_PROF experiments. The color shading on the two cross sections shows the ensemble mean inversion wind projected in the direction of density current propagation (U_0; color shading), with negative (positive) values indicating flow oriented towards (away) from the density current. Negative (positive) differences in U_0 with respect to the BASELINE experiment are displayed as solid blue (red) contours. The virtual potential temperature from AERI/WIND_PROF and BASELINE is plotted with solid and dashed black contours, respectively.

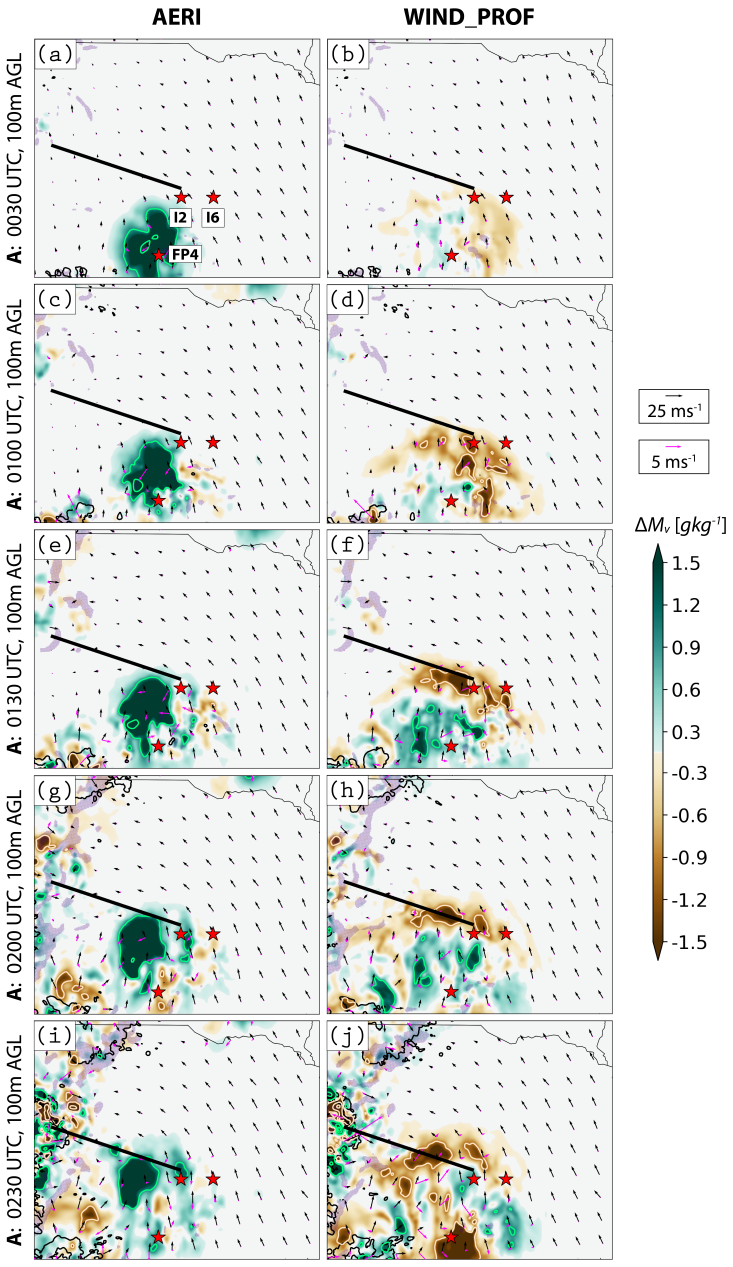

Figure 4.13: Moisture impacts on the explicit bore forecasts for the AERI (left column) and WIND_PROF (right column) experiments. Color shading refers to ensemble mean differences in mixing ratio relative to BASELINE (the letters **A** and **F** stand for analysis and forecast differences). Contours are plotted every 2 gkg^{-1} with solid lime and bisque colors (first contour appears at ±1 gkg^{-1}). Black and magenta arrows show the ensemble mean wind in AERI/WIND_PROF and their difference with BASELINE. The 30 dBZ composite reflectivity and the regions where vertical velocity at 1km AGL exceeds 0.5 ms^{-1} are visualized as solid black contours and purple dots. (*Continue to Fig. 4.14*)

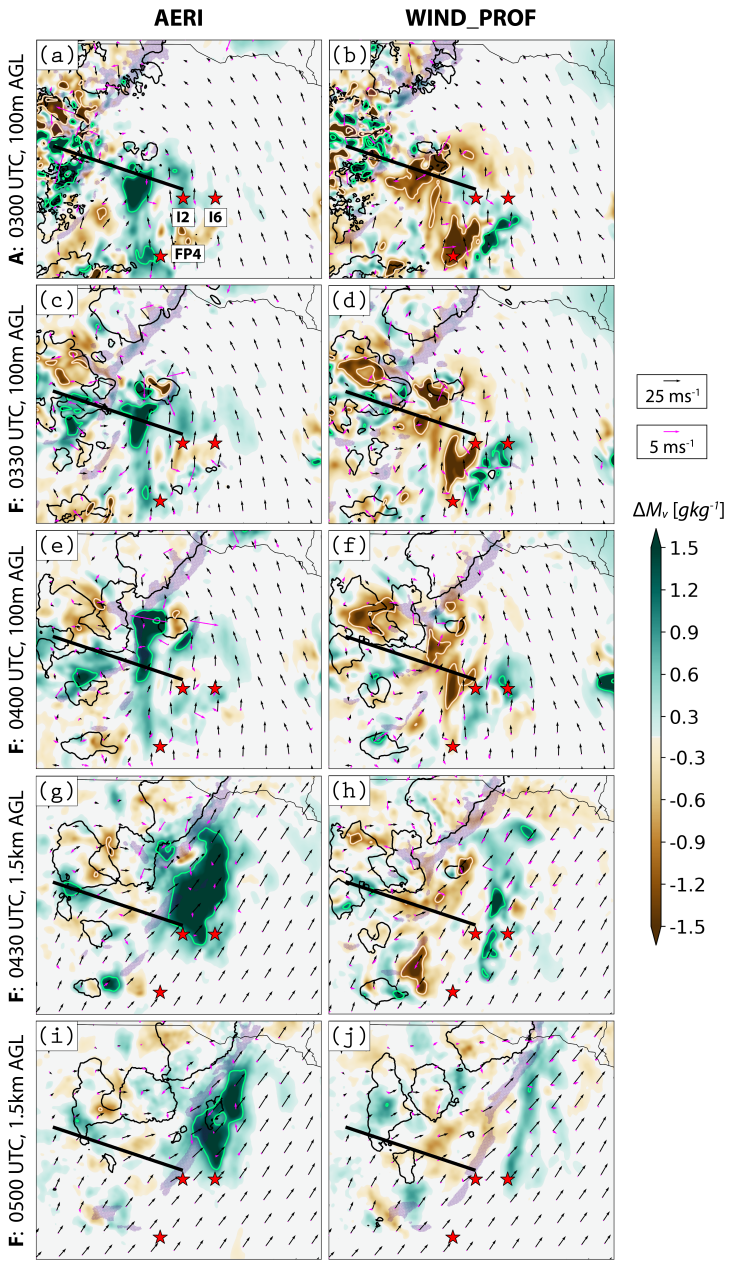

Figure 4.14: (*Continued from Fig. 4.13*) The 3 red stars at the bottom portion of the panel figures show the location of the FP4 site and the two UWKA intercepts (labelled in panel a), while the heavy solid black line – the position of the density current cross section from Fig. 4.12. Note that both the mixing ratio and vertical velocity fields are smoothed using a Gaussian filter with $\sigma = 2.0$ km.

4.6 Bore-initiated convection

The development of bore-initiated convection can be viewed as a manifestation of all multi-scale processes driving the evolution of the bore and its surrounding ambient environment. Therefore, the purpose of this section is to perform an objective assessment of the convective forecasts and then link them to the previously discussed PECAN data impacts. Note that our analysis only focuses on the first episode of bore-initiated convection (0500-0615 UTC; Fig. 4.2) when the experimental differences were most pronounced.

4.6.1 Radar observations and forecast impacts

The convectively-generated bore in Nebraska was captured very well in the low-level reflectivity data from the KOAX radar site (Fig. 4.15), where it shows up as a series of three radar fine lines propagating towards east-southeast. Convection initiation along the bore was discrete and characterized by the occurrence of two main convective clusters. The northern one, denoted as N, started its development around 0500 UTC at the leading edge of the nocturnal MCS. As the bore propagated away from the MCS, convection initiation associated with cluster N shifted ahead of the main convective system. The southern cluster (S) developed approximately 30 minutes after N and moved in the direction of bore propagation.

The skill of the convective forecasts is assessed objectively using neighborhood ensemble probability (NEP; Schwartz et al. 2010) with a threshold of 30 dBZ and a neighborhood radius of 30 km. Comparison of the NEP field from BASELINE and the observed 30 dBZ value derived from Multi-Radar Multi-Sensor (MRMS; Zhang et al. 2016a) data in Figs. 4.16a-c shows that the first episode of bore-initiated convection is underpredicted in the control experiment. Despite an initial increase of NEP to 50% near the location of cluster N (Fig. 4.16a), the BASELINE forecasts do not maintain the newly developed bore convection for a sufficiently long time.

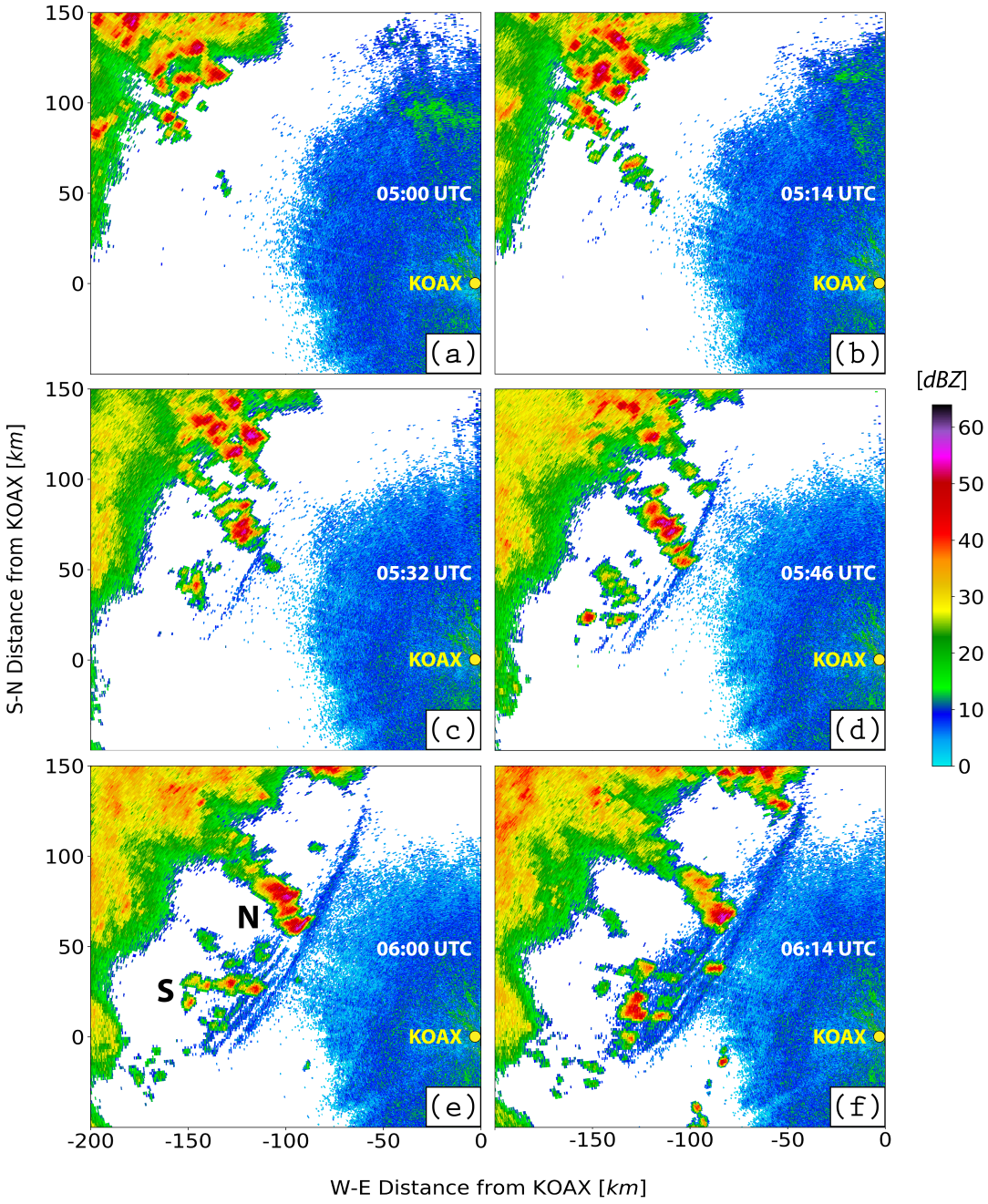

Figure 4.15: Equivalent radar reflectivity (lowest elevation angle) from the KOAX radar site (Omaha, Nebraska) depicting the evolution of the first episode of bore-initiated convection for the 6 July 2015 case study. The letters **N** and **S** show the location of the northern and southern convective clusters. Radar images are generated using the Python Atmospheric Radiation Measurement (ARM) Radar Toolkit (Py-ART Helmus and Collis 2016).

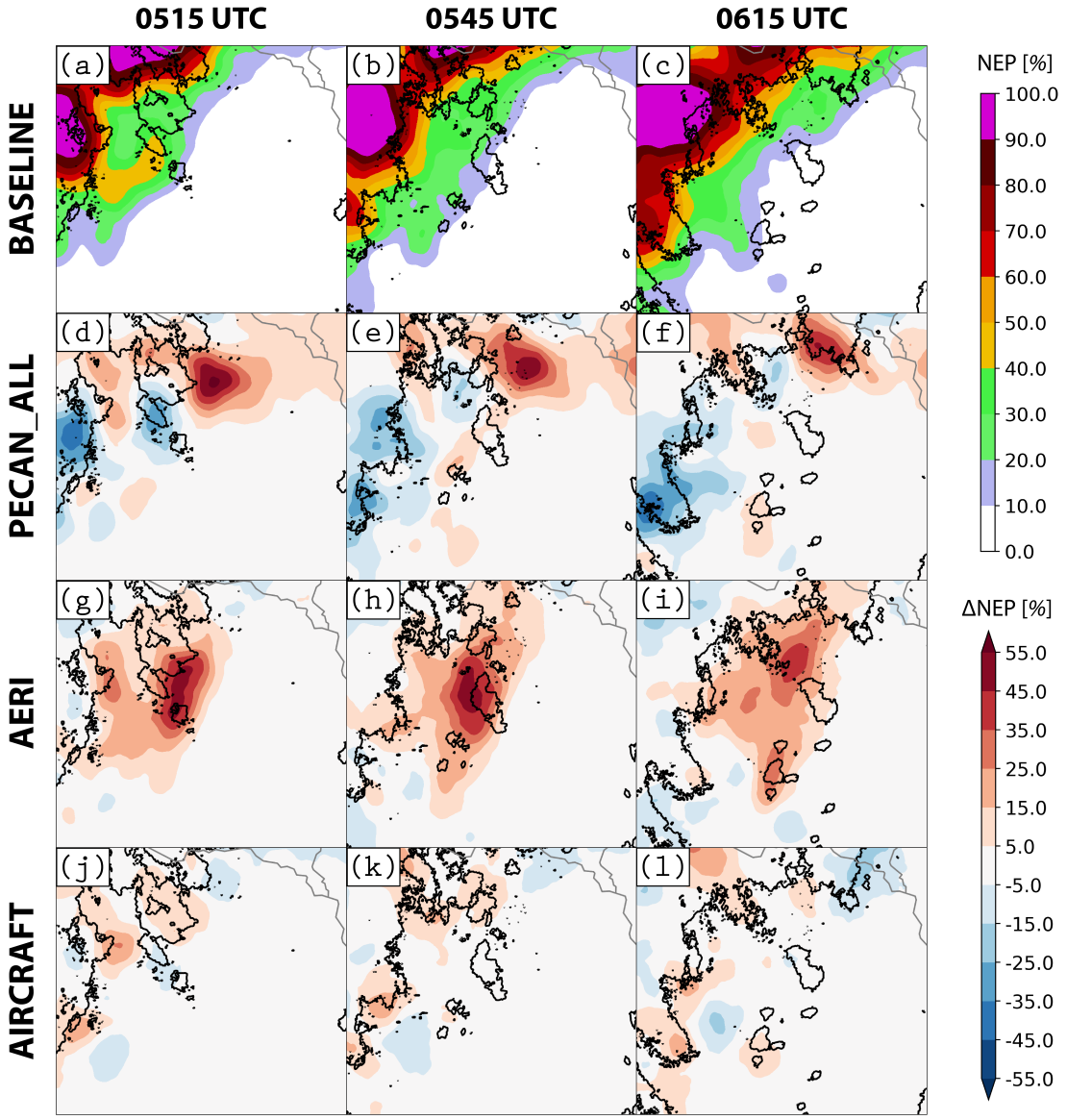

Figure 4.16: Impact of assimilating PECAN observations on the forecasts of bore-initiated convection. The first row shows results for the BASELINE experiment through the Neighborhood Ensemble Probability (NEP; color shading) of model-simulated reflectivity exceeding 30 dBZ with a neighborhood radius of 8 km. (*Continue to Fig. 4.17*)

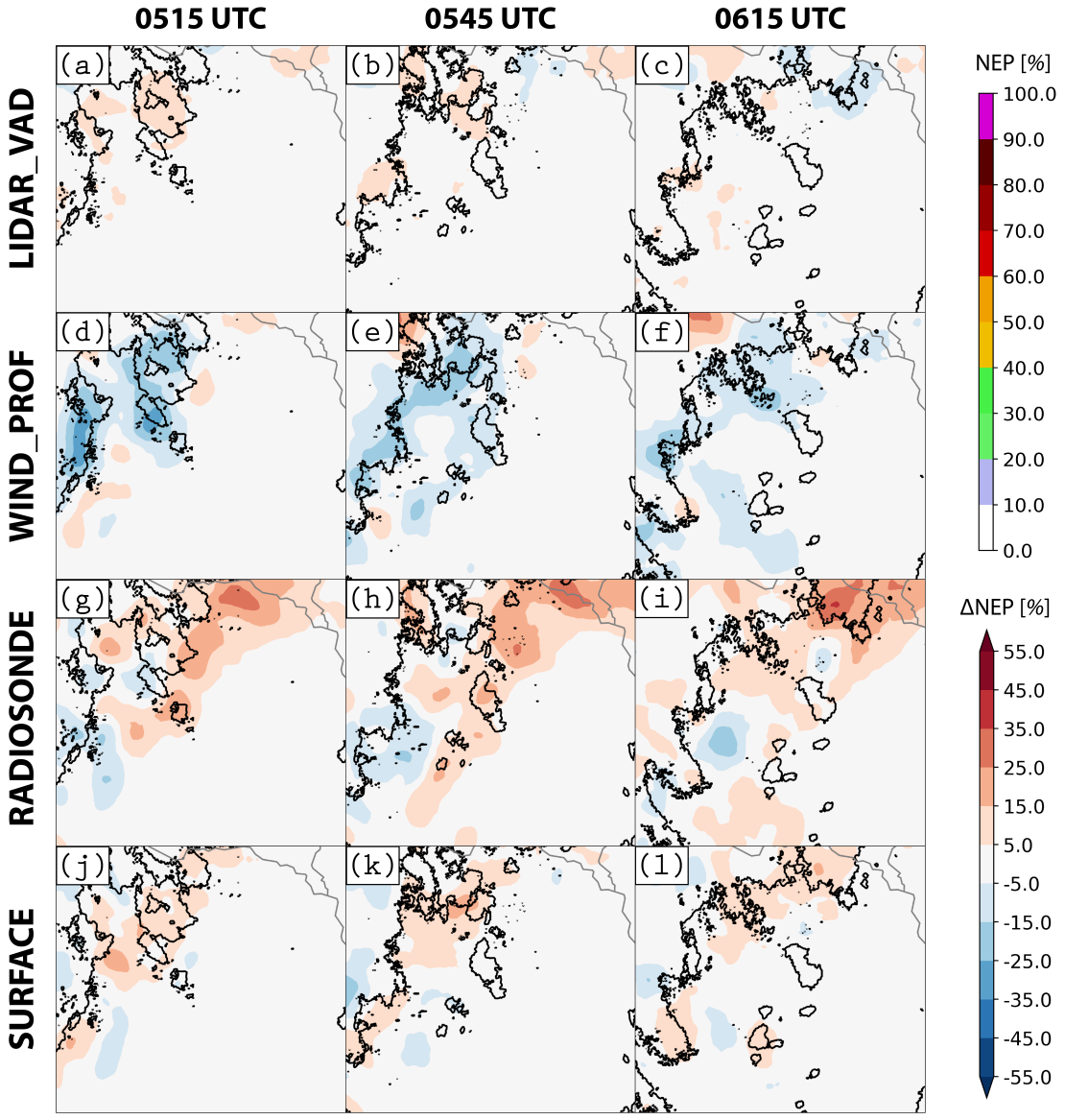

Figure 4.17: (*Continued from Fig. 4.16*) The rest of the panel figures display differences in NEP with respect to the other data assimilation experiments. The observed 30 dBZ composite reflectivity from the Multi-Radar Multi-Sensor (MRMS) system is contoured in black.

The convective impacts from the other data addition experiments are shown as differences in NEP relative to the BASELINE experiment. Examination of these difference fields reveals that LIDAR_VAD (Figs. 4.17a-c), AIRCRAFT (Figs. 4.16j-l) and SURFACE (Figs. 4.17j-l) exert a negligible impact on the convective forecasts. The latter is not so surprising due to (i) the absence of DWL and aircraft data upstream of the forecasted bore convection and (ii) the relatively small impact that surface observations have had on the forecast results so far (*cf.* Sections 4.4 and 4.5). The most successful prediction of the observed bore-initiated convection is produced by the AERI experiment (Figs. 4.16g-i), which is able to (i) increase the NEP values by more than 50% and (ii) successfully capture the initiation and propagation of the southern convective cluster (S). By contrast, assimilation of the FP4 wind profiler data leads to a slight degradation in the convective forecast skill, evident by the reduction in NEP in Figs. 4.17d-f.

The significant improvement of the convective forecast skill in AERI prompted us to conduct two additional experiments aimed at exploring the sensitivity of the results to alternative DA configurations. In the first one, the AERI profiles were assimilated with static GSI radiosonde error statistics (AERI_SOUNDERR; Fig. 4.18b). Since radiosonde errors are notably larger than their AERIoe counterparts (refer to Degelia et al. 2019), AERI_SOUNDERR can be thought of as an experiment which crudely accounts for the errors of representation inherent in the AERIoe profiles. According to Figs. 4.18a and 4.18b, both AERI experiments result in similar convective forecasts, although AERI_SOUNDERR tends to slightly overestimate the convective probabilities around cluster S. Nonetheless, additional diagnostics revealed that AERI_SOUNDERR degrades the quality of the bore-related forecasts (not shown), which justifies our choice of dynamically retrieved error profiles in the control AERI experiment. The goal behind the second sensitivity experiment (AERI_REDUCED; Fig. 4.18c) was to understand the extent to which the quality of the convective forecasts is affected by the AERI's assimilation frequency. More specifically, the thermodynamic retrievals in AERI_REDUCED were assimilated at the same frequency

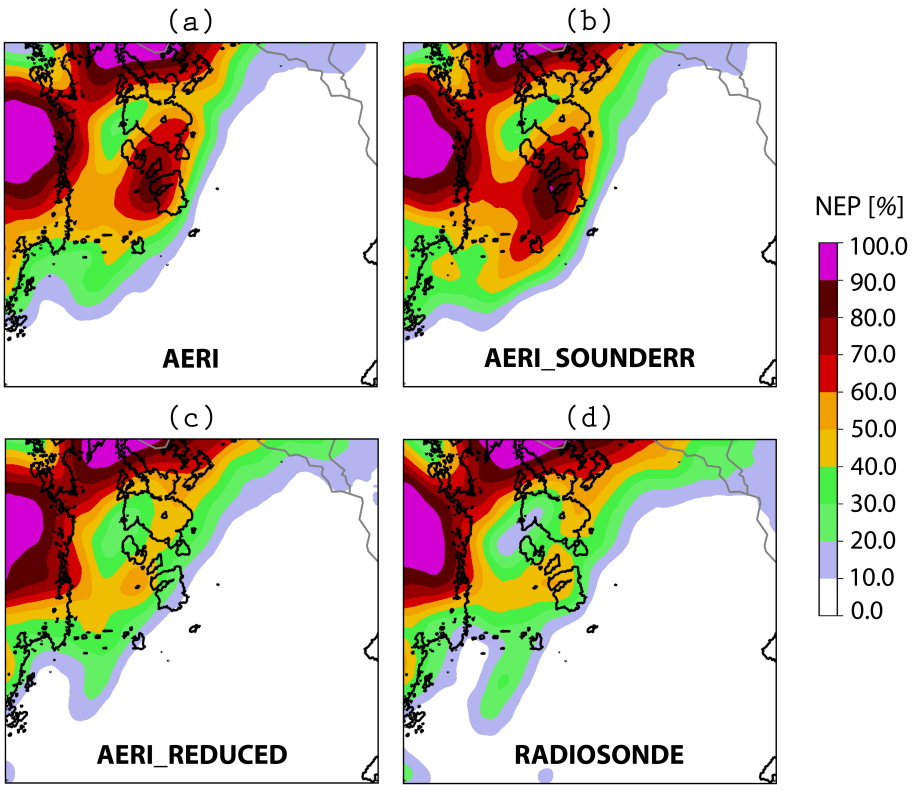

Figure 4.18: Sensitivity of the AERI convective forecasts to different data assimilation configurations. NEP fields from 0530 UTC are shown for the original (a) AERI and (d) RADIOSONDE experiments as well as the additionally conducted (b) AERI_SOUNDERR and (c) AERI_REDUCED experiments, which test the forecast sensitivity to different observation errors and assimilation frequencies, respectively. The rest of the symbols remain the same as in the first row of Fig. 4.16.

as the FP4 radiosonde observations, i.e. every 3 hours. The striking resemblance of the AERI_REDUCED and RADIOSONDE (Fig. 4.18d) forecasts implies that the assimilation of novel AERI data adds no value to the quality of the NWP forecasts unless it is assimilated at a high temporal frequency. Observation space statistics from the FP4 site (not shown) further confirm that the continuous assimilation of AERI profiles over a 3-hour period results in a model state that agrees favourably with the collocated radiosonde observations at 0300 UTC.

Lastly, we note that the simultaneous assimilation of all PECAN observations yields mixed impacts on the convective forecasts. The higher NEP values to the east of cluster

N (Fig. 4.16d-f) appear to be associated with spurious convection that develops earlier in the PECAN_ALL simulation, which ultimately inhibits the subsequent development of bore-initiated convection over the chosen verification region. Analogous to the results from Section 4.5, the presence of mixed impacts in AERI and WIND_PROF prevents PECAN_ALL from providing the best forecast results.

4.6.2 Examination of the forecast impacts

The accuracy of bore-initiated convection depends on the representation of the explicitly resolved bore as well as the ambient environment ahead of it. Verification results presented so far indicate that the assimilation of PECAN profilers affects both of these factors. By generating composite cross sections near the region of bore-initiated convection (aqua dots in Fig. 4.4c), this section seeks to establish a link between the skill of the convective forecasts and the PECAN impacts discussed in Sections 4.5.2 and 4.6.2. Similar to Section 4.4, the analysis herein focuses on the AERI and WIND_PROF experiments since they produce the largest deviations from the control forecasts.

It is clear from Figs. 4.19a,d,g that the explicitly resolved bores simulated in the three experiments differ from each other. Consistent with the verification results in Section 4.5, the post-bore height (h_1) is higher in AERI, and lower in WIND_PROF, than in BASELINE. Changes in the ambient moisture environment also align with the verification results from the previous section. For example, the AERI experiment leads to a significant increase in mixing ratio (M_v) that reaches nearly 2 gkg^{-1} in the 3-3.5 km AGL layer (Fig. 4.19d). As a result, the elevated CAPE in this experiment increases by 100-500 Jkg^{-1} (Fig. 4.19e). Combined with a more pronounced bore lifting and nearly neutral changes in the elevated CIN values (Fig. 4.19f), conditions in AERI become favourable for the development of stronger and longer-lived bore convection. By contrast, the slight decrease of moisture in WIND_PROF (~0.2-0.3 gkg^{-1} at 3-3.5 km; Fig. 4.19g) tends to lower CAPE by ~100 Jkg^{-1}

(Fig. 4.19h) and, together with a slight reduction in the amount of bore lifting (Fig. 4.19g), results in a lower probability of bore-initiated convection (Figs. 4.17d-f).

The analysis presented so far serves as a good example of how the assimilated profiling instruments lead to multi-scale forecast impacts. The moisture perturbations in AERI and WIND_PROF affect the quality of the convective forecasts by simultaneously modifying the elevated instability in the ambient environment and changing the height of the explicitly resolved bore.

4.7 Summary

Recent studies have suggested that bores are an inherent component of the nocturnal environment over the Great Plains (Geerts et al. 2017; Haghi et al. 2017), capable of maintaining ongoing nocturnal convection by destabilizing broad regions in their wake (Parsons et al. 2019a), and initiating deep convection on their own (Parker 2008; Grasmick et al. 2018). Despite the growing need to adequately represent bores in NWP models, capturing their initiation and evolution depends on the ability of these models to accurately simulate a wide range of multiscale processes, such as the formation of cold pools from late afternoon/early evening convection as well as the simultaneous development of a stable boundary layer and a low-level jet in the nocturnal environment. Since the individual modelling of these processes is already a difficult task on its own (e.g., Weisman et al. 2008), prediction of bore-driven nocturnal convection poses significant challenges to current convective-scale NWP models. One of the possible ways to reduce errors associated with these processes is by improving the model's initial conditions in a carefully designed multi-scale data assimilation system. The present article represents the first attempt to address this idea by assimilating novel kinematic and thermodynamic profilers deployed during the 2015 PECAN campaign. Using data from the 6 July 2015 PECAN case study, we try to understand whether the initial conditions obtained after assimilating these PECAN profilers can improve various aspects of the bore-driven nocturnal convection, including (i)

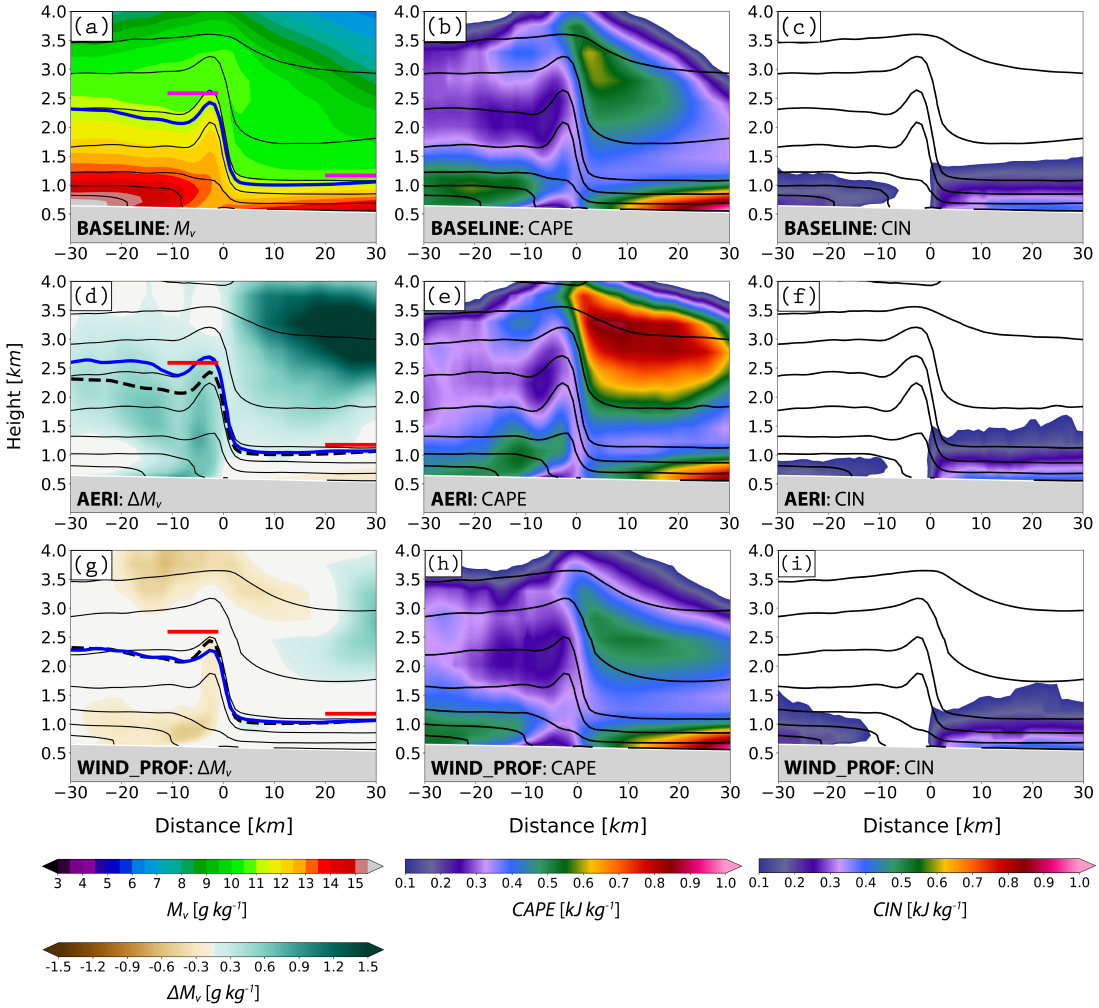

Figure 4.19: Composite cross sections for the BASELINE, AERI and WIND_PROF experiments generated in the neighborhood of the southern convective cluster (*S*; refer to the aqua reference points in Fig. 4.4). The first column shows the distribution of moisture from these three experiments (mixing ratio for BASELINE and differences in mixing ratio for AERI and WIND_PROF). The SBL height (based on the 11.25 gkg^{-1} mixing ratio value) is plotted either with a heavy solid blue curve for individual experiments or with a heavy dashed black curve for the BASELINE experiment in panels (d) and (g). The pre- and post-bore heights from UWKA I6 are overlaid as heavy horizontal magenta lines. The color shading in the second and third columns shows the composite CAPE and CIN fields for the three experiments. Virtual potential temperature is plotted in all panels with solid black contours.

Table 4.7: Summary of the key PECAN impacts for the 6 July 2015 case study. The upward- and downward-pointing arrows correspond to positive and negative forecast impacts with respect to BASELINE, while the neutral forecast impacts are denoted with a dash. The number of arrows in each of the three forecast categories provides a subjective ordering of the data assimilation experiments according to the magnitude of their impacts.

Experiment	**Bore Environment**	**Explicitly Resolved Bore**		**Bore-Initiated Convection**
		UWKA I2	UWKA I6	
PECAN_ALL	↑↑	mixed	↓	mixed
AERI	-	↓↓	↑	↑↑
AIRCRAFT	-	↓	-	-
WIND_PROF	↑	↑	↓↓	↓
LIDAR_VAD	↑↑	-	-	-
RADIOSONDE	↑↑	-	-	↑
SURFACE	↑	↓	-	-

the environment in which the bore develops, (ii) the characteristics of the explicitly resolved bore, and (iii) the accuracy of the convective forecasts.

For the reader's convenience, Table 4.7 presents a summary of all forecast impacts discussed throughout Chapter 4. The verification statistics outlined in Table 4.7 suggest that the clearest impacts from assimilating PECAN data refer to the numerically simulated bore environment where nearly all observation types improve the forecasted flow regime. Section 4.4.3 demonstrates that these improvements arise from a better representation of the low-level jet that interacts with the bore-generating cold pool.

By contrast, the PECAN impacts on the explicitly resolved bore and bore-initiated convection appear to be mixed and largely dependent on the chosen verification time. For example, while the AERI experiment produces a large positive bias in the predicted bore height early in the forecasts, it also provides the closest match to the verifying UWKA retrievals around the time of convection initiation. Combined with a better depiction of the moisture content in the ambient environment, the AERI experiment provides the best forecast of the observed bore-initiated convection. These mixed forecast impacts can be explained by the fact that bores and bore-initiated convection are associated with motions that act on very small spatiotemporal scales. The parameterization of these subgrid-scale processes inevitably leads to model errors and may even mask any benefits brought by the assimilation of high-frequency PECAN profilers. Although the assimilation of thermodynamic and

kinematic remote sensors appears to be beneficial for the prediction of nocturnal convection in NWP models, there are still a lot of open research questions. One of the them concerns the optimal design of a profiler network. Even though our findings highlight the advantages of assimilating high-frequency profiler data, more work still needs to be done in order to determine the optimal spacing between profiling instruments. In addition, the relative merits of assimilating collocated thermodynamic and kinematic profilers need to be better understood. Past Observation System Simulation Experiments (OSSEs) have reported benefits from such an observation design (e.g., Hartung et al. 2011), but the results from this study suggest that the simultaneous assimilation of kinematic and thermodynamic profilers often leads to mixed forecast results. Therefore, one of the goals of future research should be to determine effective ways of combining the information from collocated profiling instruments. A systematic data impact study featuring 10 bore IOPs from the PECAN field campaign is currently underway to provide more insight into this question and generalize the findings of this chapter.

Chapter 5

The value of assimilating different ground-based profiling networks on the forecasts of bore-generating nocturnal convection

5.1 Introduction

The Planetary Boundary Layer (PBL) has crucial implications for many Earth system processes, such as radiative transfer, air pollution and land-atmosphere exchanges (Wulfmeyer et al. 2015). But compared to other parts of the atmosphere, the PBL is characterized by considerably smaller spatiotemporal scales, especially with respect to water-related variables (Lilly and Perkey 1976). Therefore, to adequately describe the inherently large variability within the PBL, we require a dense observing network that can frequently sample the thermodynamic and kinematic properties of the lower atmosphere.

Despite its significance, the PBL is poorly observed by the current observing systems. This fact became first apparent in early studies of convection initiation. For example, Crook (1996) used a high-resolution, non-hydrostatic model to show that small changes in the PBL structure, which are comparable in magnitude to typical measurement uncertainties, "can make the difference between no initiation and intense convection". Similarly, Weckwerth et al. (1996) found that there is large moisture variability within daytime PBLs ($1.5 - 2.5$ g kg^{-1}) and concluded that water vapor is undersampled by traditional observation techniques (see

also Weckwerth and Parsons 2006). Having realized these limitations, the National Research Council (NRC) developed a comprehensive report in 2009 which proposed the establishment of 400 sites with ground-based remote sensors (NRC 2009). These recommendations were further refined in subsequent NRC reports (NRC 2010, 2012) and recently updated by the World Meteorological Organization (WMO 2018) to address the needs of future high-resolution NWP systems.

Importantly, the growing awareness of the PBL's observation gap catalyzed research efforts aimed at examining the ability of various ground-based remote sensors to improve the regional NWP performance. At the very beginning, the technology underpinning thermodynamic remote sensors was still not sufficiently well developed and most of the original investigations were conducted with the more widely available radar wind profiler (RWP). After several studies demonstrated the short-range forecast value coming from the National Oceanic and Atmospheric Administration (NOAA) Profiler Network (NPN), some of the leading NWP centers decided to start assimilating these novel wind datasets (Bouttier 2001; Benjamin et al. 2004). Recently, experiments have also been conducted with another kinematic profiler – the Doppler wind lidar (DWL), whose ability to capture some of the fine-scale features in the wind field makes it particularly suitable for high-resolution applications. The forecast potential of DWL retrievals was first demonstrated in Zhang and Pu (2011) on a warm-season mesoscale convective system (MCS). Kawabata et al. (2014) confirmed the forecast value of this instrument, but also discussed the important synergy between lidar and radar observations in improving the overall convective skill.

The microwave radiometer (MWR) was the first thermodynamic remote sensor to be used for NWP purposes, including fog forecasting (Vandenberghe and Ware 2002) and 1D-Var retrievals (Martinet et al. 2015, 2017). Although its ability to operate under all-sky conditions is an important advantage, the vertical resolution of the MWR (300-1000m in the first 2km above the ground) is too coarse for most contemporary convection-allowing models. As a result, most recent impact studies have focused on exploring the advantages

of another passive thermodynamic remote sensor – the Atmospheric Emitted Radiance Interferometer (AERI; Revercomb et al. 1988; Feltz et al. 2003; Knuteson et al. 2004a,b; Turner and Löhnert 2014), and have demonstrated that its assimilation can be beneficial for a variety of convective applications (Coniglio et al. 2019; Hu et al. 2019; Chipilski et al. 2020; Degelia et al. 2020; Lewis et al. 2020). Concurrently, the past decade has also seen advances in active thermodynamic sensing. Instruments such as the Raman lidar (RL; Melfi and Whiteman 1985; Melfi et al. 1989; Wandinger 2005; Dai et al. 2018) and the differential absorption lidar (DIAL; Browell et al. 1998; Weckwerth et al. 2016) have been crucial in improving our understanding of near-surface Earth system processes (Wulfmeyer et al. 2015, and references therein). Research-grade RLs have also been found to improve the simulated PBL structure (Adam et al. 2016) as well as the ability of regional NWP models to predict heavy precipitation (Leuenberger et al. 2020; Yoshida et al. 2020).

In this Chapter, we will provide more evidence about the NWP value of ground-based remote sensing by demonstrating its systematic benefits on the relatively newly studied problem of *bore-generating nocturnal convection* (Haghi et al. 2018; Parsons et al. 2019a). This goal will be achieved by using 10 diverse cases from the Plains Elevated Convection at Night (PECAN; Geerts et al. 2017) field campaign. Many of these cases have been already examined as part of recent publications (Mueller et al. 2017; Trier et al. 2017; Johnson et al. 2018; Johnson and Wang 2019; Smith et al. 2019; Miller et al. 2020; Parker et al. 2020; Stechman et al. 2020; Carroll et al. 2021; Lin et al. 2021), giving us an important context for discussing our results. Crucially, the forecast impacts presented here will confirm and further generalize some of the positive single case findings of Chipilski et al. (2020; CWP20 hereafter), which is highly encouraging on account of the wide spectrum of atmospheric bores and convective environments sampled in our dataset.

By further refining the experimental design of CWP20, the second goal of this study would be to compare the relative merits of different ground-based profiling networks. The motivation here is that most research in the past has focused on the assimilation of single

remote sensors that only measure the thermodynamic or kinematic components of the unknown model state (e.g., Lewis et al. 2020; Li et al. 2020; Yoshida et al. 2020; Wang et al. 2020; Leuenberger et al. 2020; Qi et al. 2021). While several studies have attempted to simultaneously assimilate multiple profiling instruments, they have reached somewhat inconsistent conclusions. For instance, Hu et al. (2019) found AERIs to be more important than DWLs in improving the early evolution of a tornadic supercell. At the same time, the study of Fourrië et al. (2021) indicated that RWPs outperform RLs in forecasting heavy precipitation events. A careful look at the present literature also reveals that even fewer studies have attempted to evaluate the performance of remote sensors against a reference radiosonde network. Throughout this work, we will demonstrate that the impacts from assimilating thermodynamic and kinematic remote sensors are highly flow-dependent and their combination is often necessary for achieving a statistically meaningful increase in the forecast skill. We will also present evidence that the most robust forecast benefits come from hybrid ground-based networks that host both in situ and remote sensing profilers.

The remainder of this Chapter is organized as follows: Section 5.2 offers a schematic illustration of our problem by showing the typical evolution of bore-generating nocturnal convection in the context of the assimilated ground-based profiling networks. Section 5.3 gives more details about the underlying experimental design, system configurations and available PECAN observations. Aggregated verification statistics associated with the parent MCSs and explicitly resolved bores are presented in Section 5.4, while Section 5.5 offers an interpretation of our main findings based on 3 representative cases. Finally, we conclude with a brief summary, a critical discussion and future outlooks in Section 5.6.

5.2 Problem statement

Throughout this study, we will be concerned with the forecast accuracy of a particular class of nocturnal convection – one associated with the generation of atmospheric bores (*bore-generating nocturnal convection* hereafter). Our interest in these convective systems

is motivated by their common occurrence during the night (Haghi et al. 2017) and inherently low predictability (see Section 1 of CWP20). Fig. 5.1 illustrates the typical evolution of bore-generating nocturnal convection within the 10 PECAN cases used in this study. Our data assimilation (DA) period usually covers the time from the initial formation of small convective cells (Fig. 5.1a) to their upscale growth and eventual merging into a mesoscale convective system (MCS) with a well-developed surface-based cold pool (Fig. 5.1b). Note that while surface-based cold pools do not necessarily form in all nocturnal MCSs (e.g., Maddox 1980; Trier and Parsons 1993), they were found to be a ubiquitous feature during the PECAN field campaign (Hitchcock et al. 2019) and an important precursor for the initiation of bores in our experiments.

A critical requirement for our case study selection was the presence of ground-based profilers upstream of the convective developments shown in Figs. 5.1a and 5.1b. Because of this strategic deployment, the PECAN instruments provided valuable information about the mesoscale environment in which the bore-generating convective systems developed. Therefore, it was expected that the assimilation of these PECAN observations will also bring measurable forecast improvements. Our dynamically relevant DA period attempts to evaluate this hypothesis in a more controlled manner: by ensuring that the model initial conditions feature a mature MCS with a well-developed cold pool, we know that the future convective evolution will be mostly driven by the characteristics of the environment in which it propagates. By contrast, if the forecasts were to be initialized earlier (e.g., during the process of upscale convective growth), the subsequent MCS changes will be highly sensitive to the exact precipitation history of the system (Parker et al. 2020; Parker 2021), making it challenging to quantify how different environmental conditions affect the forecasts.

Once the DA period finishes, the bore-generating MCS is forecasted for another 5 hours. During this time, the interaction between its cold pool and the nocturnal PBL generates a hydraulic response in the form of an atmospheric bore (Fig. 5.1c). In some our PECAN cases, the bore remained closely attached to its parent MCS and was responsible for the initiation

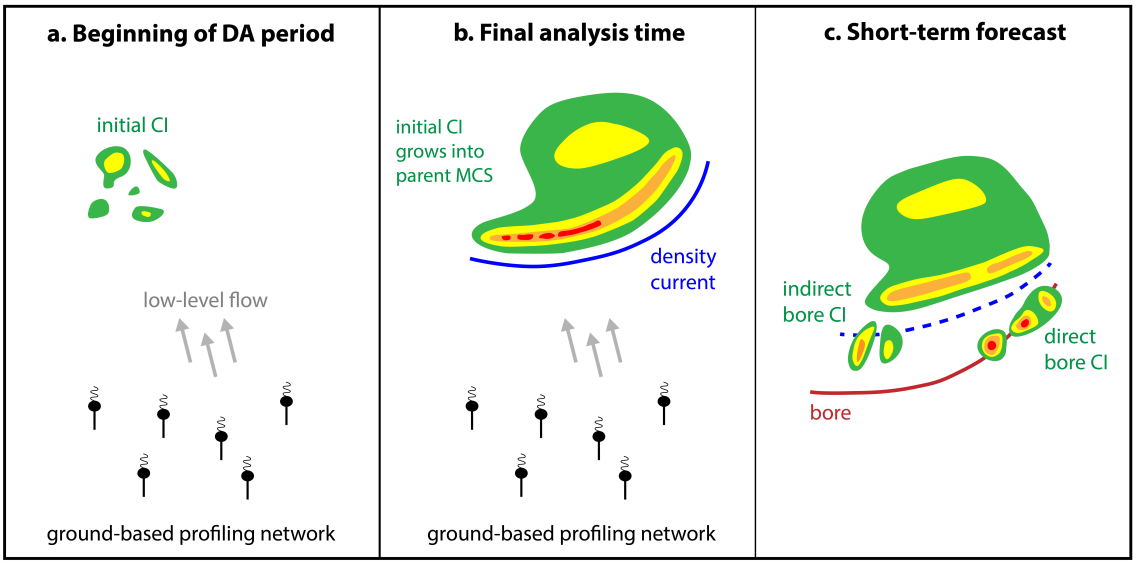

Figure 5.1: A schematic illustrating the typical evolution of a bore-generating convective system in the context of the ground-based profiling instruments assimilated in this study. Our main objective is to evaluate the impact of the assimilated profilers on the forecasted parent MCS, bore-induced convection initiation (CI; both direct and indirect) and explicitly resolved atmospheric bore (all shown in panel c).

of new convection (i.e., bore-initiated convection), whereas in other cases it propagated far away from its source region and did not produce any additional convective activity. To account for this inherent dynamical coupling, we adopt a verification approach that is similar to CWP20 in that the impact from different profiling instruments is examined according to their ability to improve both the convective and bore components of the nocturnal system depicted in Fig. 5.1c [1].

5.3 Experimental design

To better understand the synergies between different ground-based profiling networks, we refine the experimental design of CWP20 such that only sites with collocated radiosondes and remote sensing instruments are assimilated. This approach is similar to Degelia et al. (2020)

[1] The main difference with CWP20 is that we verify over both the parent MCS and any bore-initiated convection, whereas CWP20 only focused on the forecast skill of the latter.

with the exception that our control experiments do not assimilate any PECAN soundings. The rationale behind this choice is that the PECAN radiosondes are released at a much higher frequency compared to the operational radiosonde network, meaning that they can no longer be treated as a conventional data source. Degelia et al. (2020) sidestep this problem by only assimilating observations close to the operational 00 UTC launch; in our case, all available radiosondes are assimilated and subsequently treated as a reference against which the performance of ground-based remote sensors can be evaluated.

Our observation network with collocated in situ and remote sensing instruments serves two distinct purposes. First, it allows us to compare the impacts of remote sensors and radiosondes in a more objective way in which the increased (or decreased) sensitivity of the forecasts to the initial conditions in different parts of the model domain is implicitly accounted for. Given that the assimilated PECAN instruments observe the environmental conditions over the same location, it follows that differences in their performance can be solely attributed to the underlying measurement technique, sampling rate and observation error characteristics. The second advantage of assimilating collocated instruments is that we can explore the benefits of several different ground-based observation networks by seeking answers to the following critically relevant questions:

- Is it more beneficial to assimilate the highly frequent, but less accurate remote sensing retrievals than the less frequent, but highly accurate radiosonde measurements?
- How competitive is the performance of networks that consist of single remote sensors compared to networks which host both thermodynamic and kinematic profilers? Do the added benefits of such combined remote sensing networks justify the additional expenses for their initial deployment and subsequent maintenance?
- Do we notice any observation synergies after combining (i) thermodynamic and kinematic profilers or (ii) remote sensing and in situ instruments? In other words, does the simultaneous assimilation of these instruments result in forecast improvements which are visibly larger than the forecast improvements brought by individual instruments?

Table 5.1: List of WRF physics options.

Parameterization	Scheme	Reference
Microphysics (EnKF cycling)	WRF single-moment 6-class (WSM6)	Hong and Lim (2006)
Microphysics (forecast)	Thompson	Thompson et al. (2008)
Planetary Boundary Layer and Surface Layer	Mellor-Yamada-Nakanishi-Niino (MYNN)	Nakanishi and Niino (2006)
Land surface	Unified Noah Land Surface Model	Tewari et al. (2004)
Longwave radiation	Rapid Radiative Transfer Model for General Circulation Models (RRTMG)	Iacono et al. (2008)
Shortwave radiation	Goddard Shortwave	Chou and Suarez (1994)
Cumulus (d01 domain only)	Kain-Fritsch, Grell-Freitas Ensemble and Grell 3D Ensemble	Kain (2004) Grell and Freitas (2014) Grell and Devenyi (2002)

- Does the forecast value of different ground-based profiling networks depend on the inherent predictability of the atmospheric flow?

5.3.1 System configurations

The impact results presented here were obtained with the same GSI-EnKF-WRF ensemble data assimilation and forecast system as described in CWP20. However, the systematic nature of our PECAN experiments necessitated several minor changes in its configuration. Most notably, simulations were carried out on two (instead of three) model domains – an outer (d01) 12-km one and an inner (d02) 4-km one. The size of the d02 domains was the same for all 10 cases (352 by 301 grid points), but their position (see gray rectangles in Fig. 5.2) was modified according to the location of the bore-generating convective systems. The model physics were chosen to be broadly consistent with CWP20, with the exception of several minor changes, which can be identified by comparing Table 5.1 to Table 2 in CWP20.

All experiments were initialized by downscaling the 00 UTC global GEFS/SREF ensemble (40 members in total) valid on the day before each bore-generating MCS event (see Fig. 5.2c). Conventional observations from the North American Mesoscale Forecast System Data Assimilation System (NDAS) were then assimilated every 3 hours for a total of 8 cycles. Afterwards, much more frequent EnKF cycling was carried out on the inner 4-km domain where conventional observations were assimilated together with radar data

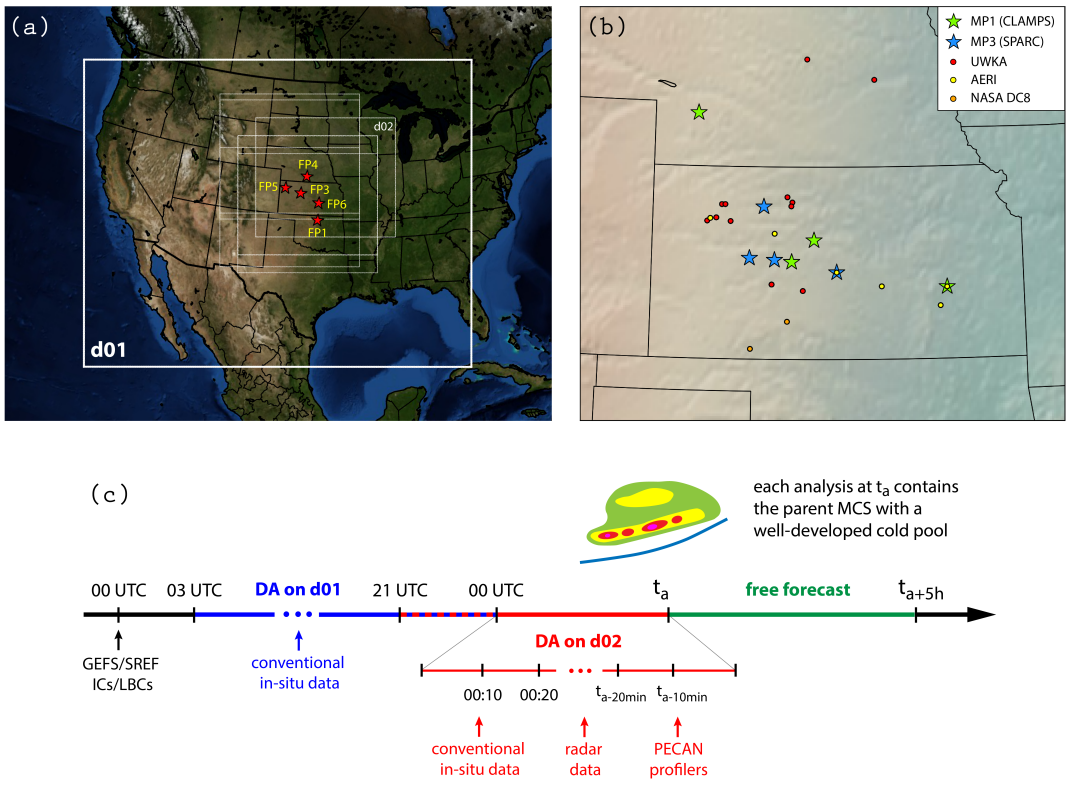

Figure 5.2: Some aspects of the experimental design used in this study. *Panel a*: Location of the outer 12-km (d01; thick white rectangle) and inner 4-km (d02; thinner white rectangles) model domains as well as the assimilated fixed PISA (FP) sites (red stars). *Panel b*: Location of the assimilated mobile PISAs (MPs) (filled stars) and thermodynamic remote sensors used for bore verification (filled dots). *Panel c*: A timeline corresponding to our analysis-forecast system. Following Section 5.2, the final analysis time in each PECAN case (t_a) is chosen such that the bore-generating (parent) MCS has a well-developed cold pool. The alternating red and blue lines between 21 UTC and 00 UTC indicate that the d02 EnKF cycling can begin at either of these two times (see main text for more details).

Table 5.2: EnKF cycling period and assimilated PISA sites for the 10 PECAN cases used in this study. The numbers in the last 7 columns of the table indicate how many radiosondes were launched at each of the assimilated PISA site.

Case	EnKF cycling on the d02 domain		Assimilated PISA sites						
	start	end	FP1	FP3	FP4	FP5	FP6	MP1	MP3
5 June 2015	0000 UTC on 5 June	0430 UTC on 5 June	x	1	1	x	x	x	x
6 June 2015	0000 UTC on 6 June	0330 UTC on 6 June	x	1	1	x	x	x	1
7 June 2015	2100 UTC on 6 June	0200 UTC on 7 June	1	x	x	x	x	x	x
20 June 2015	0000 UTC on 20 June	0700 UTC on 20 June	x	13	4	x	x	4	5
26 June 2015	0000 UTC on 26 June	0300 UTC on 26 June	x	2	x	2	x	1	x
2 July 2015	0000 UTC on 2 July	0300 UTC on 2 July	x	1	1	1	x	x	x
5 July 2015	0000 UTC on 5 July	0500 UTC on 5 July	x	2	2	x	2	2	x
11 July 2015	0000 UTC on 11 July	0600 UTC on 11 July	x	4	4	4	5	3	3
14 July 2015	0000 UTC on 14 July	0300 UTC on 14 July	x	2	2	2	2	x	x
16 July 2015	0000 UTC on 16 July	0230 UTC on 16 July	x	3	3	2	3	x	2

and PECAN ground-based profilers at 10-min intervals. As explained in Section 5.2, the length of the inner DA window was dependent on the convective evolution in each case, but varied between 2.5 hours on 16 July 2015 to 7 hours on 20 June 2015 (see Table 5.2 for more details). For the majority of the PECAN cases, the d02 EnKF cycling started at 00 UTC on the day of the bore-generating MCS event; one exception to this setup, however, was the 7 June 2015 case where the 4-km DA period began 3 hours earlier to account for the early convective initiation on that day.

5.3.2 PECAN observations

The PECAN profiling observations assimilated in our experiments were obtained from 6 fixed and 2 mobile PECAN Integrated Sounding Arrays (PISAs), whose location relative to the inner (d02) WRF domains is indicated in Figs. 5.2a and 5.2b. These PISAs were a unique aspect of the PECAN field campaign as they hosted both in situ and remote sensing instruments. Analogous to CWP20, AERI was the only thermodynamic profiler assimilated in our study, whereas the RWPs and DWLs were blended into a single kinematic profiler following Degelia et al. (2020).

The number of PISA sites available for each case was determined based on the overall availability of PECAN radiosonde data. Specifically, a certain PISA site was assimilated in our experiments only if there was at least one radiosonde release during the selected

DA period. As a result of this restriction, the number of assimilated stations was usually reduced to 3 or 4 (see Table 5.2). At each of the assimilated PISA sites, the typical number of radiosonde launches was between 3 and 5, although on one occasion (20 June 2015), the FP3 site released a total of 13 radiosondes over the 7-hour DA period.

5.3.3 Experiments

To examine the value of different ground-based profiling networks, we adopted a data addition framework whereby each new PECAN instrument was added on top of operationally assimilated NDAS data. Our first group of experiments only considered single instrument types: SONDE assimilated the special PECAN radiosondes, TQPROF – the thermodynamic AERI retrievals, while UVPROF – the wind retrievals from the combined DWL and RWP instruments. By contrast, our second group of experiments sought to explore the value of assimilating multiple profilers and to identify the existence of any synergies between them. For instance, ALLPROF combined the two ground-based remote sensors, whereas ALL considered all available PECAN observations for a given case. The performance of these 5 ground-based profiling networks was then compared against a control (CTL) experiment in which only conventional NDAS data were assimilated.

5.4 Results

5.4.1 Convective impacts

5.4.1.1 Aggregated statistics

We first assess the impact of assimilating different ground-based profilers on the quality of the convective forecasts. For each of the 10 cases, we compute the Fractions Skill Score (FSS) based on the Neighborhood Ensemble Probability (NEP) of radar reflectivity exceeding 30 dBZ and the merged composite reflectivity product from the Multi-Radar Multi-Sensor

(MRMS; Zhang et al. 2016a) program. These scores are evaluated at 15-min increments within a verification domain centered over the bore-generating MCS.

Fig. 5.3 displays the aggregated FSSs for 3 different neighborhood radii (R) – 5 km, 25 km and 150 km. Each of these scores carries a different physical meaning. For example, the smallest R value is comparable to the model's horizontal grid spacing, in which case the FSSs provide a nearly point-wise measure of the convective skill. The intermediate R value is commensurate with the smallest scales resolved by the model ($\sim 8\Delta x$), whereas the largest one is located toward the upper end of the meso-β spectrum, making it comparable to the characteristic scale of large density currents and bores (Zuidema et al. 2017). As expected, the FSSs increase with R for a given lead time, reflecting correctly the higher predictability of larger scales. On average, the experimental differences persist for ~2 hours, although this tends to be slightly longer as R increases.

Regardless of the chosen verification scale, the ALL experiment provides the best forecast performance, with the FSS differences being statistically significant at smaller R and when the forecast lead time is between 1 and 2 hours. Given that the forecast skill at these smaller scales is completely lost toward the end of the 5-hour forecasting window [2], our verification statistics indicate that the analysis benefits brought by ALL last for more than 30% of the typical convective predictability timescale experienced by CTL. Another interesting aspect of these aggregated statistics is the similarity of the FSSs at the start of the forecasting period – a result which is opposite to some of the findings reported in Degelia et al. (2020) (e.g., see their Fig. 4). The comparable short-term performance of CTL and ALL in our study implies that the environmental perturbations brought by the assimilation of PECAN profilers need to first experience additional growth before they affect the subsequent convective evolution.

Some marginal improvements are also observed with respect to the ALLPROF experiment, but they are considerably smaller and much shorter-lived. We further note that while the

[2] The loss of convective skill is evident in the small FSS changes at the end of the forecasting window. Error saturation for $R = 5$ km, for instance, occurs when the lead time is 4.5 hours.

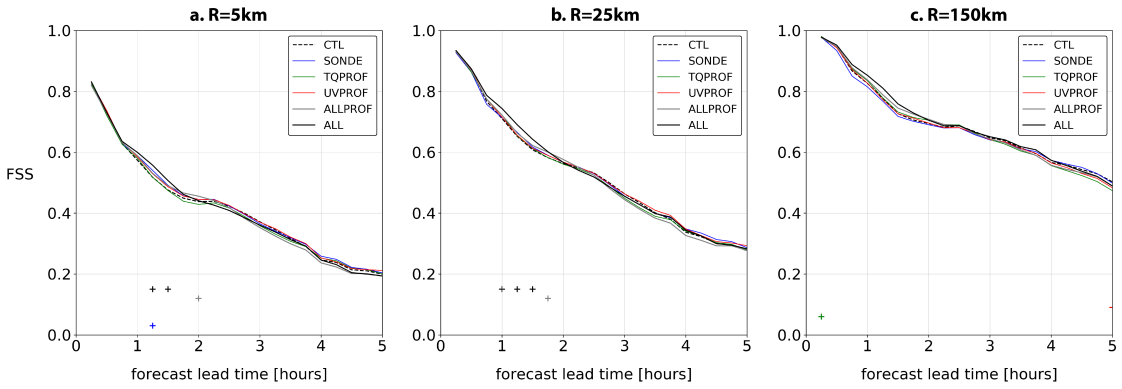

Figure 5.3: Fractions skill scores (FSSs) averaged over the 10 PECAN cases and calculated for 3 different neighborhood radii (5, 25 and 150 km). The markers at the bottom of each panel indicate whether the FSS differences between a given PECAN experiment and CTL are statistically significant at the $\alpha = 0.01$ level, as determined by a bootstrap method with 10,000 resamples. The + and – symbols differentiate between positive and negative impacts, respectively.

most pronounced ALLPROF benefits occur at $R = 150$ km (where ALLPROF is nearly as skillful as the best performing ALL experiment), the FSS changes at this verification radius are not statistically significant.

The impacts from single profiler experiments (SONDE, TQPROF and UVPROF) are generally smaller than both ALL and ALLPROF. In addition, the verification statistics here are sensitive to the chosen verification radius: even though the 3 single profiler experiments generally improve upon the CTL skill scores at $R = 5$ km (especially SONDE), the forecast impacts at larger R values become neutral or even slightly negative.

5.4.1.2 Dependence of the forecast impacts on the convective predictability

One of the most interesting characteristics of this systematic study was the strong variability of the overall convective skill. To understand how this variability modulated the average observation impacts discussed so far, the 10 PECAN cases were split into 3 predictability categories based on the 2-hour FSS in the CTL experiment (see Fig. 5.4). The choice of this specific lead time was motivated by our observation that the least predictable PECAN cases (LP category; 5 July, 11 July and 14 July) tended to completely lose their

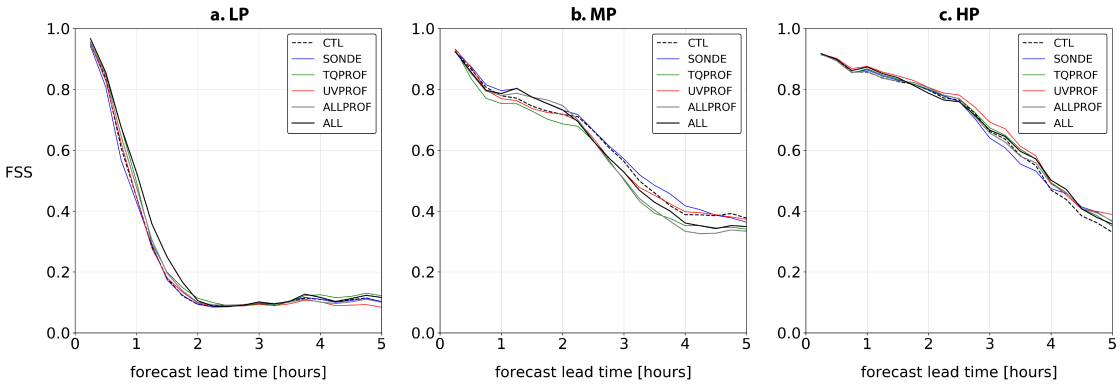

Figure 5.4: As in Fig. 5.3, but the FSSs here are conditioned on the 3 predictability categories (LP, MP and HP; see main text for more details) and are only shown for $R = 25$ km. Note that statistical significance has not been tested here due to the small number of cases in each predictability category.

convective skill 2 hours into the forecast. In addition, this predictability definition is consistent with the average longevity of the experimental differences in the aggregated FSS statistics (see Fig. 5.3).

The FSS behaviour in the other 2 predictability categories – medium (MP; 5 June, 26 June and 16 July) and high (HP; 6 June, 7 June, 20 June and 2 July), was fairly similar, although the experimental differences in the HP cases become visible only after the 2nd forecast hour. It is also interesting to note that while the 20 June simulations were the most skillful ones across our entire PECAN dataset, the parent convective system from this case has been previously found to incite significant errors in a global NWP model (Parsons et al. 2019b). The aforementioned discrepancy with our results ultimately suggests that even small errors on the convective scale can sometimes interact with the large-scale flow and limit the overall atmospheric predictability.

Similar to the average FSS results, ALL remains the best performing experiment in the LP category (Fig. 5.4a): the peak differences with CTL reach 0.1 and translate to 15 min of additional convective predictability. The largest contributions to these improvements come from TQPROF, though its impacts are much shorter-lived. We also notice that the skill of ALLPROF is bounded by TQPROF and UVPROF, suggesting that the thermodynamic and

kinematic remote sensors do not provide synergistic information. This is to be contrasted with the visible improvements in ALL which differs from ALLPROF only due to the additionally assimilated PECAN radiosondes.

In comparison to the LP category, the MP verification statistics are much more difficult to interpret. Beyond 2 hours of forecast lead time, for example, we observe that the impacts from TQPROF and UVPROF are consistently negative. Nevertheless, the forecast impacts for such long periods of time should be interpreted with extra caution; this is because the highly nonlinear convective evolution in our forecasts makes it increasingly difficult to establish a link between the observed experimental differences and the analysis changes brought by the assimilation of certain profilers. During the first 2 hours, when the effect of such model nonlinearities is less pronounced, the single remote sensors still degrade the forecasts, but their combined assimilation in ALLPROF leads to a visible gain in the convective skill. Given that competitive short-term forecasts are also produced by SONDE, we can conclude that the simultaneous assimilation of mass and wind observations is a critical aspect in these MP cases.

As discussed earlier, the experimental differences in the HP category are most prominent beyond the first 2 hours of model integration. Except from SONDE, consistent improvements appear in all other PECAN experiments, which suggests that ground-based remote sensors are quite effective in this predictability regime. In contrast to the LP category, however, UVPROF performs better than TQPROF; in fact, UVPROF is the most skillful PECAN experiment, which implies that the two combined profiling networks (ALLPROF or ALLPROF) are not synergistic in nature.

A concise summary of the main convective impacts is given by the violin plots in Fig. 5.5. The color shaded distributions in each panel show how the FSS differences change according to the underlying convective predictability. We first notice that the interquartile ranges (IQRs) associated with the best performing LP and HP experiments (ALL and UVPROF, respectively) lie entirely above 0, which in turn indicates that the forecast improvements in

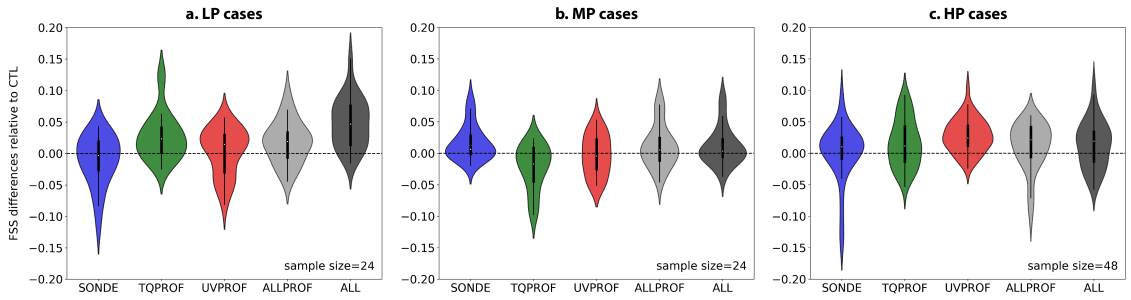

Figure 5.5: Violin plots showing the predictability-dependent FSS differences between the 5 PECAN experiments and CTL. The LP and MP cases combine all FSS differences during the first 2 hours, whereas the HP category only considers FSS differences with lead times between 2 and 5 hours.

this predictability category are statistically robust. It is also evident that the variability of the forecast impacts is highly dependent on the type of assimilated ground-based network. This effect is most pronounced in the HP regime where the distribution spread associated with the best performing UVPROF experiment is much smaller compared to SONDE. Finally, the striking similarity between the SONDE, ALLPROF and ALL violins in the MP category (Fig. 5.5b) reaffirms our earlier conclusions regarding the importance of simultaneously observing the thermodynamic and kinematic components of the model state.

5.4.2 Bore impacts

5.4.2.1 Verification methodology

Atmospheric bores are particularly challenging to identify and track in view of their complex dynamical footprint on several meteorological variables. Although NWP-based algorithms have been proposed in the past (Chipilski et al. 2018), the objective detection of bores in observational datasets remains elusive. In spite of these limitations, our study attempts to provide a comprehensive assessment of how the assimilation of different ground-based profilers affects the forecast skill of explicitly resolved bores. Toward this end, ensemble mean forecasts from all PECAN experiments are verified in two different ways. Similar to Geerts et al. (2017) (see their Fig. 8), we first examine the spatial representation of

bores by comparing model fields of vertical velocity at 1 km AGL ($w_{1\text{km}}$) against the position of fine lines in low-level reflectivity data. This methodology is similar to the one utilized in Wilson and Roberts (2006) and aims to examine the realism of various bore attributes, including position, extent and propagation direction.

Our second verification method examines the extent to which the ensemble mean forecasts are able to accurately simulate the amount of bore lifting (Δh), i.e. the difference between the post- and pre-bore PBL heights. The choice of this metric is motivated by its relevance to the initiation and maintenance of nocturnal convection: a larger Δh value translates to more pronounced mechanical lifting at the leading edge of the bore, which in turn creates more favorable conditions for air parcels to reach their level of free convection. To estimate Δh, we follow Chipilski et al. (2018) and search for the water vapor mixing ratio (q) or virtual potential temperature (θ_v) contour that exhibits the largest vertical displacement near the ground. Together with the University of Wisconsin King Air (UWKA) moisture retrievals used in CWP20, the present bore verification dataset features additional thermodynamic profiles from ground-based AERI sites as well as moisture retrievals from the National Aeronautics and Space Administration (NASA) DC-8 aircraft. All 20 Δh measurements (see filled circles in Fig. 5.2) are then compared to model-derived Δh estimates obtained by constructing vertical cross-sections in proximity to the observed bore locations.

5.4.2.2 Spatial impacts

Analysis of $w_{1\text{km}}$ fields revealed that bores were successfully forecasted in all 10 PECAN cases, which confirms the suitability of our chosen model initialization times. In terms of the CTL experiment, our summary in Table 5.3 indicates that the spatial structure of the simulated bores was consistent with the verifying radar observations in 4 out of the 10 cases. For the remaining 6 cases, the most common forecast issues pertained to the *maintenance* and *extent* of the predicted bores. Interestingly, these problems occurred most frequently in the LP regime where the parent MCSs also dissipated too quickly. This close relationship

Table 5.3: Subjective evaluation of the forecast impacts pertaining to the spatial characteristics of the explicitly resolved bores; the + and − symbols denote positive and negative impacts, respectively. Some of the entries in the last column contain the word *synergy*, which indicates that the positive impacts in ALLPROF and/or ALL exceed those caused by the assimilation of single profiling instruments.

Case	CTL forecast problems	Impacts in ALLPROF and ALL	Contribution from individual instruments
5 June 2015	orientation	+ in both	+ from TQPROF and UVPROF; synergy
6 June 2015	orientation, higher speed	+ in ALLPROF and - in ALL	+ from TQPROF and UVPROF; synergy
7 June 2015	smaller extent	- in ALLPROF and + in ALL	+ from SONDE and − from TQPROF; synergy
20 June 2015	no	no	N/A
26 June 2015	no	no	N/A
2 July 2015	no	no	N/A
5 July 2015	maintenance, smaller extent	+ (extent) in both	+ from TQPROF; synergy (only in ALL)
11 July 2015	maintenance, smaller extent	+ (maintenance) in ALLPROF and + (maintenance, extent) in ALL	+ from all; synergy
14 July 2015	maintenance	+ in both	+ from TQPROF
16 July 2015	no	no	N/A

between the forecast skills of the bore and its parent MCS has a clear dynamical explanation; namely, the premature dissipation of the parent MCS leads to a weaker and shorter-lived cold pool that is in turn not capable of sustaining upstream-propagating disturbances for a very long time (see Section 7 of White and Helfrich 2012). In the majority of these situations, the assimilation of ground-based profilers resulted in visible forecast improvements. One such example is the 5 July case (see Fig. 5.6) where the ALL experiment was able to successfully recover the eastern segment of the bore (originally missing in the CTL forecast). In agreement with the convective LP findings from Section 5.4.1.2, the largest contribution to this positive impact came from TQPROF.

The second, less common problem in CTL involved the *spatial orientation/propagation direction* of the explicitly resolved bores. The assimilation of PECAN profilers was also found to be valuable here. One relevant example comes from the 5 June case in Fig. 5.7 where the baseline experiment incorrectly simulated a southeast- rather than a southwest-propagating bore (compare Figs. 5.7a and 5.7b). Similar to the 5 July case, the simultaneous assimilation of thermodynamic and kinematic remote sensors was essential for producing better forecast results (Fig. 5.7d); however, unlike the 5 July case, the inclusion of PECAN radiosondes did not bring any additional forecast benefits (compare Figs. 5.7c and 5.7d).

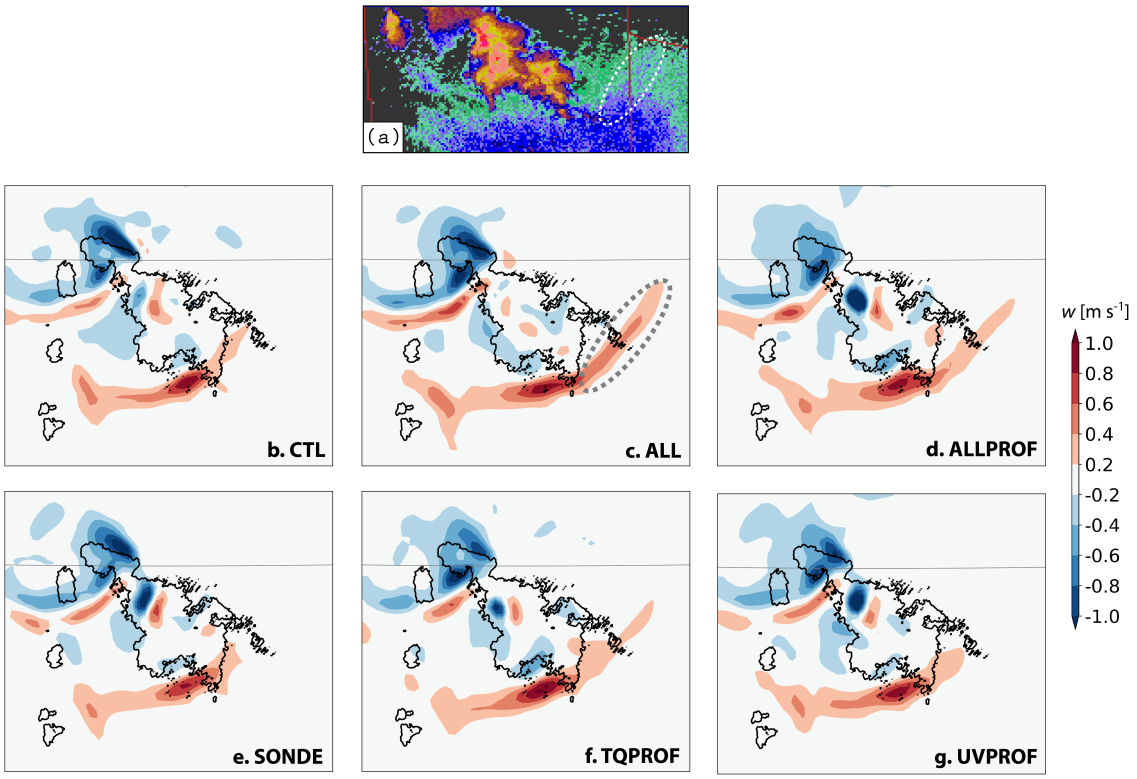

Figure 5.6: Example of how the assimilation of different ground-based profiling networks affects the predicted bore extent during the 5 July 2015 case. *Panel a*: Observed low-level reflectivity mosaic at 0554 UTC (taken from the PECAN field catalogue). *Panels b-g*: Analysis mean vertical velocity at 1 km AGL (w; color shading) and 30 dBZ composite MRMS reflectivity (black contours) at 0600 UTC. The dashed ellipses in panels (a) and (c) mark the location of the eastern bore segment discussed in the main text.

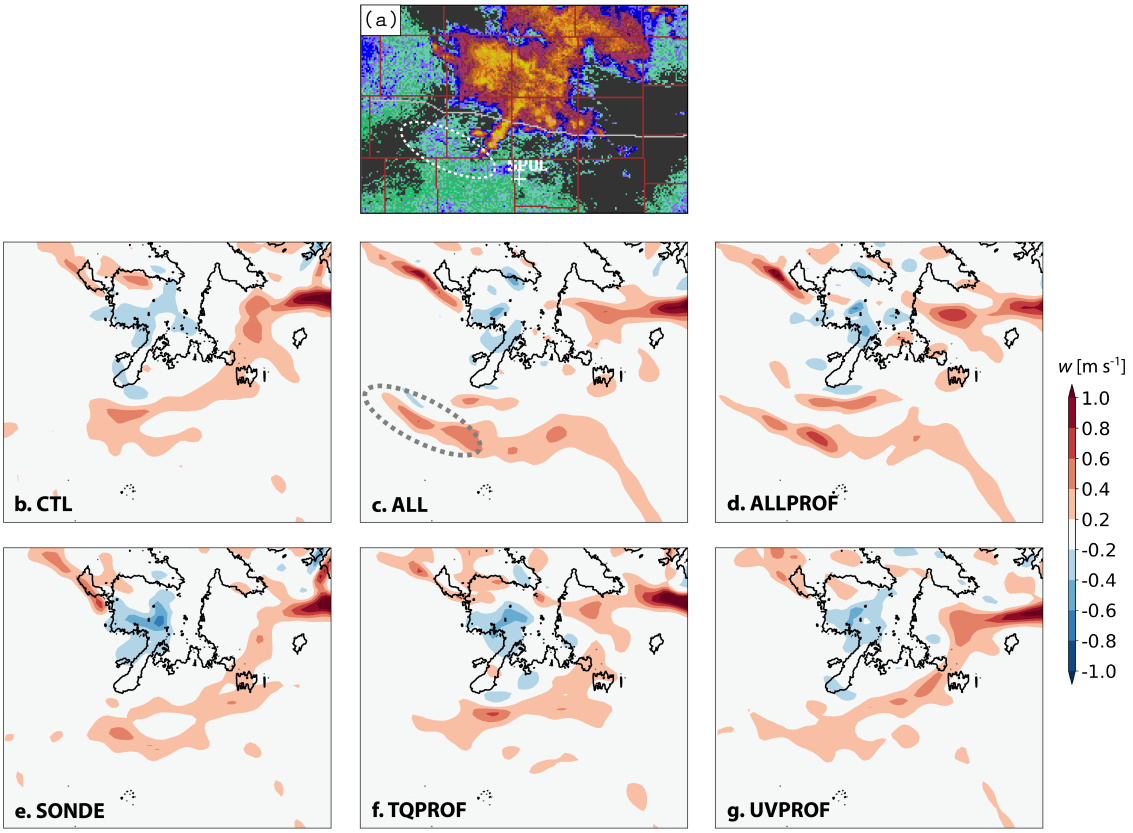

Figure 5.7: Same as Fig. 5.6, but with respect to the propagation direction of the explicitly resolved bore during the 5 June 2015 case. Both observed and forecasted data are displayed at 0530 UTC on that day.

5.4.2.3 Structural impacts

In Fig. 5.8, the Δh ensemble mean forecasts from all 6 experiments are objectively compared against the available bore observations. But before commenting on the performance of different ground-based networks, we would like to first note that the average Δh value in our observation dataset (810.5 m) is commensurate with other recently published composite bore studies (Parsons et al. 2019a; Loveless et al. 2019). Furthermore, the wide range of observed Δh values indicates that the thermodynamic profilers used in our observation analysis were able to sample a large variety of atmospheric bores.

The CTL forecasts were generally skillful at discriminating between weak and strong bore events, but tended to underestimate the amount of bore lifting, especially with respect to the high-amplitude bore cases. Amongst the single profiler experiments (Figs. 5.8d-5.8f), TQPROF led to the strongest forecast changes; however, the impacts from this ground-based network were not necessarily all positive: while the root-mean-square (RMS) error was reduced by ~60 m, TQPROF further exacerbated the negative bias in CTL by ~10 m. On the other hand, the two combined ground-based networks (Figs. 5.8b and 5.8c) were able to improve both of the aforementioned verification metrics. We also observe that the performance of ALLPROF and ALL was very similar, which implies that the assimilation of radiosonde data on top of ground-based remote sensing retrievals had a negligible impact overall.

5.5 Case studies

The results from Section 5.4.1.2 indicated that the forecast skill associated with single profiling networks (SONDE, TQPROF and UVPROF) can be strongly dependent on the underlying convective predictability. To better understand this important sensitivity, the following sequel presents a detailed analysis of 3 representative cases, in which we attempt

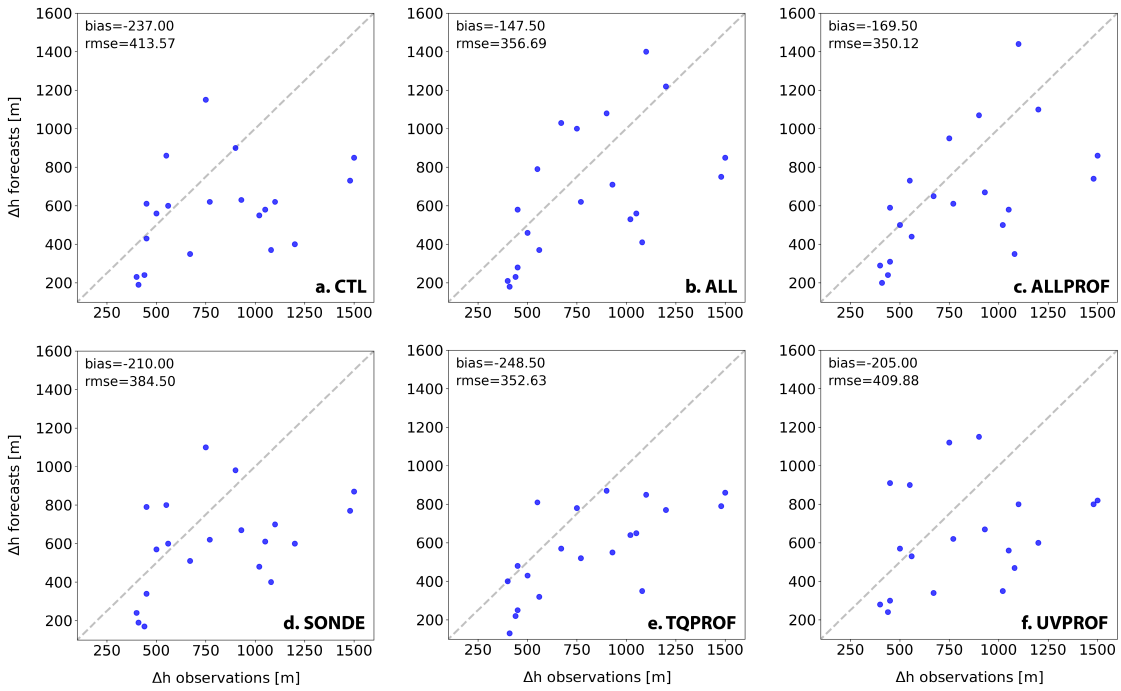

Figure 5.8: Systematic verification of the forecasted bore lifting (Δh). The bias and root-mean-square error (RMSE) associated with different experiments are summarized in the upper left corner of each panel.

to establish a relationship between the forecast performance of single profiling experiments to both their DA impacts as well as the governing convective dynamics.

5.5.1 Low predictability case: 11 July 2015

For the LP category, we selected the 11 July case since its FSS time series were most representative of the average impacts in this predictability regime (see Fig. 5.4a). The same 11 July case was also the focus of a recently published work by Carroll et al. (2021) who combined lidar observations and Rapid Refresh model analyses to study the mesoscale moisture transport responsible for the initiation of the parent bore-generating MCS on this date.

Fig. 5.9 shows the forecast performance at 0700 UTC – the time when the experimental differences reached their peak values. The low NEPs that the CTL experiment predicted inside the parent MCS are a manifestation of rapid convective dissipation, which was quite a common feature in this and the other 2 LP cases. Based on the FSS values in the upper left corner of each panel, we can conclude that the most significant gains in forecast skill come from ALL and TQPROF, despite the tendency of these experiments to generate regions of spurious convection to the east of the parent MCS.[3] Slight improvements were also produced by ALLPROF, whereas the assimilation of SONDE and UVPROF led to a marginal degradation of the CTL forecast.

The green scatter dots in Figs. 5.9b-f indicate that the aforementioned convective impacts are correlated with differences in the low-level moisture field. In particular, it appears that the continuous assimilation of the thermodynamic AERI retrievals resulted in a significant moisture increase that helped maintain the MCS for a longer time. The magnitude of these moisture changes was slightly reduced when kinematic profilers were added (see ALLPROF in Fig. 5.9c), but further increased when all PECAN instruments were assimilated together

[3] Additional tests showed that including the region of spurious convection in the FSS calculations did not change the fact that ALL and TQPROF were the best performing experiments for this case.

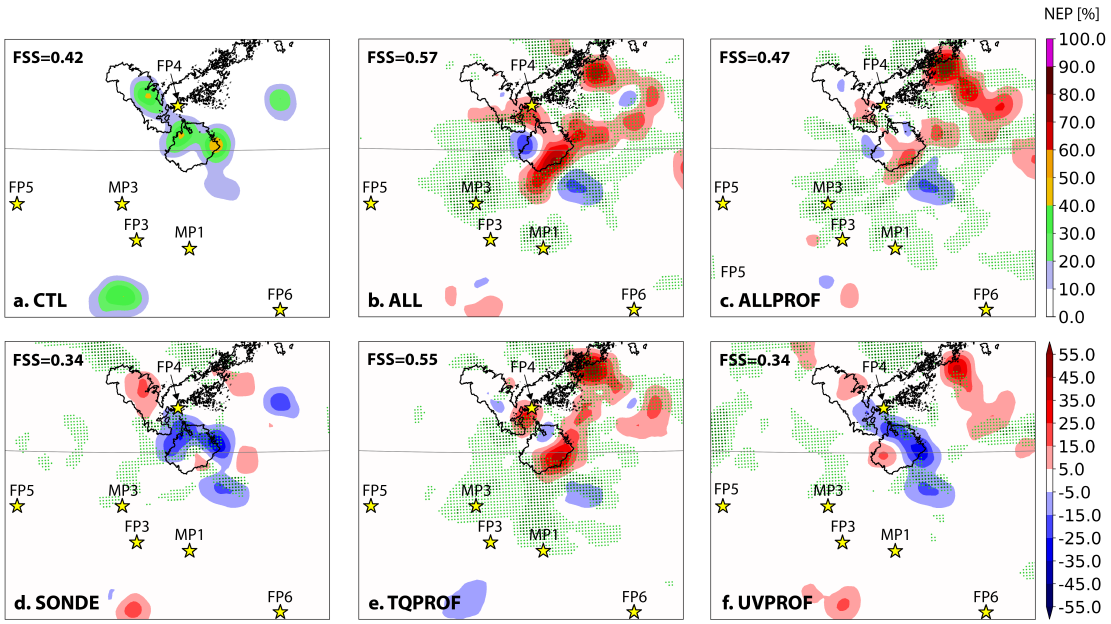

Figure 5.9: Convective forecasts for the 11 July 2015 case, valid at 0700 UTC (corresponding to a 1h forecast lead time). The color shading in panel (a) represents the NEP values associated with CTL, whereas the color shading in the remaining panels – the NEP differences between a given PECAN experiment and CTL. Overlaid on these plots are also the 30 dBZ composite MRMS reflectivity (solid black contours), the experimental differences in the ensemble mean of water vapor mixing ratio at 500 m above the ground (Δq; light and dark green dots correspond to areas where Δq exceeds 0.5 and 1 gkg^{-1}, respectively) as well as the position of assimilated ground-based PISA sites (yellow stars).

(see ALL in Fig. 5.9b). To gain further insights into these results, an additional experiment termed ALLTQ was conducted where only thermodynamic data (either in situ or remotely sensed) were assimilated. ALLTQ produced the highest FSSs amongst all experiments (not shown), implying that the forecast improvements in ALL (relative to TQPROF) were caused by the thermodynamic component of the radiosonde observations. This enhanced sensitivity to the low-level moisture aligns well with the recently published work of Carroll et al. (2021) which showed that convection initiation during the 11 July case was coincident with an observed maximum in the water vapor flux.

Although both the AERIs and the radiosondes provided valuable moisture information that was crucial for the accurate simulation of the bore-generating MCS, the positive moisture differences created by the former were significantly larger. To explain this effect, we now

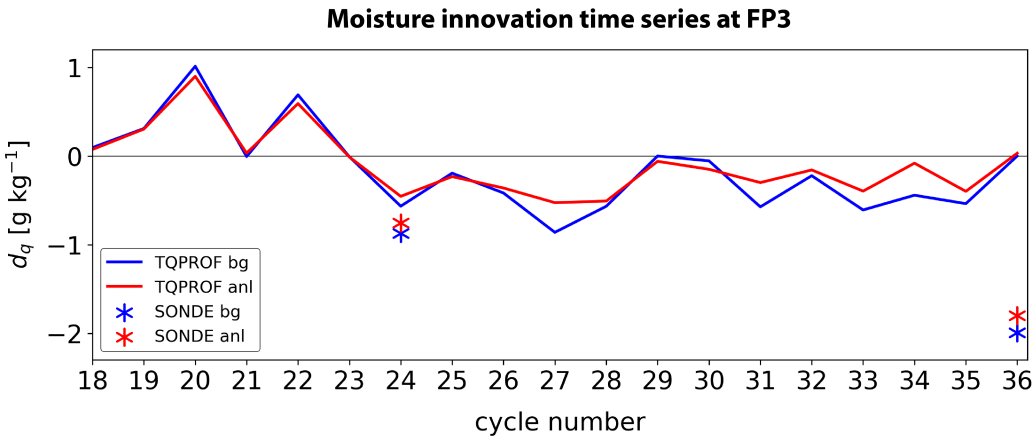

Figure 5.10: FP3 innovation time series of specific humidity (d_q) averaged over the 950-850 hPa layer and shown for the second half of the 6-hour EnKF cycling period on 11 July 2015. Note that the innovation values plotted here represent the ensemble mean minus observation differences; the blue and red colors refer to the background (bg) and analysis (anl) innovations, respectively.

refer to Fig. 5.10 which shows the low-level moisture innovations at one of the PECAN sites (FP3). First focusing on the two solid curves, we observe that the TQPROF background is consistently drier after cycle 23. However, the frequent assimilation of AERI retrievals continuously nudges the TQPROF forecasts toward the observed state such that the moisture innovations during the last EnKF cycle become negligible. During cycle 24, the SONDE innovations are also negative and similar in magnitude to TQPROF. However, due to the complete lack of observations in the upcoming cycles, the background innovations continue to grow, reaching 2 gkg^{-1} during the final analysis time – values that resemble the Rapid Refresh model analysis errors reported in Carroll et al. (2021). At this point, even though the assimilation of FP3 radiosonde data produces large moisture increments, the SONDE analysis innovations remain strongly negative. In other words, our diagnostics suggest that the lack of appreciable moisture changes in SONDE is caused by the small number of PBL observations that cannot effectively suppress the growing background errors in this experiment.

In an effort to justify the forecast degradation caused by UVPROF, we compare its DA performance relative to TQPROF at 0600 UTC (Fig. 5.11). During this last EnKF cycle,

the low-level moisture background in both experiments contains a localised region of dry air ahead of the parent MCS. Assimilating the MP1 AERI instrument, which happens to be located within the dry region, generates positive increments in water vapor mixing ratio (red contours in Fig. 5.11a). By contrast, the MP1 kinematic profiler further enhances the strength of the dry region. To understand where these opposite impacts come from, we need to first recall that q_v is not a directly observed variable in UVPROF, meaning that all moisture corrections in this experiment are entirely determined by the empirical covariances provided by the background ensemble. And since q_v represents a passive tracer in the absence of moisture sources or sinks, the background covariances in UVPROF mostly reflect the advection of q_v by the wind. With this in mind, we now observe that the MP1 kinematic profiler induces a westerly wind increment (eastward-pointing white arrows in Fig. 5.9b) that acts upon a sharp moisture gradient around the MP1 site. But since q_v is considerably smaller upstream of the MP1 site, an increase in the westerly component of the wind will be inevitably correlated with a decrease in the moisture content.

5.5.2 High predictability case: 2 July 2015

The observation impacts in the HP category are exemplified through the 2 July case, which was characterized by a quickly moving MCS with a large, eastward propagating bore. As expected, the CTL experiment had a very satisfactory forecast of the parent MCS even 3h into the forecast (Fig. 5.12a). Notably, the excellent forecast performance in this HP case occurred even though the total DA period was twice as small compared to its LP counterpart. The latter observation further confirms our overall impression that the convective skill across the 10 PECAN cases was mostly driven by differences in the inherent atmospheric predictability rather than specific details in our employed DA methodology.

The main motivation for selecting the 2 July event was the superior performance of UVPROF (*cf.* NEP changes in Fig. 5.12f) – a typical characteristic in this HP category (see Fig. 5.5c). Unlike the 11 July case, the convective forecasts here were most sensitive

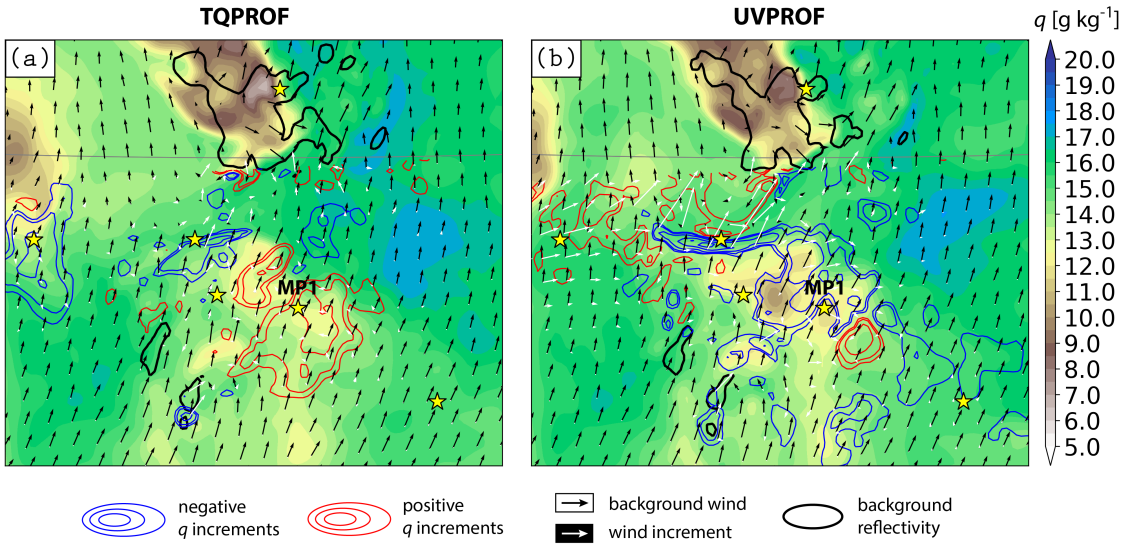

Figure 5.11: Comparing the 500 m AGL analysis increments in (a) TQPROF and (b) UVPROF during the last EnKF cycle on 11 July 2015. The color shading, black arrows and solid black contours represent the background ensemble means of water vapor mixing ratio (q), wind and 30 dBZ reflectivity, respectively. Positive (negative) q increments are shown as red (blue) contours and are displayed for the following values: ±0.15, ±0.25, ±0.5, ±1, ±1.5, ±2 and ±2.5 gkg^{-1}. Wind increments are shown as white arrows and are additionally magnified ~10.6 times relative to the background wind. Note that the moisture and wind increments inside the parent MCS are deliberately clipped in order to better highlight the environmental changes brought by the assimilated ground-based remote sensors (see yellow stars).

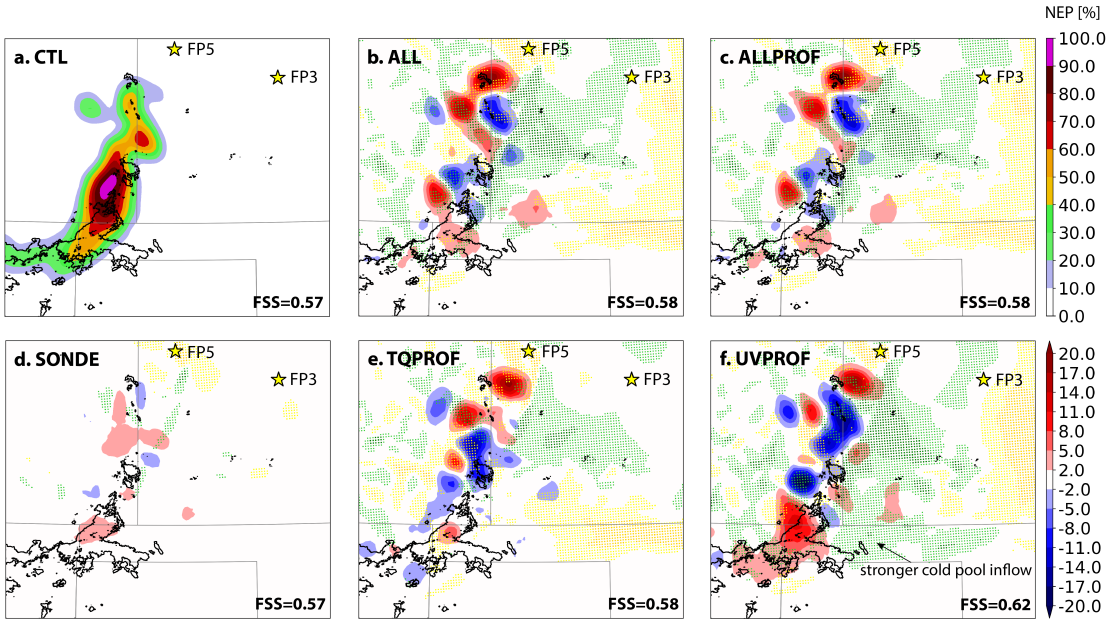

Figure 5.12: Same as Fig. 5.9, but for 0600 UTC on 2 July 2015 (corresponding to a 3h forecast lead time). The green (yellow) dots show negative (positive) differences in the u-component of the ensemble mean wind at 500 m AGL; the lighter (darker) colors mark regions where these differences exceed 0.5 (1) ms^{-1}.

to differences in the forecasted low-level wind field. In particular, the black arrow in Fig. 5.12f indicates that UVPROF predicted a stronger inflow toward the parent MCS. To reveal how these wind changes affected the subsequent convective evolution, we examined the vertical structure of the simulated cold pools. The cross sections in Fig. 5.13 show that the stronger inflow in UVPROF enhanced the low-level convergence along the cold pool's leading edge. The resulting updraft increase promoted a more sustained growth of new convective cells, largely alleviating the premature MCS dissipation in CTL. Interestingly, slight increases in the updraft's strength were also observed in the other PECAN experiments, especially ALLPROF and ALL. Despite their opposite near-surface wind impacts, these two experiments were still able to deepen the cold pool's inflow region and thus increase the height-integrated convergence along the cold pool's leading edge.

Similar to the LP analysis, we now seek to understand why the kinematic remote sensors were more effective at improving the forecast skill than the corresponding radiosonde

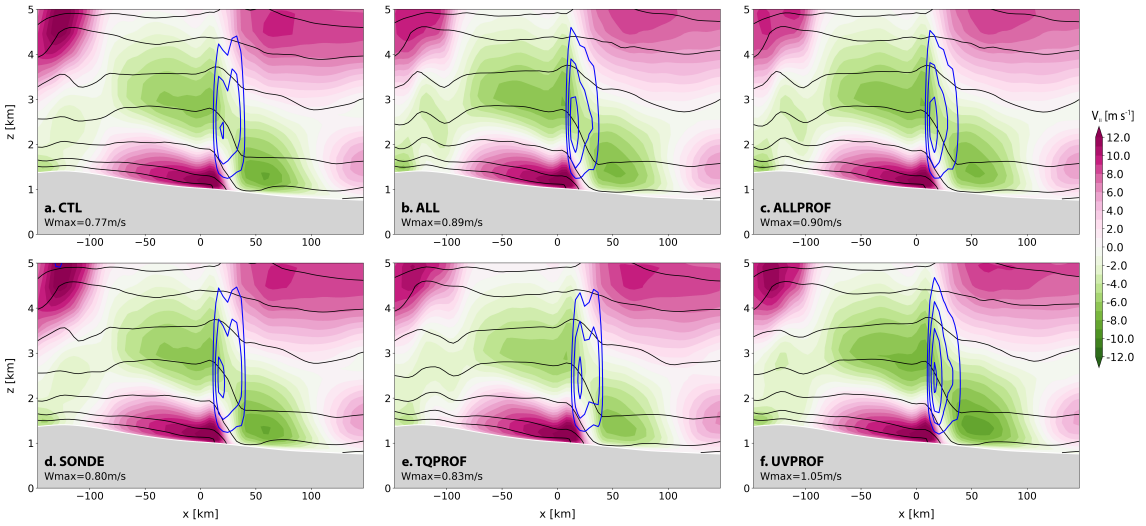

Figure 5.13: Vertical cross sections through the cold pool associated with the parent MCS on 2 July 2015. The color shading displays the horizontal wind speed parallel to the cross section $(V_{||})$, with positive (negative) values indicating flow oriented in the positive (negative) x-direction. The solid black contours show the virtual potential temperature and are plotted every 2 K, starting from 310 K near the surface. Vertical velocities are also shown as solid blue contours whose spacing and initial value are both set to 0.25 ms^{-1}. The maximum value of the vertical velocity (Wmax) is additionally labelled in the lower-left corner of each panel. All cross sections are valid at 0530 UTC, which corresponds to a 2.5h forecast lead time for this PECAN case.

instruments. To answer this question, we consider innovation statistics from the FP3 site where most of the forecasted inflow differences in UVPROF originated from. It it clear from Fig. 5.14a that the wind innovations in UVPROF become negligible after the first EnKF cycle (compare the solid and dashed blue lines). The small UVPROF increments throughout most of the cycling period suggest that the high observation frequency of the kinematic remote sensor was not an essential ingredient for improving the forecast skill in this case. Instead, it was the ability of UVPROF to correct the model state early enough in the DA window so that the resulting wind changes can affect the subsequent convective evolution[4]. While this reduced sensitivity to the temporal frequency makes radiosondes a potentially useful observing platform, the FP3 crew launched their first weather balloon only during the last EnKF cycle, not leaving sufficient time for the wind corrections to be advected toward the cold pool. In fact, comparison between the solid red and blue curves in Fig. 5.14a indicates that the initial wind errors at FP3 amplified over the cycling period and created an even greater observation misfit during SONDE's first assimilation time.

The inability of TQPROF to create meaningful wind increments in this HP case can be primarily attributed to the high accuracy of the background low-level moisture fields (relative to the LP case), as evidenced by the root-mean-square innovation (RMSI) profiles in Fig. 5.14b. In particular, the absence of large moisture innovations prevented the EnKF from making significant changes to either observed or unobserved state variables. Additional diagnostics, however, revealed that the small moisture innovations in TQPROF were further compounded by the relatively small moisture-wind correlations. As a result, even the very few EnKF cycles that featured relatively large moisture corrections were not able to produce sizeable wind increments.

[4] One could also argue that the increased sampling frequency of the kinematic remote sensor represents an indirect benefit since it ensures that observations will be made at dynamically critical times.

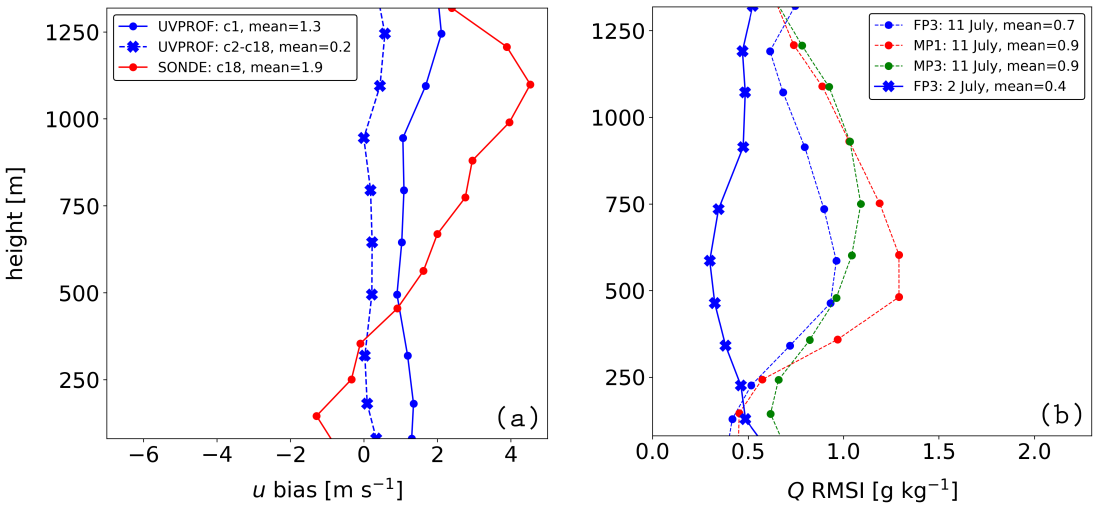

Figure 5.14: Observation space diagnostics for the 2 July 2015 case. *Panel a*: Background u-wind bias profiles for UVPROF and SONDE (blue and red colors, respectively) at the FP3 site. The two solid curves show statistics from a single cycle ($c1$ or $c18$; see legend), while the dashed curve – an average bias profile calculated between the 2nd and 18th cycles. *Panel b*: Background root-mean-square innovation (RMSI) profiles of specific humidity (Q) associated with TQPROF for the 2 July 2015 (solid curve) and 11 July 2015 (dashed curves) cases. All RMSI profiles are averaged over the last 3 hours prior to model initialization.

5.5.3 Medium predictability case: 5 June 2015

We close this Section by discussing the forecast impacts on 5 June when the convective evolution was considerably more complex than the previous two cases. In particular, the bore-generating MCS here interacted with another, much larger MCS to its northeast (see the upper-right corner of Fig. 5.15a). Problems with the CTL experiment included the low NEP values inside the parent MCS as well as the simulation of spurious NEP probabilities to its east. Consistent with our conclusions for the MP category, forecast improvements in this case required the simultaneous assimilation of thermodynamic and kinematic profilers. By contrast, the use of single remote sensors resulted in either neutral or slightly negative impacts, primarily due to further NEP reductions within the parent MCS (see Figs. 5.15e,f).

The location of the FP3 site (see yellow star in Fig. 5.16a), which was assimilated as part of our 5 June experiments, partly explains why it was necessary to observe both the thermodynamic and kinematic components of the model state. In particular, the FP3 site was

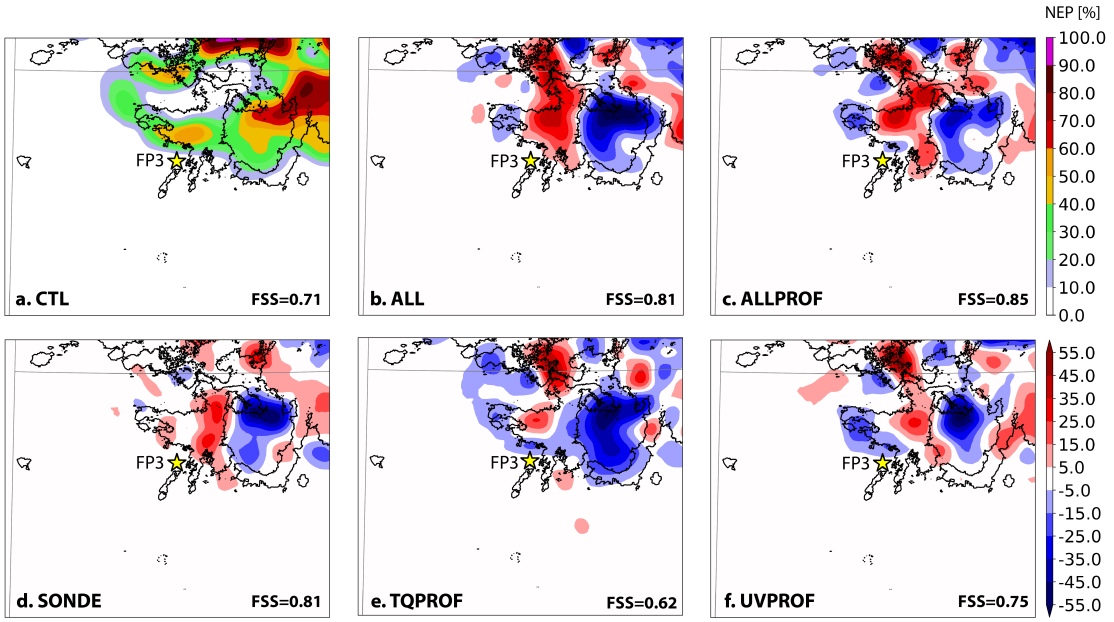

Figure 5.15: As in Fig. 5.9, but for 0600 UTC on 5 June 2015 (corresponding to a 1.5h forecast lead time).

positioned very close to a sharp near-surface boundary characterized by strong variations in moisture and wind, and along which the bore-generating convective system developed in later EnKF cycles.

Given that SONDE was the best performing single profiling experiment during this case, we now examine its low-level increments (overlaid in Fig. 5.16a) in order to justify some of the subsequent forecast improvements. First, we observe that the assimilation of FP3 radiosondes induced a widespread region of negative q increments at 500 m AGL. These negative increments also extended to 2 km AGL where the background wind was oriented from south-southwest (see Fig. 5.16a). The resulting negative SONDE-CTL moisture differences were then advected into the region of spurious convection and helped suppress the excessively large NEP values in CTL. Insofar as the wind impacts in SONDE are concerned, the white arrows in Fig. 5.16a indicate the existence of two main increment types. The first one pertained to a broad area of southerly wind increments around the FP3 site that reflected an underestimation of the background LLJ speed around the FP3 site. We also observe northeasterly wind increments between the two convective cells to the northwest of FP3 (see

yellow ellipse in Fig. 5.16a), which were instead caused by the spatial wind covariances in the background ensemble. Regardless of their origin, however, the effect of both these increment types was to strengthen the pre-existing low-level convergence to the north of FP3. Somewhat analogous to the dynamical mechanisms discussed as part of the HP case, the resulting enhancement in the low-level vertical velocity (see red contours in Fig. 5.16c) created more favourable conditions for convective growth and likely explains the higher NEP values in SONDE.

To understand why the TQPROF and UVPROF predictions were not as skillful compared to SONDE, we examine the DA impacts in these single profiling experiments during two different EnKF cycles. The first one is valid at 0310 UTC (first row of Fig. 5.17), which is only 10 minutes after the assimilation of the first FP3 radiosonde observations. Although the moisture and wind increments in TQPROF and UVPROF are not as coherent or widespread as those in SONDE, they appear to be subjectively consistent – both in terms of the reduced moisture content as well as the strengthened LLJ. This similarity between TQPROF and UVPROF, which occurred during several other EnKF cycles, comes in contrast to the LP case where the two experiments produced opposite increments. To explain this apparent discrepancy, we note that the low-level moisture on 5 June varied on much larger scales compared to the LP case and was also strongly correlated with the low-level wind field. In particular, the dry air mass was clearly associated with south-southwesterly winds, whereas the flow in the moist air mass had a predominantly easterly component. In this much simpler dynamical context, measurements of either moisture or wind would be sufficient to accurately estimate both of these variables.

The aforementioned dynamical situation changes during the last hour of EnKF cycling when convection begins to develop over the FP3 site. As a result of the highly nonlinear convective dynamics, the wind-moisture relationship becomes more complex and it is no longer possible to accurately estimate the model state by only assimilating single remote sensors. This effect is illustrated well on the bottom row of Fig. 5.17. Here we see that

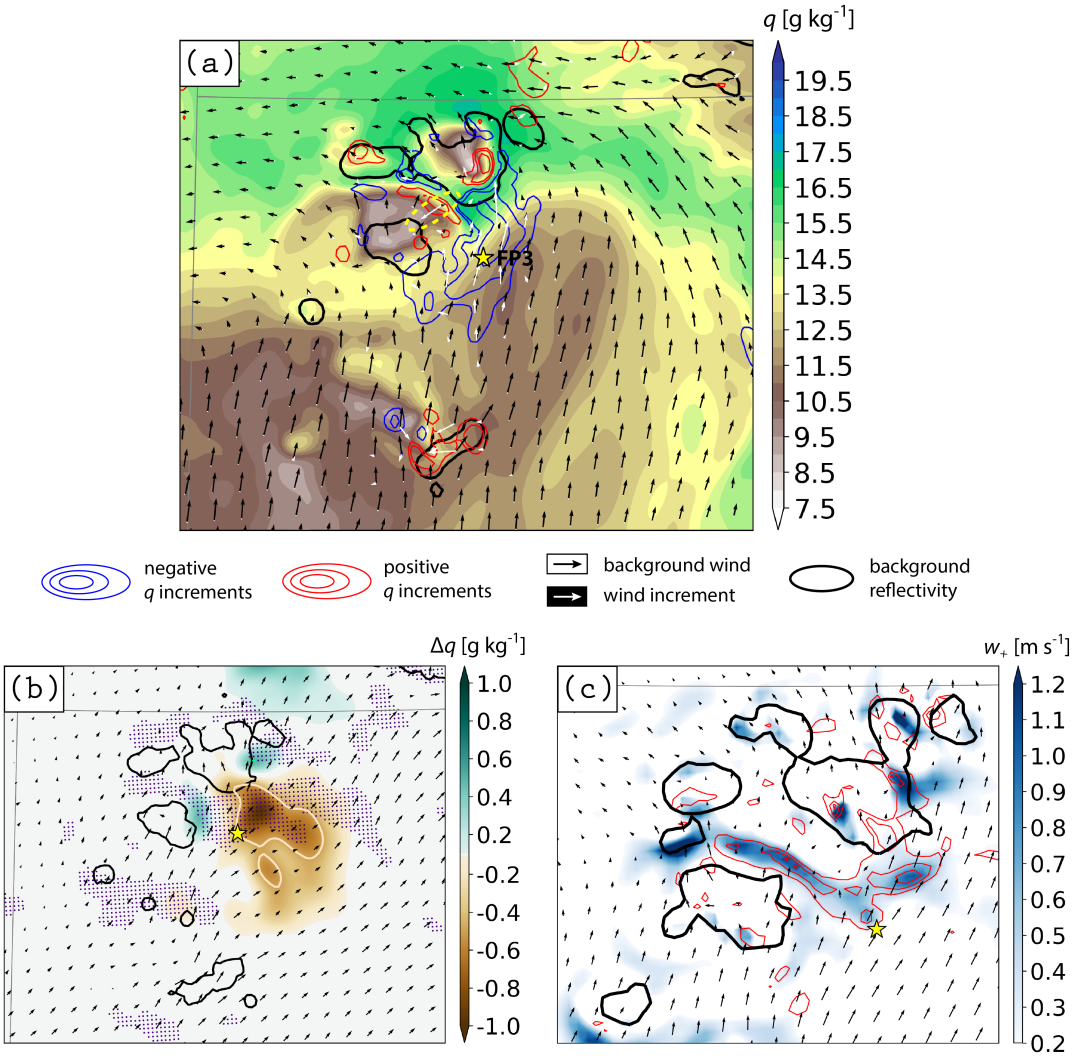

Figure 5.16: Dynamical interpretation of the forecast improvements during the 5 June 2015 case. *Panel a*: Analysis increments for SONDE at 0300 UTC. The meaning of all symbols is the same as in Fig. 5.11, except that the q increments are drawn at ±0.5, ±1, ±2 and ±4 gkg^{-1}, whereas the ratio of background to increment wind (represented by the black and white arrows, respectively) is ∼1:3. The dashed yellow ellipse shows the position of the northeasterly wind increment discussed in the main text. *Panel b*: SONDE-CTL analysis mean q differences (Δq; color shading) at 2 km AGL and valid at 0300 UTC. Regions where Δq is equal to -0.5 gkg^{-1} are highlighted with bisque contours. The solid black contours and black arrows represent SONDE's analysis mean of 30 dBZ reflectivity and wind at 2 km AGL, respectively, while the purple dots indicate grid points where the analysis mean vertical velocity at 1 km AGL exceeds 0.15 ms^{-1}. *Panel c*: SONDE's analysis mean updraft strength at 1 km AGL (w_+; blue shading) and its change relative to CTL (red contours starting at 0.1 ms^{-1} and plotted every 0.2 ms^{-1}) at 0310 UTC. The solid black contours and black arrows have the same meaning as in panel (b), but are shown for 1 km AGL. Finally, the position of the FP3 site is marked with a yellow star in all panels.

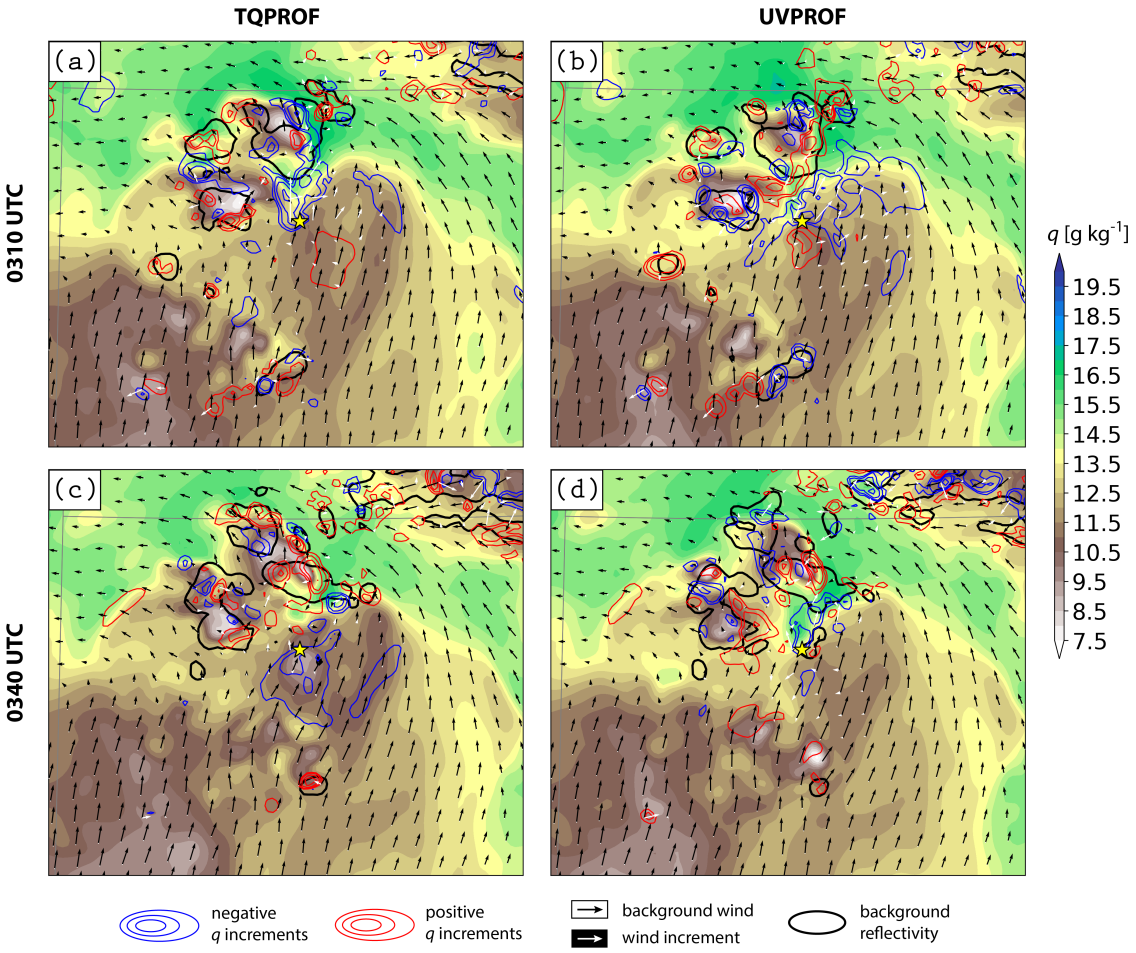

Figure 5.17: Comparing the low-level analysis increments in TQPROF and UVPROF during two EnKF cycles on 5 June 2015: one before and another after the initiation of convection over the FP3 site (top and bottom rows, respectively). The data shown in these panels are the same as in Fig. 5.16a, except that the ratio of background to increment wind (black and white arrows, respectively) here is ~2:5 and the ±0.25 gkg^{-1} q increment is additionally plotted.

TQPROF produces a distinctly negative moisture increment around the FP3 site, whereas the moisture changes in UVPROF are more or less neutral, despite the fact that the background moisture content in UVPROF is much larger. We hypothesize that it is namely these cross-variable analysis errors that eventually degrade the TQPROF and UVPROF forecast performance.

Finally, it is worth remarking that the strategic timing of the FP3 balloon launch likely enhanced the overall forecast benefits brought by the SONDE network. In particular, the FP3 radiosonde provided vital observations shortly before convection initiation when the relatively linear model state dynamics still allowed the EnKF algorithm to generate meaningful PBL corrections. This setup is to be contrasted with the HP case where the lack of radiosonde measurements early in the DA window limited their subsequent impacts.

5.6 Summary

This work evaluated the benefits of various ground-based profiling networks across 10 diverse cases from the Plains Elevated Convection at Night (PECAN) field campaign. We explored the impact of assimilating both in situ and remote sensing instruments on the short-range forecasts of bore-generating nocturnal convection. A total of 5 data addition experiments were conducted in order to evaluate the relative merits of networks with single or combined instrument designs.

Aggregated verification statistics across the 10 cases showed that the largest forecast improvements are obtained by simultaneously assimilating in situ and remote sensing profilers. Combining thermodynamic and kinematic remote sensors also resulted in measurable benefits, especially with respect to the explicitly resolved bores. On the other hand, the average impacts from single profiling networks were shown to be mostly neutral in sign. Detailed analysis revealed that the lack of statistically detectable benefits from such networks is related to their strong dependence on the underlying convective predictability. In particular, while thermodynamic and kinematic remote sensors were beneficial in low and

high predictability regimes, respectively, they were found to cause neutral or even slightly negative impacts during moderately predictable convective events.

To illustrate the aforementioned sensitivities, we used 3 representative cases and showed that the underlying dynamical context plays a critical role in shaping the forecast impacts from different ground-based profiling networks. Our examination of the low predictability case, for instance, revealed that the evolution of the bore-generating convective system was highly sensitive to the low-level moisture analysis, which in turn explained the better forecast performance caused by the assimilation of thermodynamic networks. Likewise, the positive impacts from kinematic profilers during the high predictability case were naturally linked to the enhanced sensitivity of the parent convective system to the low-level wind fields.

Aside from their strong dependence on the underlying convective predictability, our analysis demonstrated that the performance of single profiling networks is also contingent upon limitations in the underlying DA methodology. This is due to the fact that accurately estimating the unobserved portion of the model state is closely related to the quality of the background error covariances. The main advantage of the EnKF approach used in this study is that it provides a flow-dependent covariance estimate based only on a small number of ensemble members. In the special case of quasi-linear model dynamics and comparable variability in the moisture and wind fields (Figs. 5.17a,b), we find that the EnKF-based covariances are sufficiently accurate and allow single profilers to introduce physically sound corrections to both mass and wind variables.

On the contrary, when the flow is governed by highly nonlinear dynamics (Figs. 5.17c,d) and/or the background moisture varies on scales that are much smaller than the corresponding wind field (Figs. 5.11), an accurate estimation of the thermodynamic and wind characteristics of the PBL with single remote sensors is no longer possible. In these situations, the background covariances cannot faithfully describe the true wind-moisture relationship – either as a direct consequence of the more complicated dynamics or due to the insufficient number of ensemble members needed to accurately resolve the small-scale

moisture variability. Consequently, errors in the analysis of unobserved state variables accumulate over time and have an adverse impact on the forecasts. All in all, these findings suggest that the spatiotemporal characteristics of the low-level moisture transport, which is an archetypal feature of the nocturnal environment over the Great Plains (Trier and Parsons 1993; Trier et al. 2017; Hitchcock et al. 2019; Weckwerth and Romatschke 2019), have important consequences on our ability to extract meaningful information from single remote sensing instruments.

Undoubtedly, future developments in DA theory would be vital for the better utilization of ground-based remote sensing technology. One possible research direction involves the development of novel methods for estimating the optimal observation error statistics. The high vertical resolution and temporal frequency of remote sensors, for instance, make it necessary to introduce spatial and temporal correlations in the error covariance matrices. Recent findings from Degelia and Wang (2021) have also demonstrated that convective forecasts can be further improved by adopting a flow-dependent treatment of the observation error statistics. Another interesting line of future research would be to explore the benefits of directly assimilating the raw remote sensing measurements (as opposed to having to rely on separate retrieval algorithms). Such an idea is highly appealing as it would allow for a more straightforward quantification of the measurement uncertainties in the estimation process. Finally, the contrasting moisture variability found in our cases naturally lends itself to a multiscale DA approach that can impose different correlation structures as a function of the analyzed scales (e.g., Wang et al. 2021).

Chapter 6

Conclusions

6.1 Overall summary

Numerical weather prediction (NWP) is an initial-value problem which requires reliable measurements of the entire Earth system in order for skillful predictions to be made. Ever since the generation of the first successful computer-based weather forecast in 1950 (Charney et al. 1950), the NWP field has been revolutionized through continuous, but gradual advances in model formulation,initialization techniques and the introduction of new observation types (Bauer et al. 2015). The increasing availability of computational resources has also enabled unprecedented increases in model resolution, making it possible to treat convective motions explicitly. As might be expected, however, the development of these new NWP systems has also opened the doors for new scientific challenges that limit the overall practical utility of NWP forecasts. For example, the ability of high-resolution models to resolve the -5/3 portion of the kinetic energy spectrum allows small errors in the initial conditions (ICs) to grow rapidly and contaminate the overall forecast quality. Typically, these small-scale analysis errors would originate in the Planetary Boundary Layer (PBL) – the lowest portion of the atmosphere, where processes are characterized by smaller scales compared to other parts of the atmosphere. Despite the wealth of information provided by the Global Observing System (GOS), the currently available instruments cannot effectively suppress the IC errors in the PBL. Therefore, the last two decades have been dedicated toward the development of

novel ground-based remote sensing profilers that can faithfully capture the thermodynamic and kinematic structure of the PBL. Their high sampling frequency is believed to hold great promise for the next generation of high-resolution NWP models. In this dissertation, we have corroborated this claim by showing the value of ground-based remote sensing on the forecasts of bore-generating convective systems observed during the Plains Elevated Convection at Night (PECAN) field campaign.

In order to accurately assess the quality of our forecasts, we first developed an object-based algorithm for the identification and tracking of convective outflow boundaries (*cf.* Chapter 3). The ability of the proposed method to simultaneously detect density currents and bores made it particularly suitable for evaluating the night-time forecast skill when the evolution of these features is closely related. The new algorithm was further extended in Chapter 4 to accommodate a neighborhood-based verification of the forecasted bores that makes use of the available remote sensing data. This new functionality allowed us to quantitatively evaluate the impact of the newly added observations on different aspects of a bore-initiated convection event that took place on 6 July 2015, including the ambient environment in which the bore formed, its explicitly resolved structure as well as its ability to trigger new convective cells. Our experiments showed that ground-based remote sensors have the largest forecast impact out of all assimilated PECAN observations. Overall, the thermodynamic retrievals from the Atmospheric Emitted Radiance Interferometer (AERI) led to the strongest positive impacts. Kinematic profilers, such as the Radio Wind Profiler (RWP) and Doppler Wind Lidar (DWL), appeared to be highly beneficial for the bore-related components of the forecasts, but degraded the subsequent convective skill.

In Chapter 5, the validity of the aforementioned conclusions was systematically tested against 10 additional PECAN cases. By only assimilating collocated instruments, we evaluated the relative merits of different ground-based profiling networks. The best forecasts were obtained by combining in situ and remote sensing profilers, although statistically significant improvements were also achieved through the simultaneous assimilation of

thermodynamic and kinematic remote sensors. By contrast, the value of single profilers was found to be highly case dependent, with thermodynamic (kinematic) instruments being most beneficial in cases with low (high) convective predictability.

6.2 Discussion

The visible dependence of the forecast impacts on the underlying atmospheric predictability was an overarching topic in Chapter 5. Our systematic results suggested that the convective evolution can be sensitive to both the mass and wind characteristics of the initial state, making the value of individual profiling instruments highly case dependent. For example, we found that thermodynamic (kinematic) profilers do not bring forecast improvements when the simulated MCS is mostly sensitive to the kinematic (thermodynamic) component of the initial state. In these situations, ideally, the assimilation of single profiler networks should not affect the overall forecast quality. However, deficiencies in the EnKF method – either due to the limited ensemble size or complexities in the governing moisture dynamics – inevitably led to forecast degradations. These problems were largely mitigated by assimilating ground-based networks containing both thermodynamic and kinematic remote sensors, which were able to provide a more complete description of the initial PBL state.

The considerable forecast gains brought by the simultaneous assimilation of remote sensing and in situ instruments was another important finding in Chapter 5 that deserves a special mention in view of its novelty. The value of radiosondes was found to be particularly high with respect to the convective forecasts where the addition of these instruments was able to further reduce the sensitivity of the observation impacts to the underlying convective predictability. Given the relatively low costs of operating radiosondes as well as their pronounced benefit, it appears that investment in such hybrid profiling systems should be strongly considered as part of future mesoscale networks.

Weather-sensing uncrewed aerial systems (WxUAS), frequently referred to as drones, represent another viable alternative for confronting the PBL observation gap (Bell et al.

2020). Compared to ground-based remote sensors, drones are much cheaper, especially considering that a single drone can simultaneously observe the thermodynamic and kinematic structure of the PBL. Another notable advantage of WxUAS is their superior accuracy due to the use of in situ sensors. While the current use of drones is subject to a lot of restrictions from the Federal Aviation Administration (FAA), it is expected that their high adaptability will make them increasingly more important in future efforts to address the PBL observation gap. Recent experiments have shown that WxUAS data can improve the accuracy of thermodynamic retrievals (Tyler Bell, personal communication), which serves as an additional evidence for the synergies between in situ and remote sensing instruments. However, the high sampling frequency of drones relative to radiosondes will make them even more valuable in the context of the hybrid ground-based profiling systems mentioned above.

Other possible observation synergies involve satellite measurements. The NWP community has recently started to make increasing use of hyperspectral infrared (IR) sounders such as the Atmospheric Infrared Sounder (AIRS), the Infrared Sounding Interferometer (IASI) and the Cross-track Infrared Sounder (CrIS), which can be found on-board of various polar orbiting satellites. While the accuracy and resolution of these instruments in the lower atmosphere is still not comparable to radiosondes, they can resolve important changes in the PBL structure over large geographical areas. As a result, the continued development of hyperspectral IR sounders has been identified as an important priority for confronting the PBL observation gap National Academy of Sciences, Engineering and Medicine (2018). In the shorter term, the development of combined retrievals from ground-based and space-borne stations could provide additional benefits for convective-scale numerical models.

6.3 Future work

While the results presented in this dissertation create a strong case for the operational assimilation of ground-based remote sensing profilers, several questions still remain open. One of them is whether the underlying DA technique might affect the presented observation

impacts. Ensemble-based methods, such as the EnKF used here, have the advantage of providing flow-dependent ICs; however, our systematic experiments have indicated that the accuracy of the EnKF analyses might be compromised in the presence of spurious cross-variable correlations. Variational DA methods like 4D-Var sidestep this problem by explicitly modeling the dynamical balances between model state variables (see Bannister 2017). Given that, it might be possible to limit some of the negative impacts we have observed in single profiling experiments by incorporating the effects of moisture advection in the DA algorithm. Some combination between a static and an ensemble-based background covariance estimate might be especially beneficial in convective-scale applications.

Another aspect of the DA system that our results might be sensitive to is the choice of a moisture control variable (CV), as demonstrated recently by Thundathil et al. (2020) and Wang et al. (2020). Our moisture CV (water vapor mixing ratio) happens to be the same as the prognostic moisture variable used by our NWP model. In this case, the EnKF produces a straightforward estimate of how moisture is correlated with other components of the state vector. However, inaccurately estimated sample covariances due to a small ensemble size could do more harm to the analysis than the absence of any covariance information at all (Ross Bannister, personal communication). One possible solution to circumvent this problem would be to construct an uncorrelated moisture CV, such as the pseudo-relative humidity (Dee and da Silva 2003), although the latter may necessitate other changes in the underlying DA algorithm (e.g., treatment of non-Gaussian distributions).

Finally, there is still a lot of scope to enhance the verification metrics used in convective-scale NWP models. As discussed in Chapter 3, most of the work in this field has focused on developing new techniques that permit an objective comparison between simulated and observed convective clouds. However, there are many other small-scale features that either affect the convective forecast skill or are important in their own right. One of the them is the Nocturnal Low-Level Jet (NLLJ), which has been previously linked to the distribution of warm-season precipitation in both South and North America. Recent work has been

able to successfully detect NLLJ in model output (Oliveira et al. 2018), opening exciting new opportunities for quantifying the accuracy of these features at convection-permitting resolutions. Likewise, this dissertation documents the formulation of an object-based algorithm for the identification and tracking of another pertinent mesoscale phenomenon – convectively-generated atmospheric bores. However, the lack of adequate observational datasets is an obstacle for both of these algorithms. For example, the detection of radar fine lines that mark the position of bores is only possible in the absence of precipitation echoes. Similarly, the lack of accompanying thermodynamic information precludes the unambiguous discrimination between density currents and bores. To eliminate some of these deficiencies, future investigators could attempt to design new observation-based bore algorithms that combine radar and surface observations. Densely packed surface networks, such as the Oklahoma mesonet, have already proven to be valuable for tracking the evolution of night-time convective outflows (e.g., Haghi et al. 2017; Toms et al. 2017) and could be potentially utilized in this type of research.

Bibliography

Adam, S., A. Behrendt, T. Schwitalla, E. Hammann, and V. Wulfmeyer, 2016: First assimilation of temperature lidar data into an NWP model: impact on the simulation of the temperature field, inversion strength and PBL depth. *Quart. J. Roy. Meteor. Soc.*, **142**, 2882–2896.

Ahmed, N., T. Natarajan, and K. R. Rao, 1974: Discrete cosine transform. *IEEE Trans. Comput.*, **C-23**, 90–93.

Anderson, J. L., and N. Collins, 2007: Scalable implementations of ensemble filter algorithms for data assimilation. *J. Atmos. Oceanic Technol.*, **24**, 1452–1463.

Arritt, R. W., T. D. Rink, M. Segal, D. P. Todey, and C. A. Clark, 1997: The Great Plains low-level jet during the warm season of 1993. *Mon. Wea. Rev.*, **103**, 2176–2192.

Baer, F., and J. J. Tribbia, 1977: On complete filtering of gravity modes through nonlinear initialization. *Mon. Wea. Rev.*, **105**, 1536–1539.

Baines, P. G., 1984: A unified description of two-layer flow over topography. *J. Fluid Mech.*, **146**, 127–167.

Bannister, R. N., 2017: A review of operational methods of variational and ensemble-variational data assimilation. *Q. J. R. Meteorol. Soc.*, **143**, 607–633.

Bauer, P., A. Thorpe, and G. Brunet, 2015: The quiet revolution of numerical weather prediction. *Nature*, **525**, 47–55.

Bell, T. M., B. R. Greene, P. M. Klein, M. Carney, and P. B. Chilson, 2020: Confronting the boundary layer data gap: evaluating new and existing methodologies of probing the lower atmosphere. *Atmos. Meas. Tech.*, **13**, 3855–3872.

Benjamin, S. G., B. E. Schwartz, E. J. Szoke, and S. E. Koch, 2004: The value of wind profiler data in U. S. weather forecasting. *Bull. Amer. Meteor. Soc.*, **85**, 1871–1886.

Benjamin, T. B., 1968: Gravity currents and related phenomena. *J. Fluid. Mech.*, **31**, 209–248.

Bertino, L., G. Evensen, and H. Wackernagel, 2002: Sequential data assimilation techniques in oceanography. *International Statistical Review*, **71**, 223–241.

Blake, B. T., D. B. Parsons, K. R. Haghi, and S. G. Castleberry, 2017: The structure, evolution, and dynamics of a nocturnal convective system simulated using the WRF-ARW model. *Mon. Wea. Rev.*, **145**, 3179–3201.

Bleck, R., and R. Brummer, 1984: Enhancement of remotely sensed temperature fields by wind observations from a VHF radar network. *Mon. Wea. Rev.*, **112**, 1795–1803.

Bodine, D. J., and K. L. Rasmussen, 2017: Evolution of mesoscale convective system organizational structure and convective line propagation. *Mon. Wea. Rev.*, **145**, 3419–3440.

Bouttier, F., 2001: The use of profiler data at ECMWF. *Meteorol. Zeitschrift*, **10**, 497–510.

Browell, E. V., S. Ismail, and W. B. Grant, 1998: Differential Absorption Lidar (DIAL) measurements from air and space. *Appl. Phys. B Lasers Opt.*, **67**, 399–410.

Brunelli, R., 2009: *Template Matching Techniques in Computer Vision: Theory and Practice*. Wiley.

Burgers, G., P. J. van Leeuwen, and G. Evensen, 1998: Analysis scheme in the ensemble Kalman filter. *Mon. Wea. Rev.*, **126**, 1719–1724.

Carbone, R. E., J. W. Conway, N. A. Crook, and M. W. Moncrieff, 1990: The generation and propagation of a nocturnal squall line. Part I: Observations and implications for mesoscale predictability. *Mon. Wea. Rev.*, **118**, 26–49.

Carroll, B. J., B. B. Demoz, D. D. Turner, and R. Delgado, 2021: Lidar observations of a mesoscale moisture transport event impacting convection and comparison to Rapid Refresh model analysis. *Mon. Wea. Rev.*, **149**, 463–477.

Charney, J. G., R. Fjörtoft, and J. von Neumann, 1950: Numerical integration of the barotropic vorticity equation. *Tellus*, **2**, 237–254.

Chipilski, H. G., X. Wang, and D. B. Parsons, 2018: Object-based algorithm for the identification and tracking of convective outflow boundaries in numerical models. *Mon. Wea. Rev.*, **146**, 4179–4200.

Chipilski, H. G., X. Wang, and D. B. Parsons, 2020: Impact of assimilating PECAN profilers on the prediction of bore-driven nocturnal convection: a multi-scale forecast evaluation for the 6 July 2015 case study. *Mon. Wea. Rev.*, **143**, 1147–1175.

Chou, M.-D., and M. J. Suarez, 1994: An efficient thermal infrared radiation parameterization for use in general circulation models. NASA Tech. Memo. 104606, Vol. 3, NASA/Goddard Space Flight Center, Greenbelt, MD 20771, 85 pp.

Clark, A. J., R. G. Bullock, T. L. Jensen, M. Xue, and F. Kong, 2014: Application of object-based time-domain diagnostics for tracking precipitation systems in convection-allowing models. *Wea. Forecasting*, **29**, 517–542.

Clark, A. J., W. A. Gallus, and T. C. Chen, 2007: Comparison of the diurnal precipitation cycle in convection-resolving and non-convection-resolving mesoscale models. *Mon. Wea. Rev.*, **135**, 3456–3473.

Clark, A. J., A. MacKenzie, A. McGovern, V. Lakshmanan, and R. A. Brown, 2015: An automated, multiparameter dryline identification algorithm. *Wea. Forecasting*, **30**, 1781–1794.

Cohn, S., 1997: An introduction to estimation theory. *J. Met. Soc. Jap.*, **75**, 257–288.

COMET® Program, 2018: Rapid scan applications and benefits. UCAR, http://kejian1.cmatc.cn/vod/comet/EUMETSAT/rapid_scan/navmenu.php_tab_1_page_6_0_0_type_flash.htm.

Coniglio, M. C., G. S. Romine, D. D. Turner, and R. D. Torn, 2019: Impacts of targeted AERI and Doppler lidar wind retrievals on short-term forecasts of the initiation and early evolution of thunderstorms. *Mon. Wea. Rev.*, **147**, 1149–1170.

Courtier, P., J.-N. Thépaut, and A. Hollingsworth, 1994: A strategy for operational implementation of 4D-Var, using an incremental approach. *Q. J. R. Meteorol. Soc.*, **120**, 1367–1388.

Cram, J. M., M. L. Kaplan, C. A. Mattocks, and J. W. Zack, 1991: The use and analysis of profiler winds to derive mesoscale height and temperature fields: Simulation and real-data experiments. *Mon. Wea. Rev.*, **119**, 1040–1056.

Crook, N. A., 1986: The effect of ambient stratification and moisture on the motion of atmospheric undular bores. *J. Atmos. Sci.*, **43**, 171–181.

Crook, N. A., 1996: Sensitivity of moist convection forced by boundary layer processes to low-level thermodynamic fields. *Mon. Wea. Rev.*, **124**, 1767–1785.

Crook, N. A., R. E. Carbone, M. W. Moncrieff, and J. W. Conway, 1990: The generation and propagation of a nocturnal squall line. Part II: Numerical simulations. *Mon. Wea. Rev.*, **118**, 50–66.

Crook, N. A., and M. W. Moncrieff, 1988: The effect of large-scale convergence on the generation and maintenance of deep moist convection. *J. Atmos. Sci.*, **45**, 3606–3624.

Crum, T. D., and R. L. Alberty, 1993: The WSR-88D and the WSR-88D operational support facility. *Bull. Amer. Meteor. Soc.*, **27**, 1669–1687.

Dai, G., and Coauthors, 2018: Calibration of raman lidar water vapor profiles by means of aeronet photometer observations and gdas meteorological data. *Atmos. Meas. Tech.*, **11**, 2735–2748.

Davis, C. A., B. G. Brown, and R. Bullock, 2006: Object-based verification of precipitation forecasts. Part I: Methodology and application to mesoscale rain areas. *Mon. Wea. Rev.*, **134**, 1772–1784.

Davis, C. A., B. G. Brown, and R. Bullock, 2009a: Spatial and temporal object-based evaluation of numerical prediction forecasts. *23rd Conf. on Weather Analysis and Forecasting/19th Conf. on Numerical Weather Prediction*, Omaha, NE, Amer. Meteor. Soc.

Davis, C. A., B. G. Brown, R. Bullock, and H.-G. J, 2009b: The method for object-based diagnostic evaluation (MODE) applied to numerical forecasts from the 2005 NSSL/SPC spring program. *Wea. Forecasting*, **24**, 1252–1267.

Davis, C. A., K. W. Wanning, R. E. Carbone, S. B. Trier, and J. D. Tuttle, 2003: Coherence of warm-season continental rainfall in numerical weather prediction models. *Mon. Wea. Rev.*, **131**, 2667–2679.

Dee, D. P., and A. M. da Silva, 2003: The choice of variable for atmospheric moisture analysis. *Mon. Wea. Rev.*, **131**, 155–171.

Degelia, S. K., and X. Wang, 2021: Impacts of flow-dependent and static observation error estimation for the frequent assimilation of thermodynamic profilers on convective-scale forecasts. *Mon. Wea. Rev.*, in review.

Degelia, S. K., X. Wang, and D. Stensrud, 2019: An evaluation of the impact of assimilating AERI retrievals, kinematic profilers, rawinsondes, and surface observations on a forecast of a nocturnal convection initiation event during the PECAN field campaign. *Mon. Wea. Rev.*, **147**, 2739–2764.

Degelia, S. K., X. Wang, D. Stensrud, and D. D. Turner, 2020: Systematic evaluation of the impact of assimilating a network of ground-based remote sensing profilers for forecasts of nocturnal convection initiation during PECAN. *Mon. Wea. Rev.*, **148**, 4703–4728.

Delanoy, R. L., and S. W. Troxel, 1993: Machine intelligent gust front detection. *Linc. Lab. J.*, **6**, 187–212.

Delanoy, R. L., J. G. Verly, and D. E. Dudgeon, 1992: Functional templates and their application to 3-d object recognition. *ICASSP-92: 1992 IEEE International Conference on Acoustics, Speech, and Signal Processing*, San Francisco, CA, IEEE.

Denis, B., J. Côté, and R. Laprise, 2002: Spectral decomposition of two-dimensional atmospheric fields on limited-area domains using the Discrete Cosine Transform (dct). *Mon. Wea. Rev.*, **130**, 1812–1829.

Dijkstra, E. W., 1959: A note on two problems in connection with graphs. *Numeric. Math.*, **271**, 269–271.

Dougherty, E. R., 1992: *An Introduction to Morphological Image Processing*. SPIE Optical Engineering Press.

Dougherty, E. R., and R. A. Lotufo, 2003: *Hands-On Morphological Image Processing*. SPIE Digital Library.

Drager, A. J., and S. C. van den Heever, 2017: Characterizing convective cold pools. *J. Adv. Model. Earth Syst.*, **9**, 1091–1115.

Du, J., G. DiMego, B. Zhou, D. Jovic, B. Ferrier, B. Yang, and B. S, 2014: NCEP regional ensembles: Evolving toward hourly-updated convection-allowing scale and storm-scale predictions within a unified regional modeling system. *26th Conf. on Weather Analysis and Forecasting/22nd Conf. on Numerical Weather Prediction*, Atlanta, GA, American Meteorological Society.

Eilts, M. D., S. Olson, G. J. Strumpf, L. G. Hermes, J. C. Abrevaya, K. Thomas, K. Hondl, and D. Klingle-Wilson, 1991: An improved gust front detection algorithm for the TDWR. *Proc. 4th Intl. Conf. on the Aviation Weather System*, Paris, France, J37.

Evensen, G., 1994: Sequential data assimilation with a nonlinear quasi-geostrophic model using monte carlo methods to forecast error statistics. *J. Geophys. Res.*, **99**, 10 143–10 162.

Feltz, W. F., W. L. Smoth, H. B. Howell, R. O. Knuteson, H. Woolf, and H. E. Revercomb, 2003: Near-continuous profiling of temperature, moisture, and atmospheric stability using the Atmospheric Emitted Radiance Interferometer (AERI). *J. Appl. Meteor.*, **42**, 584–597.

Ferrare, R. A., A. Nehrir, S. Kooi, C. Butler, and A. Notari, 2016: NASA DC-8 LASE Data. Version 1.0. UCAR/NCAR - Earth Observing Laboratory, accessed 14 April 2019, doi:https://doi.org/10.5065/D69C6VM6.

Fourriè, N., M. Nuret, P. Brousseau, and O. Caumont, 2021: Data assimilation impact studies with the AROME-WMED reanalysis of the first special observation period of the Hydrological cycle in the Mediterranean Experiment. *Nat. Hazards Earth Syst. Sci.*, **21**, 463–480.

Fovell, R. G., G. L. Mullendore, and S.-H. Kim, 2006: Discrete propagation in numerically simulated nocturnal squall lines. *Mon. Wea. Rev.*, **134**, 3735–3752.

French, A. J., and M. D. Parker, 2010: The response of simulated nocturnal convective systems to a developing low-level jet. *J. Atmos. Sci.*, **67**, 3384–3408.

Gaspari, G., and S. E. Cohn, 1999: Construction of correlation functions in two and three dimensions. *Quart. J. Roy. Meteor. Soc.*, **125**, 723–757.

Geerts, B., and Coauthors, 2017: The 2015 Plains Elevated Convection At Night (PECAN) field project. *Bull. Amer. Meteor. Soc.*, **98**, 767–787.

Gentine, P., A. Garelli, S.-B. Park, J. Nie, G. Torri, and Z. Kuang, 2016: Role of surface heat fluxes underneath cold pools. *Geophys. Res. Lett.*, **43**, 874–883.

Goff, R. C., 1976: Vertical structure of thunderstorm outflows. *Mon. Wea. Rev.*, **104**, 1429–1440.

Grasmick, C., B. Geerts, D. D. Turner, Z. Wang, and T. M. Weckwerth, 2018: The relation between nocturnal MCS evolution and its outflow boundaries in the stable boundary layer: an observational study of the 15 July 2015 MCS in PECAN. *Mon. Wea. Rev.*, **146**, 3203–3226.

Grell, G. A., 1993: Prognostic evaluation of assumptions used by cumulus parameterizations. *Mon. Wea. Rev.*, **121**, 764–787.

Grell, G. A., and D. Devenyi, 2002: A generalized approach to parameterizing convection combining ensemble and data assimilation techniques. *Geophys. Res. Lett.*, **29**, 1–4.

Grell, G. A., and S. R. Freitas, 2014: A scale and aerosol aware stochastic convective parameterization for weather and air quality modeling. *Atmos. Chem. Phys.*, **14**, 5233–5250.

Guo, Y.-R., Y.-H. Kuo, J. Dudhia, D. B. Parsons, and C. Rocken, 2000: Four-dimensional variational data assimilation of heterogeneous mesoscale observations for a strong convective case. *Mon. Wea. Rev.*, **128**, 619–643.

Haghi, K. R., 2017: Theory and observations of bores in the nocturnal environment of the great plains. Ph.D. thesis, University of Oklahoma.

Haghi, K. R., and D. R. Durran, 2021: On the dynamics of atmospheric bores. *J. Atmos. Sci.*, **78**, 313–327.

Haghi, K. R., D. B. Parsons, and B. T. Blake, 2015: Forecasting bores during PECAN 2015: a case study. *16th Conf. on Mesoscale Processes*, Boston, MA, Amer. Meteor. Soc., 13.5.

Haghi, K. R., D. B. Parsons, and A. Shapiro, 2017: Bores observed during IHOP_2002: the relationship of bores to the nocturnal environment. *Mon. Wea. Rev.*, **145**, 3929–3946.

Haghi, K. R., and Coauthors, 2018: Bore-ing into nocturnal convection. *Bull. Amer. Meteor. Soc.*, **100**, 1103–1121.

Hartung, D. C., J. A. Otkin, R. A. Petersen, D. D. Turner, and W. F. Feltz, 2011: Assimilation of surface-based boundary layer profiler observations during a cool-season weather event using an observing system simulation experiment. Part II: Forecast assessment. *Mon. Wea. Rev.*, **139**, 2327–2346.

Helmus, J. J., and S. M. Collis, 2016: The Python ARM Radar Toolkit (Py-ART), a library for working with weather radar data in the Python programming language. *J. Open Res. Softw.*, **4**, 1–6.

Hitchcock, S. M., R. S. Schumacher, G. Herman, M. C. Coniglio, M. D. Parker, and C. L. Ziegler, 2019: Evolution of pre- and postconvective environmental profiles from mesoscale convective systems during pecan. *Mon. Wea. Rev.*, **147**, 2329–2354.

Hogg, D. C., F. O. Guiraud, J. B. Snider, M. T. Decker, and E. R. Westwater, 1983a: A steerable dual-channel microwave radiometer for measurement of water vapor and liquid in the troposphere. *J. Clim. Appl. Meteorol.*, **22**, 789–806.

Hogg, D. C., and Coauthors, 1983b: An automatic profiler of the temperature, wind and humidity in the troposphere. *J. Clim. Appl. Meteorol.*, **58**, 807–831.

Hong, S., and J. J. Lim, 2006: The WRF single-moment 6-class microphysics scheme (WSM6). *J. Korean Meteor. Soc.*, **42**, 129–151.

Houghton, D. D., and A. Kasahara, 1968: Nonlinear shallow fluid flow over an isolated ridge. *Comm. on Pure and Applied Math.*, **21**, 1–23.

Hu, J., N. Yussouf, D. D. Turner, T. A. Jones, and X. Wang, 2019: Impact of ground-based remote sensing boundary layer observations on short-term probabilistic forecasts of a tornadic supercell event. *Wea. Forecasting*, **34**, 1453–1476.

Hutchinson, C. E., 1984: The Kalman filter applied to aerospace and electronic systems. *IEEE Trans. Aero. Elect. Syst.*, **AES-20**, 500–5004.

Iacono, M. J., J. S. Delamere, E. J. Mlawer, M. W. Shephard, S. A. Clough, and W. D. Collins, 2008: Radiative forcing by long-lived greenhouse gases: Calculations with the AER radiative transfer models. *J. Geophys. Res.*, **113**, 1–8.

Illingworth, A. J., and Coauthors, 2019: How can existing ground-based profiling instruments improve European weather forecasts? *Bull. Amer. Meteor. Soc.*, **100**, 605–619.

Ingleby, B., C. Burrows, and S. Healy, 2020: Coordinated response mitigates loss of aircraft-based weather data. ECMWF, https://www.ecmwf.int/en/newsletter/164/news/coordinated-response-mitigates-loss-aircraft-based-weather-data.

IPCC, 2007: Climate Change 2007: The Physical Science Basis. Contribution of Working Group I to the Fourth Assessment Report of the Intergovernmental Panel on Climate Change [Solomon, S., D. Qin, M. Manning, Z. Chen, M. Marquis, K.B. Averyt, M. Tignor and H.L. Miller (eds.)]. Cambridge University Press, Cambridge, United Kingdom and New York, NY, USA, 996 pp. Tech. rep., IPCC.

Janjić, T., and Coauthors, 2018: On the representation error in data assimilation. *Quart. J. Roy. Meteor. Soc.*, **144**, 1257–1278.

Jazwinski, A. H., 1970: *Stochastic processes and filtering theory*. Academic Press.

Johnson, A., and X. Wang, 2012: Verification and calibration of neighborhood and object-based probabilistic precipitation forecasts from a multimodel convection-allowing ensemble. *Mon. Wea. Rev.*, **140**, 3054–3077.

Johnson, A., and X. Wang, 2013: Object-based evaluation of a storm-scale ensemble during the 2009 NOAA Hazardous Weather Testbed spring experiment. *Mon. Wea. Rev.*, **141**, 1079–1098.

Johnson, A., and X. Wang, 2017: Design and implementation of a GSI-based convection-allowing ensemble data assimilation and forecast system for the PECAN field experiment. Part I: Optimal configurations for nocturnal convection prediction using retrospective cases. *Wea. Forecasting*, **32**, 289–315.

Johnson, A., and X. Wang, 2019: Multicase assessment of the impacts of horizontal and vertical grid spacing, and turbulence closure model, on subkilometer-scale simulations of atmospheric bores during PECAN. *Mon. Wea. Rev.*, **147**, 1533–1555.

Johnson, A., X. Wang, J. R. Carley, L. J. Wicker, and C. Karstens, 2015: A comparison of multiscale GSI-based EnKF and 3DVar data assimilation using radar and conventional observations for midlatitude convective-scale precipitation forecasts. *Mon. Wea. Rev.*, **143**, 3087–3108.

Johnson, A., X. Wang, K. R. Haghi, and D. B. Parsons, 2018: Evaluation of forecasts of a convectively generated bore using an intensively observed case study from PECAN. *Mon. Wea. Rev.*, **146**, 3097–3122.

Johnson, A., X. Wang, F. Kong, and M. Xue, 2011a: Hierarchical cluster analysis of a convection-allowing ensemble during the Hazardous Weather Testbed 2009 spring experiment. Part I: Development of the object-oriented cluster analysis method for precipitation fields. *Mon. Wea. Rev.*, **139**, 3673–3693.

Johnson, A., X. Wang, F. Kong, and M. Xue, 2013: Object-based evaluation of the impact of horizontal grid spacing on convection-allowing forecasts. *Mon. Wea. Rev.*, **141**, 3413–3425.

Johnson, A., X. Wang, M. Xue, and F. Kong, 2011b: Hierarchical cluster analysis of a convection-allowing ensemble during the Hazardous Weather Testbed 2009 spring experiment. Part II: Ensemble clustering over the whole experiment period. *Mon. Wea. Rev.*, **139**, 3694–3710.

Jorgensen, D. P., C. L. Ziegler, and T. Schuur, 2016: NOAA P-3 1Hz Flight Level Data. Version 1.0. UCAR/NCAR - Earth Observing Laboratory, accessed 14 April 2019, doi:https://doi.org/10.5065/D67D2SB0.

Kain, J. S., 2004: The Kain–Fritsch convective parameterization: an update. *J. Appl. Meteorol.*, **41**, 170–181.

Kalman, R. E., 1960: A new approach to linear filtering and prediction problems. *J. Basic Eng.*, **82**, 35–45.

Kamineni, R., T. N. Kirshnamurti, R. A. Ferrare, S. Ismail, and E. V. Browell, 2003: Impact of high resolution water vapor cross-sectional data on hurricane forecasting. *Geophys. Res. Lett.*, **30**, 1–4.

Kamineni, R., T. N. Krishnamurti, S. Pattnaik, E. V. Browell, S. Ismail, and R. A. Ferrare, 2006: Impact of CAMEX-4 datasets for hurricane forecasts using a global model. *J. Atmos. Sci.*, **63**, 151–174.

Karyampudi, V. M., S. E. Koch, C. Chen, J. W. Rottman, and M. L. Kaplan, 1995: The influence of the Rocky mountains on the 13–14 april 1986 severe weather outbreak. Part II: Evolution of a prefrontal bore and its role in triggering a squall line. *Mon. Wea. Rev.*, **123**, 1423–1446.

Kawabata, T., H. Iwai, H. Seko, Y. Shoji, K. Saito, S. Ishii, and K. Mizutani, 2014: Cloud-resolving 4d-var assimilation of Doppler wind lidar data on a meso-gamma-scale convective system. *Mon. Wea. Rev.*, **142**, 4484–4498.

Khodkar, M. A., M. M. Nasr-Azadani, and E. Meiburg, 2018: Gravity currents propagating into two-layer stratified fluids: vorticity-based models. *J. Fluid Mech.*, **844**, 994–1025.

Klein, P., D. D. Turner, E. Smith, and J. Gebauer, 2016: Mobile PISA 1 OU/NSSL CLAMPS radiosonde data, version 1.0. UCAR/NCAR - Earth Observing Laboratory, accessed 01 June 2018, doi:https://dx.doi.org/10.5065/D6416VDH.

Knupp, K., 2015: Mobile PISA 2 UAH MIPS Radiosonde Data. Version 1.0. UCAR/NCAR - Earth Observing Laboratory, accessed 14 April 2019, doi:https://doi.org/10.5065/D6MC8X3V.

Knuteson, R. O., and Coauthors, 2004a: Atmospheric Emitted Radiance Interferometer. Part I: Instrument design. *J. Atmos. Ocean. Technol.*, **21**, 1763–1776.

Knuteson, R. O., and Coauthors, 2004b: Atmospheric Emitted Radiance Interferometer. Part II: Instrument performance. *J. Atmos. Ocean. Technol.*, **21**, 1777–1789.

Koch, S. E., and W. L. Clark, 1999: A nonclassical cold front observed during COPS-91: Frontal structure and the process of severe storm initiation. *J. Atmos. Sci.*, **56**, 2862–2890.

Koch, S. E., P. B. Dorian, R. Ferrare, S. H. Melfi, W. C. Skillman, and W. D, 1991: Structure of an internal bore and dissipating gravity current as revealed by Raman lidar. *Mon. Wea. Rev.*, **119**, 857–887.

Koch, S. E., W. Feltz, F. Fabry, M. Pagowski, B. Geerts, K. M. Bedka, D. O. Miller, and J. W. Wilson, 2008a: Turbulent mixing processes in atmospheric bores and solitary waves deduced from profiling systems and numerical simulation. *Mon. Wea. Rev.*, **136**, 1373–1400.

Koch, S. E., C. Flamat, J. W. Wilson, B. M. Gentry, and B. D. Jamison, 2008b: An atmospheric soliton observed with Doppler radar, differential absorption lidar, and a molecular Doppler lidar. *J. Atmos. Ocean. Technol.*, **25**, 1267–1287.

Kuo, Y.-H., E. G. Donall, and M. A. Shapiro, 1987: Feasibility of Short-Range numerical weather prediction using observations from a network of profilers. *Mon. Wea. Rev.*, **115**, 2402–2427.

Lakshmanan, V., 2012: *Automating the Analysis of Spatial Grids: a Practical Guide to Data Mining Geospatial Images for Human and Environmental Applications*. Springer Netherlands.

Lakshmanan, V., R. Rabin, and V. DeBrunner, 2003: Multiscale storm identification and forecast. *J. Atmos. Res.*, **67**, 367–380.

Lakshmanan, V., T. Smith, G. Stumpf, and K. Hondl, 2007: The warning decision support system-integrated information. *Wea. Forecasting*, **22**, 596–612.

Langhans, W., and D. M. Romps, 2015: The origin of water vapor rings in tropical oceanic cold pools. *Geophys. Res. Lett.*, **42**, 7825–7834.

Leuenberger, D., A. Haefele, N. Omanovic, M. Fengler, G. Martucci, B. Calpini, O. Fuhrer, and A. Rossa, 2020: Improving high-impact Numerical Weather Prediction with lidar and drone observations. *Bull. Amer. Meteor. Soc.*, **101**, 1036–1051.

Lewis, W. E., T. J. Wagner, J. A. Otkin, and T. A. Jones, 2020: Impact of AERI temperature and moisture retrievals on the simulation of a Central Plains severe convective weather event. *Atmosphere*, **11**, 1–20.

Li, L., N. Xie, L. Fu, K. Zhang, A. Shao, Y. Yang, and X. Ren, 2020: Impact of lidar data assimilation on low-level wind shear simulation at lanzhou zhongchuan international airport, china: A case study. *Atmosphere*, **11**, 1–14.

Li, Y., and R. B. Smith, 2010: The detection and significance of diurnal pressure and potential vorticity anomalies east of the Rockies. *J. Atmos. Sci.*, **67**, 2734–2751.

Li, Z., P. Zuidema, and P. Zhu, 2014: Simulated convective invigoration processes at trade wind cumulus cold pool boundaries. *J. Atmos. Sci.*, **71**, 2823–2841.

Lilly, D. K., and D. Perkey, 1976: Sensitivity of mesoscale predictions to mesoscale initial data. *Quart. J. Roy. Meteor. Soc.*, **116**, 779–798.

Lin, G., C. Grasmick, B. Geerts, Z. Wang, and M. Deng, 2021: Convection initiation and bore formation following the collision of mesoscale boundaries over a developing stable boundary layer: a case study from PECAN. *Mon. Wea. Rev.*, **149**, 2351–2367.

Liu, C., and M. W. Moncrieff, 2002: A numerical study of the effects of ambient flow and shear on density currents. *Mon. Wea. Rev.*, **124**, 2282–2303.

Locatelli, J. D., M. T. Stoelinga, and P. V. Hobbs, 2002: A new look at the super outbreak of tornadoes on 3–4 April 1974. *Mon. Wea. Rev.*, **130**, 1633–1651.

Loehrer, S. M., T. A. Edmands, and J. A. Moore, 1996: TOGA COARE upper-air sounding data archive: Development and quality control procedures. *Bull. Amer. Meteor. Soc.*, **77**, 2651–2672.

Long, R. R., 1954: Some aspects of the flow of stratified fluids, II. Experiments with a two-fluid system. *Tellus*, **6**, 97–115.

Long, R. R., 1974: Some experimental observations of upstream disturbances in a two-fluid system. *Tellus*, **26**, 313–317.

Loveless, D. M., T. J. Wagner, D. D. Turner, S. A. Ackerman, and W. F. Feltz, 2019: A composite perspective on bore passage during the PECAN campaign. *Mon. Wea. Rev.*, **147**, 1395–1413.

Lynch, P., and X.-Y. Huang, 1992: Initialization of the HIRLAM model using a digital filter. *Mon. Wea. Rev.*, **120**, 1019–1034.

Maddox, R. A., 1980: Mesoscale convective complexes. *Bull. Amer. Meteor. Soc.*, **61**, 1374–1387.

Mandel, J., L. Cobb, and J. Breezley, 2011: On the convergence of the ensemble Kalman filter. *Applied Mathematics*, **56**, 533–541.

Martin, E. R., and R. H. Johnson, 2008: An observational and modeling study of an atmospheric internal bore during NAME 2004. *Mon. Wea. Rev.*, **136**, 4150–4167.

Martinet, P., D. Cimini, F. De Angelis, G. Canut, V. Unger, R. Guillot, D. Tzanos, and A. Paci, 2017: Combining ground-based microwave radiometer and the arome convective scale model through 1dvar retrievals in complex terrain: an alpine valley case study. *Atmos. Meas. Tech.*, **10**, 3385–3402.

Martinet, P., A. Dabas, J.-M. Donier, T. Douffet, O. Garrouste, and R. Guillot, 2015: 1D-Var temperature retrievals from microwave radiometer and convective scale model. *Tellus A: Dynamic Meteor. And Ocean.*, **67**, 1–14.

Melfi, S. H., and D. Whiteman, 1985: Observation of lower-atmospheric moisture structure and its evolution using a raman lidar. *Bull. Amer. Meteor. Soc.*, **66**, 1288–1292.

Melfi, S. H., D. Whiteman, and R. Ferrare, 1989: Observation of atmospheric fronts using raman lidar moisture measurements. *J. Appl. Meteor.*, **28**, 789–806.

Michalakes, J., J. Dudhia, D. Gill, T. Henderson, J. Klemp, W. Skamarock, and W. Wang, 2004: The Weather Research and Forecast Model: Software architecture and performance. *11th ECMWF Workshop on the Use of High Performance Computing In Meteorology*, 25–29 October 2004, Reading U.K.

Miller, R. L., C. L. Ziegler, and M. I. Biggerstaff, 2020: Seven-Doppler radar and in situ analysis of the 25-26 June 2015 Kansas MCS during PECAN. *Mon. Wea. Rev.*, **148**, 211–240.

Mlawer, E. J., S. J. Taubman, P. D. Brown, M. J. Iacono, and S. A. Clough, 1997: Radiative transfer for inhomogeneous atmospheres: RRTM, a validated correlated-k model for the longwave. *J. Geophys. Res. Atmos.*, **102**, 16 663–16 682.

Moore, A. S., and Coauthors, 1997: Development of the Lidar Atmospheric Sensing Experiment (LASE) - an advanced airborne DIAL instrument. *Advances in Atmospheric Remote Sensing with Lidar*, A. Ansmann, R. Neuber, P. Rairoux, and U. Wandinger, Eds., Springer, 281–288.

Mueller, D., B. Geerts, Z. Wang, M. Deng, and C. Grasmick, 2017: Evolution and vertical structure of an undular bore observed on 20 june 2015 during PECAN. *Mon. Wea. Rev.*, **145**, 3775–3794.

Nakanishi, M., and H. Niino, 2006: An improved Mellor–Yamada level-3 model: its numerical stability and application to a regional prediction of advection fog. *Bound.-Layer Meteor.*, **119**, 397–407.

Nasr-Azadani, M. M., and E. Meiburg, 2016: Gravity currents propagating into ambients with arbitrary shear and density stratification: vorticity-based modelling. *Bound.-Layer Meteor.*, **119**, 397–407.

National Academy of Sciences, Engineering and Medicine, 2018: Thriving on our changing planet: A decadal strategy for earth observation from space. National Academies Press, Washington, D.C., https://www.nap.edu/catalog/24938. Tech. rep., NAS.

National Research Council, 2009: Observing weather and climate from the ground up: A nationwide network of networks. Tech. rep., The National Academies of Sciences, Engineering and Medicine, National Academies Press, Washington, D.C. https://doi.org/10.17226/12540.

National Research Council, 2010: When weather matters: Science and service to meet critical societal needs. Tech. rep., The National Academies of Sciences, Engineering and Medicine, National Academies Press, Washington, D.C. https://doi.org/10.17226/12888.

National Research Council, 2012: Weather services for the nation: Becoming second to none. Tech. rep., The National Academies of Sciences, Engineering and Medicine, National Academies Press, Washington, D.C. https://doi.org/10.17226/13429.

Oliveira, M. I., E. L. Nascimento, and C. Kannenberg, 2018: A new look at the identification of low-level jets in south america. *Mon. Wea. Rev.*, **146**, 2315–2334.

Orlanski, I., 1975: A rational subdivision of scales for atmospheric processes. *Bull. Amer. Meteor. Soc.*, **56**, 527–530.

Otkin, J. A., D. C. Hartung, D. D. Turner, R. A. Petersen, W. F. Feltz, and E. Janzon, 2011: Assimilation of surface-based boundary layer profiler observations during a cool-season weather event using an Observing System Simulation Experiment. Part I: Analysis impact. *Mon. Wea. Rev.*, **139**, 2309–2326.

Parker, M. D., 2008: Response of simulated squall lines to low-level cooling. *J. Atmos. Sci.*, **65**, 1323–1341.

Parker, M. D., 2021: Self-organization and maintenance of simulated nocturnal convective systems from PECAN. *Mon. Wea. Rev.*, **149**, 999–1022.

Parker, M. D., B. S. Borchardt, R. L. Miller, and C. L. Ziegler, 2020: Simulated evolution and severe wind production by the 25-26 June 2015 nocturnal MCS from PECAN. *Mon. Wea. Rev.*, **148**, 183–209.

Parrish, D. F., and J. C. Derber, 1992: The National Meteorological Center's spectral statistical-interpolation analysis system. *Mon. Wea. Rev.*, **120**, 1747–1763.

Parsons, D. B., K. R. Haghi, K. T. Halbert, B. Elmer, and J. Wang, 2019a: The potential role of atmospheric bores in the initiation and maintenance of nocturnal convection over the southern Great Plains. *J. Atmos. Sci.*, **76**, 43–68.

Parsons, D. B., S. P. Lillo, C. P. Rattray, P. Bechtold, M. J. Rodwell, and C. M. Bruce, 2019b: The role of continental mesoscale convective systems in forecast busts within global weather prediction systems. *Atmosphere*, **10**, 681.

Penny, S. G., and T. M. Hamill, 2017: Coupled data assimilation for integrated Earth system analysis and prediction. *Bull. Amer. Meteor. Soc.*, **98**, ES169–ES172.

Persson, A., 2020: Right for the wrong reason?: A new look at the 6 June 1944 D-Day forecast by a neutral Swede. *Bull. Amer. Meteor. Soc.*, **101**, E993–E1006.

Potter, J. E., 1964: W matrix augmentation. MIT Instrumentation Laboratory Memo SGA 5-64, Cambridge, Massachusetts, January 1964. Tech. rep., MIT.

Powers, J. G., and Coauthors, 2017: The Weather Research and Forecasting model: Overview, system efforts, and future directions. *Bull. Amer. Meteor. Soc.*, **98**, 1717–1737.

Pratt, L. J., 1983: A note on nonlinear flow over obstacles. *Geophys. Astrophys. Fluid Dyn.*, **24**, 63–68.

Qi, Y., S. Fan, J. Mao, B. Li, C. Guo, and S. Zhang, 2021: Impact of assimilating ground-based microwave radiometer data on the precipitation bifurcation forecast: A case study in beijing. *Atmosphere*, **12**, 551.

Reif, D. W., 2020: Initiation mechanisms of nocturnal convection without nearby surface boundaries over the Great Plains. Ph.D. thesis, University of Oklahoma.

Reitebuch, O., C. Werner, I. Leike, P. Delville, P. H. Flamant, A. Cress, and D. Engelbart, 2001: Experimental validation of wind profiling performed by the airborne 10-µm heterodyne doppler lidar WIND. *J. Atmos. Oceanic Technol.*, **18**, 1331–1344.

Reiter, P., G. O, L. Schefczyk, G. Heinemann, and M. Casper, 2018: Does applying quantile mapping to subsamples improve the bias correction of daily precipitation? *Int. J. Climatol.*, **38**, 1623–1633.

Revercomb, H. E., B. H, H. B. Howell, D. D. LaPorte, W. L. Smith, and L. A. Sromovsky, 1988: Radiometric calibration of IR fourier transform spectrometers: solution to a problem with the High-Resolution Interferometer Sounder. *Appl. Opt.*, **27**, 3210–3218.

Rogers, E., and Coauthors, 2009: NCEP North American mesoscale modeling system: Recent changes and future plans. *19th Conf. on Numerical Weather Prediction and 23rd Conf. on Weather Analysis and Forecasting*, Omaha, NE, Amer. Meteor. Soc., 2A.4.

Rottman, J., and J. Simpson, 1989: The formation of internal bores in the atmosphere: a laboratory model. *Q. J. R. Meteorol. Soc.*, **115**, 941–963.

Rotunno, R., J. B. Klemp, and M. L. Weisman, 1988: A theory for strong, long-lived squall lines. *J. Atmos. Sci.*, **45**, 463–485.

Schwartz, C. S., and Coauthors, 2010: Toward improved convection-allowing ensembles: Model physics sensitivities and optimizing probabilistic guidance with small ensemble membership. *Wea. Forecasting*, **25**, 263–280.

Scorer, R. S., 1949: Theory of waves in the lee of mountains. *Q. J. R. Meteorol. Soc.*, **75**, 41–56.

Seigel, R. B., 2014: Shallow cumulus mixing and subcloud-layer responses to variations in aerosol loading. *J. Atmos. Sci.*, **71**, 2581–2603.

Shapiro, A., E. Fedorovich, and S. Rahimi, 2016: A unified theory for the Great Plains nocturnal low-level jet. *J. Atmos. Sci.*, **73**, 3037–3057.

Skamarock, W. C., and Coauthors, 2008: A description of the Advanced Research WRF version 3. Tech. Note NCAR/TN-4751STR, NCAR.

Smalley, D. J., B. J. Bennett, and R. Frankel, 2005: MIGFA: the Machine Intelligent Gust Front Algorithm for NEXRAD. *32nd Conference on Radar Meteorology/11th Conference on Mesoscale Processes*, Albuquerque, NM, Amer. Meteor. Soc.

Smith, E. N., G. J. Gebauer, P. M. Klein, E. Fedorovich, and J. A. Gibbs, 2019: The Great Plains low-level jet during PECAN: Observed and simulated characteristics. *Mon. Wea. Rev.*, **147**, 1845–1869.

Smith, S., A. Witt, M. D. Eilts, L. G. Hermes, K.-W. D, S. Olson, and J. P. Stanford, 1989: Gust front detection algorithm for the terminal Doppler weather radar. Part I: Current status. *Proc. 3rd Intl. Conf. on the Aviation Weather System*, Anaheim, CA, 31.

Smith, T. J., S. G. Benjamin, J. M. Brown, S. Weygandt, T. Smirnova, and B. Schwartz, 2008: Convection forecasts from the hourly updated, 3-km High Resolution Rapid Refresh (HRRR) model. *24th Conf. on Severe Local Storms*, Savannah, GA, Amer. Meteor. Soc.

Smith, T. L., and S. G. Benjamin, 1993: Impact of network wind profiler data on a 3-h data assimilation system. *Bull. Amer. Meteor. Soc.*, **74**, 801–807.

Snyder, C., and F. Zhang, 2003: Assimilation of simulated Doppler radar observations with an ensemble Kalman filter. *Mon. Wea. Rev.*, **131**, 1663–1677.

Soille, P., 2003: *Morphological Image Analysis: Principles and Applications*. Springer.

Stechman, D. M., G. M. McFarquhar, R. M. Rauber, B. F. Jewett, and R. A. Black, 2020: Composite in situ microphysical analysis of all spiral vertical profiles executed within BAMEX and PECAN mesoscale convective systems. *J. Atmos. Sci.*, **77**, 2541–2565.

Stewart, R. W., 1979: *The Atmospheric Boundary Layer*. WMO.

Surcel, M., M. Berenguer, and I. Zawadzki, 2010: The diurnal cycle of precipitation from continental radar mosaics and numerical weather prediction models. Part I: Methodology and seasonal comparison. *Mon. Wea. Rev.*, **138**, 3084–3106.

Tewari, M., and Coauthors, 2004: Implementation and verification of the unified Noah land surface model in the WRF model. *20th Conference on Weather Analysis and Forecasting/16th Conference on Numerical Weather Prediction*, Seattle, WA, Amer. Meteor. Soc., 14.2A, https://ams.confex.com/ams/84Annual/techprogram/paper_69061.htm.

Thompson, G., P. R. Field, R. M. Rasmussen, and W. D. Hall, 2008: Explicit forecasts of winter precipitation using an improved bulk microphysics scheme. Part II: Implementation of a new snow parameterization. *Mon. Wea. Rev.*, **136**, 5095–5115.

Thundathil, R., T. Schwitalla, A. Behrendt, S. K. Muppa, S. Adam, and V. Wulfmeyer, 2020: Assimilation of lidar water vapour mixing ratio and temperature profiles into a convection-permitting model. *J. Meteorol. Soc. Jpn.*, **98**, 959–986.

Tippett, M. K., J. L. Anderson, C. H. Bishop, T. M. Hamill, and J. S. Whitaker, 2003: Ensemble square root filters. *Mon. Wea. Rev.*, **131**, 1485–1490.

Tobias, O. J., and R. Seara, 2002: Image segmentation by histogram thresholding using fuzzy sets. *IEEE Trans. Image Process.*, **11**, 1457–1465.

Tompkins, A. M., 2001: Organization of tropical convection in low vertical wind shears: the role of water vapor. *J. Atmos. Sci.*, **58**, 529–545.

Toms, B. A., J. M. Tomaszewski, D. D. Turner, and S. E. Koch, 2017: Analysis of a lower tropospheric gravity wave train using direct and remote sensing measurement systems. *Mon. Wea. Rev.*, **145**, 2791–2812.

Torri, G., Z. Kuang, and Y. Tian, 2015: Mechanisms for convection triggering by cold pools. *Geophys. Res. Lett.*, **42**, 1943–1950.

Trenberth, K. E., A. Dai, R. M. Rasmussen, and D. B. Parsons, 2003: The changing character of precipitation. *Bull. Amer. Meteor. Soc.*, **84**, 1205–1217.

Trier, S., 2003: *Encyclopedia of Atmospheric Sciences*, chap. Convective Storms/Convective initiation. Elsevier.

Trier, S. B., and D. B. Parsons, 1993: Evolution of environmental conditions preceding the development of a nocturnal mesoscale convective complex. *Mon. Wea. Rev.*, **121**, 1078–1098.

Trier, S. B., J. W. Wilson, D. A. Ahijevych, and R. A. Sobash, 2017: Mesoscale vertical motions near nocturnal convection initiation in PECAN. *Mon. Wea. Rev.*, **145**, 2919–2941.

Troxel, S. W., R. L. Delanoy, J. P. Morgan, and W. L. Pughe, 1996: Machine Intelligent Gust Front Algorithm for the Terminal Doppler Weather Radar (TDWR) and Integrated Terminal Weather System (ITWS). *AMS Workshop on Wind Shear and Wind Shear Alert Systems*, Oklahoma City, Amer. Meteor. Soc., 70–79.

Turner, D. D., 2016a: FP4 AERIoe Thermodynamic Profile Retrieval Data. Version 2.0. UCAR/NCAR - Earth Observing Laboratory, accessed 14 April 2019, doi:https://doi.org/10.5065/D6PN93T3.

Turner, D. D., 2016b: MP1 OU/NSSL CLAMPS Doppler lidar VAD wind data, version 1.0. UCAR/NCAR – Earth Observation Laboratory, accessed 01 June 2018, doi:https://dx.doi.org/10.5065/D6BR8QJH0.

Turner, D. D., 2018: MP1 OU/NSSL CLAMPS AERIoe Thermodynamic Profile Retrieval Data. Version 1.2. UCAR/NCAR - Earth Observing Laboratory, accessed 14 April 2019, doi:https://doi.org/10.5065/D6VQ312C.

Turner, D. D., and U. Löhnert, 2014: Information content and uncertainties in thermodynamic profiles and liquid cloud properties retrieved from the ground-based Atmospheric Emitted Radiance Interferometer (AERI). *J. Appl. Meteor. Climatol.*, **53**, 752–771.

UCAR/NCAR, 2015: FP4 NCAR/EOL 915 MHz profiler NIMA consensus winds and moments, version 1.0. UCAR/NCAR – Earth Observation Laboratory, accessed 01 June 2018, doi:https://dx.doi.org/10.5065/D6RV0KXH.

UCAR/NCAR, 2016a: FP3 FP4 FP5 QC 5 min surface data, tilt corrected, version 1.0. UCAR/NCAR – Earth Observation Laboratory, accessed 01 June 2018, doi:https://dx.doi.org/10.5065/D6BZ645V.

UCAR/NCAR, 2016b: FP4 NCAR/EOL QC soundings, version 2.0. UCAR/NCAR – Earth Observation Laboratory, accessed 01 June 2018, doi:https://dx.doi.org/10.5065/D63776XH.

UCAR/NCAR, 2016c: MP4 NCAR/EOL MISS 915 MHz profiler 30 minute consensus winds and moments and surface meteorology data, version 1.0. UCAR/NCAR – Earth Observation Laboratory, accessed 01 June 2018, doi:https://dx.doi.org/10.5065/D6RJ4GPJ.

UCAR/NCAR, 2016d: MP4 NCAR/EOL QC soundings, version 2.0. UCAR/NCAR – Earth Observation Laboratory, accessed 01 June 2018, doi:https://dx.doi.org/10.5065/D6707ZNV.

Uyeda, H., and D. S. Zrnić, 1986: Automatic detection of gust fronts. *J. Atmos. Ocean. Technol.*, **3**, 36–50.

van Leeuwen, P. J., 2020: A consistent interpretation of the stochastic version of the ensemble Kalman filter. *Q. J. R. Meteorol. Soc.*, **146**, 1–11.

Vandenberghe, F., and R. Ware, 2002: 4-dimensional variational assimilation of ground-based microwave observations during a winter fog event. *Proceedings International Symposium on Atmospheric Sensing with GPS*, Tsukuba, Japan, http://radiometrics.com/wp-content/uploads/2012/08/Vandenberghe_Int.GPS_.Symp_2002.pdf.

Vickers, D., and L. Mahrt, 2004: Evaluating formulations of stable boundary layer height. *J. Appl. Meteorol.*, **43**, 1736–1749.

Wagner, T., D. D. Turner, and R. Newsom, 2016a: MP3 University of Wisconsin SPARC AERIoe thermodynamic profile data, version 1.0. UCAR/NCAR – Earth Observing Laboratory, accessed 01 June 2018, doi:https://dx.doi.org/10.5065/d60z71hc.

Wagner, T., D. D. Turner, and R. Newsom, 2016b: MP3 University of Wisconsin SPARC Doppler lidar VAD wind data, version 2.0. UCAR/NCAR - Earth Observing Laboratory., accessed 01 June 2018, doi:https://dx.doi.org/10.5065/D6V9869Bh.

Wagner, T., D. D. Turner, and R. Newsom, 2016c: MP3 University of Wisconsin SPARC surface meteorological data, version 1.0. UCAR/NCAR - Earth Observing Laboratory., accessed 01 June 2018, doi:https://dx.doi.org/10.5065/d6n014xz.

Wallace, J. M., 1975: Diurnal variations in precipitation and thunderstorm frequency over the conterminous united states. *Mon. Wea. Rev.*, **103**, 406–419.

Wandinger, U., 2005: Raman lidar. *Lidar: Range-resolved optical sensing of the atmosphere*, C. Weitkamp, Ed., Springer, 241–271.

Wang, C., Y. Chen, M. Chen, and J. Shen, 2020: Data assimilation of a dense wind profiler network and its impact on convective forecasting. *Atmos. Res.*, **238**, 1–12.

Wang, X., H. G. Chipilski, C. H. Bishop, E. Satterfield, N. Baker, and J. S. Whitaker, 2021: A multiscale local gain form ensemble transform kalman filter (MLGETKF). *Monthly Weather Review*, **149**, 605–622, https://doi.org/10.1175/MWR-D-20-0290.1.

Wang, X., D. Parrish, D. Kleist, and J. Whitaker, 2013: GSI 3DVar-based ensemble-variational hybrid data assimilation for NCEP Global Forecast System: single resolution experiments. *Mon. Wea. Rev.*, **141**, 4098–4117.

Wang, Y., and X. Wang, 2017: Direct assimilation of radar reflectivity without tangent linear and adjoint of the nonlinear observation operator in the GSI-based EnVar system: Methodology and experiment with the 8 May 2003 Oklahoma City tornadic supercell. *Mon. Wea. Rev.*, **145**, 1447–1471.

Wang, Z., and Coauthors, 2016: University of Wyoming King Air Compact Raman Lidar Data. Version 1.0. UCAR/NCAR - Earth Observing Laboratory, accessed 14 April 2019, doi:10.5065/D6MS3R0P.

Waugh, S., and C. Ziegler, 2017: NSSL mobile mesonet data, version 1.1. UCAR/NCAR - Earth Observing Laboratory, accessed 01 June 2018, doi:https://dx.doi.org/10.5065/D64M92RG.

Weber, B. L., and Coauthors, 1990: Preliminary evaluation of the first NOAA demonstration network wind profiler. *J. Atmos. Ocean. Technol.*, **7**, 909–918.

Weckwerth, T. M., and D. B. Parsons, 2006: A review of convection initiation and motivation for IHOP_2002. *Mon. Wea. Rev.*, **134**, 5–22.

Weckwerth, T. M., and U. Romatschke, 2019: Where, when, and why did it rain during PECAN? *Mon. Wea. Rev.*, **147**, 3557–3573.

Weckwerth, T. M., K. J. Weber, D. D. Turner, and S. M. Spuler, 2016: Validation of a water vapor micropulse differential absorption lidar (DIAL). *J. Atmos. Ocean. Technol.*, **33**, 2353–2372.

Weckwerth, T. M., J. W. Wilson, and R. M. Wakimoto, 1996: Thermodynamic variability within the Convective Boundary Layer due to horizontal convective rolls. *Mon. Wea. Rev.*, **124**, 769–784.

Wei, M., Z. Toth, R. Wobus, and Y. Zhu, 2008: Initial perturbations based on the ensemble transform (ET) technique in the NCEP global operational forecast system. *Tellus*, **60A**, 62–79.

Weisman, M. L., and R. Rotunno, 2004: "a theory for strong long-lived squall lines" revisited. *J. Atmos. Sci.*, **61**, 361–382.

Westwater, E. R., W. B. Sweezy, L. M. McMillin, and C. Dean, 1984: Determination of atmospheric temperature profiles from a statistical combination of ground-based profiler and operational 6/7 satellite retrievals. *J. Clim. Appl. Meteorol.*, **23**, 689–703.

Whitaker, J. S., and T. M. Hamill, 2002: Ensemble data assimilation without perturbed observations. *Mon. Wea. Rev.*, **130**, 1913–1924.

Whitaker, J. S., and T. M. Hamill, 2012: Evaluating methods to account for system errors in ensemble data assimilation. *Mon. Wea. Rev.*, **140**, 3078–3089.

White, B. L., and K. R. Helfrich, 2012: A general description of a gravity current front propagating in a two-layer stratified fluid. *J. Fluid Mech.*, **711**, 1–32.

White, B. L., and K. R. Helfrich, 2014: A model for internal bores in continuous stratification. *J. Fluid Mech.*, **761**, 282–304.

Whiteman, D. N., and Coauthors, 2006: Raman lidar measurements during the international h_2o project. Part II: Case studies. *J. Atmos. Ocean. Technol.*, **23**, 170–183.

Wilson, J. W., and R. D. Roberts, 2006: Summary of convective storm initiation and evolution during IHOP: Observational and modeling perspective. *Mon. Wea. Rev.*, **134**, 23–47.

WMO, 2021: Global Observing System. WMO, https://public.wmo.int/en/programmes/global-observing-system.

World Meteorological Organization, 2018: Statement of guidance for high-resolution numerical weather prediction (NWP). WMO rep., WMO, 10 pp.

Wulfmeyer, V., and Coauthors, 2015: A review of the remote sensing of lower tropospheric thermodynamic profiles and its indispensable role for the understanding and the simulation of water and energy cycles. *Rev. Geophys.*, **53**, 819–895.

Yoshida, S., S. Yokota, H. Seko, T. Sakai, and T. Nagai, 2020: Observation system simulation experiments of water vapor profiles observed by Raman lidar using LETKF system. *SOLA*, in press.

Zhang, J., and Coauthors, 2016a: Multi-Radar Multi-Sensor (MRMS) quantitative precipitation estimation: Initial operating capabilities. *Bull. Amer. Meteor. Soc.*, **97**, 621–638.

Zhang, L., and Z. Pu, 2011: Four-dimensional assimilation of multitime wind profiles over a single station and numerical simulation of a mesoscale convective system observed during IHOP_2002. *Mon. Wea. Rev.*, **139**, 3369–3388.

Zhang, X., Y. Luo, Q. Wan, W. Ding, and J. Sun, 2016b: Impact of assimilating wind profiling radar observations on convection-permitting quantitative precipitation forecasts during SCMREX. *Wea. Forecasting*, **31**, 1271–1292.

Ziegler, C., M. Coniglio, M. Parker, and R. Schumacher, 2016: CSU/NCSU/NSSL MGAUS radiosonde data, version 3.0. UCAR/NCAR - Earth Observing Laboratory, accessed 01 June 2018, doi:https://dx.doi.org/10.5065/D6W66HXN.

Zuidema, P., G. Torri, C. Muller, and A. Chandra, 2017: A survey of precipitation-induced atmospheric cold pools over oceans and their interactions with the larger-scale environment. *Surv. Geophys.*, **38**, 1283–1305.